Controls on paleokarst heterogeneity

Integrated study of the Upper Permian syngenetic karst in Rattlesnake Canyon, Guadalupe Mountains, USA

Gemma Labraña de Miguel

Controls on paleokarst heterogeneity.

Integrated study of the Upper Permian syngenetic karst in Rattlesnake Canyon, Guadalupe Mountains, USA.

Gemma Labraña

PhD Thesis

Universitat de Barcelona

Octubre 2011

Controls on paleokarst heterogeneity. Integrated study of the Upper Permian syngenetic karst in Rattlesnake Canyon, Guadalupe Mountains, USA.

A thesis submitted by

Gemma Labraña

Deptm. de Geoquímica, Petrologia i Prospecció Geològica
Universitat de Barcelona

PhD Thesis supervised by:

David William Hunt, PhD
Statoil, Research Center.
Bergen, Norway.

Dr. Juan José Pueyo Mur
Dptm. Geoquímica, Petrologia
i Prospecció Geològica (UB).

CONTROLS ON PALEOKARST HETEROGENEITY.

Integrated study of the Upper Permian syngenetic karst in Rattlesnake Canyon, Guadalupe Mountains, USA.

Memòria de tesi doctoral presentada per Gemma Labraña de Miguel per optar al grau de Doctora en Geologia.
La tesi doctoral ha estat desenvolupada en el marc del Programa de Doctorat de Ciències de la Terra (Bienni 2004-2006) sota la direcció del Dr. David William Hunt i del Dr. Juan José Pueyo.

Gemma Labraña de Miguel

Els directors de la tesi:

David William Hunt, PhD **Dr Juan José Pueyo**

Agraïments/Acknowledgments

Many people have been part of this project to a lesser and greater degree of involvement and I am indebted to thank them for their collaboration. This thesis could not have developed without the financing of Statoil, therefore firstly thank Dave Hunt for having trusted me to carry out this study in one of the areas he just loves such as the Guadalupe Mountains.

Many people of the Statoil Research Centre in Bergen have collaborated in parts of the project, from the first field campaign through the course of the thesis and in my visits to Bergen. I especially thank the collaboration of John Thurmond and Terry Lee Scarrott to introduce me into the world of virtual outrcrops and help me in the petrophysics, respectively. The reception in Bergen has always been excellent and for this reason I couldn't spare my shows of gratitude to Jean-Christophe Embry, Fabio Lapponi, Giulio Casini, Ian Sharp, Paul Gillespie, Josep Bernaus, Ole Jacob Martinsen among other locals that I surely forget, as the Norwegian surnames are quite difficult to remember (and pronounce) for a latin.

Un especial agraïment al directors de tesi David Hunt i Juan José Pueyo per l'ajuda i supervisió prestada.

Gràcies a Conxita Taberner per haver-me introduït en el món de l'investigació. Gràcies a Santi Giralt per la gestió econòmica del projecte.

I wish to thank George Von Knorring for the English reviews of this volume.

Agraeixo a Jaume Vergés les revisions estructurals del Capítol 4.

Agraeixo la cordialitat i eficiència tant al personal tècnic dels Serveis Cientificotècnics de la Universitat de Barcelona (SCT-UB) com als respectius de l'Institut Jaume Almera (ICTJA) i del Departament de Geoquímica i Petrologia de la Facultat de Geologia. Els meus agraïments a: Javier García Veigas, Eva Prats i Ana Domínguez (SEM); Toni Padró (ICP); Pep Elvira ICTJA (DRX); Eva Aracil, Rosa Marimón i Joaquim Perona (Isotopia); Jordi Illa (tractament de mostres) i al Servei de Làmina Prima de la Facultat de Geologia.

A tots els meus companys de despatx que han sigut varis d'ençà de l'inici d'aquesta tesi. Gràcies Guillem Gisbert, Edmundo Polanco i Flavia Ruggieri.

Una especial deferència pels meus companys de grup. Moltes gràcies Almudena Lorenzo, Alfonso Muñoz, Marta Rejas i en especial a l'Armand Hernández per la seva col·laboració en la primera campanya de camp.

Han estat prous anys per compartir experiències i inquietuds amb els semblants de la Facultat de Geologia. Gràcies Diego Iaffa, Daniel Bello, Marta Guinau, Mireia Butillé, Anna Quintà, Núria Carrera, Bahman Soleimany.

Als amics de sempre malgrat distànciaments geogràfics i no tan geogràfics. Gràcies Rosa Liñan, Marc Rabasa, Mònica Martínez, David Freixas i Roger Gibert.

I sobretot gràcies a la Pati, Xim, Oskar, Jordi, Montse, Irene i Eduard pels cicles de sopars que tant han alleujat les tensions i moments de desesperança durant la tesi.

I de les presències a les abscències, de l'afecció al dolor, del desequilibri a la fermesa, del coratge a la pau interior. Gràcies mama, segueixes i seguiràs formant part de mi.

Gràcies Marc, tu hi tens molt a veure en aquesta tesi i sobretot en els meus estats emocionals. Gràcies per la felicitat brindada durant aquests anys!

Índex

Resum extens

Aquesta tesi contribueix al coneixement dels mecanismes de dissolució que controlen el desenvolupament dels karsts singenètics i proporciona les claus per establir la seqüència de formació del sistema paleokàrstic de Rattlesnake Canyon, Guadalupe Mountains, New Mexico, EEUU. Degut al potencial com a reservori que tenen aquest tipus de sistemes, aquesta tesi no solament concorre al coneixement científic en relació als paleokarsts sinó que també pot ésser d'interès per la indústria del petroli.

L'aflorament de Rattlesnake Canyon ha resultat ser un escenari polivalent per l'estudi dels controls globals del sistema paleokàrstic, atès que les xarxes de fractures sindeposicionals del Pèrmic Superior i les geometries de dissolució romanen excel·lentment preservades. És comú que els sistemes paleokàrstics paleozoics estiguin afectats per col·lapse i enterrament dificultant la reconstrucció de les estructures de dissolució primerenca. En el cas del sistema kàrstic de Rattlesnake Canyon, el caràcter sindeposicional de la sequència de rebliment i la manca de deformació tectònica significativa han facilitat extraordinàriament la preservació d'aquestes estructures, ajudant a esclarir les relacions entre la fracturació i els processos de dissolució.

El treball previ de David Hunt i Edward Koša (Koša, 2003; Koša and Hunt, 2005, 2006) difongué les relacions estructurals i estratigràfiques entre les falles sindeposicionals de marge de plataforma i les estructures de dissolució a l'Slaughter Canyon. El treball a Rattlesnake Canyon fou inicialment concebut com una continuació a la investigació prèvia d'aquests autors per tal de desentrellar els buits que romangueren sense resoldre. La implementació d'estratègies resolutives conformà l'articulació del projecte derivant en un estudi multidisciplinari sòlid, fruit d'una activa investigació. El repte personal d'aquesta tesi ha estat aprofundir en el coneixement dels mecanismes de dissolució, establir una seqüència dels processos kàrstics i oferir una seqüència diagenètica completa que permetés l'avaluació d'heterogeneitats tempranes i l'avaluació del grau de modificació de les propietats de reservori.

Els resultats obtinguts en aquesta tesi han estat acomesos a la Universitat de Barcelona (UB) dins del marc d'un projecte de l'Institut de Ciències de la Terra "Jaume Almera" (ICTJA-CSIC). Aquest projecte fou finançat per Statoil.

Objectius

Aquest estudi cerca contribuir en el coneixement de les relacions entre les falles i fractures sindeposicionals i les estructures de dissolució a Rattlesnake Canyon, així com en el coneixement dels controls globals per la formació de karsts singenètics costaners.

La tesi inclou estudis multidisciplinaris dirigits a la determinació de la heterogeneïtat multi-escala del paleokarst de Rattlesnake Canyon mitjançant els següents objectius concrets: a) l'acompliment d'un model conceptual d'evolució del sistema kàrstic, b) la construcció d'un model 3D del sistema kàrstic, c) la determinació de la història diagenètica del paleokarst i d) la caracterització de les propietats de reservori del sistema.

Model hidrogeològic d'Illa Carbonatada

Els karsts costaners es desenvolupen preferencialment per interaccions químiques entre volums d'aigua fresca i volums d'aigua salada. Aquest model de dissolució és altament efectiu quan la recàrrega és autogèna. En general, les costes carbonatades dels continents tenen una recàrrega derivada de zones adjacents no carbonatades. Quan les plataformes i illes oceàniques tenen una extensió reduïda, el cicle hidrogeològic esdevé controlat pel medi local i la recàrrega pot ésser considerada autogèna. Sota aquestes particulars condicions, el Model d'Illa Carbonatada (Carbonate Island Model) s'aplica per explicar la generació de karsts singenètics que s'originen actualment a les illes Bahames, les illes Caimans i l'Illa de la Mona (Puerto Rico).

El Model d'Illa Carbonatada contempla la generació de lens d'aigua dolça que suren sobre volums més densos d'aigua salada. Aquestes lens es creen gràcies a l'acció d'un flux difòs d'aigua dolça subterrani en les àrees de costa. La interfície entre el volum d'aigua dolça i salada s'anomena haloclina i és en aquesta zona on es produeix el procés de dissolució. La relació espaial entre aquesta interfície i les posicions del nivel del mar és sovint emprada per explicar molts karsts costaners com a *composite karsts*.

Àrea d'estudi

Les Guadalupe Mountains es troben actualment als límits sudoest de l'estat de Texas i s'extenen cap al nordest més de 50 km cap a la part sudest de l'estat de New Mexico. En elles aflora la plataforma carbonatada del Pèrmic Superior vorejant els marges de la conca de Delaware.

Els estrats de la plataforma no presenten deformació tectònica intensa però estàn tallats per falles i fractures sindeposicionals documentades en l'àrea per Koša i Hunt (2005, 2006). Les falles i sistemes de fractures sindeposicionals afloren al llarg dels diversos canyons en les Guadalupe Mountains tallant perpendicularment i paral·lelament els estrats respecte la direcció de capa dels materials. A l'àrea d'estudi, les falles i sistemes de fractures estan modificats per dissolució i presenten una direcció paral·lela a la direcció de capa i als marges de la plataforma. És per aquesta raó que el canyó de Rattlesnake és un magnífic escenari per l'estudi de les relacions entre la deformació sindeposicional, l'estratigrafia i els processos diagenètics.

L'escull del Capitan i la seva plataforma guadalupiana associada constitueixen el denominat Permian Reef Complex. Aquest complex pèrmic consisteix en tres tractes de fàcies: les fàcies de rere escull, les fàcies de marge d'escull i les fàcies de conca (Hill, 1996). Les fàcies rere escull a la zona de plataforma de Northwest Shelf són el focus d'aquest estudi i estan composades per les formacions Seven Rivers, Yates i Tansill. Aquestes tres formacions representen seqüències deposicionals de tercer ordre (Kerans and Tinker, 1998). A la vegada aquestes seqüències contenen seqüències d'alta freqüència de quart ordre com són Seven Rivers 1–4, Yates 1–5 i Tansill 1–2 HFSs (Osleger, 1998; Tinker, 1998; Kerans and Tinker, 1999; Hunt et al., 2002). Aquestes seqüències d'alta freqüència presenten una geometria que s'engruixeix cap a mar amb alts volums de siliciclàstics a la base i fàcies carbonatades cap a sostre.

L'àrea d'estudi es troba a Rattlesnake Canyon i engloba aproximadament 200 m d'apilament de la unitat estratigràfica Yates i part del sostre de Seven Rivers. Dues falles normals conjugades (M i N) tallen la successió estratigràfica desde Yates 1 fins a Yates 4. Ambdues falles foren descrites com a falles sindeposicionals per Koša and Hunt (2006) i evidències d'acreixement dels estrats (*growth strata*) s'han observat al camp i descrit al Capítol 4.

La successió de Yates consisteix en un apilament de materials interpretats com a cicles transgressius-regressius de 1–10 m de gruix (Osleger, 1998; Hunt et al., 2002). El

sostre de la formació Seven Rivers aflora només al sector nord de la Falla M, en el bloc inferior. Al camp no s'han reconegut superfícies d'exposició. Estructures de *tepee* són abundants en la part superior del registre sedimentari, en les fàcies de cresta de plataforma (*shelf crest*) i estan lligades a zones de fracturació, fàcies amb abundant contingut en pisoids i precipitació de ciments.

Les fàcies de cresta de plataforma presenten fàcies dolomítiques amb fàbrica fenestral de textura grainstone i textura grainstone-packstone quan el seu contingut en pisoids és abundant. Els grainstone-packstone pisolítics s'han interpretat pertanyents a medis intermareals amb gradació cap a medis supramareals.

La zona de plataforma externa consta de grainstones amb components esquelètics i peloids. Un dipòsit de plataforma externa molt comú està constituït per grainstones amb fusulínids representant zones marines someres i obertes a la circulació d'aigua. Aquesta zona de plataforma externa es fa evident a la base de la successió estudiada gradant cap a fàcies de cresta de plataforma cap a les parts més superiors de la sèrie estratigràfica.

Estudi de camp del paleokarst i processos a meso-escala

Fent una anàlisi de l'acreixement dels estrats podem corroborar que la Falla M és sintectònica a Yates 1, Yates 2 i Yates 3; i la Falla N és sintectònica a Yates 3. Ambdues falles presenten una població associada de fractures de baix cabussament. Aquesta generació de fractures es formà a conseqüència d'extensió sobre plecs sinsedimentaris causats per l'acomodació del sediment.

Fent una anàlisi de fractures obtenim dues poblacions dominants de fractures en cada falla (Capítol 4: Figs. 4.5 i 4.6). Una població és comuna per les dues falles i representa l'estadi de fracturació associat a la formació de les falles. Les fractures associades a aquesta població són sub-verticals en cabussament i estan orientades NE-SW (Azimut mitjà: 44º). Cada falla té associada una població de fractures de baix cabussament amb orientacions NW-SE (Azimut mitjà: 45º) i NNE-SSW (Azimut mitjà: 7º) respectivament per la Falla M i la Falla N.

L'estudi de camp revela que les vores de les falles i fractures sindeposicionals estan modificades per dissolució així com els materials de la seqüència de rebliment del karst. Els materials afectats pel karst apareixen colorejats i aquesta característica facilita el

seu reconeixement a distància i l'observació de les seves relacions amb les estructures geològiques.

La seqüència de rebliment del karst està formada per grans volums de materials siliciclàstics amb interrupcions de nivells carbonàtics de gra fi. Tant la roca encaixant com la seqüència de rebliment del karst estan totalment dolomititzats.

S'observen dues geometries de dissolució que suggereixen dos mecanismes de dissolució que poden interactuar entre sí d'acord amb la interpretació del sistema. Una morfologia de dissolució accentúa i modifica la geometria vertical de la falla donant lloc a coves de fracturació que enregistren episodis de col·lapse. Aquests espisodis es fan evidents per la troballa de dipòsits de bretxa a les parts més internes d'ambdues falles formant part de la seqüencia de rebliment del paleokarst. D'altra banda, destaca la presència d'una altra geometria de dissolució que s'extén en nivells laterals seguint la direcció dels estrats, neixent en els marges de les falles i atenuant-se lateralment cap a la roca encaixant. Aquest tipus de dissolució defineix nivells sub-horitzontals kàrstics evidents en el camp per les seves coloracions vermelloses i groguenques.

Existeix una nomenclatura prèvia referent a tipologies de dissolució similars a les extensions laterals kàrstiques trobades a Rattlesnake Canyon. Quinlan (1978) proposà el terme karst interestrat per definir morfologies de dissolució similars que afecten a roques depositades abans de l'espeleogènesi. Palmer i Palmer (1989) es referíen a karst intraestrat per descriure processos de dissolució que tenen lloc durant l'enterrament. L'espeleogènesi a l'àrea d'estudi sembla concordar més amb la distribució intraestrat de Palmer i Palmer (1989), però la nostra interpretació del mecanisme de formació ens allunya d'un ambient d'enterrament. Degut a això, en aquesta tesi apliquem un nou terme per referir-nos genèricament a aquesta dissolució estratiforme: dissolució lligada als estrats (*stratabound dissolution*).

A partir de l'observació in situ de la distribució espaial de les litofacies kàrstiques i les diferents geometries de dissolució es va crear un mapa localitzant els diferents tipus de dipòsits de bretxes, les zones de fractura i delineant dues zones que defineixen l'arquitectura del sistema en funció del grau de desorganització (Capítol 4: Fig.4.3). La discriminació d'aquestes zones, com es veurà més endevant, té un efecte directe en la generació de diferents patrons de cimentació diagenètics. Aquestes dues zones han estat anomenades com a zona de paleocova (*paleocave zone*) i zona de modificació kàrstica (*karst damage zone*).

La zona de paleocova representa l'espai físic de les paleocoves i es caracteritza per la presència constant de dipòsits de bretxa. Té dimensions de desenes de metres en amplitud i pot sobrepassar el centenar de metres en alçada. La zona de modificació kàrstica sensu strictu conté la zona de paleocova però també engloba una zona amb menys afectació de processos gravitacionals i molt menys desorganitzada. En la tesi sovint ens referim a la zona de modifació kàrstica quan fem referència a la zona menys modificada, i a la zona de paleocova quan fem esment de la zona més desorganitzada, malgrat la inclusió de la zona de paleocova dins la zona de modificació kàrstica. Aquesta zona menys modificada es caracteritza per la presència de porositat vacuolar (pocs centímetres), xarxes de fractures de baix cabussament a les parts superiors, i passatges estratiformes. Aquests passatges s'anomenen a la tesi com a coves lligades a l'estratificació (*stratabound caves*).

L'observació en camp de les litofàcies del karst portà a la distinció de dipòsits de bretxes associats a processos de col·lapse. La classificació d'aquests dispòsits de bretxa es va dur a terme d'acord amb la sistemàtica de Loucks (1999).

Les bretxes caòtiques són el dipòsit predominant a les àrees internes de les falles. Es caracteritzen per un grau alt de desordre en la distribució dels seus clastes. Són predominants a la base i les parts intermèdies de la seqüència de rebliment de la Falla M i a la base i les parts altes de la seqüència de rebliment de la Falla N. Són generalment matriu-suportades i la provinença dels seus clasts és diversa incloent clastes de nivells superiors de la roca encaixant (clastes de grainstones amb fusulínids). Les vores dels clastes sovint presenten contactes de sutura i evidències de dissolució. Molts dels seus clastes estan retreballats.

Aquestes bretxes s'atribueixen a col·lapses de les parets o sostres de cova. És freqüent trobar ciments dolomítics, especialment dins de clastes retreballats.

Les bretxes de mosaic es localitzen a les zones altes de les paleocoves i són properes a les seves parets, essent adjacents a zones de roca encaixant no desorganitzades per col·lapses. Acostumen a trobar-se immediatament per sota de zones de fractura. La característica més rellevant d'aquest tipus de dipòsits és la lleugera rotació dels seus clastes respecte a la posició original de l'estratificació, observant una gradació des dels estrats continuus de la roca encaixant cap a una lleu desestabilització en aquests dipòsits. El sediment interclaste presenta les mateixes característiques que el sediment de les bretxes caòtiques malgrat presentar una tendència cap a colors groguencs per contra dels vermells trobats en les matrius de les bretxes anteriorment descrites.

Les bretxes de mosaic són menys freqüents que les caòtiques i es pensa que estan associades als processos de dissolució lateral. Es creu, però, que les zones de fractura suprajacents afavoriren un flux de fluid que incrementà la dissolució cap a zones inferiors en aquestes àrees.

Les bretxes tipus crackle o d'esquerdes de la roca encaixant estan sovint associades amb els marges de les zones de falla. Els seus clastes són angulars i no tenen desplaçament associat aparent. No són matriu-suportades.

Les bretxes tipus crackle són interpretades com el resultat de moviments gravitacionals cap a la zona de cova quan les falles eren actives.

La dissolució lligada als estrats es detecta al llarg de determinats horitzons estratigràfics que no es correlacionen estratigràficament entre sí. Això fa pensar en un control hidrogeològic que pugui ser encabut dins el Model d'Illa Carbonatada. Aplicant aquest model, aquests horitzons de dissolució podrien ésser indicadors de les posicions de la paleohaloclina durant l'època d'activitat del paleokarst.

Quan la tectònica local interfereix amb la migració vertical de les lens d'aigua dolça, la distribució final de les coves d'haloclina resulta en una complexa distribució de nivells reutilitzats que sovint es superposen. Aquest és el cas de Rattlesnake Canyon, on el patró final de dissolució és difícil d'entendre sense una restitució de les dues falles estudiades. La Figura 4.8 del Capítol 4 il·lustra el procés que genera aquests passatges d'acord amb l'evolució de les falles. Aquest procés promou el reutilitzament de passatges laterals abandonats a mesura que l'activitat de les falles evoluciona. Per tal de validar aquesta hipòtesi es va fer una restitució de les falles sindeposicionals durant l'època de deposició de les unitats de la formació Yates. El temps de restitució comprèn des del sostre de Yates 2 fins a la part superior del cicle Yates 4 (Capítol 4: Fig. 4.9).

La restauració d'ambdues falles manifesta que els nivells de dissolució lligada als estrats esdevenen horitzontalment alineats en cada estadi de restitució. Això evidencia que la formació de coves lligades als estrats fou controlada per les falles sindeposicionals i pel règim hidrogeològic que operava durant la deposició de la formació Yates. El patró final posa de manifest la generació de passatges estratiformes abandonats i reutilitzats, presumiblament originats durant èpoques d'estabilització del nivell del mar. El mètode de restauració prova que la correlació d'aquests nivells és precisa durant el marge de temps emprat. D'acord amb aquesta interpretació, el període de més freqüència de formació d'aquests nivells de dissolució a Rattlesnake Canyon fou durant la deposició de Yates 3.

Durant la deposició del cicle Yates 3 s'observa una tendència someritzant de la paleo-haloclina suggerint una disminució de la recàrrega d'aigua dolça i/o una transició cap a condicions climàtiques més àrides. La presència de fàcies evaporítiques a les parts superiors dels cicles Yates 2 i Yates 3 recolza un canvi climàtic.

S'ha establert una seqüència de processos espeleogenètics en relació a l'època de formació de les coves lligades als estrats obtenint un model conceptual d'evolució del sistema kàrstic.

Processos anteriors a la generació de coves lligades als estrats:

Anteriorment a la dissolució lligada als estrats tenim un patró de dissolució controlat per fractures que queda palès en l'observació de camp. Els sistemes de fractures estan fortament afectats per dissolució així com les vores de les falles. Molts processos s'atribueixen a aquest tipus de dissolució durant aquest estadi inicial (Capítol 4: Fig. 4.10).

a) Dissolució controlada per fractures. La dissolució en les xarxes de fractures extensionals de baix cabussament causà eixamplament d'aquestes. Aquesta tipologia de dissolució es troba restringida a zones d'escala mètrica. El paleoflux probablement esdevingué molt canalitzat i els seus efectes corrossius es manifesten a les parets de les fractures, plans d'estratificació i matriu adjacent. En aquestes àrees el component gravitacional és menor tot i tenir efecte en la generació de dipòsits de bretxa de mosaic.

b) Col·lapse de cova. La dissolució és afavorida pel flux al llarg de fractures. Aquests processos comprenen àrees de desenes de metres. En aquestes zones el component gravitacional és major i queda palès per la presència de bretxes de mosaic i dilatació d'estrats.

c) Passatges oberts verticals-sòl de cova. Al llarg dels passatges verticals la dissolució és localment extensa al llarg de les parets de la cova degut al flux difòs podent penetrar pocs metres cap a la roca encaixant. El component gravitacional és alt contribuint extensament a la formació de dipòsits de bretxa caòtics en àrees d'extensió de desenes de metres.

d) Aport de sediment. L'entrada de sediment siliciclàstic s'interpreta com un procés continuu durant l'activitat kàrstica. La presència d'acumulacions de sediment siliciclàstic en la seqüència de rebliment de les dues falles i la presència de dics a l'entrada superior d'ambdues coves apunta a un flux continuat de sediment.

Processos relacionats amb la formació de coves lligades als estrats:

Els processos de *sagging* i la formació de bretxes de mosaic són processos derivats de la corrossió produïda a l'haloclina. La corrossió produeix nova porositat i flexió dels gresos suprajacents com a resultat de deformació plàstica de materials poc competents. La creació de nou espai permet la rotació de clastes derivats de fracturació originant bretxes de mosaic.

La distribució espaial d'aquest tipus de bretxes en ambdues falles es troba restringida als blocs superiors, immediatament per sota de zones amb fractures extensionals de baix cabussament, suggerint una contribució de la dissolució amb control per fractures. A més a més, però, aquests dipòsits sempre es troben en continuació lateral amb nivells de coves lligades als estrats, suggerint que el mecanisme de formació de les bretxes de mosaic resultà de la interacció entre la dissolució d'haloclina i un flux canalitzat provinent de les xarxes superiors de fractures.

Processos posteriors a la generació de coves lligades als estrats:

L'espeleogènesi de Rattlesnake Canyon cessà en major grau cap a la fi del període de deposició del cicle Yates 3, però, a més petita escala el sistema presenta evidències de reactivació durant l'interval de deposició del baix Yates 5. Aquesta reactivació consisteix en llentions d'escala sub-mètrica reomplerts de sediment groguenc. La zona de reactivació presenta forma de T invertida indicant que part del flux de fluid provenía de la part alta de la plataforma i estava molt canalitzat. Aquestes morfologies de dissolució es pensa que es varen formar per damunt de l'aqüitard i s'interpreta que són conseqüencia d'estadis incipients de dissolució en el sistema kàrstic.

Construcció d'un model 3D amb integració de dades d'aflorament, perfils de GPR i dades de Poroperm.

La construcció del model 3D de Rattlesnake Canyon constitueix un exemple d'integració de dades d'aflorament, perfils de GPR (Ground Penetrating Radar) i dades petrofísiques en un entorn tridimensional. La construcció del model s'ha dut a terme a partir de la integració, tant de dades de camp com d'anàlisis petrogràfiques a un model digital d'aflorament. El model digital d'aflorament fou obtingut a partir de l'ús d'escàners de làser terrestre LIDAR (Light Detection and Ranging). La combinació de la digitalització de polilínies interpretades en el model digital junt amb dades estructurals (direccions de capes i cabussaments) permeté la construcció de les superfícies.

El model consisteix en la reproducció dels límits de la zona de paleocova i la zona de modificació kàrstica. També incorpora la distribució espaial dels dipòsits de bretxa i diversos horitzons estràtigràfics correlacionats de la roca encaixant.

Els paràmetres diagenètics són difícils d'integrar en un model 3D, especialment quan no són dependents d'estructures geològiques. Atès que el sistema kàrstic de Rattlesnake Canyon està fortament controlat per fractures, ofereix gran potencial de reproducibilitat sota modelització geomètrica basada en objectes.

El Capítol 5 de la tesi documenta el flux de treball específicament dissenyat per minimitzar les incerteses en la construcció d'aquestes superfícies tan irregulars en direcció i cabussament. El mètode de dominis de cabussament (*dip domain*) ha resultat eficaç per la construcció d'aquestes superfícies diagenètiques. L'acompliment del model ha comportat el fet de treballar en diferents entorns de software (OpensceneGraph (OSG), Microstation i Gocad).

La integració de perfils de GPR al model ha permès quantificar localment la penetració del sistema cap a la plataforma. El model d'evolució del paleokarst junt amb observacions de camp suggereixen que el sistema és dimensionalment més pronunciat al llarg del marge sud de la plataforma. Els resultats mostren que el paleokarst s'extén almenys 70 m penetrant la plataforma cap al nord, en la zona superior del karst i dins les fàcies de cresta de plataforma (Yates 3 i Yates 4). L'observació de dipòsits de col·lapse més caòtics cap a l'altra banda del canyó, juntament amb el model d'evolució proposat pel sistema kàrstic, fa pensar que el sistema pot ésser molt més extens cap al sud.

Diagènesi

La dolomitització és massiva a Rattlesnake Canyon i afecta tant la roca encaixant com el sediment que rebleix el karst. Els sediments dolomititzats del paleokarst coexisteixen junt amb ciments de calcita dins les zones de modificació kàrstica. Els sediments de rebliment del paleokarst han patit diferents episodis diagenètics de reemplaçament, seqüències de cimentació dolomítica, desdolomitització i precipitació de ciments de calcita. La dolomita de reemplaçament es reconeix com a producte de dolomitització primerenca del carbonat de plataforma i dels sediments siliciclàstics en les zones de karst. La interpretació de la dolomitització primerenca es basa en evidències isotòpiques i en l'anàlisi d'elements traça de les diferents generacions de dolomites, que quadra amb el model de dolomitització per

reflux de salmorres evaporítiques proposat prèviament per diferents autors (Melim, 1991; Melim and Scholle, 2002).

Dos patrons de cimentació són identificats en el sistema kàrstic de Rattlesnake Canyon:

• ciments de dolomita omplint vacuoles i amb una senyal isotòpica en ^{18}O més baixa que la dolomita de reemplaçament

• desdolomites i calcites associades a sulfato-reducció bacteriana (empobrides en ^{13}C) en porositats de fractura i reomplint motlles d'anhidrita

El patró de cimentació de dolomita s'observa a través d'una seqüència multifàsica d'evolució textural generant carcasses dolomítiques. En zones d'increment de porositat, els rombes grollers de dolomita sucrosa es troben envoltats per corticles límpids i fins que mostren catodoluminiscència (CL) brillant. Aquests grups de dolomita sacaroide estan sovint cimentats per una dolomita límpida, més tardana, ocloent la porositat intercristal·lina. Els ciments de dolomita generalment presenten catodoluminiscències brillants amb diferents zones de sobrecreixement revelant patrons de zonació concèntrics. Els patrons de cimentació de la dolomita es troben restringits a zones preservades de l'activitat de les falles i a zones de menor modificació diagenètica tardana, aïllades de les xarxes de fractures.

La desdolomitització, per contra, està limitada a àrees d'intensa circulació de fluids, com ara són les xarxes de fractures, i a zones de porositat vacuolar intercomunicada. La desdolomitització està lligada a un patró de cimentació que conté calcites i ciments de dickita. Els ciments de desdolomita són extremadament heterogenis en CL amb diverses subzones luminiscents: Dd1, Dd2 i Dd3. Dd1 està sovint corroïda per Dd2. Dd2 apareix zonada i sovint corroïda per Dd3. Dd3 grada de no luminescent a tons vermell fosc apagats. Dd1 i Dd2 es troben regularment associades a dickita. Aquestes subzones s'interpereten com resultants de desdolomitització, en base a l'ocurrència de fàbriques de dissolució i per la presència de relictes de dolomita tals com rombes calcititzats dins els mosaics de desdolomites amb continguts de calcita superiors al 50%.

Aquells ciments sense relictes de calcitització i amb luminiscències més baixes s'han interpretat com a ciments de calcita (Cc1) que es reconeixen en zones de fractura, microconductes de dissolució cònics (micro solution pipes) i reomplint motlles d'anhidrita.

El patró de cimentació trobat a les zones de fractures inclou ciments de desdolomita i calcita no fèrrics amb gradació de no luminiscents cap a luminiscències apagades, indicatiu d'ambients moderadament òxics. Dins les desdolomites, les gradacions en subzones de

diferent luminiscència i patrons de zonacions s'intueixen com a a variacions de Eh en el medi, que poden anar acompanyades de variacions en el pH. Els ciments de dolomita, per contra, estan enriquits en ferro i presenten luminiscències fortes, indicatiu d'ambients subòxics. La progressiva reducció en ferro i manganès dels ciments de desdolomita i calcita està directament associada a l'etapa terciària d'aixecament en la zona, amb la conseqüent entrada d'aigua meteòrica al sistema.

La cimentació amb dickita està regularment associada als ciments de desdolomita amb evidències de corrossió generalment en zones de fractures.

En l'estratigrafia de ciments de l'àrea d'estudi, es reconeix també una calcita de mida de cristalls més grollera (fins a centimètrica) que es troba sempre per damunt de la calcita i les desdolomites anteriors. Aquesta calcita mostra una senyal isotòpica diferent, està empobrida significativament en ^{18}O i dóna una composició isotòpica de carboni positiva. La senyal isotòpica concorda amb un origen hidrotermal d'alta temperatura i per aquesta raó se la relaciona amb un hidrotermalisme miocè, fet que és coherent amb els episodis documentats en la zona (Hill, 1996).

Gran part de les desdolomites i ciments esparítics de calcita amb baixes luminiscències presenten valors de $\delta^{13}C$ baixos (assolint -15 ‰ PDB), suggerint un increment de CO_2 i fluids parentals associats a sulfato-reducció bacteriana (Capítol 6: Fig. 6.11). La generació d'aquests productes amb valors baixos de $\delta^{13}C$ s'atribueix a processos d'oxidació bacteriana dels hidrocarburs de la conca. La presència d'inclusions fluides riques en hidrocarburs tant primàries com secundàries en aquests ciments ha estat també un bon indicador de la coetanietat d'aquests productes amb la recàrrega terciària d'hidrocarburs en la zona. Així doncs, els ciments de desdolomites i calcites són interpretats com a productes diagenètics tardans, íntimament relacionats amb la recàrrega d'hidrocarburs de la conca de Delaware.

Durant l'etapa d'aixecament, la diagènesi siliciclàstica fou la responsable de la generació de ciments de dickita i de la mobilització de ferro, resultant en la formació d'òxids i hidròxids de ferro generats per oxidació de sulfurs i enriquiment supergènic de la zona d'alteració kàrstica. Durant aquesta etapa, els canvis de proporció en la barreja de fluids de diferent origen (dissolució d'evaporites, entrada d'aigua meteòrica i recàrrega d'hidrocarburs) probablement originaren desdolomitització i precipitació de calcita lleugera en ^{13}C. Els diferents graus de barreja de fluids resultaren en la creació de porositat secundària en molts intervals del karst.

Els ciments de dolomita s'interpreten com a ciments d'enterrament somer d'acord amb la seva senyal isotòpica i la seva semblança a les carcasses dolomítiques de Choquette i Hiatt (2008). La diagènesi tardana aprofità les xarxes de fractures sindeposicionals modificant així les estructures kàrstiques primàries per crear porositat secundària. La deposició de ciments argilosos contribuí significativament en el segellat d'aquesta porositat. I aquest procés diagenètic tardà apareix coetani amb la recàrrega d'hidrocarburs de la conca.

Avaluació de les propietats de reservori del sistema kàrstic.

Per tal d'avaluar les propietats petrofísiques del sistema es varen escollir tres horitzons estratigràfics a fi d'estudiar l'expansió lateral del karst envers la roca encaixant. Els nivells escollits presenten textures grano-suportades però les seves propietats petrofísiques varien independentment de la natura de les seves textures. Les textures dels nivells superiors són definides com a grainstones pisolítics, mentre que la de l'inferior varia de packstone cap a grainstone de fusulínids. Els dos horitzons inferiors presenten desplaçament vertical significatiu degut a l'activitat d'ambdues falles. Els nivells contemporanis a les falles presenten permeabiitats més elevades que el nivell superior estudiat, que pràcticament no presenta desplaçament i fossilitza el sistema.

El nivell inferior amb fusulínids és també contemporani a l'activitat de les falles i forma part de la base del cicle Yates 3. Aquest nivell localitza valors alts de permeabilitat i porositat intrapartícula.

El nivell pisolític mig forma part del sostre del cicle Yates 3 i mostra una expansió del karst d'uns 40 metres des de les vores de les falles. Els majors valors de permeabilitat es localitzen a les vores del karst i en zones modificades per dissolució, amb porositat de tipus intercristal·lina i vacuolar.

El nivell pisolític superior depositat durant els estadis finals de l'evolució del sistema kàrstic (part superior de Yates 4) és el que pateix la menor expansió lateral del karst (pocs metres). El nivell enregistra els valors més baixos de permeabilitat i porositat de tipus interpartícula.

L'anàlisi dels tres nivells demostra que el desenvolupament del karst, lligat directament amb l'evolució de les falles, fou un control important en l'evolució de les propietats petrofísiques de la roca encaixant.

La cimentació de dickita i desdolomitització, preferentment al llarg de zones de fractura, reduíren significativament la permeabilitat dins la seqüència de rebliment kàrstic durant la diagènesi tardana. Els porus de la roca encaixant estan menys modificats que els de dins la seqüència de rebliment del karst i, per tant, la porositat intercristal·lina i vacuolar cimentada primerencament amb dolomita es troba preservada majoritàriament en aquestes zones. Encara que els valors més alts de Poroperm es troben confinats a zones de porositat de fractura i de bretxa al voltant de les vores de falla, l'heterogeneïtat lateral és un reflex de l'efectivitat de la dissolució produïda per les lens d'aigua dolça.

Integració global de resultats

El particular emplaçament del karst en els marges de la plataforma i el sistema hidrogeològic que afavorí la formació de lens d'aigua dolça, han permès integrar la cicloestratigrafia per establir una seqüència kàrstica.

L'arquitectura de col·lapse de la zona de paleocova fa pensar que les primeres etapes de dissolució es produiren en condicions vadoses durant etapes de baixada del nivell del mar, mentre que la formació d'extensions laterals de modificació kàrstica semblen haver estat formades durant períodes d'estabilització del nivell del mar. L'absència de ciments vadosos junt amb la seqüència evolutiva de les lents interpretada a partir de la restitució d'ambdues falles i la conseqüent correlació dels nivells sub-horitzontals kàrstics, fa pensar que el mecanisme de dissolució per aquestes tipologies kàrstiques tingué lloc en condicions freàtiques, segurament en condicions molt someres.

Els mecanismes d'evolució del sistema kàrstic es veieren, per tant, condicionats per la ciclicitat del sistema deposicional encaixant juntament amb la interacció de les falles. La tendència someritzant de les lens indica un trànsit cap a condicions climàtiques més àrides a sostre de les seqüències, quedant confinat el sistema a un ambient de sebkha amb precipitació d'evaporites.

La dissolució a l'haloclina donà lloc a la generació de porositat vacuolar i intercristal·lina. Aquests tipus de porus es concentren al llarg dels nivells horitzontals de les coves. La progressiva modificació textural dels ciments de dolomita pot ésser un indicador del grau de permeabilitat primerenca generada en el sistema kàrstic. Els ciments d'enterrament somer que segellen la porositat kàrstica són compatibles amb la precipitació d'aigües mesosalines sota condicions lleugerament reductores, d'acord amb la isotopia de carboni i oxigen i la geoquímica d'elements traça. Els ciments de dolomita precipitats dins

les cavitats condicionaren l'espai romanent després del reemplaçament de dolomita i d'una possible etapa primerenca de dissolució parcial de les evaporites. En les àrees laterals de dissolució, aquest estadi de cimentació ha quedat preservat, podent observar la seqüència completa cap a la formació multiepisòdica de carcasses de dolomita que segellen gran part de la porositat primerenca. Aquestes àrees han quedat molt poc modificades per processos tardans de diagènesi meteòrica esdevinguts durant l'etapa d'aixecament. Per contra, en les zones de paleocova (molt més desorganitzades i fracturades) la modificació diagenètica tardana és intensa indicant que la porositat i permeabilitat atribuides a l'etapa singenètica del karst foren significatives i efectives per la circulació posterior de fluids durant el Terciari. La dissolució de les evaporites podría haver començat durant les primeres etapes de formació del sistema, però s'accentuà tardanament degut a l'entrada d'aigua meteòrica en l'etapa d'aixecament. Aquest procés de dissolució també fou responsable d'un augment del flux, creant nova porositat en el sistema cavernós.

A partir del reconeixement dels rebliment de fractura (desdolomites i calcites associades a la presència de dickita) es pot afirmar que les tendències d'increment de permeabilitat foren condicionades per les xarxes de fracturació sindeposicional i per la porositat de bretxa en les parts més caòtiques i desorganitzades, dins les zones de paleocova. Un model diagenètic predictiu del sistema hauria, per tant, de tenir en compte la densitat de fracturació i l'estimació quantitativa dels volums de porositat kàrstica. La densitat de fracturació està ben determinada en el sistema. L'estimació del volum de porositat kàrstica en les zones bretxificades és molt més difícil de predir ja que la diagènesi siliciclàstica ha modificat les textures deposicionals inicials sense cap patró aparent. Les zones de major desestabilització gravitacional (zones de paleocova) queden ben fixades en el sistema i constitueixen zones de retenció de porositat esdevenint, però, molt més sensibles a una modificació diagenètica posterior, una modificació molt agressiva quan s'involucren fluids aquosos amb hidrocarburs. Les condicions d'acidesa de la barreja d'aquests fluids amb fluids meteòrics i salins provinents de la dissolució d'evaporites foren favorables per la dissolució de feldspats amb la posterior precipitació de ciments caolinítics que disminuiren dràsticament la permeabilitat en aquestes àrees. La història diagnètica de Rattlesnake Canyon és complexa incloent l'episodi més tardà d'hidrotermalisme amb la conversió de caolinita-dickita i la cimentació massiva de calcita en la porositat romanent.

L'anàlisi de formes cristal·lines de goethita trobades dins les calcites poiquilotòpiques Cc1 i els ciments de desdolomites, atribueix la formació d'aquests compostos a la precipitació directa a partir de solucions aquoses amb ferrihidrita a temperatura ambient. Això indica que el procés de mobilització del ferro fou actiu durant l'etapa tardana d'aixecament.

L'origen del ferro podría estar relacionat amb la dissolució de siliciclàstics causada per la càrrega d'hidrocarburs. Els colors groguencs dels rebliments de coves es deu a la presència de goethita, especialment en zones amb bretxes mosaic, immediatament per sota de xarxes de fractures sindeposicionals. El camp d'estabilitat de la goethita indica que aquest mineral pot precipitar amb pH bàsics. La paragènesi d'aquest mineral, amb els ciments de desdolomites i calcites Cc1, indica coetaneitat amb la càrrega d'hidrocarburs. A partir de la localització d'aquests rebliments s'interpreta que la goethita precipità en zones d'alta dissolució quan s'aconseguia un efecte tampó que reduia significativament les condicions àcides anteriors, favorables per la precipitació de dickita i la dissolució de carbonat. Es pensa que la circulació de fluids, en aquestes zones, era afavorida per la xarxa de fractures immediatament superior.

El reconeixement de pseudomorfs de pirita (Capítol 6: Fig. 6.9), com ara hematites, intímament relacionats amb romboedres de dolomita, i majoritàriament preservats en els passatges laterals del karst, és també indicador d'una possible activitat bacteriana sulfato-reductora molt primerenca.

El pla de treball inicialment disenyat per la construcció del model 3D cercava delimitar dues zones en cada falla, la zona de paleocova i la zona de modificació kàrstica, en base a la distribució de litofacies i a la geometria de les zones de dissolució. Després dels estudis diagenètics es pot argumentar que cadascuna d'aquestes zones, o parts d'elles, reflecteixen també comportaments diagenètics diferents. El patró de sindiagènesi associat a un model de barreja d'aigües meteòriques i marines es preserva al llarg de les coves lligades a l'estratificació dins les àrees de modificació kàrstica. Aquest estadi de diagènesi inicial és reponsable dels alts valors de Poroperm preservats en aquestes zones. Les zones de fracturació sindeposicional que han quedat preservades a les parts superiors d'ambdues zones de modificació kàrstica i a les zones de bretxa dins les zones de paleocova han estat massivament cimentades segellant porositat secundària.

Conclusions

Aquesta tesi focalitza en les relacions entre les falles sindeposicionals i l'evolució del sistema kàrstic en el context geològic de marge de la plataforma del Capitan. La tesi proporciona informació relativa a l'estudi detallat de dues falles (M i N) que tallen materials del Pèrmic Superior. L'escenari ha resultat especialment satisfactori per desxifrar la seqüència del paleokarst i per establir els seus controls. El model 3D fou construït per

representar l'heterogeneitat espaial del paleokarst i per determinar l'extensió penetrativa del sistema. L'estudi també ofereix noves aportacions en l'evolució diagenètica del sistema que condicionaren la modificació de les seves propietats de reservori.

A continuació es detallen les conclusions més rellevants de la tesi agrupades en apartats específics:

Evidències de camp relatives a episodis d'espeleogènesi primerenca

• Les xarxes de fractures sindeposicionals estan modificades per dissolució kàrstica i contenen clastes retreballats amb evidència de corrossió en les seves vores.

• Gran part dels clastes retreballats del rebliment d'aquestes xarxes provenen de nivells carbonatats de la roca encaixant.

• Els rebliments de les fractures i la seqüència de rebliment del paleokarst estan dolomititzats amb l'excepció dels ciments de calcita Cc1 que presenten una paragènesi poc clara al camp.

Distribució espaial de les geometries kàrstiques i distinció de zones kàrstiques

• Es reconeixen dues geometries de dissolució distinctives: un patró vertical continu que segueix la geometria de les falles, i horitzons sub-horitzontals discrets que neixen des dels límits de les falles cap a la roca encaixant.

-El patró vertical de dissolució accentúa la geometria d'ambdues falles i és atribuït al desenvolupament de fractures/falles.

-El patró sub-horitzontal de dissolució es concentra al llarg d'horitzons estratigràfics específics sense cap correlació estratigràfica. Aquest patró de dissolució s'anomena, en aquest treball, dissolució lligada als estrats, i és el responsable de la creació de coves o passatges lligats als estrats (*stratabound caves or passages*).

A la part alta de la seqüència de rebliment, on la seqüència roman preservada de l'activitat de les falles, la traça dels passatges lligats a l'estratificació pot ésser seguida cap a les parts internes de les falles. Aquest tipus de dissolució talla, en aquestes àrees, la seqüència de rebliment del karst evidenciant-se així que postdata la dissolució vertical.

• Dues zones són definides i cartografiades en aquest estudi en relació a la distribució de fàcies de paleokarst: la zona de paleocova i la zona de modificació kàrstica.

-La zona de paleocova delimita l'antic espai de la cova i conté àrees de significatiu col·lapse. Els dipòsits de bretxes caòtiques són molt abundants.

-La zona de modificació kàrstica inclou la zona de paleocova i una zona de menor desorganització de la roca encaixant. Inclou les coves lligades a l'estratificació i els rebliments de les fractures.

Mecanismes de formació del paleokarst

• La formació del karst amb morfología vertical s'atribueix a un flux canalitzat associat als sistemes de fractura i falles.

• Després d'una restitució del desplaçamement de les falles M i N des del sostre de Yates 2 fins a la part superior de Yates 4, els passatges sub-horitzontals esdevenen alineats en cada estadi de restitució. Això suggereix que el mecanisme de formació de les coves lligades a l'estratificació pot ésser atribuït a un desenvolupament kàrstic singenètic que encaixa amb el Model Hidrogeològic d'Illa Carbonatada.

• La presència de bretxes mosaic, immediatament sota les àrees de fracturació i amb clara associació amb les coves lligades a l'estratificació, suggereix que el flux difós sub-horitzontal fou probablement incrementat a través de la conectivitat amb el flux sub-vertical canalitzat derivat de la xarxa de fractures.

Període d'activitat kàrstica

• La restauració d'ambdues falles situa les coves lligades als estrats com a possibles indicadors de la posició de l'haloclina durant la deposició de la formació Yates.

• El període més productiu per la generació d'aquests nivells kàrstics sub-horitzontals sembla ser durant la deposició del cicle Yates 3, d'acord amb el procés de restitució.

Espeleogènesi a Rattlesnake Canyon

• Espeleogènesi anterior a la formació de les coves lligades al estrats:

(I) Dissolució controlada per fractures. La corrossió en les fractures extensionals produí un eixamplament de les fractures en zones restringides a escala métrica.

(II) Col·lapse de cova. La corrosió es localitza al llarg dels sistemes de fractures i superfícies d'estratificació en àrees d'escala de desenes de metres. El paleoflux degué ser canalitzat al llarg de nombroses fractures i plans de dilatació. Les bretxes mosaic resulten en part d'aquest procés.

(III) Formació de passatges verticals oberts. La corrossió en aquest estadi és local i s'extén al llarg de les parets verticals de les coves. El flux podría tenir un component de difusió al llarg dels passatges oberts. La desestabilització gravitacional és significativa en àrees que abarquen desenes de metres. Els dipòsits caòtics resulten d'aquest procés.

• Espeleogènesi coetània a la formació de coves lligades als estrats:

(IV) Els process de *sagging* i la presència de bretxes mosaic estan relacionades amb dissolució a l'haloclina. La corrossió en aquest estadi produeix nova porositat i deformació de materials poc competents. La formació de porositat permet la rotació de clastes accentuant la formació de bretxes mosaic.

• Espeleogènesi posterior a la formació de coves lligades als estrats:

(V) La incipient reactivació del sistema és caracteritzada per un procés de dissolució selectiva de matriu. No opera cap component gravitacional. Aquest estadi és el responsable de la formació de llentions grocs (amb goethita) que mostren com operava la dissolució inicial.

Model 3D del paleokarst

• El model de paleokarst reprodueix la distribució espaial de les fàcies del paleokarst així com també les vores irregulars de les superfícies que delimiten la zona de paleocova i la zona de modificació kàrstica.

• El flux de treball per la construcció d'aquest model és complex i s'explica en el Capítol 5 d'aquesta tesi.

• La distància de penetració del karst fou determinada integrant perfils de GPR. S'estima que el sistema penetrà al voltant d'uns 70 m en direcció nord, dins la plataforma.

Diagènesi

• La seqüència de rebliment del karst experimentà diferents episodis de modificació diagenètica. Aquests estadis inclouen: reemplaçament, cimentació dolomítica multifàsica, desdolomitització i precipitació de ciments de calcita.

• Dos patrons de cimentació són identificats a Rattlesnake Canyon: ciments de dolomita omplint vacuoles, i desdolomites i calcites situades en porositat de fractura, empobrides en ^{13}C i associades amb processos de sulfato-reducció bacteriana.

•Els ciments de dolomita que omplen vacuoles s'interpreten com una seqüència d'evolució textural multifàsica que dóna lloc a carcasses dolomítiques formades en un ambient d'enterrament somer.

• La desdolomitització es detecta per la presència de fàbriques de dissolució en la dolomita i per la presència de relictes de dolomita tals com rombes calcititzats de dolomita i relictes flotants dins els mosaic de desdolomites La distribució dels ciments demostra que la desdolomitització es va iniciar preferentment al llarg dels sistemes de fractures.

• Els ciments de calcite es troben fonamentalment com a rebliment de fractures, microestructures de dissolució còniques i omplint motlles d'anhidrita.

• Els ciments de desdolomita i calcita mostren un progressiu empobriment de ferro i manganès directament associat amb l'entrada d'aigua meteórica durant l'etapa d'aixecament. També contenen inclusions fluides d'hidrocarburs. La distribució d'aquestes inclusions indica precipitació coetània d'aquests ciments amb la càrrega de la conca durant el Terciari.

• El sediments acolorits de dins del karst són deguts a la presència d'òxids i hidròxids de Fe. Els rebliments groguencs detectats al camp contenen calcita poiquilòtopica que inclou cristalls de goethita acicular ben cristalitzada. L'estudi amb SEM revela cristalls de dolomita amb microcavitats (hollow dolomite) on s'allotgen preferencialment pseudomorfs de pirita, ara com hematites. Dos mecanismes són proposats en aquesta tesi per l'origen d'aquests minerals fèrrics: sulfato-reducció bacteriana i precipitació directa com ferrihydrita a partir de solucions aquoses.

• Els ciments de dickita resultaren de la transformació de kaolinita per hidrotermalisme durant la diagènesi tardana.

Caracterització de reservori

• Els valors més elevats de permeabilitat s'assoleixen en les fàcies kàrstiques.

• L'expansió lateral del karst mitjançant la formació de coves lligades als estrats posa de manifest la significativa presència de porus intercristal·lins i vacuolars.

• La major heterogeneïtat lateral està associada amb fàcies pisolítiques de cresta de plataforma en un nivell desplaçat verticalment per les falles. Això, junt amb l'absència de modificacions diagenètiques laterals tardanes, indica que les millors propietats de reservori en la roca encaixant s'originaren durant l'activitat de les falles sindeposicionals.

• Les propietats originals de Poroperm foren primordialment heredades de l'activitat singenètica del karst però foren posteriorment modificades durant la diagènesi tardana, especialment en les zones internes de les falles.

• La cimentació de dickita i la desdolomitització produiren un segellament parcial de la porositat i una reducció significativa de la permeabilitat, especialment en les zones de fractura. Lateralment, la modificació és menor i s'assoleixen elevats valors de permeabilitat.

Chapter 1

Thesis outline

The inspiration for this thesis has come from the work of David Hunt and Edward Koša in Slaughter Canyon (Guadalupe Mountains, New Mexico, USA). The results presented in this Ph.D. thesis were obtained in the University of Barcelona (UB) within the framework of a Spanish Research Council (ICTJA-CSIC) project financed by Statoil. This enabled us to make use of advanced techniques such as LIDAR for working in a virtual outcrop, GPR, and computer advanced tools for 3D building. The poroperm analyses were instrumental in the characterization of reservoir potential.

The present study contributes to a better understanding of early dissolution mechanisms for syngenetic karst development and provides constraints on the timing of formation of the Rattlesnake Canyon paleokarst system in the Guadalupe Mountains, New Mexico, USA. Paleozoic paleokarsts commonly undergo burial and collapse, which reduces significantly the preservation of early fracture networks and geometries of dissolution. Rattlesnake Canyon constitutes a magnificent scenario for the study of global controls on Upper Permian karsting since early fracture networks and dissolution geometries are extremely well preserved and lack major tectonic deformation.

This thesis sheds light on the scientific knowledge of paleokarsts and can be of interest to the oil industry since paleokarsts are common targets of exploration. As the evolution of the reservoir properties is often diagenetically controlled, the diagenetic study was particularly useful in determining the degree of sealing following hydrocarbon charge.

Aims

This thesis seeks to improve our understanding of the relationship between early syndepositional fracture networks that are typically found in platform margins and syngenetic karst development.

The thesis includes multidisciplinary carbonate studies aimed at understanding the multi-scale paleokarst heterogeneity by means of (i) the development of a conceptual model for the karst evolution, (ii) the construction of a 3D paleokarst model, (iii) the determination of the diagenetic history of the paleokarst system and (iv) the paleokarst reservoir characterization.

Thesis Structure

The thesis consists of 9 chapters and 2 appendices. Chapter 1 sets out the rationale for this thesis. Chapter 2 provides an introduction to the most basic aspects of karst science and to the hydrogeological model of Carbonate Island as well as an overview of the state-of-the-art paleokarst studies. The geological setting and the study area is detailed in Chapter 3. The results of the thesis are contained in Chapters 4 to 7. Because of the multidisciplinary nature of this thesis, each of these chapters is dedicated to one discipline. Chapter 4 focuses on the analysis of field data to obtain a conceptual model for the evolution of the paleokarst system. Chapter 5 discusses the methodology to implement the 3D paleokarst model and provides data to assess the dimensions of the system in subsurface. Chapter 6 focuses on the diagenetic stages that affected and controlled the karst development. Finally, Chapter 6 offers a paleokarst reservoir characterization. A comprehensive approach and discussion of the results obtained in each of these chapters are included in Chapter 8. General and specific conclusions are presented in Chapter 9.

Appendix One contains a representative image compendium of the petrographic features observed in the paleokarst filling sequence of Fault N. Appendix Two sets out the raw data from the geochemical analysis.

The paleokarst analysis using different disciplines provides a complete characterization of paleokarst heterogeneity and enables us to elucidate the controls of the system.

Chapter 2

Introduction to Karst in Carbonate Platforms

1.- Karst and Paleokarst

Many definitions of karst processes in the literature refer to geomorphological features derived from mainly carbonate dissolution. Definitions of paleokarst are less abundant and this probably reflects the very incipient paleokarst knowledge.

For this thesis two historical definitions of karst and paleokarst are provided below:

"Karst is commonly treated as a distinctive geomorphic process and/or landform region displaying a specific underground drainage and surface morphology" (Jennings, 1985).

"Paleokarst refers to karst developed largely or entirely during past geological times" (Bosák et al., 1989).

The study of paleokarst provides information about the events and environmental conditions in the past and constitutes an exploration target for the oil industry. Although much field work has focused on dissolution geometries, the origin of karst processes is still poorly achieved.

2.-Karst classification

An overview of the classification of the variety of karst in the literature is of considerable interest given that paleokarst systems preserve some of the distinctive features according to their former typology. There are many factors that finally control cave development since karst is hydrogeologically and can be depositionally and/or structurally controlled in many cases. Recognition of polyphased mixed features in karsts that had experienced complicated diagenetic histories is not easy. Fluid histories are sometimes decoded by isotopic analytical procedures but sedimentological and structural field observations can help us to better understand the karst processes. Rattlesnake Canyon paleokarst appears as a polyphased karst sequence which exhibits vertical fracture widening and stratiform dissolution.

Quinlan (1978) proposed the term **interstratal karst** to describe dissolution features that develop beneath cover rocks deposited before karstification. Palmer and Palmer (1989) suggested that intrastratal karst is more appropriate, because most dissolutional processes at depth are not limited to the boundaries between different strata. The response of intrastratal mechanisms in depth is already an active focus of study. The deep geochemical processes that can generate speleogenesis at significant depth involve a variety of fluids including those related to hydrocarbons maturation, sulphate reduction and even metamorphism. Klimchouk (1996) ascribes the **intrastratal karst** to telogenetic stages. The mechanisms of intrastratal speleogenesis dissolution involve mixing water of contrasting chemistries and dedolomitization, which can contribute considerably to the creation of porosity in interbedded sulphate-carbonate formations.

Hydraulic continuity and vertical cross-formational hydraulic permeability is of significant importance for intrastratal karstification (Töth, 1995). Thus, the study of ancient intrastratal paleokarst underscores great potential poroperm reservoir properties. Deep-seated intrastratal karstification tends to be more diffuse and less selective than shallow karsts because of hydraulic and structural controls.

In this thesis, we refer to the stratiform dissolution as **stratabound speleogenesis** since distribution of solution cavities in Rattlesnake Canyon agrees better with the intrastratal karst of Palmer and Palmer (1989) although the timing of the dissolution event fits in better with the interstratal karst of Quinlan (1978).

Syngenetic karst

Most limestones, dolostones and gypsum deposits are located on shallow oceanic or coastal platforms undergoing slow subsidence or uplift. Eustatic and glacioeustatic changes of sea level may result in alternating deposition and intermittent subaerial exposure. Eustacy also controls hydraulic head in carbonate islands. Large hydraulic conductivities in these eogenetic systems make carbonates much more permeable than the underlying basement.

In a carbonate island model, karst dissolution can also be generated without subaerial exposure as dissolution can occur under phreatic conditions. Thus, freshwater vadose and phreatic, and freshwater-marine mixing scenarios can cause substancial and rapid cave development in the young rocks generating syngenetic karsts. At present, global sea levels are exceptionally high and prevent their occurrence, but syngenetic karsts were extremely developed over past geological times. Syngenetic karsts commonly undergo burial to various depths, becoming paleokarsts that are sensitive to reactivation at any stage of intrastratal karst development.

Exposed karst

The term exposed karst is applied when the surface extent of soluble rock exceeds that of any remaining caprock (Klimchouck and Ford, 2000). The origin of this type of karst may

be derived from earlier burial and subsequent uplift or can result from subaerial exposure of earlier syngenetic karst. Three different types of karst are included in this category on the basis of the different sedimentological stages and on the removal of its cover: denuded karst, open karst and exhumed karst. **Denuded karst** (Quinlan, 1978) is the term proposed to identify subjacent intrastratal karst exposed by removal of its cover. This type results from the combination of preserved intrastratal features and neoformed speleogenesis arising from subaerial exposure. **Open karst** (Klimchouk and Ford, 2000) is mainly developed during subaerial exposure and exhibits solely epigenetic features. It is common in tropical islands and coasts where recent carbonates have been continuously exposed. It is best developed on evaporite lithologies. **Exhumed karst** (Quinlan, 1978; Bosák et al., 1989) refers to former exposed karst which has been previously buried and reactivated by exhumation. Exhumed karst exhibits complicated polyphase inheritance and is characterized by the presence of many karst features which differ in origin. Exposed karsts generate branch networks in carbonates and linear passages in sulphates.

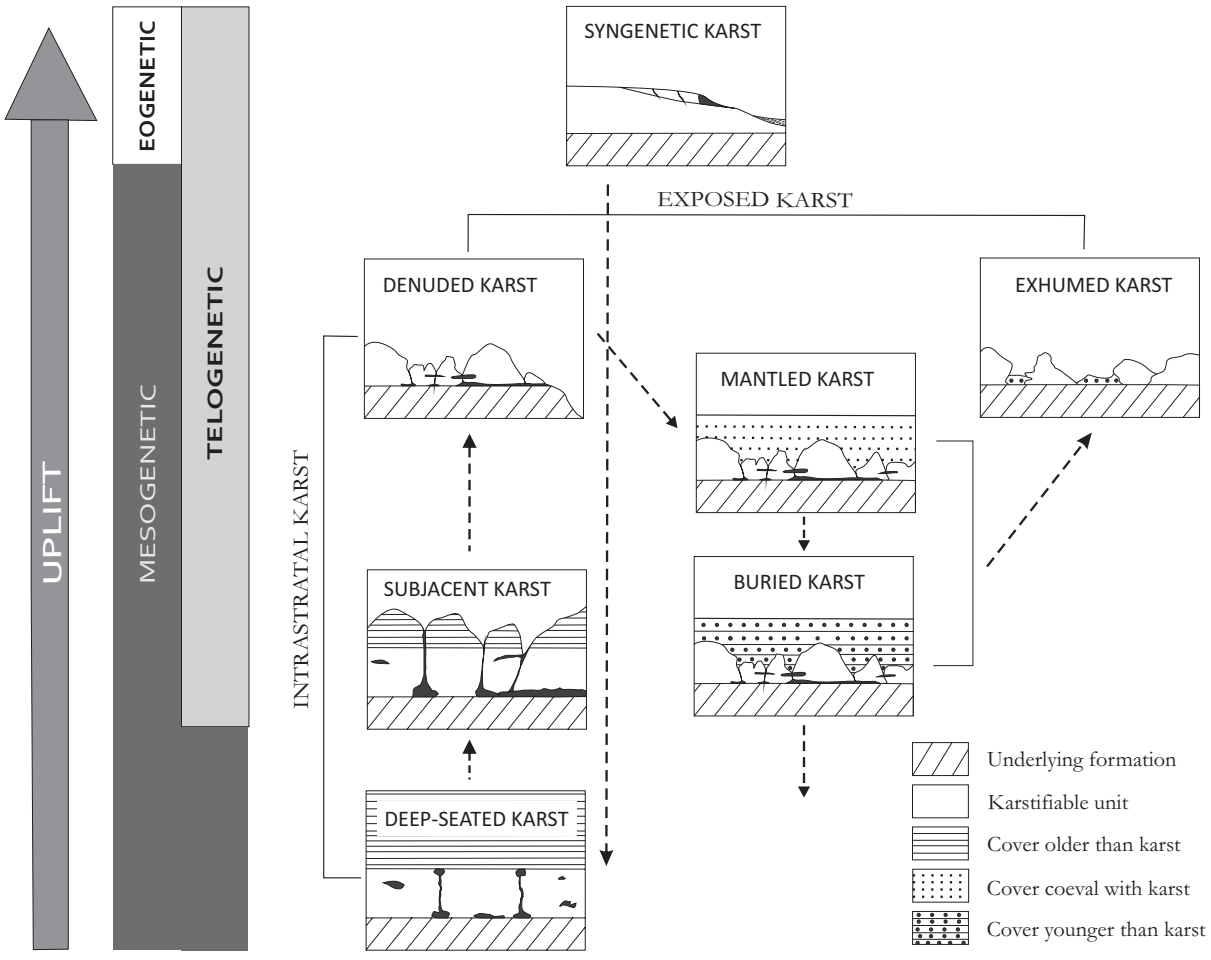

Fig. 2.1. Karst typology according to sedimentological stages. Modified from Klimchouk (1996).

Mantled karst occurs when sedimentation is coeval with karst development and then the karst is covered by unconsolidated sediment (Klimchouk and Ford, 2000).

Buried karst is a karst that has undergone prolonged exposure before burial (Klimchouk and Ford, 2000). In coastal settings, a karst system covered by transgressive sediments leading to the completion of karsting can be considered as a buried karst that contains fossilized epigenetic features.

In general, when structural controls are present in early stages they play an important role in enhancing speleogenesis, and thus the resulting cave patterns exhibit a combination of the geological processes undergone by the karst affected materials.

3.-Insights into syngenetic cave forming processes

By the mid 1970s it was well known that speleogenesis arises from flow dynamics and dissolution kinetics. New discoveries have resulted in different mechanisms that can generate syngenetic speleogenesis in mixing environments. These findings reveal halocline caves and flank margin caves formed by meteoric-marine mixing mechanisms, hydrothermal caves formed by the action of thermal waters and sulphuric acid caves generated by acid sulphuric dissolution. Good examples of syngenetic flank margin caves with strong eustatic control have been documented by Mylroie and Carew (1990) in the Bahamian Quaternary and by Frank et al (1998) in Isla de Mona, Puerto Rico.

The mixing mechanism has great potential for the creation of karsts in coastal settings, even producing macroscopic voids in telogenetic limestones (Mylroie et al, 2008). The origin of these mixing caves, especially those developed from young unconsolidated carbonates, is explained in the Carbonate Island Model (Mylroie and Vacher, 1995).

4.- The Carbonate Island Model

Coastal karsts are preferentially developed by chemical interactions between fresh and salt waters. This dissolution model operates very well when recharge is autogenic. Carbonate coasts on continents have recharge derived from adjacent non-carbonate areas. When platforms and oceanic islands have little areal extent the hydrogeological cycle is controlled by the local environment and recharge can be considered as autogenic. Under these special conditions, the Carbonate Island Model has been applied to account for modern karst development in the Bahamas, the Caymans and Isla de la Mona (Puerto Rico).

The fresh groundwater flow is diffuse over these areas and the generation of a freshwater lens is due to the difference of density between lighter freshwater and dense saline water. Freshwater floats on denser marine or mesosaline waters (35–120 ‰ salinity (Melim and Scholle, 2002)). The density interface between the fresh and saline waters is termed halocline. Halocline can be sharp or can represent a gradual transition zone towards brackish waters which result in a mixing zone. Dissolution in the mixing zone can be caused by the algebraic

effect, the salinity effect, pCO_2 together with pH variations as well as temperature oscillations (Wigley and Plummer, 1976). Mixing produces undersaturation with respect to HCO_3^- and equilibrium is achieved by dissolving carbonate (Fig. 2.2).

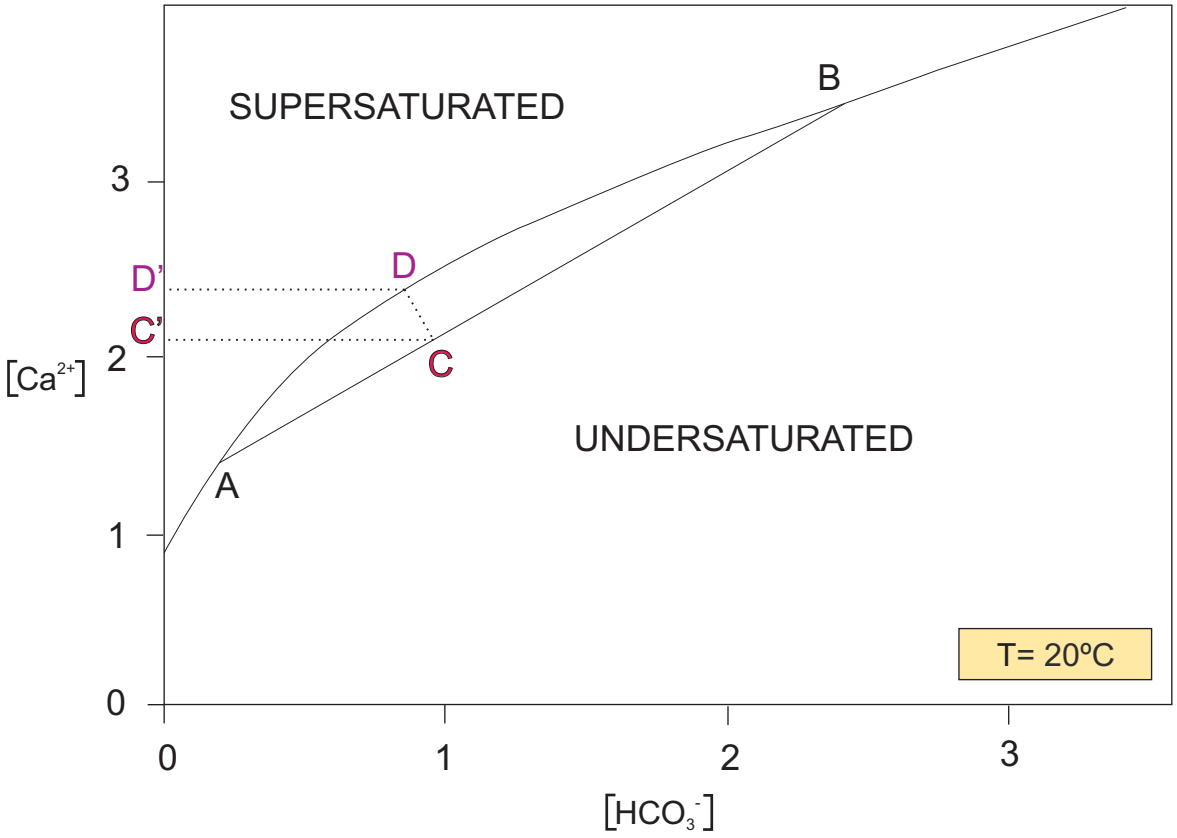

Fig. 2.2. Equilibrium curve for $CaCO_3$, after Dreybrodt (2000). Concentration of calcium and bicarbonate in water are expressed in mMol/l. Waters with different salinities (A and B) when mixed attain a salinity of water C. Water C become undersaturated and start dissolving $CaCO_3$ until reaching the equilibrium composition of water D.

Dissolution can occur at the top of the lens (water table) and/or at the bottom of the lens (halocline). Water table caves are also known as flank margin caves and their formation has been broadly used as an indicator of past sea-level stands because of the specific location of these caves at the lens margin (Fig. 2.3). Conversely, halocline caves form deeper in the phreatic realm and the position of the sea level cannot be directly inferred from them without precise knowledge of the freshwater lens thickness. The thickness of the freshwater lens is mainly controlled by the active hydrogeological parameters at the time of cave formation.

In ancient systems, these parameters are often little known, which makes the analysis more complex. Although the Ghyben-Herzberg relationship establishes that the top of the lens is located about 40 m below sea level, this distance can be increased when salinities of the saline member are higher than normal marine waters. The validated model of seepage reflux dolomitization in the Capitan platform (Melim, 1991; Melim and Scholle, 2002) involves early percolation of brine waters through the platform, suggesting salinities slightly higher

than sea water after mixing with ocean water (mesosaline waters). These brines could have long resident times in the carbonate platform, producing latent reflux even during highstands (Jones et al, 2002). The possible scenario for cave formation in Rattlesnake Canyon could therefore be associated with density–stratified groundwater in a hydrogeological model of Carbonate Island.

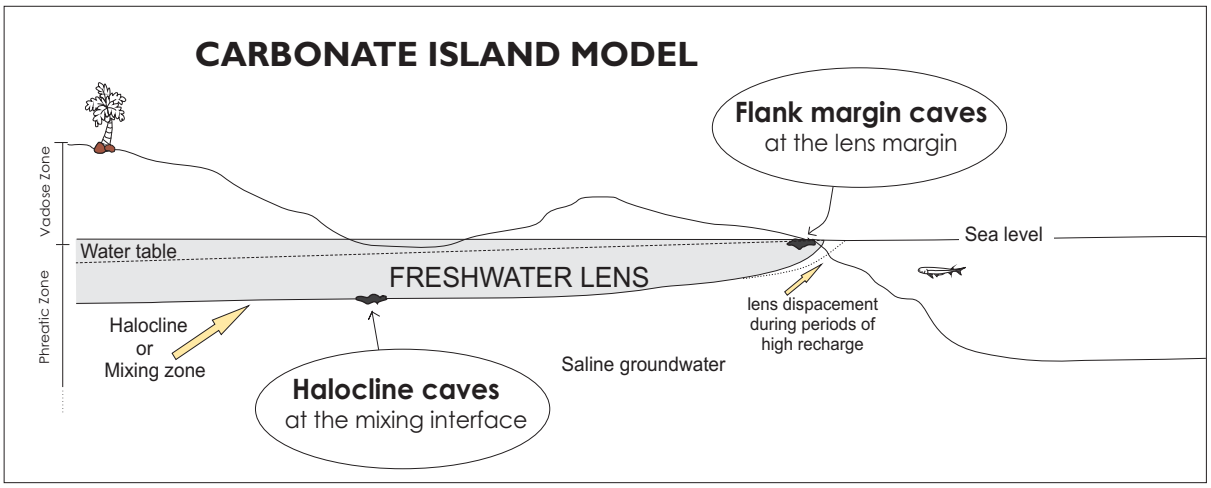

Fig 2.3. Sketch of the distribution of halocline caves and flank margin caves in platform margins under the controls of the Carbonate Island Model.

5.- Bahamian archipelago and Holocene karst systems

The Bahamian archipelago began to form practically at the same time as the North Atlantic Ocean approximately 200 million years ago. Sealey (1994) established a topographical classification for the Bahamian islands defining 4 zones: the ridgelands, the wetlands, the rocklands and the coastal zone. Ridgelands are topographically high (10-45 m above sea level) and preserve the relicts of the cave systems developed during the Pleistocene (Mylroie and Carew, 1990). Wetlands are located in the interior of the islands often as hypersaline lakes or along the coastal margins as tidal flats. Cyanobacterial mats are very common in these areas because of the elevated salinity. Dry rocklands are the most elevating zones grading to zones that are often inundated, presenting dissolution features such as solution pits with associated collapses. The coastal zone comprises tidal flats with common tidal creeks that can be hydrologically connected to the caves. This is the case of the Lucayan caves of the Grand Bahama Island.

The islands of the Bahamian archipelago offer a unique opportunity to study an active recent carbonate island model and are very helpful in extracting topographic parameters and aquifer properties to develop analogue fluid flow models applicable to ancient systems.

The role of topography is critical in controlling the distribution of freshwater lens. Cavernous porosity provides paths for enhancing discharge of both brackish and fresh groundwaters (Whitaker and Smart, 1997).

In the North Andros and Grand Bahama islands, the large thickness of the freshwater lens (>20 m) provides evidence that tidal pumping is effective for tide-induced mixing and that freshwater recharge is a significant input in the system. The thickness of the mixing zone decreases exponentially with distance inland and away from the tidal creeks because of the reduced influence of tidal head fluctuations and decreasing groundwater flux.

In the Grand Bahama Island, the inland reduction of the mixing zone occurs at the west portion in the Grand Lucayan Waterway (Fig. 2.4). In this zone the Pleistocene limestones are overlain by a Holocene transgressive beach barrier, of lower conductivity, attenuating inland propagation of the tidal pumping and maintaining larger freshwater lens and thinner mixing zone adjacent to the coast.

In the North Andros Island, the mixing zones observed in inland cenote blue holes range in thickness from 15-20 m adjacent to the coast to 3-6 m beneath the centre of the lens, at a distance of more than 10 km inland. The inland decrease appears to be similar to those of the Grand Bahama Island. Whitaker and Smart (1997) calculated an exponential tendency for this observed pattern of decrease:

MZ thickness (m) = 12.3 – (8.80•Log10 Distance Inland)

The thickness of the mixing zone depends on the tidal efficiency but whereas tidal pumping is observed to decrease linearly, the lenses appear to be much more sensitive and their thickness declines exponentially inland.

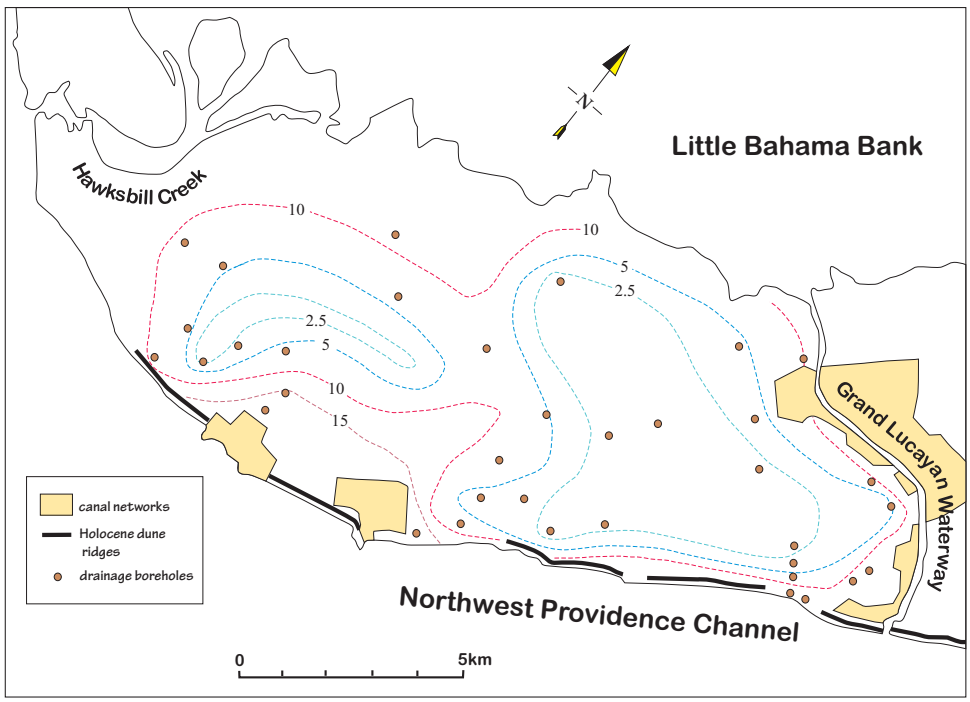

Fig. 2.4. Thickness of the mixing zone in the area of Free Port, Grand Bahama. Contours of mixing-zone thickness (dashed lines) are expressed in metres and derived from drainage boreholes (brown solid dots). Modified from Whitaker and Smart (1997).

5.1.- Blue Holes

Blue holes are karstic solution structures that actively operate in the Bahamian archipelago. Their similarity to the ancient karstic system studied is considerable and since they are active at present blue holes can provide tools to analyze the ancient controls of the system.

Blue holes are entrances to underwater caves and the term is derived from the intense blue colour of the deep water observed in their entrances. Blue holes provide paths for enhanced groundwater circulation and control the thickness and position of the mixing zone. The geochemistry of the caves controls dissolution in mixing zones and may trigger bacterial sulphate reduction processes whenever organic matter is available (Bottrell et al., 1991; Schwabe and Herbert, 2004).

The geometries of blue holes vary from vertical to lateral karstic structures. Cenotes, such as Deans Hole (Fig. 2.5), are circular shafts up to 200m deep; lateral extensions are less developed generating passages often filled with surface sediment or blocked by breakdown; and linear trends of vertical shafts are developed from fracture systems in bank margins.

Fig. 2.5. Images of the Deans Blue Hole on the north (Atlantic) side of Long Island, Bahamas. It is the world's deepest blue hole reaching a depth of 200 m. Images extracted from: http://restrictednote.wordpress.com/2010/01/29/deans-blue-hole-bahamas/

In the Bahamian islands, cenotes are very common structures (118 inland cenotes on North Andros) and often show connection with linear trends of fracture networks. Cenotes indicate

high rates of dissolution as cenote walls commonly appear corroded, especially in the upper 20-30 m., and towards the bottom of the cave gravitational processes increase, accumulating collapse deposits. Where sedimentation is high, these structures can be found filled with sediments. It is thought that cenotes form as submarine passages in mixing freshwater-saline environments because of the infiltration of groundwater flows. Mixing dissolution induces breakdown, especially during lowstands when the vadose zone is increased and buoyant support decreases. Roof collapses also induce maze cave systems preferentially around island margins. These complexes also entail the development of horizontal lateral passages along bedding planes (Whitaker and Smart, 1997). The Lucayan Caverns in the Grand Bahama Island, which have more more than 14 km of passages, are one of the longest submarine cave systems in the world. The dissolution along bedding planes is related to dissolution at the water table and/or mixing zone where dissolution is active owing to the presence of waters undersaturated with respect to calcite (Smart et al., 1998; Withaker, 1992).

Tidal pumping produces a radial flow that enhances mixing in the caves, propagating it towards the adjacent aquifer (Whitaker and Smart, 1997).

Waters of blue cenotes attain higher flow rates and retain higher contents of organic matter derived from the surface than those of the adjacent aquifer. Bacterially mediated processes produce aerobic oxidation of the organic matter in the upper mixing zones and sulphate reduction in the redox interface at the base of the halocline (Bottrell et al., 1991).

6.- Overview of paleokarst studies and late Cenozoic speleogenesis in the area

6.1.- Paleokarsts of syngenetic origin

Tinker (1995) documented core evidence of karst development in the San Andres Formation of the Yates field located at the southeastern tip of the Central Basin platform (Fig. 3.1b). The linear distribution of karst features of Yates field in the San Andres Formation bears a considerable resemblance to the lateral extensions of the Rattlesnake Canyon paleokarst system. This karst distribution is poorly documented in ancient systems and can be attributed to the development of composite karst resulting from the migration of the mixing zone because of multistage relative sea-level falls. This Leonardian karst system has been associated with subaerial exposure because of the presence of vertical solution fabrics and chaotic breccias just below an unconformity surface at the top of the San Andres Formation. The repetitive linear distributions within the San Andres Formation indicate multiple karst events that predate the surface karst episode linked with the unconformity. The sequence of karst events has been attributed to the cyclicity of the stratigraphic formation. The multiplicity of karst events is resolved by the interpretation of subaerial exposures at the top of the cycles at cycle boundaries. This conceptual interpretation based on the architecture of the stacking patterns contrasts with the sole recognition of only one surface of subaerial exposure.

Late diagenetic modification in this system is minor and major pore types consist of vuggy pores cemented with dolomite cements. Similitude in the packstone and grainstone textures of the Leonardian carbonates hosting the karst and the geological context of both systems make the San Andres paleokarst a good equivalent to the system studied.

In line with the above account, some authors have recently reported paleokarst features associated with cyclicities. Baceta et al. (2001; 2007) have reported the finding of "*swiss-cheese zones*" or "*sponge-like zones*" in the Paleocene in northern Spain. These zones also present horizontal arrangements and extend laterally over 2 m. The surfaces which contain these solution cavities do not show any symptoms of subaerial exposure but the infills display crystal silt indicative of vadose conditions. The system seems to be controlled by fractures which exhibit solution-modified boundaries and sandstone fills. The authors suggest that these fracture networks acted as conduits that favoured the entrance of clastic sediment during vadose exposure. The presence of Fe-oxide coatings in the cavity fills has been attributed to sulphate reduction horizons.

Fu et al. (2006) have accounted for the genesis of a paleokarst in mud mounds of the Middle Devonian Winnipegosis in Canada. Solution voids which present "*swiss-cheese porosity types"* are filled with carbonate and anhydrite. The system is genetically related to the carbonate platform/island model given crystal silts and calcrete layers that are in close relation to paleokarst features.

Yilmaz and Altiner (2006) have documented epikarstification associated with parasequence boundaries in the Aptian peritidal carbonate successions of southwest Turkey. Three karst levels with solution breccias developed between limestone layers are interpreted as a record of subaerial exposure on the tidal flats of an isolated carbonate platform. The position of these levels coincides with parasequences. The system lacks large vertical dissolution features.

6.2.- Burial Paleokarst

Most of the paleokarst reservoirs have undergone burial and diagenetic modification. One such case is the paleokarst reservoir of Ellenburger Group in central Texas. Extensive cave systems developed at composite unconformities in the Lower Ordovician Ellenburguer. Kerans (1988, 1989) developed paleocave models from these karst systems introducing new terms such as paleocave floor, paleocave sediment fill and paleocave roof.

Loucks (1999) and Loucks and Mescher (2001) have contributed greatly to the systematics of paleocave breccia deposits and paleocave facies. Based on this classification, Loucks et al. (2004) analyzed the 3D architecture of a Ellenburger collapsed paleocave system identifying paleocave facies by GPR data. The study shows the most recent advances in determining spatial heterogeneity and reservoir distribution of paleocave systems at detailed scale.

The diagenetic modification of Ellenburger paleokarst is complex and extensive as expected for a Paleozoic ancient system. The main diagenetic processes entail several stages

of dolomitization, karsting and tectonic fracturing (Kupecz and Land, 1991). Generations of dolomite were basically typified as early pre-karsting and late post-karsting dolomitization (Amthor and Friedman, 1991). Karsting was initiated during the exposure of the Ellenburger Group to meteoric diagenesis at the end of the Early Ordovician when a several-million–year hiatus took place. Late-stage diagenesis has been attributed to hydrothermalism during the Ouachita Orogeny (from Mississippian through Pennsylvanian). After lithification, the Ellenburger Group was affected by fracturing, giving rise to late-stage diagenesis of the paleocave system.

6.3.- Sulphuric acid speleogenesis in the Guadalupe Mountains

Big cave systems (Carlsbad Caverns, Lechuguilla Cave) are present in the Guadalupe Mountains very close to the study area. The large dimensions of the passages of these cave systems (> 15 m in height and width), their association with gypsum masses and their truncation with the Upper Permian early cave networks indicate a late prolific episode of speleogenesis in the area. Hill (1996) designated Stage 4 for this speleogenetic event in contrast to Stage 1 of Late Permian cave development in the fracture zones parallel to platform margins.

These large caves have a hypogene origin because of ascending H_2S derived from the hydrocarbons (HC). The H_2S is believed to have been oxidized to H_2SO_4 when it migrated. The time when this speleogenesis occurred is assigned to the period of major uplifting and tilting in the Late Miocene. The origin of these caves is associated with phreatic dissolution. Shallow phreatic dissolution facilitated the development of horizontal passages (e.g. Big Room of Carlsbad Caverns). Deep phreatic dissolution was responsible for the generation of vertical shafts (e.g. Main Corridor, Carlsbad). None of these caves are vadose and the sediment fill is a product of the dissolution of the siliclastic facies of the host rock.

The presence of gypsum ($CaSO_4 \cdot 2H_2O$) in these caves results from the interaction of H_2SO_4 with the dissolution of the carbonate. The recognition of endellite and alunite in the caves indicates low pH for precipitation of these minerals and supports the theory of H_2SO_4 speleogenesis. The low isotopic signal in gypsum is another indicator of the involvement of HC in the genesis of these caves.

Chapter 3

Geological setting and study area

1.- Geological setting

The Guadalupe Mountains are at present located in the southwestern limits of Texas (USA) and extend NE for more than 50 km into the southeastern part of New Mexico (Fig 1). Their outcrops of Late Permian platform carbonates, which developed along the margins of the Delaware Basin, are magnificently preserved (Fig 1).

The Capìtan reef and its associated Upper Guadalupian carbonate platform make up the Permian reef complex. The Permian reef complex consists of three facies tracts: backreef facies, reef margin and basin (Hill, 1996). The backreef Upper Seven Rivers and Yates Formations strata are equivalent to massive reefal and forereef carbonates of the Capitan Formation and to basinal siliciclastics of the Bell Canyon Formation (Fig. 1b). Backreef facies in the Northwest Shelf, which are the subject of this work, are composed of the Seven Rivers, Yates and Tansill formations. Intercalations of carbonate and siliciclastic strata in these formations have been used to interpret the progradational/agradational stratigraphic geometries of the Capitan platform (Bebout and Kerans, 1993; Ward et al., 1986). Low dip slope angles of the platform documented by Osleger (1998) in McKittrick Canyon and Slaughter Canyon support the interpretation of the backreef area as a shallow paleozone of low current which reached high salinity levels that promoted evaporite deposition during the Upper Permian. According to Franco (1983), Permian climatic changes during Yates deposition alternated between interpluvial and pluvial climates. These cycles have a direct relationship with sea level fluctuations. High stands were interglacial periods with an arid climate during which precipitation of evaporites took place in the coastal sabkhas. Low stands were glacial periods with a humid climate producing an increase of rainfall in the outer shelf areas.

The Capitan platform strata lack intense tectonic deformation but are cut by a series of syndepositional faults and fractures documented in Double, Slaughter, Rattlesnake and Walnut canyons by Koša and Hunt (2005, 2006) (Fig. 1). These steep fractures are sometimes solution-modified by paleokarst processes, as which is the case of Slaughter Canyon, Dark Canyon and Rattlesnake Canyon (Koša and Hunt, 2006). Syndepositional faults and fracture systems in the Capitan platform margins are superbly exposed through canyons which cut the strata in directions perpendicular and parallel to depositional strike. Faults and related fracture systems exhibit a consistent orientation parallel to depositional strike and Capitan platform

margins in the study area. Rattlesnake Canyon therefore constitutes a magnificent scenario to study the relationships between syndepositional faulting, stratigraphy and diagenetic processes.

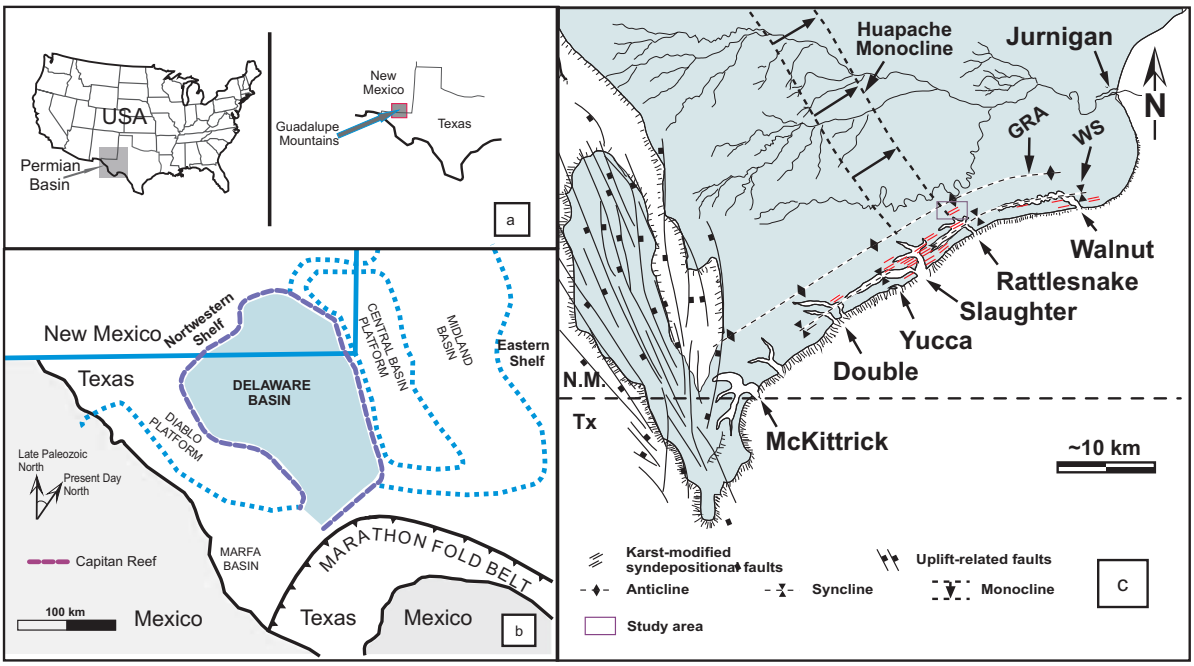

Fig. 3.1. a) Location map of the Guadalupe Mountains showing syndepositional platform margin faults and the study area. b) Paleogeographic map showing the Permian Basin. c) Structural setting of the study area.

The Guadalupe, Apache and Glass Mountains expose a small part of the Late Permian carbonate platform surrounding the margins of the Delaware Basin (Fig. 1). This basin developed as the foreland of the Marathon Fold Belt to the south, which formed during the continental collision between Laurasia and Gondwana in the late Mississippian and early Permian (Hill, 1996; 2000). Three main tectonic deformation events are recorded in the basin: a) NNW-SSE trending faults coeval with Permian deposition; b) Late Cretaceous to Eocene Laramide orogeny that resulted in almost 1.2 km of uplift on its western side, close to the fold-and-thrust belt front (Hill, 1996); and c) Oligocene-Pliocene extension with km-scale NNW-SSE oriented faults related to the formation of the Basin and Range (Hayes, 1964; Garber et al., 1989; Hill, 1996, 2000).

Strata in the Guadalupe Mountains show almost no structural deformation (e.g., Hunt et al., 2003; Koša and Hunt, 2005). Post-deposition deformation is limited to small-scale faults, fractures and folding (flexures) related to the uplift of the platform in the Oligocene–Pliocene period. Centimetre-scale normal faults and joints parallel to the platform margin are probably related to the NNW–SSE-trending, ENE-dipping Huapache monocline (Fig. 1). This monocline with about 150 m of structural relief is thought to be linked to the deep-seated Huapache blind thrust (e.g., Hayes, 1964; Hill, 1996). Syndepositional folds, faults and fractures run parallel to the platform margin for at least 33 km along the strike between Double and Walnut canyons. These systems of folds, faults and fractures are commonly

developed in the outermost 5–6 km of the platform (Fig. 1). The present study focuses on a fault graben system exposed in Rattlesnake Canyon, which exhibits solution-modified fault boundaries aa a result of karst development.

2.- Stratigraphic architecture of the permian Capitan platform

The Capitan platform is a mixed evaporite-carbonate-siliciclastic shelf that records high frequency sequences and cyclicity (Meissner, 1972; Borer and Harris, 1989; Kerans and Tinker, 1998). Facies tracts in the Yates-Capitan platform margins have been originally defined by shelf crest, outer shelf, reef margin and interbedded continental siliciclastics (Osleger and Tinker, 1999). Stratigraphic arrangement and nomenclature of the Permian strata in the Guadalupe Mountains are shown in Fig 2.

The Seven Rivers, Yates and Tansill stratigraphic units represent 3rd-order, depositional sequences (Kerans and Tinker, 1998). These contain 4th-order, high-frequency sequences (HFS), such as the Seven Rivers 1–4, Yates 1–5 and Tansill 1–2 HFSs (Osleger, 1998; Tinker, 1998; Kerans and Tinker, 1999; Hunt et al., 2002). High-frequency sequences exhibit a seaward-thickening geometry with higher volumes of siliciclastics at the base and more carbonate lithofacies towards the to the top.

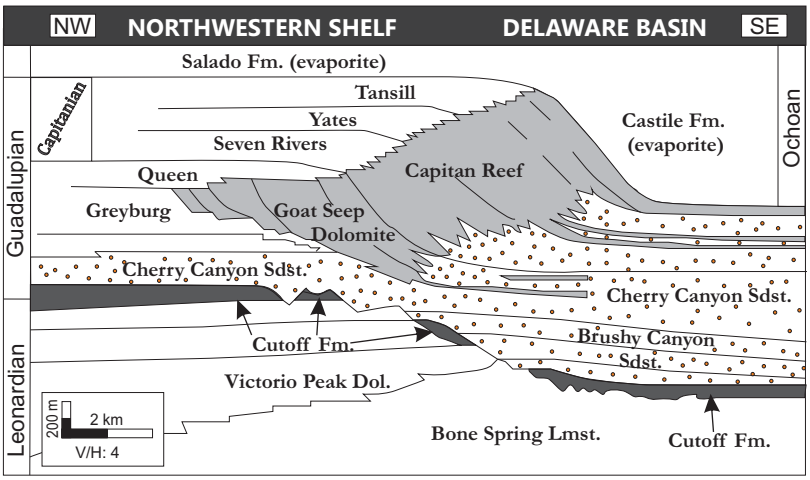

Fig. 3.2. Stratigraphic arrangement and nomenclature of the permian strata in the Guadalupe Mountains. Modified from Koša and Hunt (2006).

Siliciclastics are more common within transgressive system tracts (TST) because of their reworking during initial flooding. Each highstand system in the Yates formation tract (HST) is composed of pisolitic facies. Y3 and Y4 HFSs are characterized by the highest progradation rates (Oesleger, 1988).

The contact between the Yates and Seven Rivers Formations was interpreted as a major composite sequence boundary (Kerans et al., 1992). Stratigraphic profiles of these 4 HFSs in Slaughter and McKittrick canyons reveal an aggradational architecture within Y2 and

Y3 HFSs followed by a high progradation through Y4 HFS (Osleger and Tinker, 1999). In Rattlesnake Canyon, there is a clear overall upward trend from dominantly open marine outer-shelf facies of Y1 to dominantly shelf-crest facies of Y4.

3.- Geological history of the region

During the Permian, the Delaware Basin the region was part of the southern flank of the North American craton, and shelf edges in the Delaware and Midland Basins were oriented 40 to 60º northeast (Walker et al, 1995). The Permian was a period of tectonic stability. This stability continued until the Ochoan with a time span of 265-230 my and during this time, known as the *Permian Basin Phase*, the basin was completely filled with clastic, evaporite and red bed sediments. In the late Permian (Ochoan) an incipient stage of uplifting responsible for the basinward tilting of the forereef strata occurred. The cause of the uplift is not so clear and could be due to tectonic regimes and/or compactional subsidence. Following the intense evaporite dsposition, quiescence was again a reality during the *Stable Platform Phase* (230-80 Ma) interrupted by the Laramide orogeny responsible for the major uplifting and tilting of the Guadalupian strata.

During the late Cretaceous-early Tertiary (80-40Ma) the convergence of the Farallon and North American plates resulted in low-angle subduction and ENE compression which culminated in the uplift of the Rocky Mountain Region in New Mexico extending to Wyoming (Dickerson, 1985). The main consequences of the *Laramide Phase* were the 1.2 km of the Delaware Basin elevation, a significant tilting eastwards and a broad arching.

Volcanism began in the Delaware basin and extended into Mexico and western New Mexico (Hill, 1996) during the *Volcanic Phase* (40-30 Ma). Volcanic activity from west to east and then from east to west presumably reflected the transition from strong to weak coupling between the converging plates (Farallon and North American plates) (Keith, 1982). The end of the Laramide compression was caused by a change from negative to positive buoyancy of the Farallon plate, which resulted in the slowing of the plate. Thus, slower convergence and the weak compressional stresses caused the magma to reach the crust. The thermal gradient should then have undergone a rapid rise. Arc-magmatism controlled the volcanic activity in the western region up to about 30 Ma.

The *Basin and Range Phase* (30-0 Ma) was characterized by regional crustal extension and thinning, high heat flow, rifting and low compressional velocities in the upper mantle (Hill, 1996). The heat anomaly had deep and shallow extent. The deep anomaly was responsible for the volcanic activity whereas the shallow anomaly led to elevated heat flow with a minor contribution from the uplift. It is thought that the heat flow increase was accompanied by convective heat flow, causing hydrothermal water circulation. Fluids could circulate along favorable paths such as faults or paleokarst systems (Hill, 1996). Between the Oligocene and the Miocene this resulted from igneous intrusions which were probably due to an active hydrothermal convective system during the Miocene. Hill (1996) documented the thermal

spar as a product of the Miocene hydrothermal regime. The *Basin and Range Phase* was subdivided by Hill (1996) into three stages mostly based on rates of uplift and heat flow: The *Transition Stage* (30-20 Ma) represents the final transition from the Laramide compression to the regional extension. This phase entails the onset of block faulting and an increase in heat flow. NNW block faulting on the west side of the Delaware Basin followed Paleozoic trends and could favour a reactivation of these ancient systems. The *Main Uplift Stage* (20-2 Ma) is the period during which major uplift and tilting of the Delaware Basin took place. Heat flow increased in the Miocene (6 Ma) and persisted into the late Miocene. During the *Quaternary Stage* the geothermal gradient decreased from 40-50ºC/km during the Miocene to 20ºC/km, which is the present-day gradient documented in the zone (Hill, 1996).

4.- Diagenetic distribution of cements in the Capitan Reef Complex

Different types of cements have been found and described along the Capitan reef complex. The Permian reef complex includes both far-backreef hypersaline lagoon facies and near-backreef mesosaline carbonate lagoon to tidal flat facies (Hurley, 1989; Sarg, 1989). These cements include early synsedimentary cements, dolomite cements and calcite cements (Melim, 1991; Mruk, 1989; Hill, 1996). Calcitized pseudomorphs after evaporites have been documented in the backreef facies of Dark Canyon by Parsley and Warren, (1989). The work of Scholle et al. (1992) confirmed that evaporite minerals that formed as primary precipitates or diagenetic phases in the forereef and backreef areas were extensively replaced, or leached during uplift both at substantial depth and at the surface.

Early marine cements. Several workers have studied the Capitan reef marine cements (Yurewicz, 1976, 1977; Mazzullo and Cys, 1977; Given and Lohman, 1986; Melim, 1991). Early submarine cements formed synsedimentary with the growth of the Capitan Reef and deposition of the platform materials in the Northwest Shelf. These cements occurred as fibrous aragonite and formed botryoidal cements occupying inter-reef voids. They are very common in the reef and forereef areas. Melim (1991) documented their abundance in the upper forereef facies. Hill (1996) focused on the backreef areas, placing these cements at the margins of the platform and in the areas of shoals where porosity was significant due to the coarse-grained facies.

Slaughter Canyon

Koša (2003, 2006) contributed to the elaboration of a complete description of the type of breccias that were found in the backreef facies of Slaughter Canyon. The description addressed the general set of the breccias including both matrix, clasts and cement whenever it was was present. Some features of the spar-bearing breccias described by Koša are commented below:

LB (Limestone breccias). Matrix massive lime mudstone with disperse dolomite rhombs. Matrix to clast supported.

MSB (Microspar-cemented breccias). Cemented by fine crystalline spar. Matrix supported. With diffuse transitions between the microspar cement into coarser spar cement and lime mudstone. Grade laterally into LB associated with LB.

SB. (Spar-cemented breccias). Cemented by coarsely calcite spar, with rare hydrocarbon inclusions and sparse dolomite rhombs.

Koša interpreted the origin of these cements as early because of the scarce hydrocarbon inclusions and the presence of dolomite rhombohedra within their mosaics.

McKittrick Canyon

Diagenesis in McKittrick Canyon was first studied by Mruk (1989), who documented the existence of early aragonite cements and three different spar calcite generations in the forereef facies.

Early cements were found in McKittrick Canyon as botroydal fibrous and isopachous radial fibrous cements. According to Mruk (1989), these cements predate a major stage of dolomitization followed by a stage of inclusion-rich prismatic cements. Precipitation of the first spar generation SI) was accompanied by a stage of dissolution, fracturing and brecciation, and the author attributes SI spar to early meteoric diagenesis. Following SI, Mruk documented SII spar cementation associated with an episode of fracturing and compaction. The latest spar calcite generation documented in McKittrick Canyon is SIII, which is interpreted as precipitated under telogenetic conditions.

SI. Non-ferroan bladed to-equant crystals. SI is described as fluid inclusion poor and the CL pattern of this calcite is observed as alternating non luminescent to bright orange. This spar generation is common in the forereef massive facies and in the proximal slope its distribution is disperse. Given and Lohman(1986) and Mruk (1989) postulated that SI formed during the shelf crest exposure in the Upper Permian as a result of meteoric diagenesis.

SII is described by Mruk (1989) as pore-filling euhedral crystals which grade from nonluminescent to three pairs of bright yellow and moderate orange zones. The last zone is commonly corroded. An increase in fluid inclusions was observed with respect to SI. This spar generation is widespread in the framework pores and in brecciated boundstone of the massive facies of the forereef. In the proximal foreslopefore-slope SII postdates SI fractures. In the distal foreslope SII is found in shelter porosities. There are uncertainties concerning the origin of this calcite although Mruk (1989) suggested a burial origin due to the low salinities of its fluid inclusions.

SIII is described by Mruk (1989) as non luminescent and predating corrosion. It is found overlaying SII and is rich in fluid inclusions. In the proximal foreslope this calcite in association with SII forms patchwork calcite mosaics within extensively dolomitized samples.

Fluid inclusions reveal salinities around 14-20% and the author indicated possible thermal hot saline brine as parental fluids.

Melim (1991) revealed the presence of SII and SIII in evaporite moulds and supported the interpretation that these two calcite spar generations postdate evaporite dissolution. The author also constrained the time of their formation to the Tertiary uplift when meteoric flushing of the Capitan Formation took place.

Evaporites are absent throughout the outcrops of the different canyons but abundant evaporite minerals such as gypsum and anhydrite have been found in the Gulf PDB-04 core, which is located in the northwest margin of the Delaware Basin and provides subsurface information of the backreef, forereef and basin facies (Garber et al., 1989). Otherwise, in the Gulf PDB-04 core, there are scarce signals of the presence of spar cements.

Evaporite emplacement was early as it is observed in the lower forereef areas by evidences of compaction around some anhydrite nodules. The primary positions that occupy the evaporite minerals in the PDB core are equivalent to those found in the outcrops for the blocky spar calcites. This was another criterion to support that the spar calcites replaced evaporite minerals.

Scholle et al. (1992) compiled all the information relative to the calcite spars in the Guadalupe Mountains and added new criteria to ascribe that evaporite replacement took place during the Tertiary uplift. Hydrocarbon fluid inclusions and the generally light carbon and oxygen isotopic signatures of the spars were the main criteria indicating that calcite precipitation was a late diagenetic (telogenetic) phenomenon postdating hydrocarbon emplacement.

Kaolinite cements were first reported by Melim (1991) as pore-filling cements within biomouldic and open stylolites. Kaolinite cement is interpreted as postdating spar calcites since it is observed engulfed by calcite and cross-cut by spar filled fractures. The author attributed its origin to dissolution of feldspars or siliceous sponges also under telogenetic conditions.

Dark Canyon

Isopachous bladed and subequant high Mg-calcite and fibrous aragonite cements were found in the outer shelf facies of Dark Canyon and described by Parsley and Warren (1989). These authors also documented the presence of calcitized blocky and acicular pseudomorphs after evaporites that they temporally emplaced after the first and early diagenetic event of dolomitization. The mechanism of dolomitization was particularly elucidated as derived from reflux of marine derived brines. The source of this dolomitizing fluid was conceived as penecontemporaneous lagoonal waters or dissolution of Ochoan evaporites overlying the Tansill Formation.

Scholle et al. (1992) collected some samples of calcite spar from Dark Canyon which recorded extremely light carbon isotopic signatures (-18 to -20‰ δ PDB). The authors interpreted that these calcites were products of evaporite replacement and that the low carbon

isotopic signal was a consequence of hydrocarbon inclusion trapping. These calcites fall in the range of the "Oil Spar" calcites of Hill (1996).

Hill (1996) introduced the name "Oil Spar" referring to that calcite which contained hydrocarbon inclusions. According to Hill (1996), "Oil Spar" is spatially constrained to the backreef strata exclusively. The origin of this spar is explained as related to the biodegradation of the oil by sulphate reduction bacteria. The carbon isotopic signal of this calcite ranges from -25 to -7 ‰ δ PDB. Some of the hydrocarbon rich calcites in the Dark Canyon interpreted as late stage calcites by Scholle et al. (1992) are comprised within this range of values. The exact time of the formation of this "Oil Spar" is not well known as some authors sustain their origin coeval to the hydrocarbon recharge and others believe that the hydrocarbon fluid inclusions might be secondary.

Thermal Spar was also introduced by Hill (1996) and is equivalent to the SII and SIII calcites described by Mruk (1989). Is characterized by a narrow range of carbon isotopic values (-6 to +3 ‰ δ PDB) and light oxygen isotopic values (-14 to -11 ‰ δ PDB). Thermal spar involves a large thermal event not only restricted to the Guadalupe Mountains but to the Apache Mountains, Glass Mountains and Delaware Mountains. Thermal spar overlies SI in the reef and proximal forereef but in the distal foreslope (lower part of the forereef) is the only spar precipitated. Thermal spar is characterized by large, euhedral crystals from few mm to 30 cm. It is milky rather than transparent. Fluid inclusion homogenization temperatures were reported by Mruk (1989), Given and Lohmann (1986) and Crysdale (1987). Mruk estimated a range of temperatures varying from 35-46ºC, Given and Lohmann estimated a range of 30- 65ºC, and Crysdale homogenization temperatures were averaging 80ºC. The presence of thermal spar in the Delaware Basin is most conceivable derived from ascending thermal water rather than from burial based on the petrology and the subsidence curve of the area.

Hill (1996) also points out the existence of a meteoric non luminescent and iron rich calcite spar and she attributed its origin to the flushing of the Capitan platform by meteoric water during uplift. The isotopic signal of this meteoric spar is covered by Scholle et al. (1992) in the Rocky Arroyo area of the backreef.

Dolomite cements in the forereef facies

Much work has been done in the area relative to model a dolomitizing mechanism for the Capitan platform. Dolomitization by the density-driven sinking (seepage reflux) of hypersaline (i.e. >120‰ salinity) brines was first proposed for the Permian Reef Complex in a study that focused on the backreef facies rather than the reef and forereef of the Capitan Formation (Adams & Rhodes, 1960).

Garber et al. (1989) with the examination of the Gulf PDB-04 core interpreted that the Capitan reef complex was early dolomitized by shallow waters originated from supratidal and sabhka environments.

Melim (1991) and Melim and Scholle (2002) provided assertive bases that supported the reflux mechanism of dolomitization as the most acceptable model. The authors focused on the foreef facies dolomitization geometries and found that the amount of dolomite increases with stratigraphic age and decreases downslope. They conclude that most of the dolomite is fabric preserving and formed during early burial after marine cementation, before and/or during evaporite cementation and before stylolitization. Dolomite distribution within the reef facies was restricted to haloes around fractures and primary cavities and massive in zones where the reef facies lacks marine cements. They believed that this pattern of distribution supports dolomitization by sinking fluids of mainly mesosaline brines derived from the near-backreef carbonate lagoon. Geochemical data also gave support to the proposed reflux dolomitization model indicating dolomitizing fluids of seawater to hypersaline compositions.

Melim (1989) petrography studies also emphasized the presence of dolomite cements among dolomite components. Melim described two types of replacive dolomite and one dolomite cement type:

Fabric-preserving dolomite (Dolomite A) consists of 5–50 μm, anhedral crystals, which replace detrital material (grains and matrix), and near-surface diagenetic products (isopachous and botryoidal marine cements) with the precursor fabric easily recognized. This dolomite is non-luminescent. The internal structure of dolomitized botryoidal marine cements is preserved either as needle-shaped molds of former aragonite. This dolomite type is very common in Yates and Tansill formations.

Fabric-destructive dolomite (Dolomite B) is a non-planar dolomite mosaic with 30–200 μm, anhedral to subhedral rhombs, which gives little to no evidence of original texture. This dolomite exhibits deep red luminescence and is common in the older Lower Capitan units.

Dolomite cement (dolospar) occurs as euhedral overgrowths lining primary and secondary pores in completely dolomitized samples. When found with fabric-preserving dolomite, the dolospar crystals are small (20–30 μm), commonly have a cloudy core and have a dull red luminescence. Dolospar associated with fabric-destructive dolomite is larger (50–200 μm), limpid and has a deep red luminescence (identical to replacement dolomite in the same sample). Dolospar isotopic values appear more depleted both in carbon and oxygen than replacive dolomite. Distribution of the dolospar cements was not determined in the study.

5.-Study area

The study area covers approximately 200 m of vertical stacked Yates stratigraphic succession and part of the Seven Rivers top in Rattlesnake Canyon. Two conjugated faults (M and N) cut Yates succession from Y1 to Y4. These two faults (M and N) were described as syndepositional normal faults by Koša and Hunt (2006), and evidences for that are observed in the field (Chapter 4). What is obvious in the field is that the karst filling sequence is affected by karst processes. Karst affected materials are coloured in the field and this feature

facilitates their recognition in the distance and allows to establish relationships between them and the geological structures. Karst materials in Rattlesnake Canyon are observed affecting the graben system, the surrounding strata of the faults M and N and superimposing distinct karst episodes.

Two distinctive karst morphologies (vertical fracture caves and stratabound caves) were detected and described in Chapter 4. Vertical morphologies similar as the recent Blue Holes of the Bahamas (Palmer, 1986; Mylroie et al., 1995), produced vertical fracture caves which recorded many collapses. Thus, many breccia deposits are filling the vertical paleocaves with carbonate and siliciclastic sediments. Stratabound dissolution is parallel to the stratification and produces smaller caves (ten of metres along strata and ten of centimetres in the vertical) than fracture caves (several tens of metres width and hundred of metres height). Bed parallel solution cavities display red and yellow colours in the field, and are mainly filled by replacive dolomite and some cements recognized within vug porosities.

The outcrop shows 180 m in vertical relief, and host rock strata can be traced on both sides of the canyon for over 1 kilometre. These faults cut the Capitan platform parallel to the depositional strike (Figs.1 and 2) and follow the same ENE-WSW trending family of faults documented by Koša and Hunt (2006). Their syndepositional origin is interpreted as having resulted from down-to-the basin subsidence during Capitanian times (Hunt et al, 2002, Koša and Hunt, 2006). The Rattlesnake Canyon faults underwent maximum vertical displacements of 50 m in Fault M (Fig. 2 and 3). The faults are sealed at the top of the Yates Formation by the deposition of the Triplet sandstones and the uppermost part of the Yates Formation. Faults are associated with growth strata and tip out as in Slaughter Canyon (Koša and Hunt, 2006) below monoclines crosscut by different families of sub-vertical fractures.

New data derived from modelling the area with IRAP-RMS (Hunt et al, 2009) reveal that the graben of Faults M and N in this area is considerably tilted in the direction of the strike towards the opposite side of the canyon. The estimation of the extension of the tilted block could have exceeded 500 m according to the vertical displacement of both faults.

The outcrop under study includes the top of the Seven Rivers and Yates Formations. The main lithologies of the Yates Formation are shelf-crest pisolite shoals and tidal flats. No Tansill strata are exposed.

5.1.- Detailed stratigraphy of Rattlesnake Canyon

The succession under study consists of a stack of 1-10 m thick transgressive-regressive cycles. The base of the section is the top of the Seven Rivers Formation and is only exposed to the north of Fault M. The Yates Formation (Yates 1 to Yates 5) is the dominant record. Subaerial surfaces were not recognized. Only tepee structures are recognized in the upper part of the stratigraphical record and are linked to fracture zones, pisolite formation and cement precipitation.

Three stratigraphic sections were measured (Fig. 3) in the footwalls and graben of both faults. Eight lithofacies of the host rock were defined in the field and complemented by additional petrographic work, have been grouped into restricted peritidal, tidal flat, shallow open subtidal, open shoal and siliciclastics. Restricted peritidal lithofacies contained evaporites, now dissolved, and fine grained laminated grainstones with fenestral porosity. Evaporite facies are made up of very fine-grained carbonate sediment with pseudomorphs of selenite crystals. Tidal flat lithofacies are composed of peloidal wackestone to mudstone lithologies with fenestral porosity. Open shoal lithofacies consist of pisoid grainstones and skeletal-peloidal grainstones. Shallow open subtidal lithofacies contain fusulinid packstones and grainstones. Siliciclastics lithofacies are formed by sub-angular to angular quartz, feldspars and accessory Zr-silicate sandstones and siltstones.

Lithofacies studied in Rattlesnake Canyon include the Top of Seven Rivers and the Yates Formation. Yates shelf-crest facies tract is characterized by pisolite and fenestral lithofacies, which sometimes exhibit tepees. Pisolite grainstones are interpreted to occur in intertidal to supratidal environments. Outer shelf is composed of skeletal to peloid grainstones. Fusulinid grainstones are a common type of deposit in the outer shelf and represent shallow open-marine environments. Interbedded with the carbonate lithofacies are found fine-grained sandstones and siltstones that have been interpreted as representing lowstands episodes (Fischer and Sarnthein, 1988).

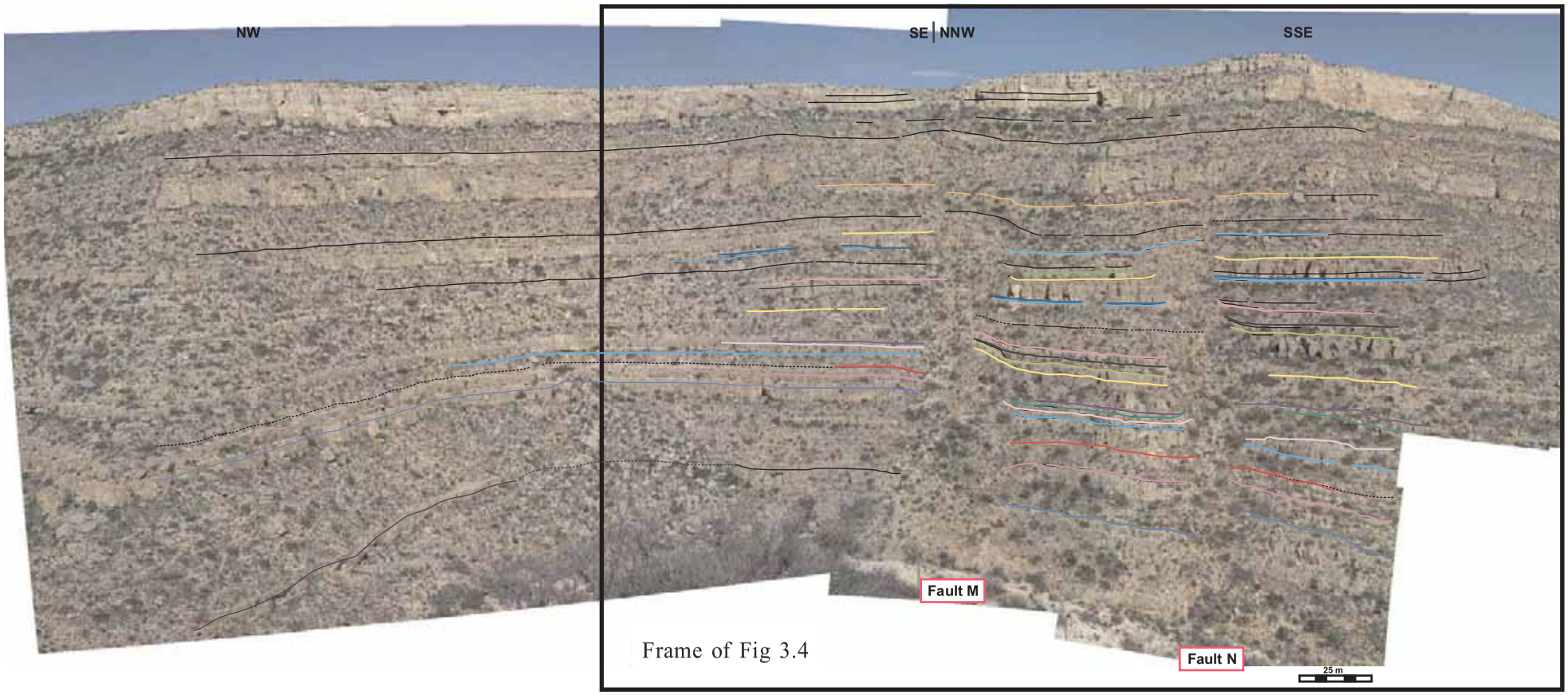

Fig 3.3. Photomosaic of the study area. Stratigraphic surfaces are correlated and shown in differnet colours. The black frame refers to the studied area and corresponds to the same area shown in Fig. 3.4. Faults M and N are discussed in the text.

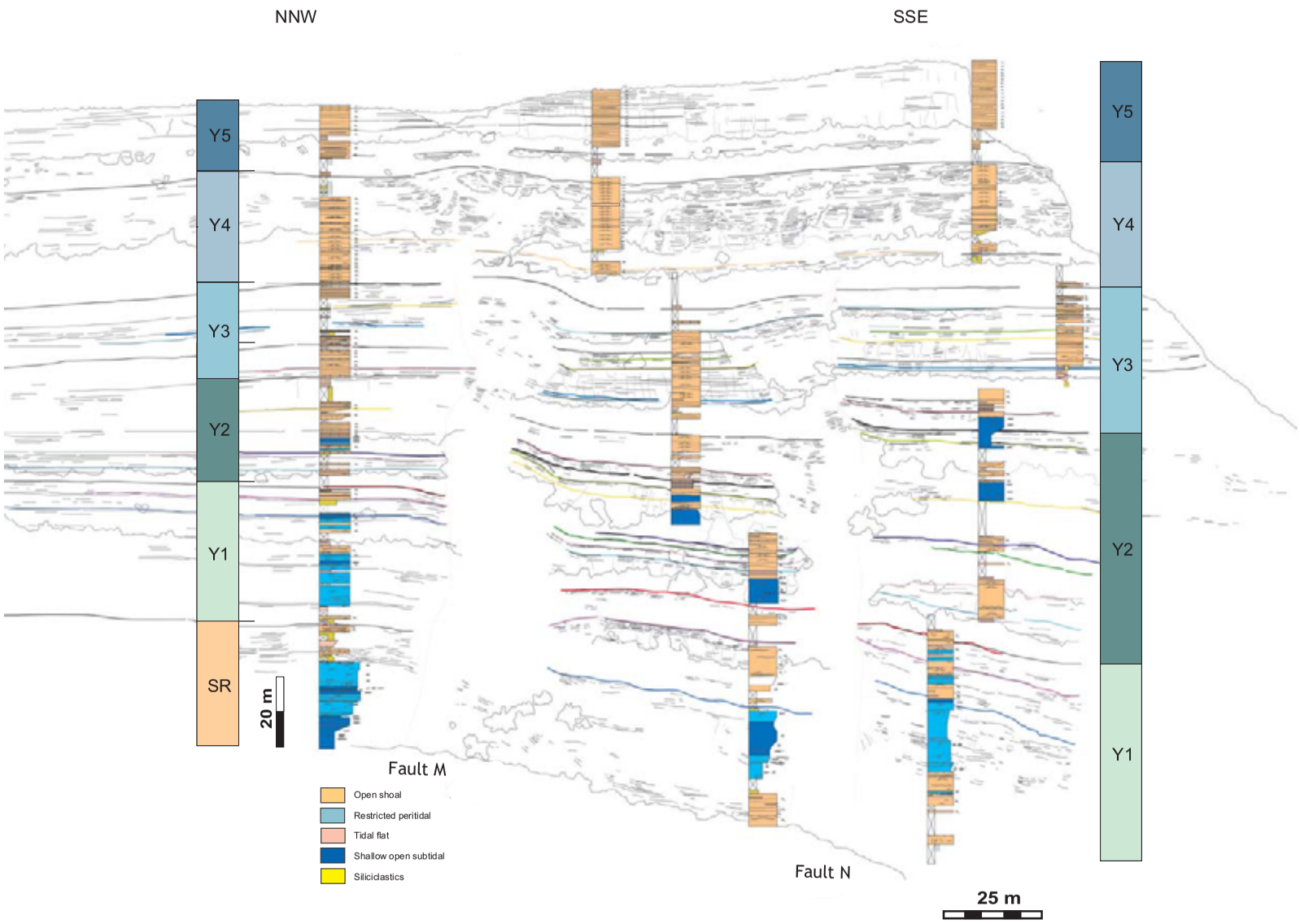

Fig. 3.4. Stratigraphic columns and correlation. Note the variations in thickness from NNW to SSE. The thickness pattern differs in the graben due to the faulting. Nomenclature Y1-Y5 after Osleger (1988). Stratigraphic columns by Simo, T and Van Alstine, J.

Chapter 4

Origin, controls and evolution of the Rattlesnake Canyon paleokarst

Abstract:

The Upper Permian carbonate platform of Guadalupe Mountains, New Mexico has been recently studied in detail by Hunt et al. (2002) and Koša and Hunt (2005; 2006), providing a large database on the regional architecture and stratigraphy of the platform and insights into syndepositional faulting and associated karsting. However, the understanding of dissolution mechanisms for cave formation during syndepositional faulting is still lacking.

The present study identifies and interprets a complex syndepositional paleokarst system that developed parallel to the Capitan platform margin during the Upper Permian. Two syndepositional normal faults (M and N) that define a graben are modified by a paleokarst system. These faults and the associated paleokarst system constitute the focus of this study. Two distinct karst zones are recognized in each fault: the paleocave zone and the karst damage zone. The paleocave zone represents the physical space of the ancient cave and is characterized by the presence of breccia deposits. It may reach tens of metres in width. The karst damage zone contains the paleocave zone but also contains an area less disrupted by gravitational processes. These zones surround paleocaves and are characterized by the presence of vugs (few centimetres), fractures and stratiform lateral passages with lateral dimensions of tens of metres. The lateral stratiform caves are here termed as stratabound caves. Karst infills display distinctive red, green and yellow colours in the field and their distribution reveals two significant dissolution mechanisms that are superimposed. Each mechanism is responsible for the resulting paleokarst morphology (vertical fracture karst and horizontal stratabound karst). Vertical paleokarst development in the two faults in Rattlesnake Canyon mimics and enhances the geometry of the faults and is fracture-controlled. Stratabound paleokarst development is detected along specific horizons in the two faults at discrete horizontal levels. No correlation with the same stratigraphic levels in footwalls and graben is possible, suggesting that these horizons are indicators of paleo-halocline positions.

Restoration of faults M and N shows that stratabound caves are horizontally aligned in each step of restoration reinforcing the hypothesis of the finding of halocline caves in Rattlesnake Canyon. The generation of these stratabound paleocaves was controlled by the syndepositional faulting and the paleo-hydrogeological regime during Yates deposition. The final pattern results in abandoned and reused stratiform passages presumably developed during stillstands. Restoration of the faults reveals the migration of the former halocline positions during faulting. After restoration the correlation of these levels is precise: beginning at the top of Yates 2 and continuing until the Upper Yates 4.

According to this interpretation, the most intense period for stratabound cave formation in Rattlesnake Canyon is during the deposition of Yates 3. During the Yates 3 cycle a shallowing upward trend for the paleo-halocline position suggests that the lens gradually thinned towards the top of the sequence.This could indicate a decrease in groundwater recharge and transition to more arid conditions. The presence of evaporite facies at the top of the cycles supports a climatic change.

A model for early karst evolution is presented on the basis of the paleokarst lithofacies distribution and the patterns of corrosion. Fracture-controlled dissolution, cave breakdown and formation of vertical open passages were the main processes responsible for the vertical cave development. Abundant siliciclastic fills and sand dikes in the paleokarst sequence suggest periods of detrital clastic input during eogenetic karst development. Stratabound cave development postdates vertical fracture development since sub-horizontal infills cross-cut the uppermost parts of paleocave sequence in zones preserved from faulting disruption.

The complexity of studying ancient coastal paleokarst systems deals with a comprehensive analysis of the stratigraphic framework, the paleo-hydrogeological regime, sea-level fluctuations and local tectonics which is commonly aggravated by the heterogeneity of the system. The present work offers new insights at oucrop scale into paleokarst development in the Guadalupe Mountains and contributes to an improved understanding of dissolution mechanisms.

Chapter 4

Origin, controls and evolution of the Rattlesnake Canyon paleokarst

1.-Introduction

Carbonate platform margins commonly present fracture and fault zones that may promote channelized flow and dissolution in groundwater mixing environments (Whitaker and Smart, 1997; Frost and Kerans, 2009). These fracture and fault sets often parallel the carbonate platform margin as in the case of the Capitan Platform and the Caspian Basin of Kazakhstan (Narr, et al., 2008). The prediction of karstic heterogeneities in carbonates of coastal settings is regulated by local eustatic controls and is influenced by the topography of the shelf and its subsidence rate (Borer and Harris, 1991; Yilmaz and Altiner, 2006). A number of authors have recently focused attention on the early fracture systems in carbonate platform margins and their efficiency for enhancing dissolution and promoting karst development (Guidry et al, 2007; Frost and Kerans, 2009).

The Permian Delaware Basin in West Texas and SW New Mexico is a classic example of a hydrocarbon rich basin with large oil fields (Craig, 1990). The basin, which is surrounded by the Glass Mountains to the South, the Apache Mountains to the West and the Guadalupe Mountains to the North, was uplifted during the Laramide orogeny. A large Permian carbonate platform is exposed along the southern rim of the Guadalupe Mountains, which constitutes the subject of this study. During the Cenozoic (Oligocene to late Miocene) volcanic processes increased the thermal gradient in the Delaware Basin. Sulphuric acid speleogenesis is thought to have formed during this period as a result of the release of H_2S, when hydrocarbons came into contact with evaporite levels (Hill, 1996). This process formed the large Lechuguilla Cave and the Carlsbad Caverns.

The Guadalupian carbonates of the Yates Formation in the Delaware Basin offer a magnificent scenario for studying carbonate fossil karsts related to faulting. As in the case of the modern Bahamas, (Stringfield and Legrand, 1971; Whitaker and Smart, 1998), vertical pit cave morphologies associated with synsedimentary faulting are preserved along the Capitan margin in the Upper Permian Yates Formation. These faults were active flow channels for meteoric water that mixed with saline groundwater during the growth of the carbonate platform, resulting in very effective coastal-related karstic dissolution processes (Ford, 1988;

Wright, 1991). Moreover, the study area displays multiple stratigraphic horizons in which lateral dissolution gave rise to stratabound karst development in Rattlesnake Canyon. This dissolution type is first documented in the area and offered great potential to constrain the timing of the early karst processes.

The Upper Permian platform has been studied in detail by Hunt et al. (2002) and Koša and Hunt (2005; 2006), who provided a large database on the regional architecture and stratigraphy of the platform and insights into fault growth timing and the nature of cave fills. However, a comprehensive understanding of the dissolution mechanisms of cave formation is still lacking.

The present study identifies and interprets a complex syndepositional paleokarst system that developed parallel to the Capitan platform margin during the Upper Permian. A detailed mapping of the paleokarst system reveals the distribution of fractures, karstic facies, damage zones and paleocave geometries in close relation to the Rattlesnake Canyon graben system. Analysis on the links between sub-vertical caves and stratabound caves in relation to syndepositional faulting has allowed us to establish the timing for the early karst development. In addition, an evolution model of the paleokarst system also links the spatial controls of the early fracture networks with the carbonate margin progradation dynamics and fault graben activity.

2.- Paleokarst system

In Rattlesnake Canyon faults M and N are modified by a paleokarst system. The process is easily recognizable in the field as fault boundaries are solution-modified. Karst extension shows vertical continuity along each fault for approximately 100 m and from few to tens of metres widening the fault zones. The karst affected materials are easily distinguishable in the field because of their reddish to yellowish, greenish and black tonalities.

Two distinct karst zones are recognized in each fault: the paleocave zone and the karst damage zone. The paleocave zone represents the physical space of the ancient cave system and is characterized by the presence of breccia deposits (crackle, mosaic and chaotic, following Loucks, 1999). It may reach tens of metres in width. The karst damage zone contains the paleocave area but also contains areas with minor disruption. These areas surround paleocaves and are characterized by the presence of vugs (few centimetres), fractures and stratiform lateral passages with lateral dimensions of tens of metres.

2.1.- Paleocave Lithofacies

Different types of breccia deposits in the paleocave zones are distinguished and described next.

2.1.1.- Chaotic Breccias.

Chaotic breccias are the predominant breccia type in the paleocaves. These brecciated bodies are recognized by a lack of stratification and by a chaotic appearance (Figs. 4.2 and 4.3). They are exposed in isolated areas at the base and in the middle of the Fault M paleokarst filling sequence, and at the base and the top of the Fault N paleokarst filling sequence. They form deposits of tens of metres. The clasts, which are 10 cm in diameter, are supported by the matrix and are occasionally cemented by spar calcite. Clast boundaries often display sutured contacts and have dissolved edges and coatings (Fig. 4.2: c). The clast origin is diverse including clasts from lithologies from upper horizons of the host rock, such as fusulinid grainstones. Both matrix and clasts show evidence of multiple episodes of brecciation.

These breccias are ascribed to multiple collapses of the walls and roofs of the paleocaves. Porosity within these breccias is often filled by calcite spar, carbonate sediment and dolomitized siltstones. Dolomite cements are observed, especially within reworked clasts. Shelter porosity is also present in these types of breccias and is mainly filled by calcite spar.

Early carbonate chaotic breccias were identified at the bottom of the two faults. These breccias contain dominant proportions of carbonate clasts derived from platform tops and are thought to be the older karst related breccia deposits outcropping in the canyon (Fig. 4.2: n).

2.1.2.- Mosaic Breccias.

Mosaic breccias are found at the top of the paleocaves and along the walls near non disrupted host rock beds. Mosaic deposits are usually found underlying fracture zones. They may be tens of metres in width. These breccia clasts are metre-to-centimetre scale and show a slight rotation of their clasts that barely interrupt the continuity of stratification (Fig 4.2: j and l). The sediment between clasts has the same characteristics as the sediment inside chaotic breccias, although the yellow matrix is dominant.

Mosaic breccias are less frequent than chaotic breccias and are thought to result from dissolution processes related to lateral karst extensions. It is believed that fracture zones favoured fluid flow as they enhanced dissolution downwards to the mosaic deposits areas.

2.1.3.- Crackle Breccias.

Crackle breccias are commonly associated with fractured host-rock nearby fault zones and do not exceed more than 2 m in width. Clasts are angular and have an insignificant displacement. They are not matrix supported and present no shelter porosity. The cements that fill the fractures are similar to the ones found inside the karst. The outcrop appearance is such that the breccias can be easily assembled (Fig. 4.2: a).

The crackle breccias are thought to be the result of gravitational movements towards the paleocave when faulting was active, and are genetically related to the fractures in the damage zone described below.

2.2.- Damage Zone Lithofacies

2.2.1.- Vugs and fractures

Vuggy porosity is widespread present throughout the paleokarst system in the form of micrometre to centimetre cavities usually cemented by dolomite and calcite cements.

Vuggy porosity cemented with dolospar is especially common and attributed to the formation of intercrystalline porosity in the sequence formation of indurated dolomite frameworks during shallow burial episodes of fabric-obliterative dolomitization (Chapter 6). These vugs are solution-modified by the leaching of later fluids of different origin, especially in zones of open flow, triggering dedolomitization along fracture systems (Chapter 6). It is thought that vuggy porosity could have been partly occluded by evaporite formation on the basis of the recognition of replacement calcites (Chapter 6). Therefore, it is believed that during telodiagenesis dissolution of the evaporites resulted in the formation of secondary porosity. Anhydrite mould porosity and microsolution pipes are now found occluded by calcite cements (Chapter 6).

Three types of vertical fractures related to the evolution of a paleokarst system are considered. In general, sedimentary structures are volumetrically much more abundant at the top of the two faults owing to the absence of major paleo-collapses in the upper areas, which has favoured their preservation.

a) Most of the vertical fractures are unfilled and located along the margins of the paleocave area and are often adjacent to crackle breccia deposits. The largest fractures present sharp contacts with the host rock and define the vertical walls of the paleocaves.

They probably represent the early stages of the formation of the paleokarst system given that they delimit abrupt changes between the slightly karstified adjacent host rock and the paleocave area. These fractures may be regarded as the remnants of earlier fractures of the platform linked to fault growth. These fractured areas crop out in zones where no adjacent lateral extensions towards the host rock have been detected.

b) At the top of the faults, especially in Fault M, dolomitized sand dikes are well preserved. The structures crop out at the top of the paleocave areas (Fig. 4. 2: e) and represent sediment entrances to the system. This mechanism seems to have been active during the whole karst record. Evidence of this is the presence of sand matrix supported breccias and dolomitized bedded sandstones at the base of Fault M (Fig. 4.2: b) as well as dispersed accumulations in the middle zones of the two faults. Sand dikes are preserved in the upper areas where major collapses did not occur.

These dikes are filled with dolomitic sandstones and display a beige colour in the field. Dikes are not dissolution enlarged and display sharp contacts with the dolomitic host rock whereas chaotic sand matrix breccias at the base are corroded by late spar calcite cements.

c) Another fracture type was identified in the field in the upper areas of both faults. This fracture type presents lower dip measurements and is related to the structural evolution of both normal faults. Fractures of this type are interpreted as having initiated as dilational fractures when fault tips were buried during the growth of monoclines (Koša and Hunt, 2005).

They are very well preserved in the Y2-Y3 units in Fault N and in the Y2-Y4 units in Fault M. They display a mean orientation of 45º (azimuth of the major trend fracture in both faults) and represent a minor population in Fault N with an azimuth of 7º (Fig. 4.5). These fracture networks are all karst affected as they seem to have acted as fluid channels that intensified dissolution processes. Some of these fractures have a significant extension of tens of metres, which facilitates mapping in the field (Fig 4.2: g).

Karst modification includes enlarged fractures which sometimes display corroded boundaries. They are filled with red and yellow dolomitic siltstones because they probably constituted cave sediment entrance channels for the system.

2.2.2.- Bedding Parallel and sub-horizontal fracture fills

One distinctive feature of the karst damage area is the presence of coloured fracture fills such as lateral extensions following specific stratigraphic horizons with enhanced dissolution processes (Fig 4.2: f). Sub-horizontal fracture fills are the most common fills in the karst damage zones and are less preserved in the paleocave zones. The responsible dissolution process involved in the creation of this porosity is thought to be not fracture-controlled and deserves separate consideration (Section 4).

The fact that the coloured fills of the Rattlesnake Canyon are mainly disposed following two different trends (early fracture networks and bed parallel horizons) indicates that the early depositional and fracture controls have strongly influenced the later episodes of karst diagenesis when the Fe mobilization took place (Chapter 6).

2.3.- Karst morphologies

Rattlesnake Canyon is a prominent karst outcrop since it exhibits two significant dissolution mechanisms that are superimposed. Each mechanism is responsible for the resulting paleokarst morphology, which depends on the local tectonic and paleo-hydrogeological regime of the study area.

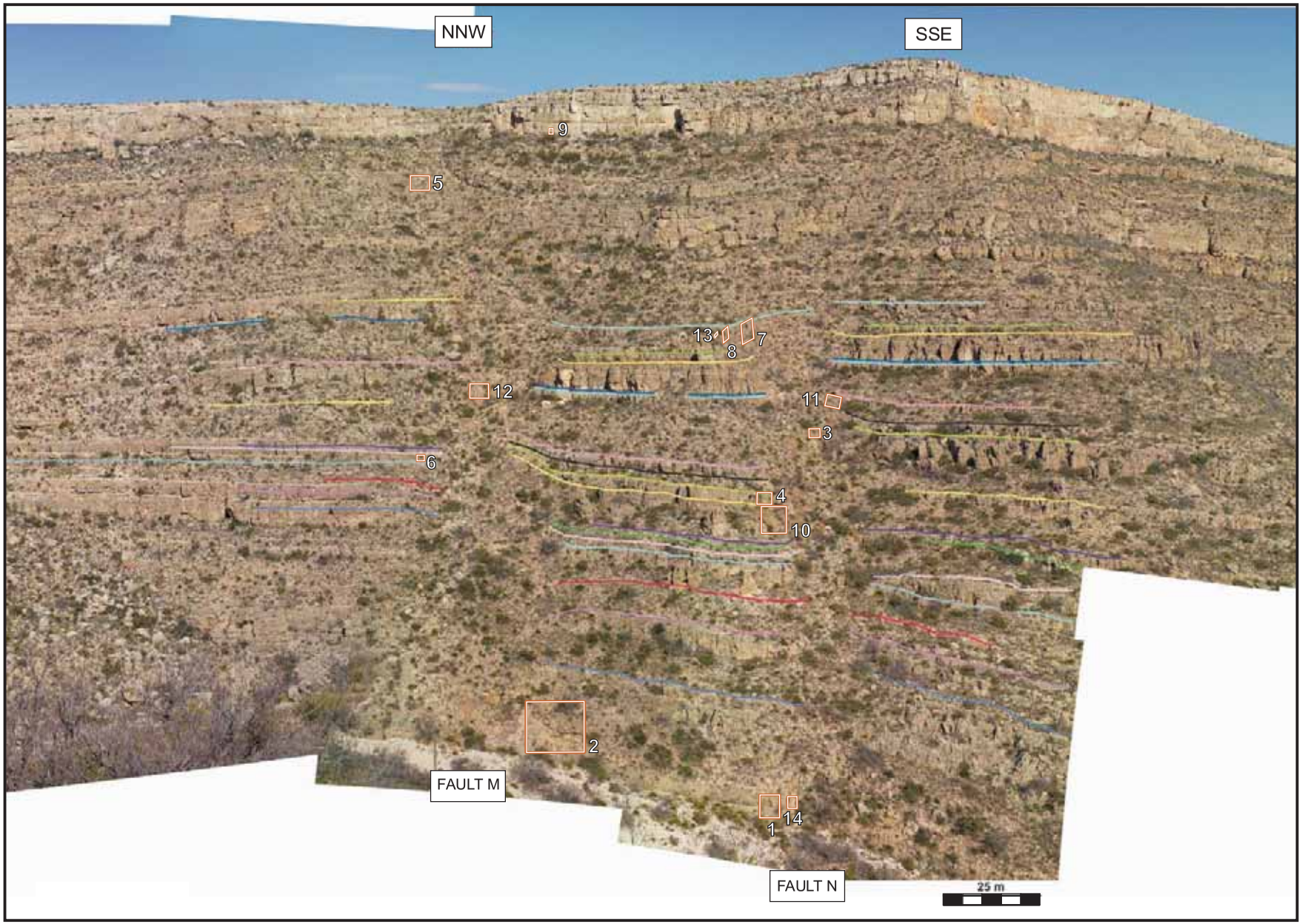

Fig. 4.1. Frame of Fig. 3.3 with the location of the structures and lithofacies shown in Fig. 4.2

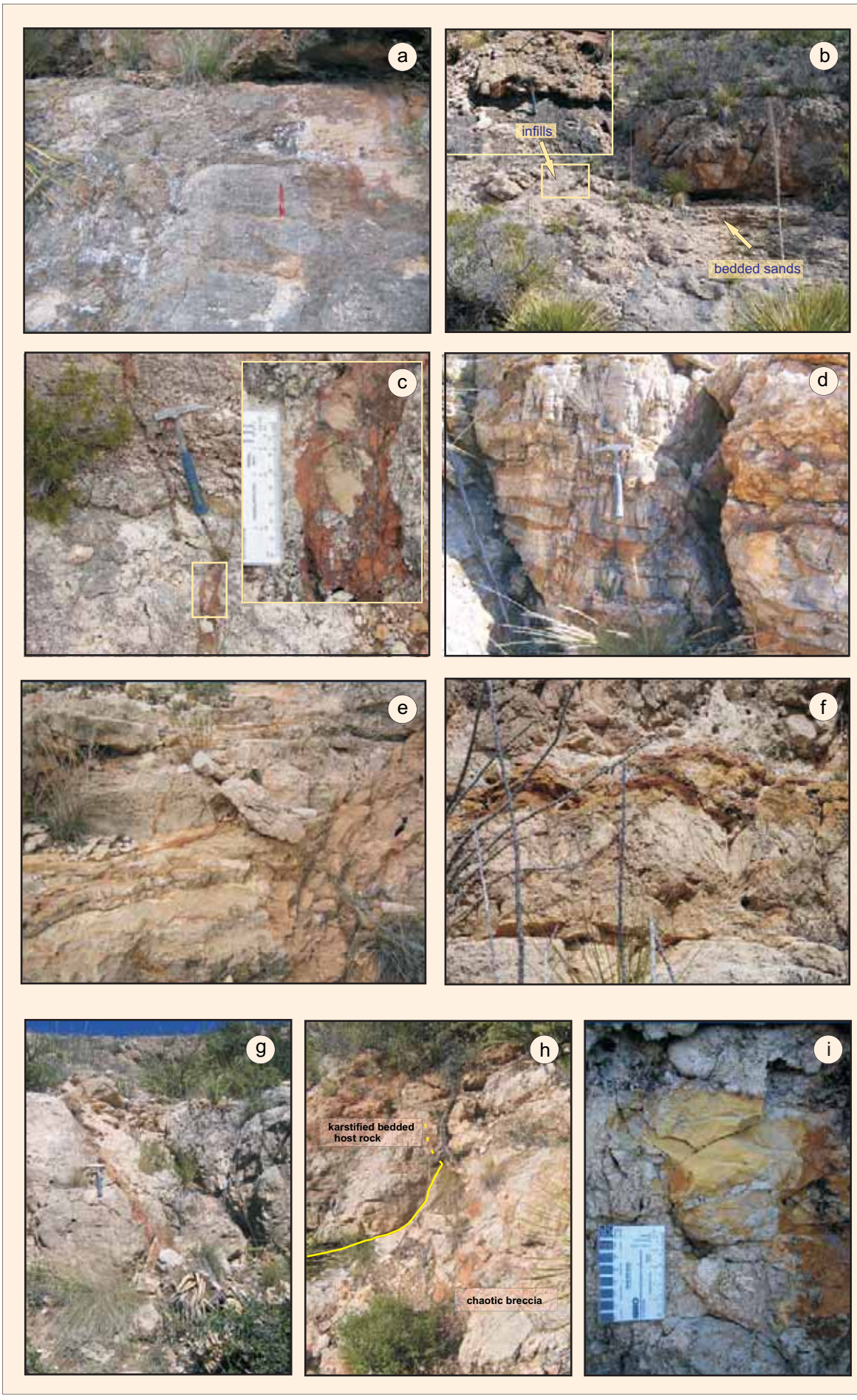
a
b
infills
bedded sands
c
d
e
f
g
h
karstified bedded host rock
chaotic breccia
i

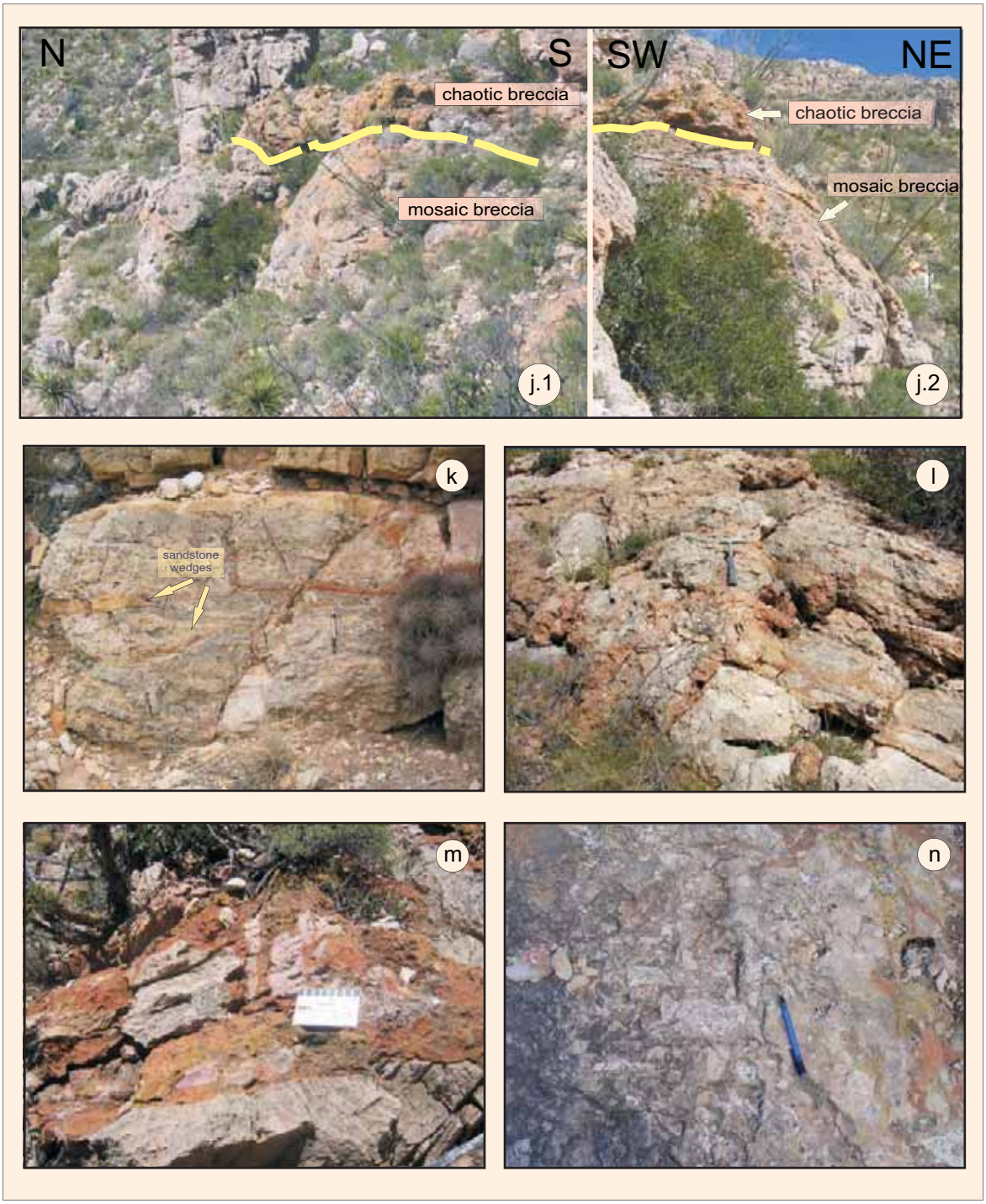

Fig. 4.2. Facies type and structures recognized in the field. a) Crackle breccia clast supported. b) Outcrop view of dolomitic bedded sandstones partially folded and overlapped by chaotic breccia deposits sand supported. Detail of the cave infills which show crustal morphologies. c) Vertical infill with reworked clasts of dolomitic sandstones. Note in the zoomed rectangle the corroded contact between the infill and the carbonate pisolitic host rock. The adjacent matrix of the pisolite grainstone underwent red karstic alteration. d) Vertical fracture separating brecciated bodies to the right versus horizontal infills to the left. e) Sharp contact between host rock and sand dike. Lateral sand interbedding is also detected. f) Interlayers of karst coloured deformed sediments and stratified sands. g) Vertical fracture dissolution enhanced at the top of the karst. h) Non-continuous contact between karstified strata and paleocave deposits. i) Karstic lens product of matrix controlled dissolution. j.1 and j.2) Different views of mosaic breccia deposits underlying chaotic breccia deposits. l) Horizontal opening of strata: dilational bedding and sandstone wedges. m) Pink chaotic breccia at the top of Fault N. Clasts show different orientations and their boundaries don't seem much corroded, especially pink clasts. n) Carbonate chaotic breccia at the low part of Fault N. Early carbonate clasts have been reworked and preserved.

2.3.1.- Introduction to common karst morphologies.

Caves in carbonate platforms can be divided into three main categories: vadose, phreatic and fracture caves. Vadose caves consist of pits that are dissolution pathways formed by descending water. Phreatic caves (flank margin caves and halocline caves) develop below the water table in the freshwater lens through mixing of different salinity waters. Fracture caves form along the margin of carbonate platforms as a result of gravitational failure of the platform margins. Pit and fracture caves display vertical morphologies whereas phreatic caves develop horizontally and produce dissolution vugs. Flank margin caves develop along the margins of the platform where the lens thins out as it approaches the sea-level position. Halocline caves form inland at the base of the lens at the water density boundary.

Sea-level change is directly related to coastal karst development. Flank margin caves are indicative of sea-level positions because of the low thickness of the lens at the platform margins. Halocline caves are more difficult to interpret as they are relative indicators of past sea-level positions. The Ghyben-Herzberg relationship is useful to calculate the thickness of the lens in carbonate paleo-islands (Budd and Vacher, 1991) but the calculation depends on annual recharge values and on the length of the platform/island, which are sometimes approximations when studying ancient materials.

2.3.2.- Fault related caves.

Two fracture paleocaves were interpreted as affecting Faults M and N in Rattlesnake Canyon. Both paleocaves show significant width (>20 m) along vertical fault boundaries (Fig. 4.3). Breccia deposits distribution, dissolution enlargement of fractures and fracture fills observed in the field enabled us to characterize two mapped zones. These zones are shown in the map in Figure 4.3 and are termed the paleocave area and the karst damage area. The paleocave areas, in each fault, define the extension of the fracture caves, and contains chaotic and mosaic breccia deposits especially along the borders of the two faults and towards the bottom of Fault M. Crackle breccias are commonly found near the paleokarst limits where the cave walls follow fracture directions. Fractures and some early depositional structures within the paleokarst filling sequence, such as tepees, are mapped as well as the lithofacies distribution in the Fig. 4.3.

The distribution of the karst lithofacies is shown in Fig. 4.3. Karst related breccia deposits are located inside paleokarst areas and define their borders. Chaotic breccias are found in the innermost parts of the paleocave areas and volumetrically represent the largest area of breccia deposits exposure. They are usually present in the paleocave area and only on one occasion were they found as a small patch inside a lateral horizontal passage. Two textural distinctions are considered in connection with chaotic breccias. Chaotic carbonate breccias are chaotic breccias that contain early reworked carbonate clasts derived from the platform. These clasts exhibit eroded and corroded borders and are light beige in colour. They are mainly preserved at the bottom of both faults and represent the oldest breccia paleokarst

products. On the other hand, chaotic breccias with sand matrix breccias are located at the bottom of Fault M, where sandstone accumulations are more frequent. Mosaic breccias are well preserved in the upper areas of the two ancient caves, limiting the host rock. Crackle breccias are the least abundant breccia deposits and appear to be related to fault boundaries and their relative kinematics. Fracture fills are well preserved in the low dip fractures. These fractures are dissolution enhanced and filled with abundant dolomitized sandstones. Horizontal bed-parallel infills are best recognized along the lateral extensions mapped in the two faults (Fig. 4.3). Tepees (mapped in the Yates 3 and 4) display internal sediment in the cores, this sediment is red coloured usually when the teppe structures are located within the karst damage areas.The presence of chaotic brecciated deposits denotes paleocollapses that occurred when caves were open and the system was active. Matrix sediments of these chaotic breccias are identified as carbonate sediments and allocthonous siliciclastic inputs. Fault M contains maximum sandstone accumulations at the base and Fault N has significantly less siliciclastic sediment inside its paleocave area. Likewise, the entrance of siliciclastic materials through the two fault paleocaves is evidenced by the fossilized sandstone dikes in the upper part of the system.

The karst damage area contains mainly horizontal coloured fills and vugs that follow strata horizons. The sedimentological record in this area shows no paleocollapses but preserves dissolution mechanisms independently of major gravitational processes. Vertical fracture dissolution enhancement is located along the fractures at the top. Karst dissolution processes have coloured fracture fills and cave sediments, and are mapped according to their colours in the field (Fig 4.3).

2.3.3.- Stratabound related passages.

Parallel to bedding karst corrosions were detected along specific horizons in the two faults. This preferential stratiform dissolution along the strata has been documented by Baceta et al. (2007) in shallow-water Paleogen limestones of the Urbasa-Andia plateau, northern Spain. The finding of bedding-parallel voids in the Neogene carbonates in the Bahamian Archipelago and in the Isla de Mona has also been documented. These caves have been termed flank margin caves because of their proximity to the coast line (Mylorie and Carew, 1990; Mylorie et al, 1995. Gonzalez et al, 1997). Lateral extensions found in Rattlesnake Canyon are observed in the field as continuous sub-horizontal levels parallel to strata and filled with coloured sediment (Fig 4.2: f). They may be recognized by their red and yellow infills showing maximum dimensions of tens of metres in length and centimetres to a few metres thick (Fig. 4.3). Bed rock dissolution generated lateral passages at discrete horizontal levels despite not being correlated with the same stratigraphic level in footwalls and graben.

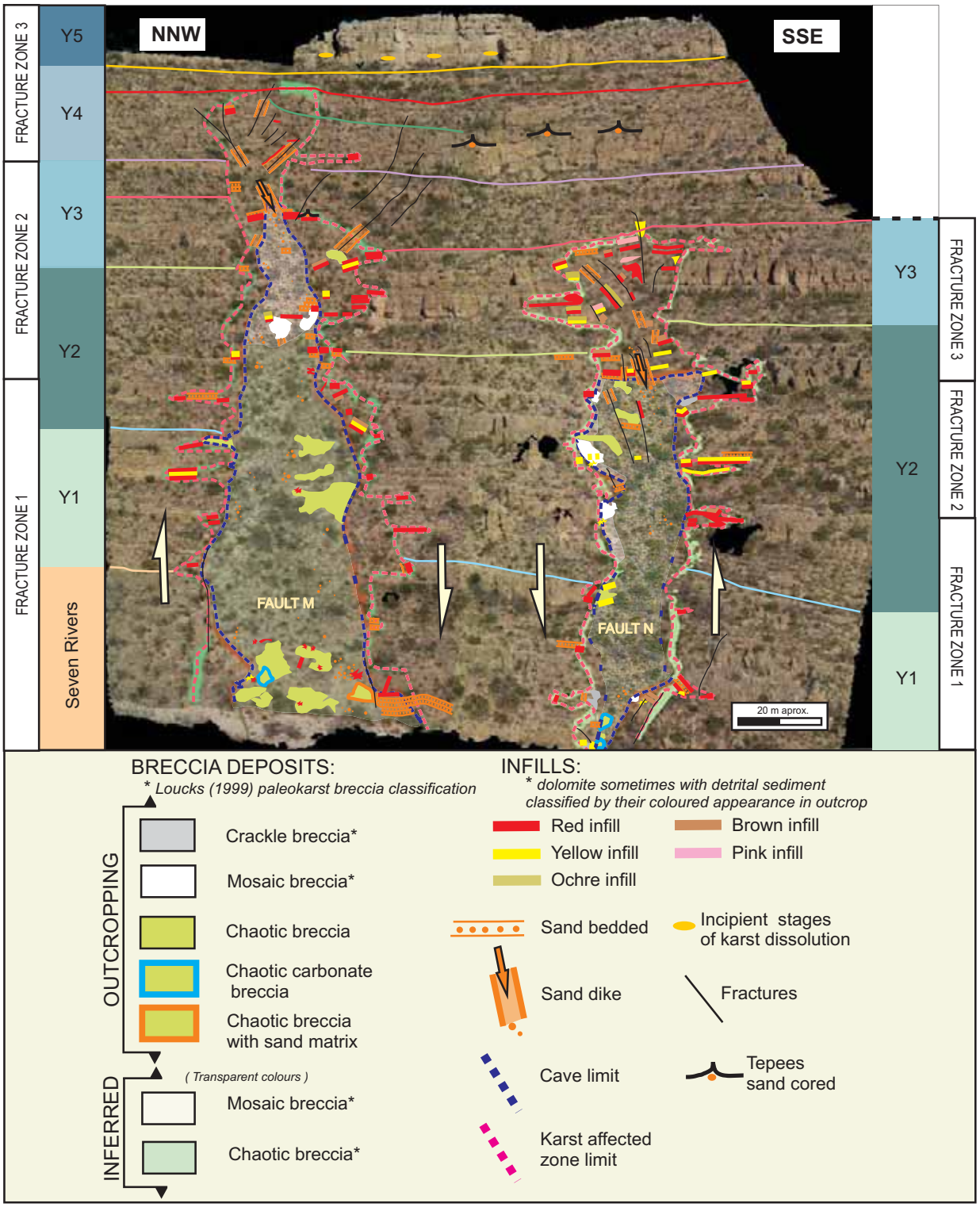

Fig. 4.3. Field mapping with the limits of karst exposure (Karst damage zones and paleocave zones). Mapping also includes breccia deposits distribution as well as karst infills, fracture zones and sand dikes. Outcropping breccia deposits are mapped in solid colours whereas inferred zones are drawn transparent with the same colours. Stratigraphic formation are placed in coloured columns at both sides of the figure. Three discrete fracture zones are symbolized according to stereonet projections (Fig. 4.6).

3.- Fault related paleokarst geometry

Vertical paleokarst development in the two faults in Rattlesnake Canyon mimics and enhances the geometry of the faults. Thus, an analysis of fracture/fault kinematics is necessary to better understand the carbonate host rock deformation and the evolution of the paleokarst system.

3.1.- Evolution of the syndepositional normal fault system

The final fault distribution and fracture pattern observed in Rattlesnake Canyon are governed by a synsedimentary fault behavior along the Capitan platform margin (Hunt and Koša, 2002). The evolution of the two faults is shown in Fig. 4.4. The timing of the faults is deduced by analyzing growth strata along the faults. Fault M is syntectonic to Y1, Y2 and Y3, which is corroborated by different strata growth in the footwall and hangingwall. Upper low dip fractures were produced as a result of extension over synsedimentary folding caused by the accommodation of sediment. Fault N is syntectonic to Y3 and exhibits the same upper low dip fracture patterns as Fault M. The vertical throw is smaller than in Fault M. In contrast to Fault N, Fault M displayed a slower rate of movement with respect to the sedimentation rate.

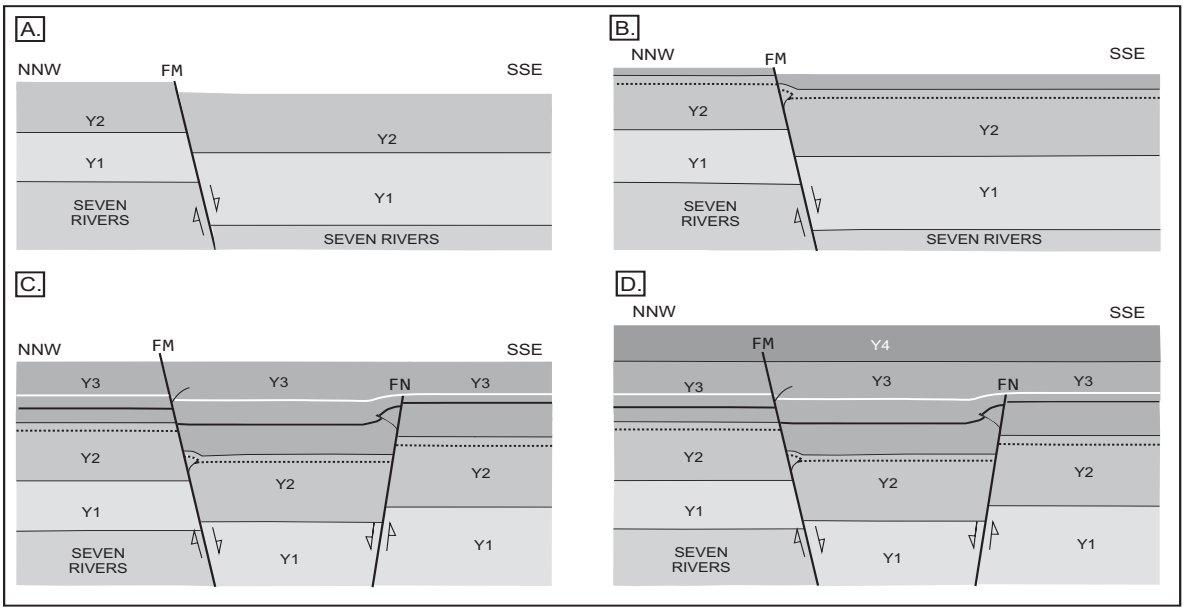

Fig. 4.4. Schematic sketch showing the formation and evolution of both faults. A) Fault M is syntectonic to Yates 1, Yates 2 and Yates3. b) Brittle fractures are produced owing to extension over synsedimentary folding. The resulting product is the formation of minor reverse faults associated with fracturation. C) Faults M and N are syntectonic to Yates 3 with most throw concentrated in Fault M. D) Fault N is fossilized by Yates 3 and Fault M by Lower Yates 4.

3.2.- Kinematics of the fault system

Spatial analysis of fracture/fault distribution leads to the discrimination of different families of fractures. Figure 4.5 shows a roseplot with all the fractures collected in the field. Two dominant populations appear in each fault. One is common to the two faults and represents the main fracture stage associated with fault formation. These fractures appear to be sub-vertical in dip. This fracture trend is oriented NE-SW (Mean Azimuth: 44º). The other fracture trends have a lower dip (Fig. 4.6) and their strike orientations are NW-SE (Mean Azimuth: 45º) for Fault M, and NNE-SSW (Mean Azimuth: 7º) for Fault N.

FAULT M

Frequency Smooth Data Gaussians
Total Data: 158 max:10 min:0 mean: 45.859 mode: 40

GAUSSIAN PARAMETERS					
#	%	Nor. H.	Max. H.	Azimuth	sd
1	73.49	100.00	5.793	45.21º	13.32º
2	28.00	23.46	1.359	-45.27º	21.64º

RMS= 0.3714906

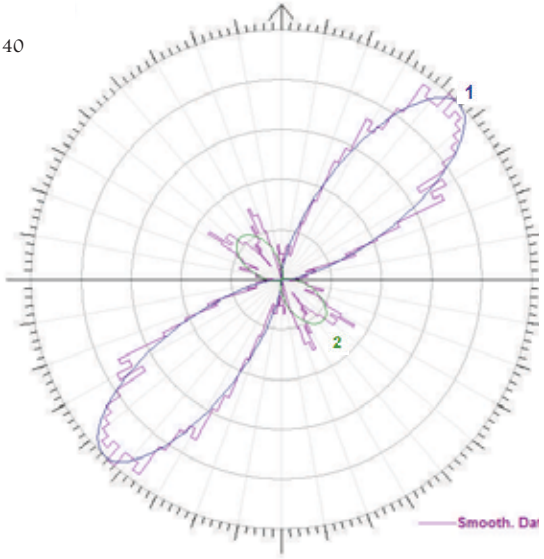

FAULT N

Frequency Smooth Data Gaussians
Total Data: 125 max:10 min:0 mean: 41.278 mode: 48

GAUSSIAN PARAMETERS					
#	%	Nor. H.	Max. H.	Azimuth	sd
1	46.39	100.00	3.554	43.43º	10.85º
2	8.547	28.23	1.003	80.32º	7.08º
3	23.89	0.9729	0.9729	7.062º	42.6º

RMS= 0.3536689

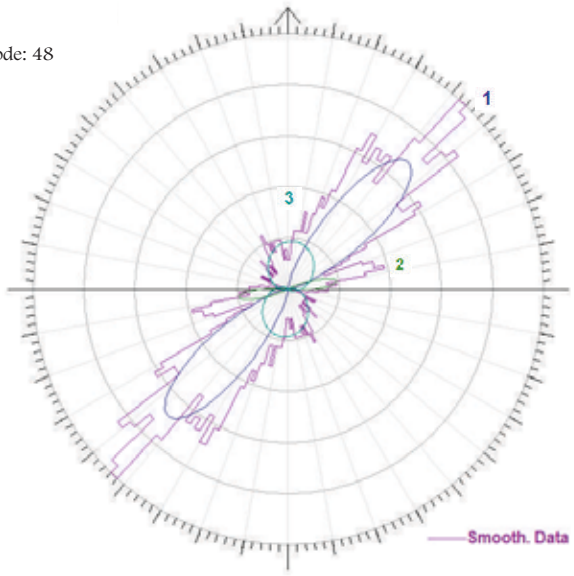

Fig. 4.5. Rose diagrams of fractures and faults M and N. Set 1 corresponds to major fault component at both faults. Set 3 in Fault N comprises shelward low dip fractures whereas the same fracture set in Fault M concurs with global Set 1.

Three zones were differentiated along the faults based on fracture distribution (Fig. 4.3 and 4.6). Discrimination between fracture zones was made in accordance with the different fracture patterns repeated in each fault at different intervals.

Fracture zone 1 represents the older karst record that crops out in the field. This zone is considerably damaged and reworked and records the maximum width of fracture caves along fault M. Strike and dip fracture data gathered in this zone show the maximum number of sub-vertical fractures associated with fault growth. The fracture population plays a major role in the morphology of the larger paleocaves. Gravitational collapses, fault activity and intense dissolution processes reduced the number of low dip extensional fractures preserved in this area.

Fracture zone 2 includes a large number of low dip fractures that are preserved in the paleocave areas. These fractures are highly solution modified and filled with coloured sediment. They are related to chaotic breccia deposits. Gravitational processes and fault activity are interpreted to be less intense in this part of the paleocave area. This zone provides evidence of dissolution processes in fracture caves controlled by channelized flow inputs. Low dip fractures seem to have been reused as flow conduits, which intensified dissolution and the resulting collapses.

Fracture zone 3 comprises the top of the system within the damage zone, where no collapse episodes are recorded. It includes the youngest low dip fracture populations. Parts of these fracture populations are fossilized as sand dikes and many of them are dissolution enlarged filled with karst sediment (Fig 4.3: top of Fault M).

4.- Stratabound paleokarst evolution

Stratabound paleokarst development in the two faults in Rattlesnake Canyon occurred along specific stratigraphic surfaces. Coloured fills are easily distinguished in the field from the non-altered carbonate host rock. Owing to the stratiform geometry, this dissolution driven process is analogous to the formation of phreatic caves documented in the literature as flank margin caves and halocline caves. This cave type develops under the control factors of the Carbonate Island Model (Mylorie and Carew, 1990; Stafford et al., 2005).

4.1.- Introduction to the Carbonate Island Model

The Carbonate Island Model accounts for the hydrologic regime in island and coastal settings where young unconsolidated geological materials have not undergone burial and are subjected to meteoric diagenesis (Mylorie and Vacher 1999; Vacher and Mylorie 2002; Mylorie and Jenson, 2002). The hydrological regime in these settings is based on the interaction between fresh and saline groundwater, which gives rise to the formation of a freshwater lens above saline waters because of the density difference between fresh and saline water. The

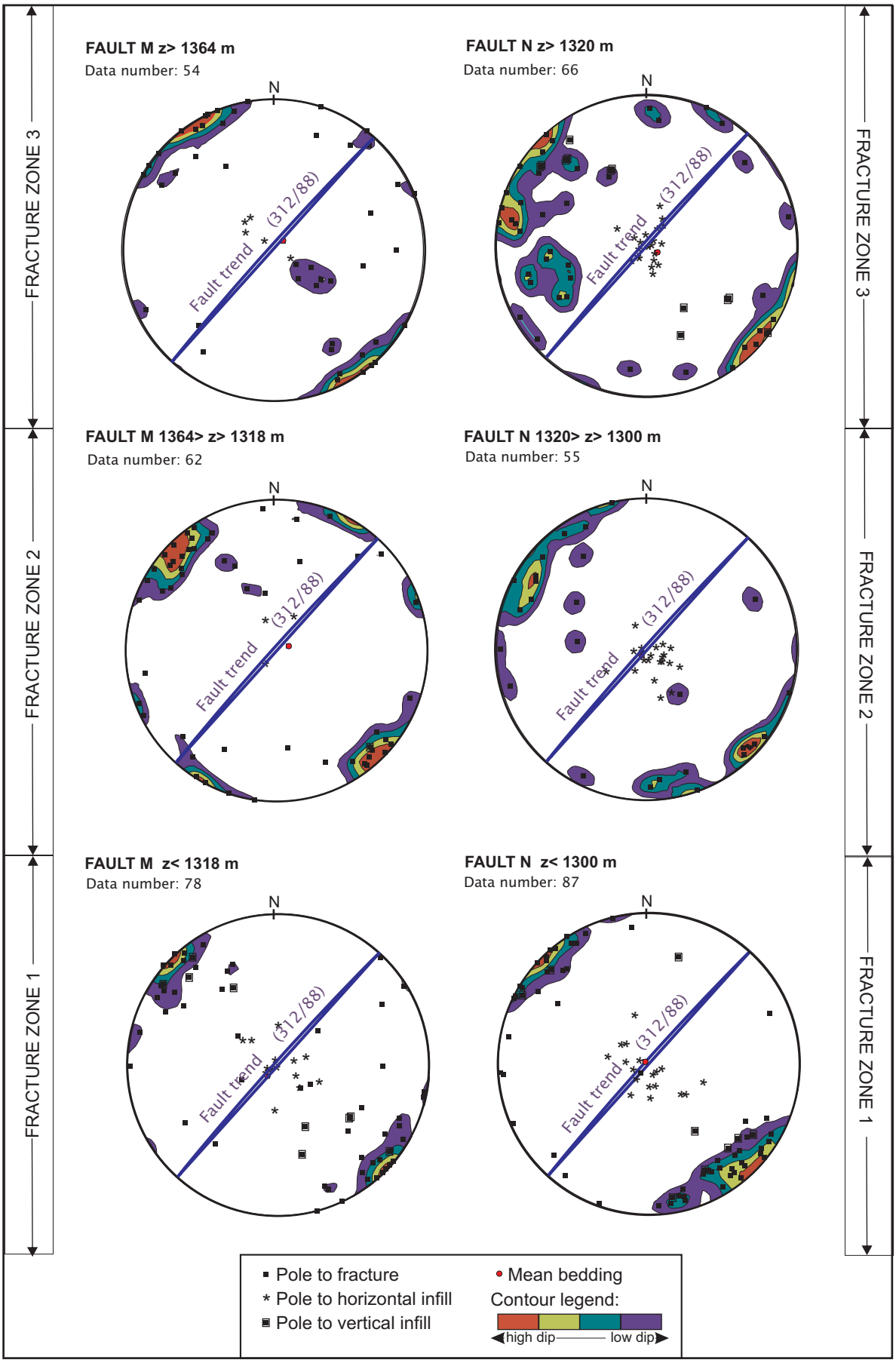

Fig. 4.6. Stereonet plots of fracture data. projections are differentiated according to three fracture zones with correspondence with Fig. 4.3. a significant number of low dip fractures is found in the upper zones but remnants of this fracture type are also preserved in teh borrom areas.

thickness of the lens is controlled by the Ghyben-Herzberg relationship, which estimates that the halocline lies approximately 40 times the height of the water table below sea-level (Fig. 4.7), (Vacher, 1988).

The hydrogeological Carbonate Island model was originally applied to the Bahamas and Bermuda karst processes, and the control factors of the model were defined as:

The dissolution power that results from the physical mixing of fresh and marine waters (Plummer, 1975; Smart et al., 1988; Mylorie and Carew, 1990) and specifically along the freshwater/saltwater boundary (halocline). Halocline may result in organic trapping horizons leading to oxidation and to the production of more CO_2 which gives rise to carbonate dissolution. Complex oxidation/reduction reactions may also occur in these horizons. Some of them involve sulphur, which produces acid conditions prone to dissolution (Bottrell et al., 1991; Mylorie and Balcerzak, 1992).

Vertical migration of the freshwater lens is controlled by Quaternary glacio-eustatic sea-level events.

The model rests upon the assumption that the karst is eogenetic.

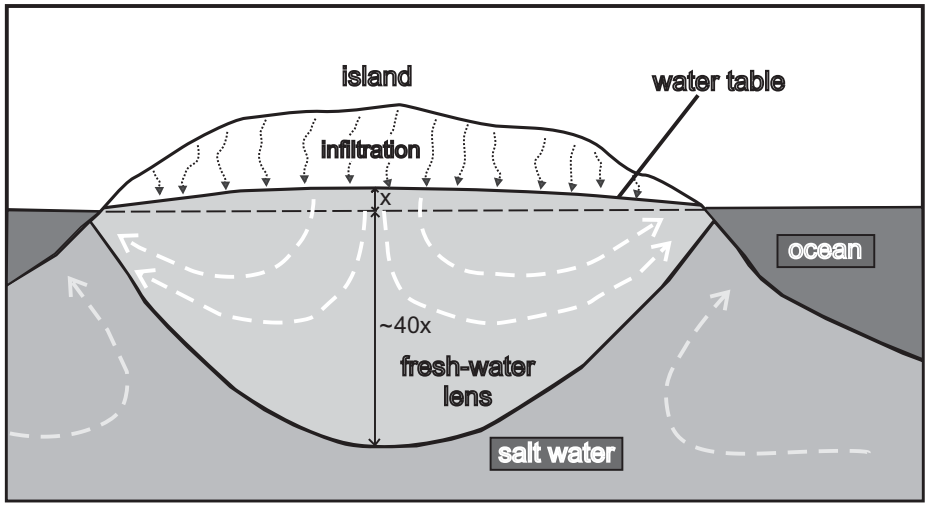

Fig. 4.7. Hydrogeological regime in a carbonate island. Meteoric infiltration forms fresh-water lens floating above denser sea salt water. The Ghyben-Hertzberg relationship establishes that the halocline is located 40 times the height of water table above sea level. Discontinuous white arrows show flow paths. Modified from Palmer (2007).

Thus lateral karst extensions in Rattlesnake Canyon are likely to be early formed in phreatic conditions as a result of freshwater lens mixing in a Carbonate Island setting (Carew and Mylorie, 1997; Palmer, 2007; Vacher L. and Quinn T, 2004). Assuming that the hydrological regime is consistent with the regime applicable to a Carbonate Island karst, these lateral karst extensions may be interpreted as indicators of the halocline level positions during Yates

times. It is in the halocline interface where corrosion is thought to produce phreatic caves. Interbedding surfaces may act as heterogeneity paths prone to dissolution fronts movement.

4.2.- Sequential restoration of the syn-faulting stratabound paleokarst level method

When local tectonics interfere with vertical migration of the freshwater lens, the distribution of the final halocline caves results in a complex model of reused horizons that are superimposed. This is the case of Rattlesnake Canyon, where the final dissolution pattern cannot be easily understood without a sequential restoration of the two affected faults. Faulting gave rise to numerous horizontal phreatic passages rarely preserved in the paleocave area. Fig. 4.8 illustrates the process that generates these passages at different stages of fault evolution. The process promotes reuse of abandoned lateral passages in the footwall and hangingwall as faulting evolves. Stratabound dissolution is thought to have occurred later than fracture/fault dissolution. Thus, halocline dissolution was superimposed over earlier episodes of dissolution produced by the channelized flow due to faulting and associated fracture networks.

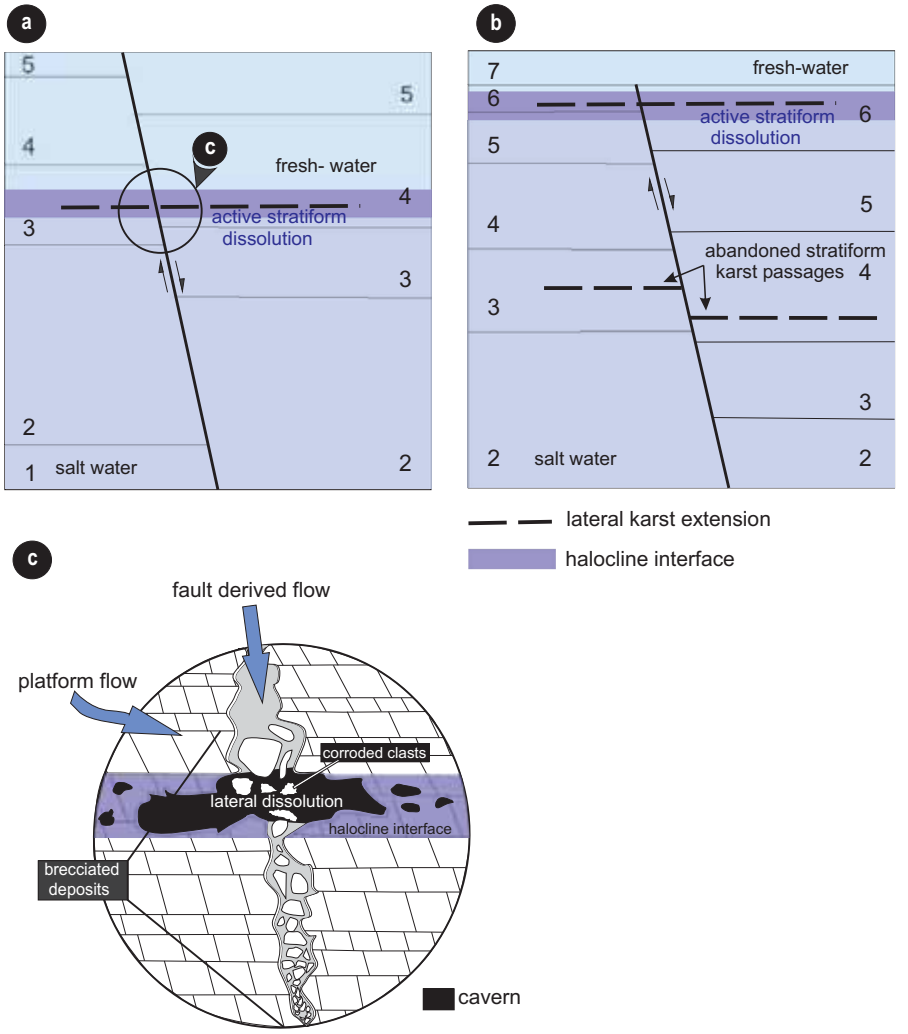

Fig. 4.8. a) and b) Sketch of the halocline derived dissolution processes at different stages of fault evolution. Stratiform disoolution occurs at the halocline interface. c) Halocline dissolution cave. Lateral dissolution generate younger caverns and corrode older clasts. Arrows indicate the direction of the meteoric flow operating from the platform top.

In order to validate this interpretation, a sequential restoration of syn-faulting stratabound paleokarst levels was used for the Yates deposition (Fig. 4.9). Reconstructions are consistent with the stratigraphy, and specific horizons were chosen to correlate different steps (Fig. 4.9: coloured horizons and top of the units). The steps of the sequential restoration during halocline dissolution are as follows:

4.2.1. Step 1. During the deposition of the top of Yates 2 HFS, three probable levels (A, B and C) (dashed lines in green Fig. 4.9: a) can be correlated. These lie approximately 70 m below the deposition line.

4.2.2. Lower Yates 3 HFS shows a good correlation for five probable levels (D, E, F, G and H) above the previous ones. D and E levels are reused in footwall M and graben.

4.2.3. During the deposition of Middle Yates 3 HFS, five levels (I, J, K, H and L) are correlated in Fig. 4.9: c. Only level L creates new dissolution passages. H thickens the previous H formed during Lower Yates 3.

4.2.4. During the deposition of Upper Yates 3 HFS, seven confident levels are marked as probable paleo-halocline positions (M, N, O, H, P and Q). All the levels formed are totally reused in this active dissolution stage.

4.2.5. During the deposition of the top of Yates 3 HFS, five active levels operate (R, S, T, U and V). However, only V creates a new passage.

7.2.6. During the deposition of Upper Yates 4 HFS, the process comes to an end and produces level W at the top of fault M. Only one level can be correlated in this step and it almost coincides with the deposition line.

The global trend decreases in depth from level A level to level W, which is sub-metre in depth with respect to the surface. All these steps are correlated with the aid of reliable stratigraphic horizons extracted from the stratigraphic correlation. Only Upper Yates 4 HFS, which is synthetic, is obtained from the correlation of level K.

The duration of the halocline dissolution process can be estimated from the top of Yates 2 HFS to Upper Yates 4 HFS. The level which shows most reuse is H, which is the thickest level observed in the field.

As shown in Fig 4.9, the overall trend ranges from paleo-halocline depths from tens of metres to sub-metres. Upper Yates 4 HFS seems to terminate the mixing dissolution since there are no more levels that can be correlated above this record. From the top of Yates 2 HFS to Upper Yates 4 HFS, the position of the halocline moves from 70 m below sea-level up to almost the sea-level position. This means that the water table thickness must have been reduced from 1.75 m at the top of Yates 2 HFS to centimetre thickness at Upper Yates 3.

This reduction may be interpreted as a climate change, which must be corroborated by the stratigraphic record. From the top of Yates 2 HFS to Upper Yates 3 HFS, marine conditions controlled this setting with repetitive episodes of siliciclastic inputs. Siliciclastics acted as a barrier against interbedded dissolution as in the case of the graben during the deposition of the top of Yates 2 HFS (Fig 4.9 : B peters out towards the south of the the graben). Siliciclastic lithology therefore does not seem to be prone to corrosion. From Upper Yates 3 HFS to Upper Yates 4 HFS, the halocline position gradually attains shallower positions up to few metres below sea level. This is in line with the facies in the stratigraphic record. These facies are the shelf-tepee crest facies that are characterized by pisoid grainstones with large metre-sized tepee structures, which suggests arid environments (Heinrich, 1984). If a significant change to arid conditions is assumed, the general chronological trend of all of these lateral karst extensions must have been from young to old in depth.

Mosaic breccias are associated with levels H, K, F, G, J, O and V from Lower Yates 3 HFS to the top of Yates 3 HFS. These levels are interpreted to have occurred when fracture caves were filled and when gravitational component was minor. This resulted in a clast arrangement that is less disordered than chaotic arrangements. Porosity generated by collapse is filled with early low-competent sandstones that record deformation.

The overall trend of the lens thickness decreases through time from thick to thin. The considerable thickness in the first stages could also reflect the great efficiency of tide-induced mixing in the transmissive carbonates as well as a significant discharge from the top of the platform. Hydraulic conductivity is assumed to increase through time because of fracture development and could also contribute to a diminution in lens thickness.

Thicker lenses in the mixing zone can also be enhanced by the decrease in permeability (often one order of magnitude) of the early unconsolidated carbonates, resulting in a slower flow rate (Melim, 2004).

5.-Karst evolution

5.1.- Karst sequence

Deposition, fault activity and karst formation along faults occurred simultaneously in the study area. Steep faults provided a natural sub-vertical channel for fluid flow. The tilting of the graben towards the west might have affected the regular hydrologic regime inducing a localized freshwater head flow that stimulated karst development (Fig. 4.11). The synchronicity of the aforementioned processes is observed because siliciclastic and carbonate fractions coexist as karst infills and also as matrix breccias and are common components in numerous re-karstification recorded episodes.

Stratabound karst developed later, exploiting normal fault porosity and permeability attributed to the sub-vertical karst. Cross-cutting relations between stratabound extensions

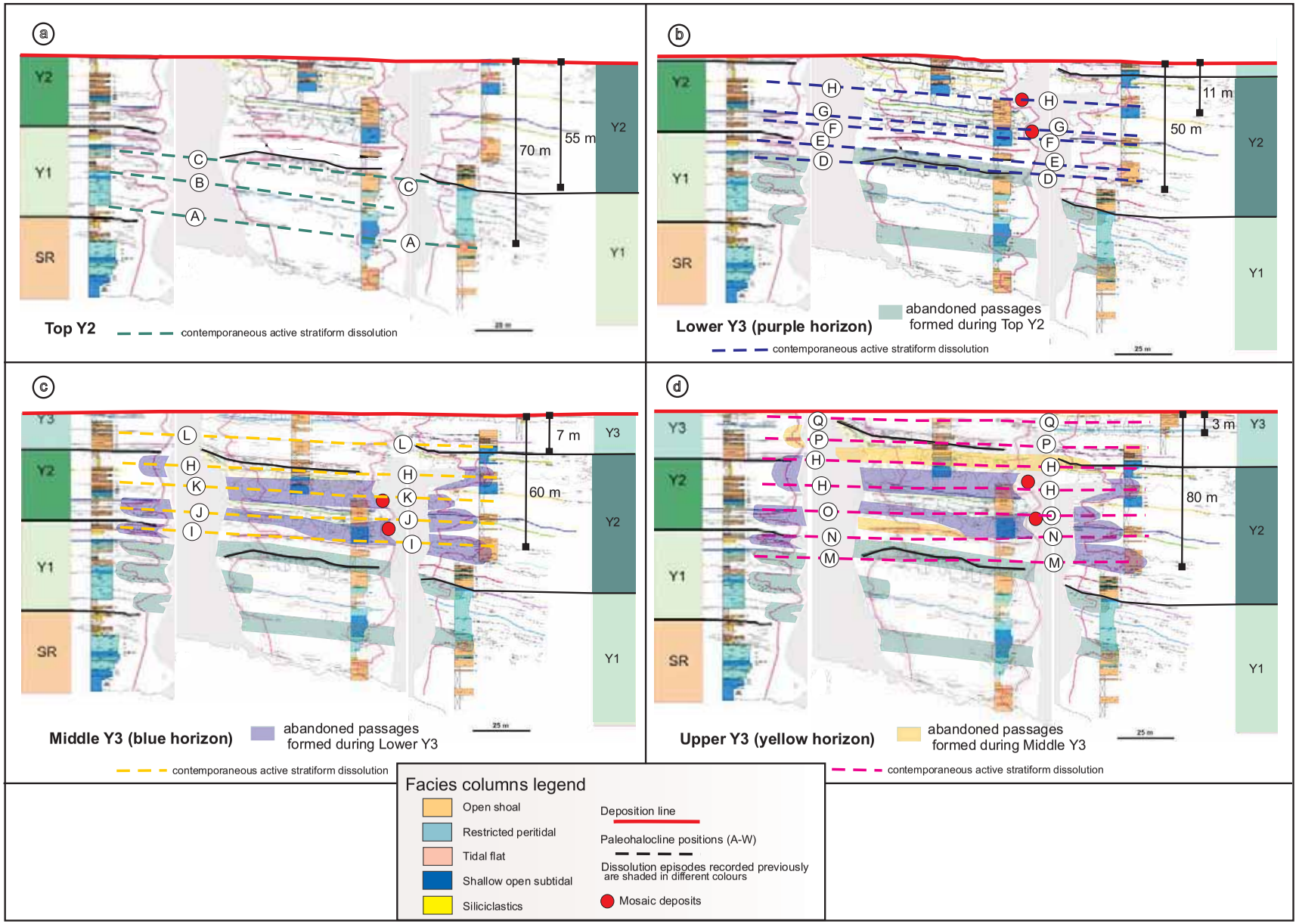

Fig. 4.9. Reconstruction of depositional and diagenetic events associated with Faults M and N. Stages a to h represent correlations at key stratigraphic levels used as datums. Maximum and minimum thickness of the paleo-halocline are shown at every stage. The thickness decreases progressively from the Top of Yates 2 as far as Upper Yates 4. The system is already paralyzed at the Top of Yates 4.

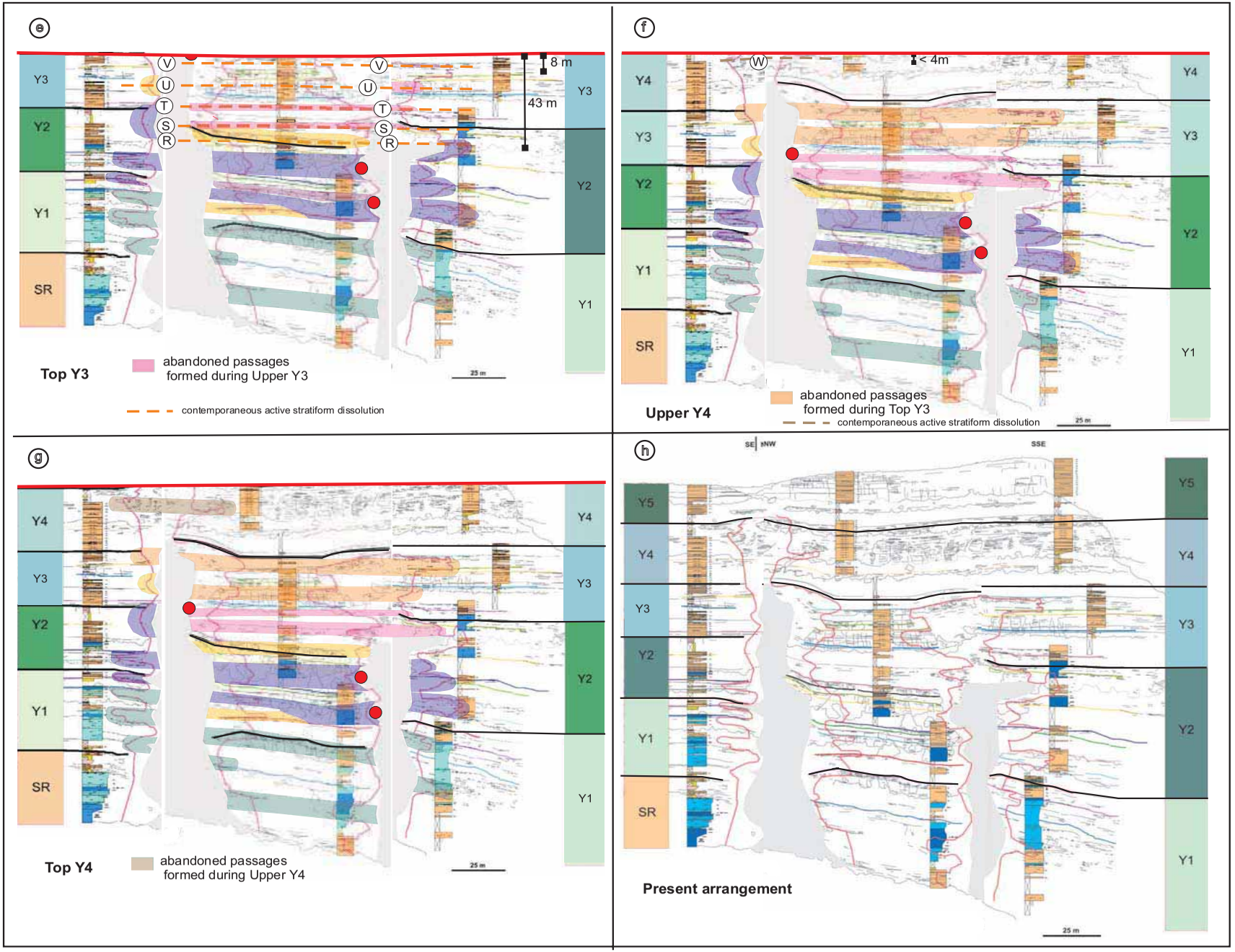
e
Y3
Y2
Y1
SR
V
U
T
S
R
8 m
43 m
Top Y3
abandoned passages
formed during Upper Y3
contemporaneous active stratiform dissolution
f
Y4
Y3
Y2
Y1
SR
W
< 4m
Upper Y4
abandoned passages
formed during Top Y3
contemporaneous active stratiform dissolution
g
Y4
Y3
Y2
Y1
SR
Top Y4
abandoned passages
formed during Upper Y4
h
SE
NW
SSE
Y5
Y4
Y3
Y2
Y1
SR
Present arrangement
25 m

and breccia deposits are difficult to establish because of fault activity. Only at the top of the paleocave areas (Fig.4.3, Fig.4.9: levels T, U and V), on the cessation of faulting, do lateral infills display a continuity from the altered host rock, crossing mosaic deposits, to the interior of the paleocave area. Cross-cutting relationships and the restoration of the complete Y3 sequence (Fig. 4.9) suggest that stratabound karst extensions modified earlier cave sediments and fracture karst fills. At the Top of Yates 3, Fault N was fossilized when Fault M activity had practically ceased.

Thus, karst is interpreted to be eogenetic and developed when sediments were not totally compacted and unconsolidated carbonates proved suitable for promoting paleo-mixing zones.

5.2. Pre-stratabound karst related processes

Prior to the stratabound dissolution, the fracture-controlled dissolution pattern developed during faulting and sedimentation of the Yates units, provided an effective architecture for fluid flow and subsequent corrosion of fault and fracture boundaries. Many processes in the field were related to this stage of active fracture karst and are described below.

(I) Fracture-controlled dissolution. Corrosion in syndepositional extensional fractures caused solution enlarged fractures restricted in metre scale zones (Fig.4.2: c and g). The paleoflow must have been highly channelized along fractures as corrosion is localized along fracture walls, bedding planes and adjacent matrix. The gravitational karst component is minor and becomes confined to few metres, normally along fault segment boundaries (see Zone 2, Fig. 4.10).

(II) Cave breakdown. Corrosion is localized along fracture and bedding surfaces and comprises areas of tens of metre scale. Paleoflow must have been channelized along numerous fractures and dilated bedding surfaces. Gravitational karst component is more significant in the hangingwall fractured areas and generates mosaic breccias in the paleocave zones owing to roof breakdowns (Fig. 4.2: l). Dilated beddings and fracture-mosaic breccia deposits are the most distinctive features recognized in this zone (see Zones 3 and 4, Fig. 4.10).

(III) Vertical open passage-cave floor. Corrosion is locally extensive along passage walls as paleoflow must have diffused along open passages. Corrosion also extends few metres through the host-rock carbonate matrix. The gravitational karst component is significant with an extension of tens of metres. Chaotic breccia deposits are common products of this stage (see Fig 4.2: n; and Zone 5, Fig. 4.10).

(IV) Siliciclastic inputs are interpreted to be continuous during karst activity. Cave fills are mainly composed of dolomitized sandstones and fine marine carbonate sediments. Fault M records siliciclastic accumulations at the bottom of the cave whereas in Fault N they are accumulated in the upper part of the cave. Sand dikes are found in the fractures of the top cave entrances in both faults.

5.3.- Stratabound karst related processes

Stratabound karst formed horizontal passages along sedimentary horizons in zones where paleo-halocline positions were deduced to have existed mainly during Yates 3 times (Fig.4.9). Strata sagging processes and the presence of mosaic breccia deposits are related to halocline corrosion. Corrosion produces new porosity and bending of the overlying sandstones as a result of plastic deformation of low-competence materials. Formation of new porosity allows rotation of the clasts giving rise to mosaic breccia deposits. Karst filling sediments were non-compacted materials, in accordance with the Carbonate Island Model of eogenetic karst. Mosaic breccias are only preserved in the zones that are minor disrupted by faulting and severe gravitational collapses.

Spatial distribution of mosaic deposits in the two faults is confined to the hangingwalls underlying low dip fracture populations. By contrast, these mosaic breccia deposits are always linked to the stratabound halocline-driven dissolution mechanism (Fig. 4.9). The spatial arrangement of these breccia deposits might have been originated as a combination of halocline dissolution and channelized flow from the upper fracture zones which reinforced the dissolution process generating open space for the rotation of the clasts and the deformation of the sandstones. Episodes of re-karsting are observed at field scale with reworked clasts and corroded boundaries (Fig 4.2: c).

5.4.- Post-stratabound karst related processes

The karstification of Rattlesnake Canyon ceased at the end of Yates 3 HFS. Nevertheless, during Upper Yates 4, karstification was reactivated to a lesser degree giving rise to level W (Fig. 4.9). On a smaller scale, the system displayed evidence of reactivation during Lower Yates 5. This reactivation consists of a zone with sub-metre scale lenses (Fig 4.2: i) around the top of the paleokarst system. The reactivation zone displays an inverted T shape distribution and indicates that part of the fluid flow contribution originated from the top of the platform through the top cave entrances (open fractures) of the system. Paleoflow must have been highly channelized in this zone and dissolution is observed as a matrix selective process. This process is thought to have developed above the aquiclude. No gravitational karst component is associated with this flow driven dissolution process. Yellow patchy vugs are interpreted as incipient stages of dissolution and could exemplify how initial dissolution could have started (see Zone 1, Fig. 4.10).

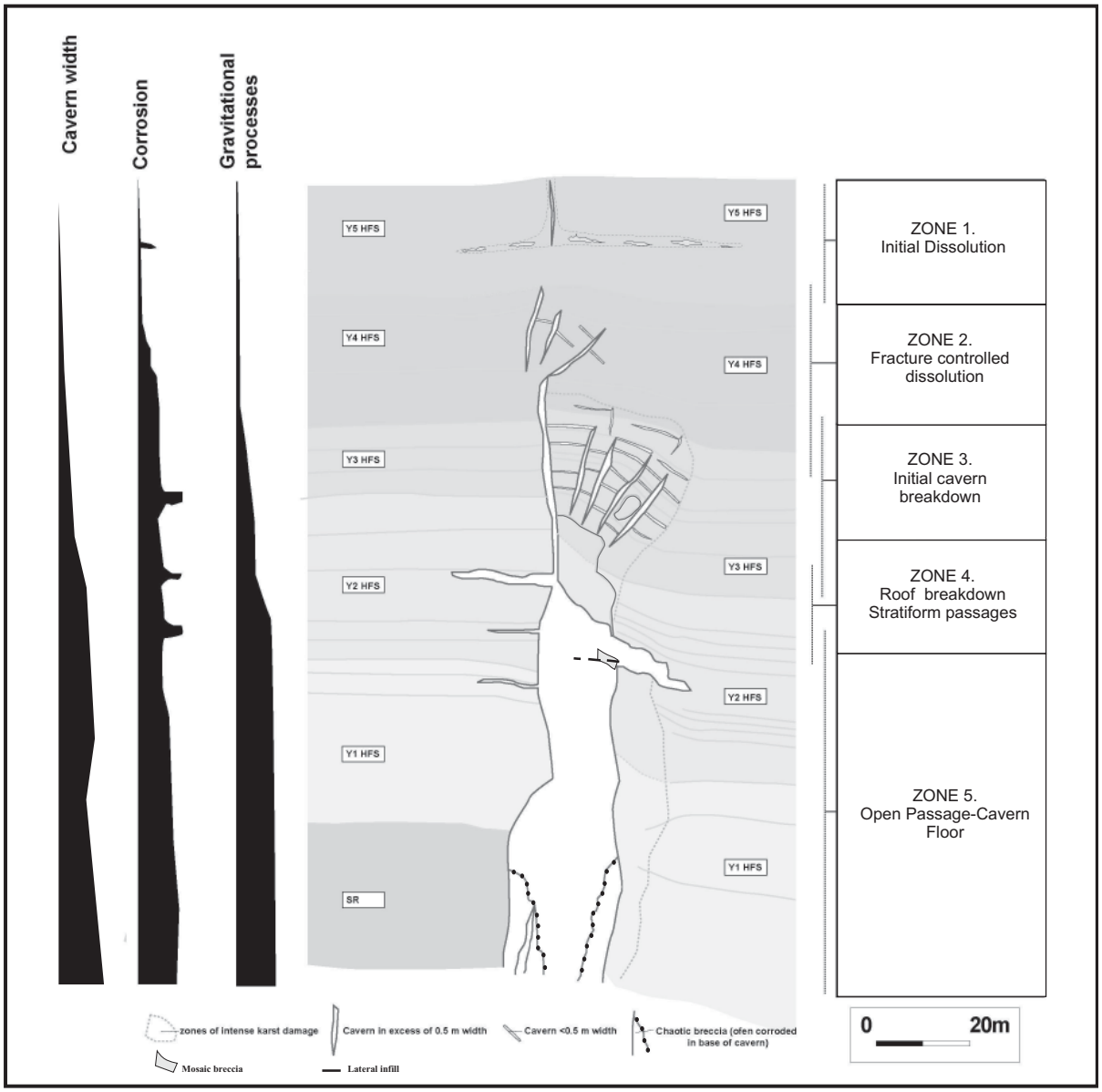

Fig. 4.10. Evolution diagram with interpreted sequence of karst processes. Intensity and dimensions of cavern width, corrosion and gravitational processes are represented by the amplitude of the black bars.

6.- Discussion

Early sub-vertical fractures and syndepositionally formed low dip fractures created a suitable network for rapid channelized flow through the young and unconsolidated platform carbonates. Corrosion operates efficiently in a mixing zone of a Carbonate Island setting and advances through the fracture network. Under these conditions, dissolution fronts spreads along the fault and fracture boundaries. Enhanced dissolution and faulting were mainly responsible for collapses and for the development of larger sub-vertical caves. Siliciclastic inputs inside the caves prevented the system from major collapses. Although faulting destroyed much of the syndepositional fractures, some of these are well preserved at the top and in the middle zone of the two faults.

Since the onset of Yates 3 HFS sedimentation, fracture-controlled dissolution occurred simultaneously with phreatic dissolution. Fracture-controlled dissolution took place in the early stages as a channelized flow for meteoric water, whereas phreatic dissolution requires a stable mixing lens in a hydrogeological Carbonate Island setting. Phreatic dissolution is responsible for the lateral corrosion extensions. The lateral corrosions were fixed by the paleo-halocline position, which migrated vertically upwards through time (see Fig. 4.9). Halocline dissolution was superimposed onto the early fracture-controlled dissolution, which was strongly active in fracture zones. Lateral passages were created from a diffuse flux. The diffuse flux became a channelized rapid flux in zones where fractures interacted with it. Thus, host-rock dissolution was promoted near cave walls and mosaic deposits that originated accompanied with the overlying strata deformation.

Superimposition of both dissolution mechanisms was preserved in the upper areas of the two faults when faulting had practically ceased (~ Top Y3 HFS). Cross-cutting relationships, redissolved clasts within the paleocave area, and solution modified fracture boundaries are evidences of the two superimposed mechanisms.

The system is complex because it developed while faults grew and sediment entered the system intermittently. Local tectonics contributed to the reuse of different lateral passages at varying times. The thickness of the horizontal passages is directly proportional to the grade of reuse. Collapse occurred in the most effective dissolution zones, i.e. in channelized syndepositional fracture zones. In the cave sediment record, these episodes are recognized from the sediments at the bottom of the cave (e.g. floor of Fault M, Fig. 4.3) to the upper fractured zones (e.g. pink breccia Fault N, Fig. 4.2: m). Gravitational processes decreased from bottom to top (see Fig. 4.10). This is evidenced by the degree of breccia clast rotation from bottom to top in the paleocave areas.

Dissolution can occur at the top of the lens or at the bottom of the lens. Water table caves or flank margin caves are typically associated with sea-level positions and are thought to have developed at the top of the freshwater lens. Halocline caves are less well known and constitute examples of dissolution under the water table. Such phreatic dissolution takes place below sea-level positions in modern caves in the Bahamas. If the caves in Rattlesnake Canyon formed as water table caves, a fall of 60 m in sea-level would occur during Yates 3 (see Fig 4.9). Ye and Kerans (1996) reported that 4th order changes during Yates times approximated a sea-level fall of over 50 m. Nevertheless, no evidence of subaerial exposure was detected along the platform. Moreover, the presence of tidal flat facies in footwall M and in the the graben during the deposition Lower Yates 3 HFS suggests close proximity to the paleo-shoreline during that time. These are the main reasons that rule out water table caves in Rattlesnake Canyon. However, the upward thinning trend of the freshwater lens sets a pattern approaching absolute sea-level positions as the karst system develops and the lens becomes shallower. If alternatively, the caves formed at the bottom of the lens it would not be necessary to assume a drastic change in the hydrological system. Nor would it be necessary to introduce significant inputs of freshwater recharge into the system to obtain a

significant thickness of the lens. The tilting of the graben enhances the occurrence of a local hydrogeological anomaly in this area. Unconsolidated carbonates tend to retain more water and produce thicker lenses (Budd and Vacher, 1991) which is the case of the young karst filling materials during the Upper Permian. As the karst system develops, the carbonates become more transmissive for water to percolate deeper through the platform. The discharge point must have been located to the west at least 500 m along the WSW - ENE direction (Fig. 4.11). The fault length (500 m) was deduced by the linear Dmax/L relationship in normal faults (Dawers et al, 1993). At the discharge point, water table dissolution cannot be ruled out as the tip of the lens coincides with sea-level positions. This is in line with field observations that reveal a more intense and chaotic pattern of dissolution towards the W. Thus, it can be considered that dissolution occured at the bottom of the lens in the phreatic realm in the study area. These arguments lend support to the hypothesis that halocline caves formed perpendicular to the dip-slope direction (parallel to the platform margin) because of a local hydrogeological anomaly in the graben system in Rattlesnake Canyon.

The halocline dissolution mechanism was much more effective during Yates 3. The mechanism was interrupted at the top of Yates 3 but was slightly reactivated in Upper Yates 4. The interruption of the system is thought to be due to a decrease in the meteoric water discharge from the top of the platform. This climate change is evidenced by the transition to the top shelf crest facies. Stratigraphic sections reveal evaporite facies and abundant tepees. According to Whitaker and Smart (1997), inland mixing zones tend to be much thinner than coastal mixing zones. The significant reduction of the lens thickness in Rattlesnake Canyon (from nearly 70 km to less than 1 m) could also be attributed to a notable increase in the rate of progradation of the platform, producing a landward migration of the paleokarst system. Osleger (1998) highlights the extreme progradation of Y3 HST and estimates that the Y3 HFS pisolitic shelf crest extends for 0.7-1 km, overlying the seaward edge of the Y2 HFS shelf crest. In Rattlesnake Canyon, the Y2 HFS seaward edge is recorded in the vicinity of the stratigraphic graben section (see Fig 3.4, Chapter 3), Thus, we record the maximum migration of the system inland. Based on these considerations, it is reasonable to speculate that the reduction in lens thickness could also have been favoured by a maximum migration of the paleokarst system inland during Yates 3 HFS.

Koša and Hunt have recently studied the Upper Permian Capitan platform syndepositional faults and related karst systems. Some of our findings in Rattlesnake Canyon are in line with their work in Slaughter Canyon. Our results obtained at outcrop scale are consistent with earlier regional interpretations and contribute to the understanding of the dissolution processes and episodes of karst evolution in the area.

Karst-modified faults and fractures in Slaughter and Rattlesnake Canyons are compared in this section. Faults in Rattlesnake Canyon present growth timing that is similar to that in Slaughter Canyon since they developed before Yates 4 HFS. Karst modified faults and fractures underwent multicyclic dissolution episodes in the two canyons. Corroded boundaries of reworked clasts within fractures and breccias in Slaughter Canyon were

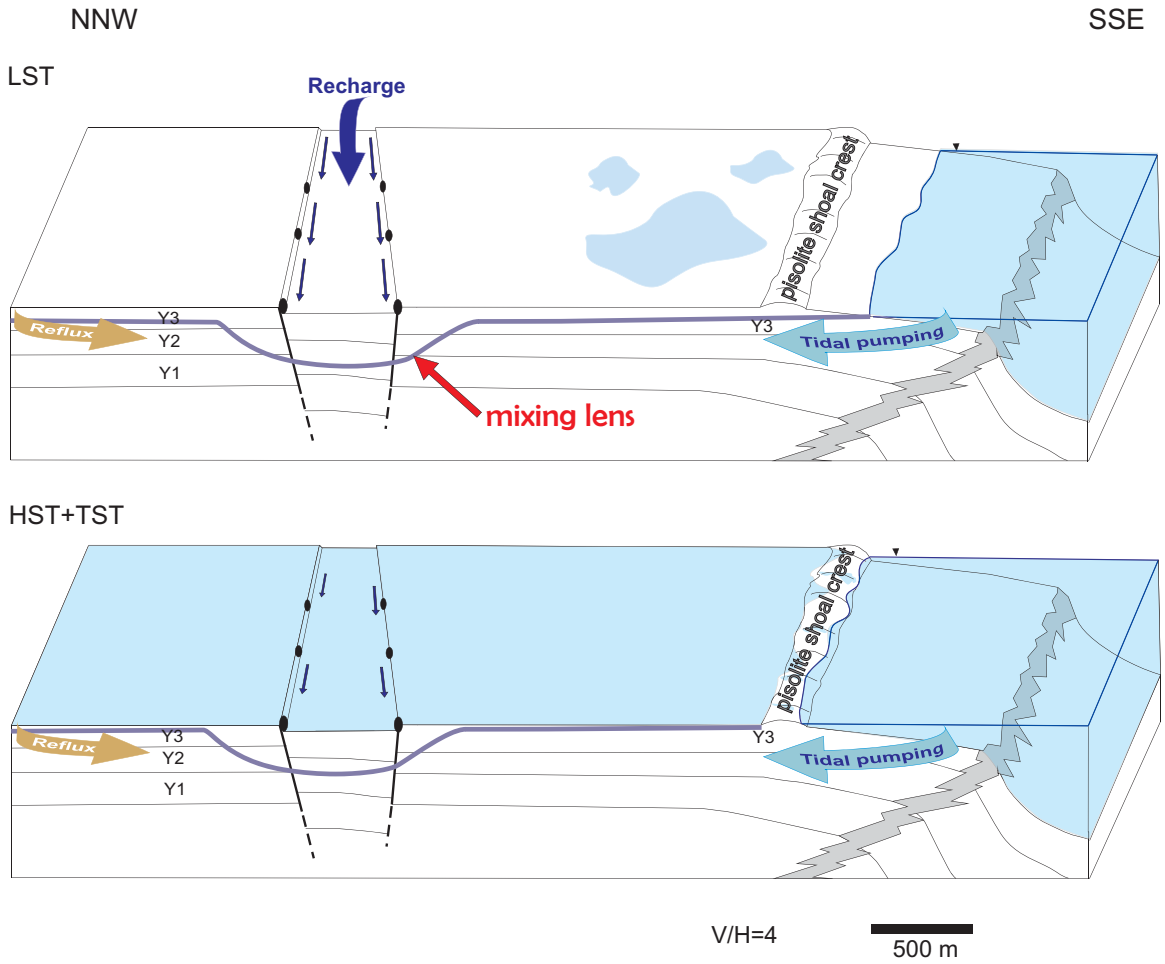

Fig. 4.11. Capitan strike parallel platform section during Yates 3 HFS. The local hydrogeological anomaly produced by the inclination of the graben produces thick lenses during Lower to Middle Yates 3. The recharge area is located towards the east so the flow is directioned in E-W direction perpendicular to the section showed. LST: Low system tract. TST: Transgressive system tract. HST: High system tract. The faulted area is exagerated in dimensions for the representation.

previously documented in the literature (Koša, 2003; Koša and Hunt, 2006). Structural fault morphologies, subsequently modified by dissolution, evolved to elongate vertical fracture paleocaves. Fractures are filled by multicoloured siliciclastic and carbonate sediments in both canyons. Some identical sedimentary structures were preserved as siliciclastic-filled chimneys, termed sand dikes in the present study. These structures are abundant in the upper part of the paleocave system. Their resistance to dissolution (Koša and Hunt, 2006) and the absence of collapse episodes above them may have accounted for their preservation. Vertical stratigraphy in paleocaves indicates that the relationship between carbonate sediment and siliciclastic sediment lithologies provides evidence of different episodes of deposition related to sea-level rises and lowstands (Koša and Hunt, 2006).

The present work offers new insights into paleokarst development in the Guadalupe Mountains and contributes to an improved understanding of dissolution mechanisms. Moreover, the relationship between stratigraphy and local tectonics is crucial for the implementation

of a new methodology in order to elucidate the relative timing of these mechanisms. The recognition of halocline caves, which have been rarely documented in ancient systems, provides useful insights into relative sea-level stands and fluid mixing mechanisms for cave formation that have so far been regarded as indicators of past sea-level positions. In an attempt to resolve the evolution patterns of ancient paleokarsts, our study highlights the importance of analyzing all the relevant factors, i.e. progradation rates, paleo-hydrogeological parameters, climate changes and local tectonics operating in a platform margin setting.

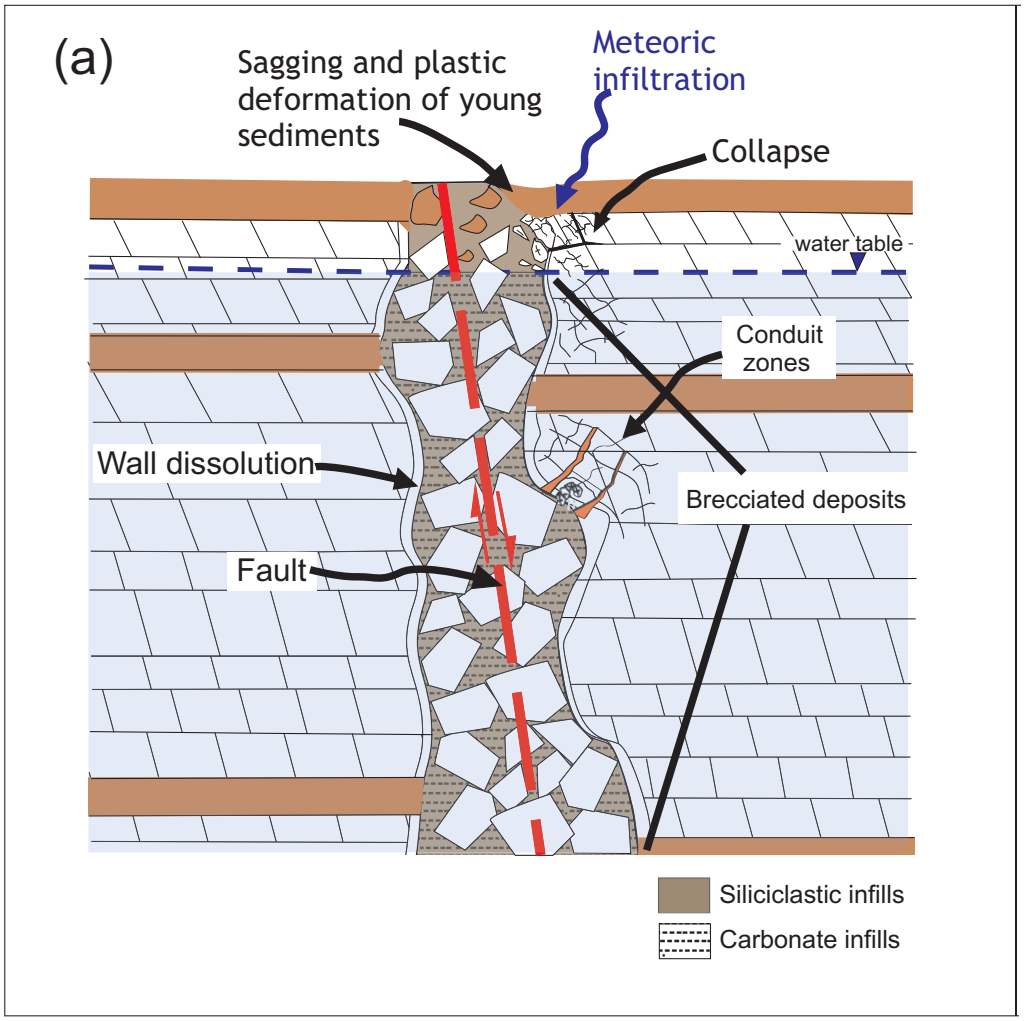

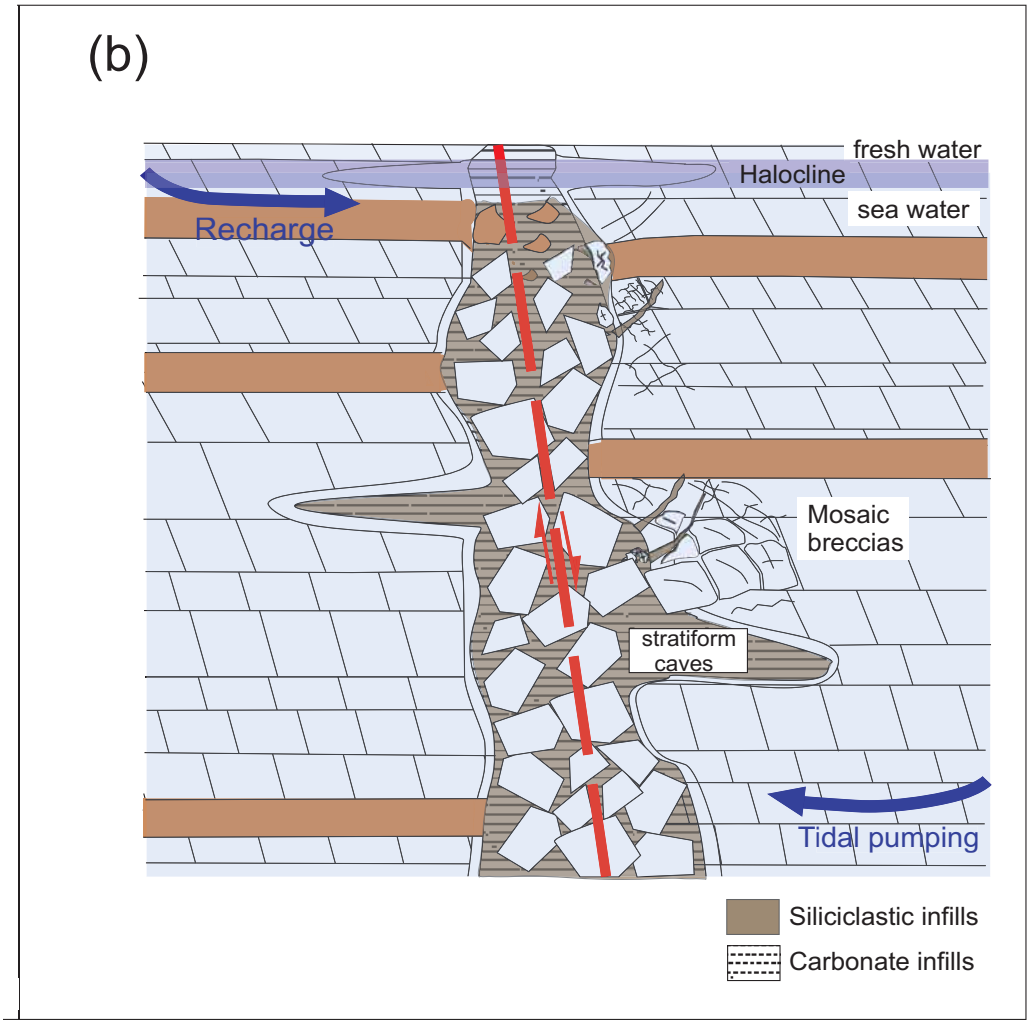

Fig. 4.12. Sketches showing the evolution of the halocline caves. a) Pre-stratabound processes during fault cave development. b) Syn-stratabound processes during halocline cave development.

7.- Conclusions

Two normal faults that define a graben parallel to the Upper Permian Capitan mixed carbonatic-siliciclastic platform rim in the Guadalupe Mountains are modified by karst. These faults, cropping out in Rattlesnake Canyon provide an excellent scenario to study a paleokarst developed along vertical faults and related fractures and along the sub-horizontal bedding in the graben system.

Two dominant sub-vertical faults limit the graben system (M and N faults). These faults are associated with two major fracture sets: a NE-SW-trending sub-vertical fracture set that is parallel to the dominant M and N faults and a lower dip fracture set (NW-SE for Fault M and NNE-SSW for Fault N) that is related to syndepositional processes as documented by Hunt et al. (2002). The former set of faults and fractures controls the direction and inclination of sub-vertical paleocaves, whereas the latter set of fractures contributes to the increase in fluid circulation through the paleocave system.

Fault-related karst is filled by platform-derived sediments, mostly siliciclastic and a large number of collapse clasts and blocks derived from the paleocave walls. Karst lithofacies are dominated by replacive dolomite, vug filling dolomite and late-stage calcite cements. Three different breccia deposits have been associated with the paleocave collapses: chaotic, mosaic and crackle breccias. Collapse chaotic breccia deposits are the most abundant. Mosaic breccias are mainly associated with sub-horizontal infills resulting in sag structures, and with products of small collapses. Mosaic breccias are thought to have taken place in phreatic conditions as sub-horizontal associated infills and are correlated with penetrative stratiform extensions towards the carbonate host rock. Crackle breccias are recognized at different locations along the boundaries of the two faults and are interpreted as fault-related fabrics.

We predicted an evolution model for the platform margin fracture-controlled karst that comprised fracture analysis, petrology and fault kinematics in a stratigraphic framework, and evaluated sea-level and hydrogeological changes in the study area. Two dissolution mechanisms are responsible for karst development in Rattlesnake Canyon: fracture controlled dissolution and stratabound dissolution. Fracture controlled karst formed sub-vertical paleocaves that exploited fracture networks and produced sub-vertical fracture cave systems in which the fluid flow was channelized. Stratabound karst developed subsequently and exploited porosity and permeability generated by the early fracture controlled karst. Stratabound dissolution was active in a paleo-mixing zone in the graben system mainly with a diffuse fluid flow. Phreatic stratabound dissolution produced stratiform passages that generated minor collapses (mosaic breccia deposits). This sub-horizontal diffuse fluid flow was enhanced by its connectivity to the sub-vertical fracture-related channelized fluid flow.

The lateral corrosions observed in the stratabound karstic levels are thought to be indicators of the paleo-halocline position mainly during the deposition of Yates 3 HFS. During this interval, the karstic system underwent phreatic dissolution as a result of changes in the

position of the halocline interface in response to sea-level changes, paleoclimatic conditions and S-directed progradation of the Capitan platform.

The tilt of the graben gave rise to a local hydrogeological anomaly. Hydraulic heads induced channelized flow through the graben system. Table water must have been thicker because of intense circulation of meteoric water during lower Y3 HFS. During Upper Yates 3 HFS, arid episodes are recorded in the stratigraphic record. This led to a decrease in meteoric fluid flow and in halocline depth coinciding with the tepee shelf facies deposition. Thicker paleo-mixing lenses are thought to have formed during lower Y3 HFS karst stages given that karst is eogenetic and given that early unconsolidated materials promoted slow paleoflow. Displacive porphyroblastic moulds of anhydrite crystals are found in the upper parts of the karst filling sequence suggesting precipitation of evaporites in a coastal sabkha environment (Chapter 6). A change to arid paleoclimatic conditions during the deposition of the top Y3 HFS tepee shelf crest facies could have favored a thinner water table. Furthermore, it is possible that the significant progradation rates of Yates 3 HFS brought about a faster landward migration of the system. All these factors led to the termination of the karst system at the top of Y4 HFS.

Chapter 5

3D building of the Rattlesnake Canyon paleokarst system: Integration of outcrop datasets and GPR profiling

Abstract:

The 3D building of the Rattlesnake Canyon paleokarst system constitutes an example of integrating outcrop datasets and GPR profiling into an object-based and diagenetically conditioned geological model. Diagenetic constraints are difficult to incorporate into a 3D model, especially when they are not dependent on structural entities. Since the Rattlesnake Canyon eogenetic paleokarst system appears to be mainly fracture-controlled, it offers great potential for 3D reproducibility under geometric object- based modelling.

The model was mainly developed from strike and dip data of fracture sets and paleokarst infills collected in the field, and is forced to integrate uncertainties into the spatial constraints in zones where fluid paths are non-structurally but matrix controlled.

This chapter documents the multiple step workflow designed to minimize uncertainties in the construction of the paleokarst irregular boundaries. In this regard, the dip-domain methodology has proved successful. The accomplishment of the 3D model implies working in different software environments (OpensceneGraph Digitizer (OSG), Microstation and GoCad).

Lidar technology and OSG software allowed us to reproduce accurately the limits of the paleokarst incorporating the third dimension. A virtual outcrop environment proved to be a powerful operative tool through the preliminary manual digitization of geological entities and extraction of data from inaccessible areas towards the ultimate integration of the surfaces in a photorealistic model.

GPR subsurface profiling in the northern region of the canyon was tested as an implement for analyzing the penetration of the paleokarst along the Upper Permian Capitan platform margin. GPR profiles were integrated into commercial GoCad software to quantify the penetration of the karst towards the north. The results show that the karst extended at least 70 m towards that direction. The evolution model of the paleokarst system and field observations suggest that the paleokarst system is dimensionally very pronounced along the southern margin of the platform.

Chapter 5

3D building of the Rattlesnake Canyon paleokarst system: Integration of outcrop datasets and GPR profiling

1.-Introduction

Paleocave reservoirs tend to record pronounced lateral and vertical heterogeneity which adds complexity to the prediction of the spatial variability of reservoir properties. Advances in data capture and computer technology have enabled the integration of 3D high-resolution surface and subsurface digital geological data into geological models. 3D geological modelling has been traditionally based on subsurface seismic data although statistical cell-based facies modelling has recently allowed the incorporation of alternative input geological data usually derived from conceptual depositional models (Weissmann et al., 1999; Strebelle et al., 2002; Falivene et al., 2007, Cabello et al., 2010, 2011). Lidar technology allows us to work with outcrop datasets (Pringle at al., 2006). Recent advances in the combination of seismic and outcrop datasets have been the subject of several studies since the early 2000s (Schwab et al., 2004; Jones et al, 2009). Research has provided multiple tools for the analysis of the spatial variability of multiple geological reservoirs and has contributed to the realization of a variety of conceptual tectonostratigraphic models (Bailey et al., 2002; Wilson et al., 2009).

The importance of integrating the third dimension when modelling complex systems is still a handicap when the geological heterogeneity is diagenetically controlled. In paleokarst systems, diagenesis plays a major role in the dissolution processes and thus, the realization of a 3D paleokarst model is indeed forced to integrate uncertainties. When the system undergoes several episodes of karsting, reactivated at different geological times, the early controls of the system may be strongly modified, especially when the paleokarst develops in carbonate rocks. On the other hand, diagenesis implies fluid flows controlled either by structural components such as fractures and faults or by the petrophysical properties of the carbonate matrix. The complexity of delineating fluid paths when not controlled by geological structures, and the variability of the petrophysical properties of the host rock through different episodes of diagenesis are the major factors limiting accurate prediction in 3D conceptual models involving diagenesis.

Rattlesnake Canyon crops out in a magnificent well exposed and preserved cliff scenario. Given that access is limited in some areas because of the very steep rocky canyon conditions,

Lidar technology and the creation of a virtual outcrop have been instrumental in developing a map that incorporates detailed observations sometimes overlooked or inaccessible in the field. Although the cut of the canyon offers an excellent view of the paleokarst system, the need to quantify the penetration of the paleokarst demands alternative ways to incorporate the third dimension. GPR subsurface profiling has been tested as an implement for analyzing the penetration of the paleokarst along the strike direction towards the north.

This chapter reproduces the methodology used for the integration of the Rattlesnake Canyon paleokarst into a 3D environment. Strike and dip data collected in the field are a fundamental part for the creation of 3D structural models, but integrating diagenetic controls requires the conversion of traditional karst alterations into measurable parameters. The employment of a photorealistic outcrop and GPR proved crucial for quantifying the paleokarst extension and for the understanding of the conceptual evolution model discussed in Chapter 4.

The aims of integrating the Rattlesnake Canyon paleokarst system into a 3D environment are threefold: i) delineate the limits and the complex geometry of the system, ii) create an in-house methodology for tracing diagenetic limits, and iii) quantify the penetration of the paleokarst system through the carbonate platform. This object-based model has been used as a baseline for incorporating paleokarst structures in stratigraphic models constructed by IRAP-RMS (Hunt et al., 2009).

2.-The use of virtual outcrops

The study of Rattlesnake Canyon, which can be used as an analogue for subsurface hydrocarbon reservoirs, enables us to better understand the mechanisms of the formation and evolution of coastal karst systems. The study uses laser scanning to elaborate a 3D map. Lidar scanning allows an extremely accurate representation of the geology with high spatial resolution and geometrical accuracy. In recent years, there have been numerous advances in the gathering of spatial georeferenced outcrop data (Bellian et al., 2005; McCaffrey et al., 2005). In a detailed study, these kinds of tools are invaluable in the representation of geological structures and diagenetic alterations with a centimetric spatial resolution.

The creation of virtual outcrops is preceded by the collection of point clouds photometrically processed and associated with terrain models. The final result consists of a high resolution representation of the outcrop which can be observed with different angles of view and zooms.

The principle of the LIDAR method is a laser pulse that leaves a gun and travels to a remote target to rebound off it. When this signal returns to the detector after the rebound, the two-way-travel time can be processed to calculate an accurate Z distance value. X and Y positions are maintained as the X and Y gun positions. High resolution radar (centimetre scale) results in accuracies of 1-4 cm/km.

Capturing outcrop photographs is a process of projecting outcrops onto image planes through a camera lens. This process can be done by correcting camera geometry and lens

distortion (Xu et al, 2000). Thus, this procedure links a digital image to a terrain model, obtaining a 3D photorealistic outcrop.

Virtual outcrops allow us inter alia to study geometries, to correlate surfaces, to identify facies transitions and to determine fracture distributions. In Rattlesnake Canyon, Lidar has made it possible to trace the precise limits of the karst, map tepee structures and fracture populations as well as the karst infills and the collapse breccia deposits. OSG digitizer software was used to visualize the virtual outcrop and manually digitize the spatial data collected in the field. The data was digitized by points which were later exported to another software environment in different stages as described in the Methodology section (pp).

The present work implements the Lidar method in the study of a paleocave system and is not concerned with the methodology for the construction of a photorealistic model. The development of the virtual outcrop of Rattlesnake Canyon was conducted by the team of Carlos Aitken of the University of Dallas, Texas, USA, and was carried out during 2005-2006.

3.- GPR technique

GPR (Ground Penetrating Radar) subsurface profiling can provide information of the different subsurface lithologies and discontinuities. GPR uses electromagnetic energy in short pulses of high energy, usually in the 10 to 1000-MHz range. The electromagnetic wavefront is propagated downward and returns to the surface at different times depending on the EM propagation velocity through the sediment and on the depth of the subsurface reflectors. The strength of the reflected signal is approximately proportional to the difference in dielectric constants at the sediment interface (Davis and Annan, 1989). These effects enable the subsurface stratigraphy and structure to be inferred from the returning radar signals.

GPR provides a profile of horizontal survey distance (m) versus vertical two-way travel time in nanoseconds (1 ns = 10^{-9} s). By measuring the propagation velocity of sediment, depth of reflections can be determined. Further GPR theory and methodology are adequately explained in technical publications (Davis and Annan, 1989; Jol, 2009).

The potential of GPR in paleocave carbonate systems has been successfully tested in the Ordovician Ellenburger of west Texas (McMechan et al, 1998, 2002; Loucks, 2004). GPR, as in seismic studies, provides tools to analyze the internal architecture of a paleocave system and constrain spatial features especially when outcrop data are not accessible.

In Rattlesnake Canyon, GPR profiling was used to determine the penetration of the paleokarst towards the north given that the profiling was made in the northern part of the canyon. The steepness of the canyon limited radar profiling and the GPR survey was therefore focused on the top of the platform alternating with some horizontal passes using the trace

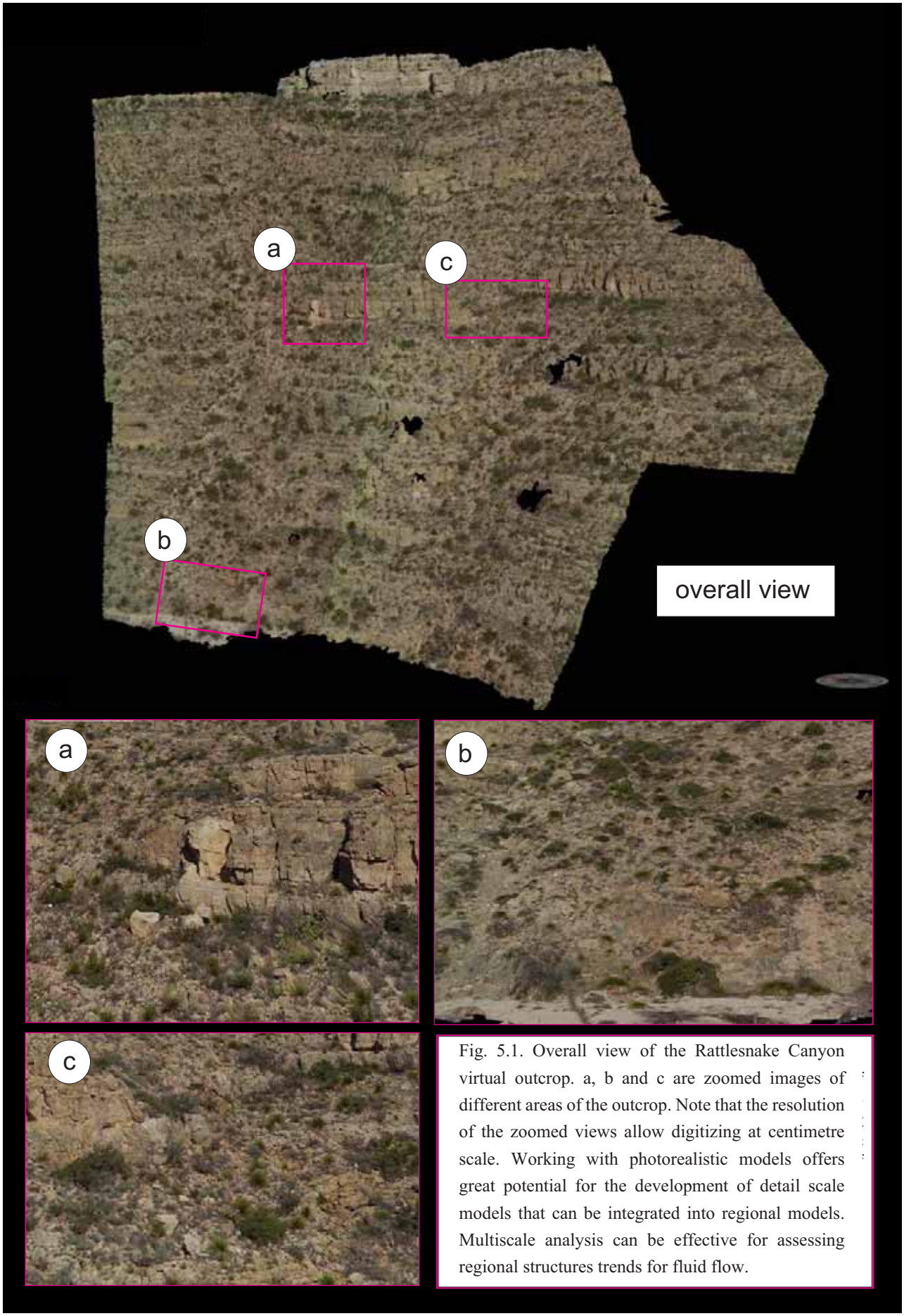

Fig. 5.1. Overall view of the Rattlesnake Canyon virtual outcrop. a, b and c are zoomed images of different areas of the outcrop. Note that the resolution of the zoomed views allow digitizing at centimetre scale. Working with photorealistic models offers great potential for the development of detail scale models that can be integrated into regional models. Multiscale analysis can be effective for assessing regional structures trends for fluid flow.

of the prominent strata that host the paleokarst system. Thus, information was obtained by increasing the depth of the reflections using different vertical radar traces.

4.- Methodology

4.1.- 3D model building

High resolution photographic panels were the main tools used in the field to achieve the detail scale desired for this study. A first mapping was carried out by data directly gathered in the field. Strike and dips of fractures and beds were collected; lithologic and diagenetic features were also integrated into the map as well as distinctive paleocave breccia deposits. Two paleokarst related zones were detected and mapped in the surroundings of faults M and N (Chapter 4). These zones surround the proximities of the fracture zones, within and near the faults. The areas that accumulate breccia deposits are termed paleocave zones. The outermost zones in the vicinities of both faults are zones with many more dissolutional processes than collapse related processes. These areas are termed karst damage zones and comprise the palecave zones. Both areas (paleocave and karst damage zones) delimit the occurrence area for the paleocave system studied.

Strike and dip data from both faults were collected for a subsequent 3D introduction into a digital object-based framework. A total of 287 samples were collected from inside the damage area and close to its boundaries. Paleokarst sampling was designed to implement the lithofacies observations in the field using conventional petrography, SEM and cathodoluminescence (CL).

A photorealistic outcrop was created by the use of LIDAR (also known as laser radar) and linked LIDAR techniques to outcrop images. This photorealistic model operates through the OSG (OpenSceneGraph) digitizer software which was kindly supplied by StatoilHydro, Bergen Research Centre, Norway. All the features mapped in the field were digitized in the photorealistic model using OSG software. The generated X, Y, Z ASCII files by OSG software were imported to Microstation software (Bentley Systems Inc.) in order to construct irregular surfaces such as the ones that limit paleocave and damage areas. Accordingly, distinctions between similar strikes and dip domains need to be attained. This is because a subsequent step in surface construction in Gocad environment (Earth Decision) implies working with constant strike and dip and non multivaluated surface pieces. The main challenge posed in the construction of these types of surfaces is how to cope with abrupt changes in strike and dip data in short ranges from 3 to 20 m. This arises because these surfaces do not represent geological structures such as folds or faults but represent areas where fluid processes have affected the host rock. Fluid trajectories are prone to follow not only fracture or fault conduits but high porosity and/or permeability paths within the host rock. Thus, fluid paths are sometimes matrix controlled and sinuous when mapping paleocave and karst damage zone boundaries. In our study, paleocave and damage karst boundaries limit dissolution affected areas and subsequently collapsed areas.

The dip-domain method (Fernández et al., 2004) has been used to construct over 80 surface pieces for each fault. Map trace analysis provided average dip values in short ranges. Despite the high number of orientation values collected in the field, the construction of the entire surfaces must cope with the difficulty of calculating orientations of surfaces that do not follow any structural trend. Thus, map trace analysis proved to be the most effective method.

The workflow used for the construction of the 3D model is detailed below (Fig. 5.2).

1.- Data input.

A total of 464 strike and dip data were collected in the field and integrated into the model. These data include bedding orientations, fracture orientations and sediment infills orientations inside the karst damage zone and surroundings. Karst brecciated deposits and other sedimentological and diagenetic structures such as tepees were also considered for incorporation into the three-dimensional model.

Breccia deposits, diagenetic structures and paleocave and damage area limits were transferred into the photorealistic model via OSG manually digitalization.

2.- Analysis of structural data.

A prior surface construction step was required to define the domains with constant strike and dip values. Stereonet projections were calculated to obtain a mean orientation value in zones with a high number of data. Map trace analysis with Microstation software also provided average dip orientation values. Thus, the structural analysis could be compared with the two procedures and reinforced by field observations to finally assign an accurate value to each domain.

Bedding planes were conceived as single domains with continuous surfaces and were created directly from field and subsurface GPR data with GoCad software.

3.- Surface construction.

Once an orientation value for each domain was obtained, the surface construction was undertaken in a digital framework.

3.1.- Microstation environment. Planes were represented by equally spaced contour lines of 1.5 m length. These lines are parallel to the strike direction of the dip domains. A moderate 75 cm length from the point measured in the field was adopted both penetrating towards the outcrop and emerging from the outcrop with a total length of 1.5 m. This limited extension is due to the uncertainty about the continuity of the non-structurally controlled surfaces.

Subsurface GPR data acquired in later surveys provided information about the penetrative dimensions of the paleokarst system.

3.2.- GoCad environment. Contours were imported into GoCad to construct surfaces honouring strike and dip. Thus, several groups of small contiguous surfaces with different orientations were generated for the two faults. The last step consisted in joining them and smoothing all the contacts.

The final result shows a complex array of surfaces that limited the paleokarst system and reproduced the heterogeneity of the diagenetic processes that controlled the flow of the paleofluids. The surfaces were introduced into the photorealistic model to allow the observation of the geometry of the system in combination with the image of the outcrop and precise location of the objects mapped (Fig. 5.3).

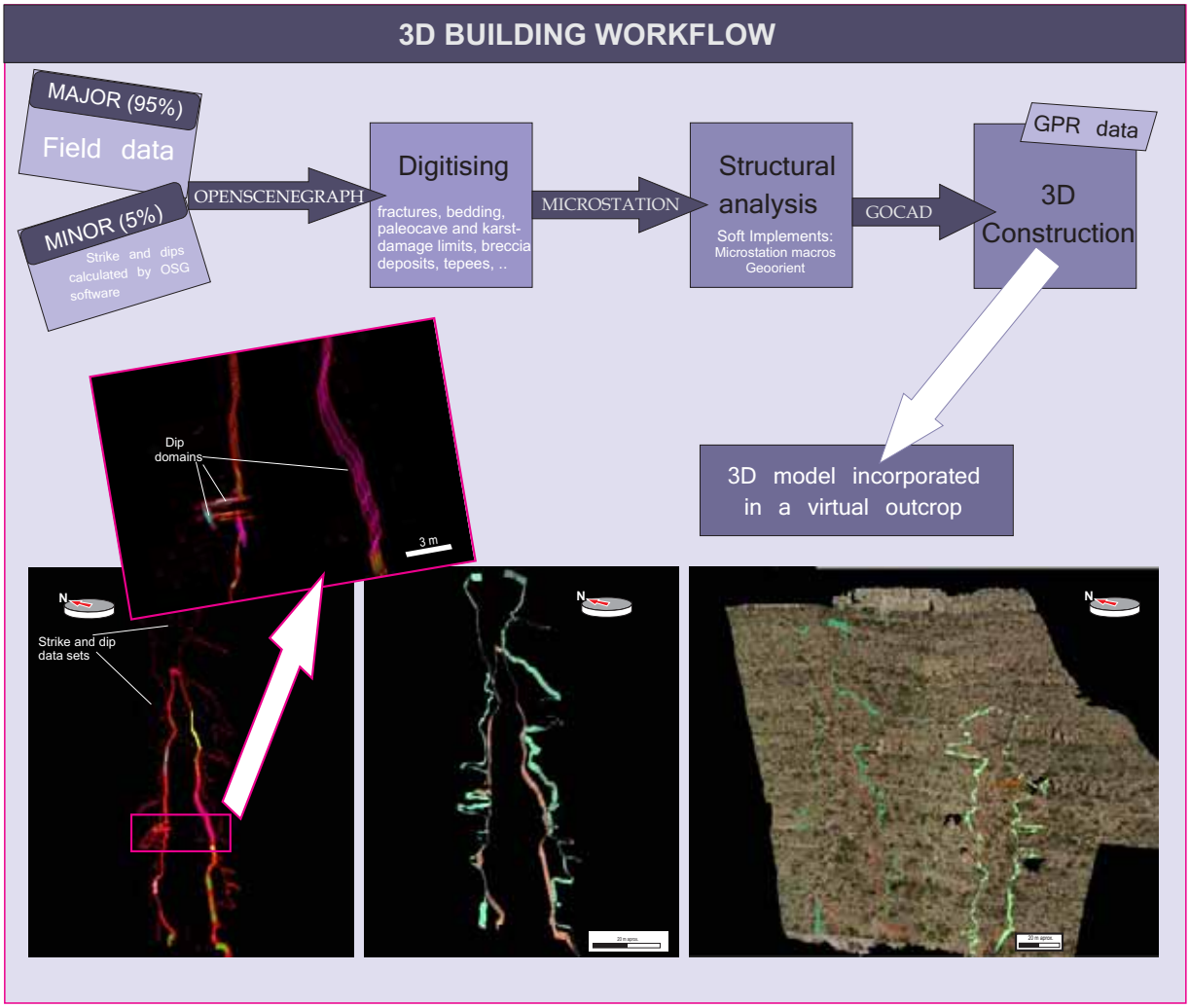

Fig. 5.2. Workflow used for the construction of the 3D paleokarst model. The model is essentially based on field data processed through different softwares. The limits of the paleokarst have been segmented in areas of constant dips in order to construct pieces of surfaces that were subsequently merged to reproduce the sinuous geometry of the paleokarst boundaries.

4.2.- GPR data acquisition

Ground Penetrating Radar (GPR) was acquired with a set of 3 antennas (frequencies of 50, 25 and 12.5 Hz) with a Parallel-Endfire Array geometry (Baker et al., 2007). Shot spacing varied between antennae and the shot location was georeferenced using a Total Station. The GPR data acquired produce single fold that was processed using a standard processing workflow (Neal 2004). Once processed, the GPR profiles were imported into the modelling software. Data acquisition was carried out by Toni Simó, who at that time was attached to the University of Wisconsin, USA.

5.- Results and discussion

The design of an in-house methodology for integrating the Rattlesnake Canyon paleokarst system into a 3D environment constitutes one result of this study. Discrete analysis of the different paleokarst infills and damage areas using structural data such as strike and dips was instrumental in the creation of the 3D model.

Converting diagenetic structures into objects involves defining limits of extension such as in the case of the creation of the paleokarst surface limits. The paleokarst surface limits were constructed and constrained to the structural data. In the areas where no data were available, the OSG software offers the possibility of calculating strike and dips. The OSG derived data were only used to provide reliable data for every dip domain in inaccessible zones.

The construction of the 3D paleokarst model enabled us to reproduce the paleocave morphology although the information of the diagenetic structures was confined to the location of the outcrop (Fig. 5.3). The continuity of such structures was established at 1.5 metres in the model owing to the uncertainty of the fluid paths. When geological structures, such as fractures, intervene, the fluid path may reliably follow the structure. However, when the diagenetic structure is controlled by the matrix conditions, a degree of uncertainty is incorporated into the design of the continuous surface. In Rattlesnake Canyon, these independent fluid paths occurred in the lateral karst extensions following distinct strata. Since the fluid paths in these extensions were strictly controlled by the petrophysical properties of such strata, the limiting surfaces were basically traced following bedding planes. Poroperm properties would be useful in the analysis of the matrix conditions but these properties were strongly modified by the late diagenetic cementation episodes of the paleokarst (Chapter 6, 7). Thus, the analysis of the poroperm properties would need processing to honour the early depositional conditions when the karst began to form. Nevertheless, the strong dependency of the paleokarst structure on the syndepositional faulting confers a valid range of 3D reproducibility to the Rattlesnake Canyon paleokarst.

The integration of GPR lines into the 3D model aids in assessing the penetration of the karst into the carbonate platform. Ten horizontal profiles were introduced into the model (Fig. 5.4). Survey lines were arranged in a grid of orthogonal lines at the top of the platform and

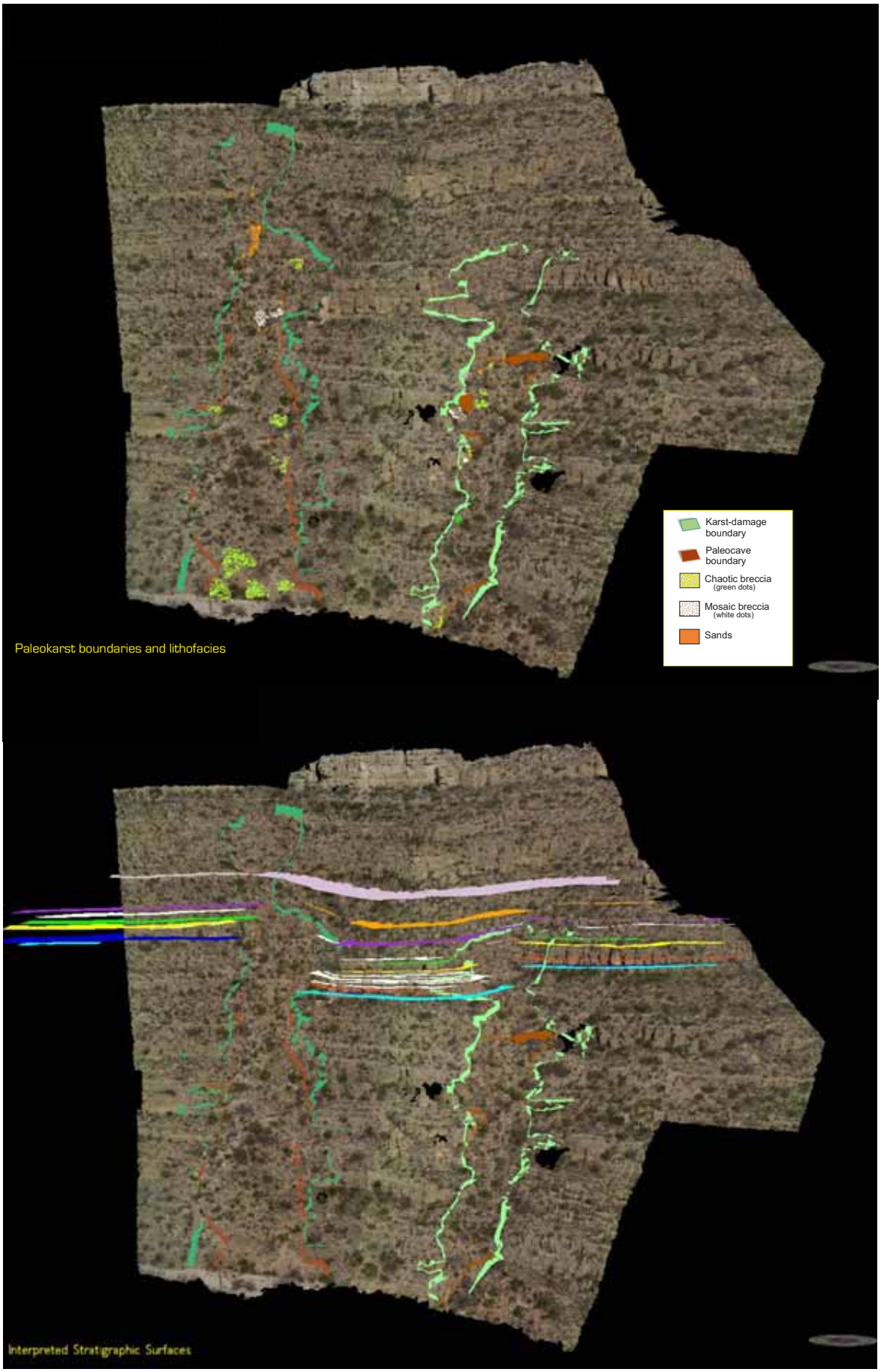

Fig. 5.3. Photorealistic model of Rattlesnake Canyon paleokarst integrating paleokarst boundaries, karst damage boundaries and stratigraphic surfaces.

single traces were captured crossing the paleokarst at different heights. The best agreement is in the undisturbed host rock, where GPR reflections are generally strong, parallel, and continuous. Discontinuity of the GPR reflections occurred in the tepee facies (Fig. 5.4) and in the disturbed paleokarst system. The GPR lines were interrupted when the radar signal detected the paleokarst facies and penetrated the tepee facies, delineating irregular surfaces as shown in Fig. 5.4.

As the Yates strata dip gently horizontal we can project distances parallel to the surface defined by the XY axes. Projecting the distance from the interrupted lowest lines of the platform perpendicularly to Z towards the paleokarst boundaries gave us a minimum distance of penetration of approximately 70 metres. The distance is not very significant in this direction. As discussed in Chapter 4, it is interpreted that the dissolution front of the Rattlesnake Canyon paleokarst system advanced towards the south because of an increase in the collapse deposits in the southern part of the canyon.

Next: Fig. 5.4. GPR profiles introduced into the 3D model. a) Front view of the model with the surfaces of the stratigraphic horizons at the top of the platform. Note that the GPR profiles limiting the top of the system display irregular geometries attributed to the tepee structures of the shelf crest facies. c) and e) West view sections of the model. The continuous traces of the GPR profiles penetrate short distances towards the platform and GPR discontinuities are present in the graben and at the top of the platform. d) Back view of the system where it may be noted that the continuous GPR profiles do not cut the limits of the karst penetrating towards the platform. f) and g) Measured distances of the penetration of the karst at the top of the platform.

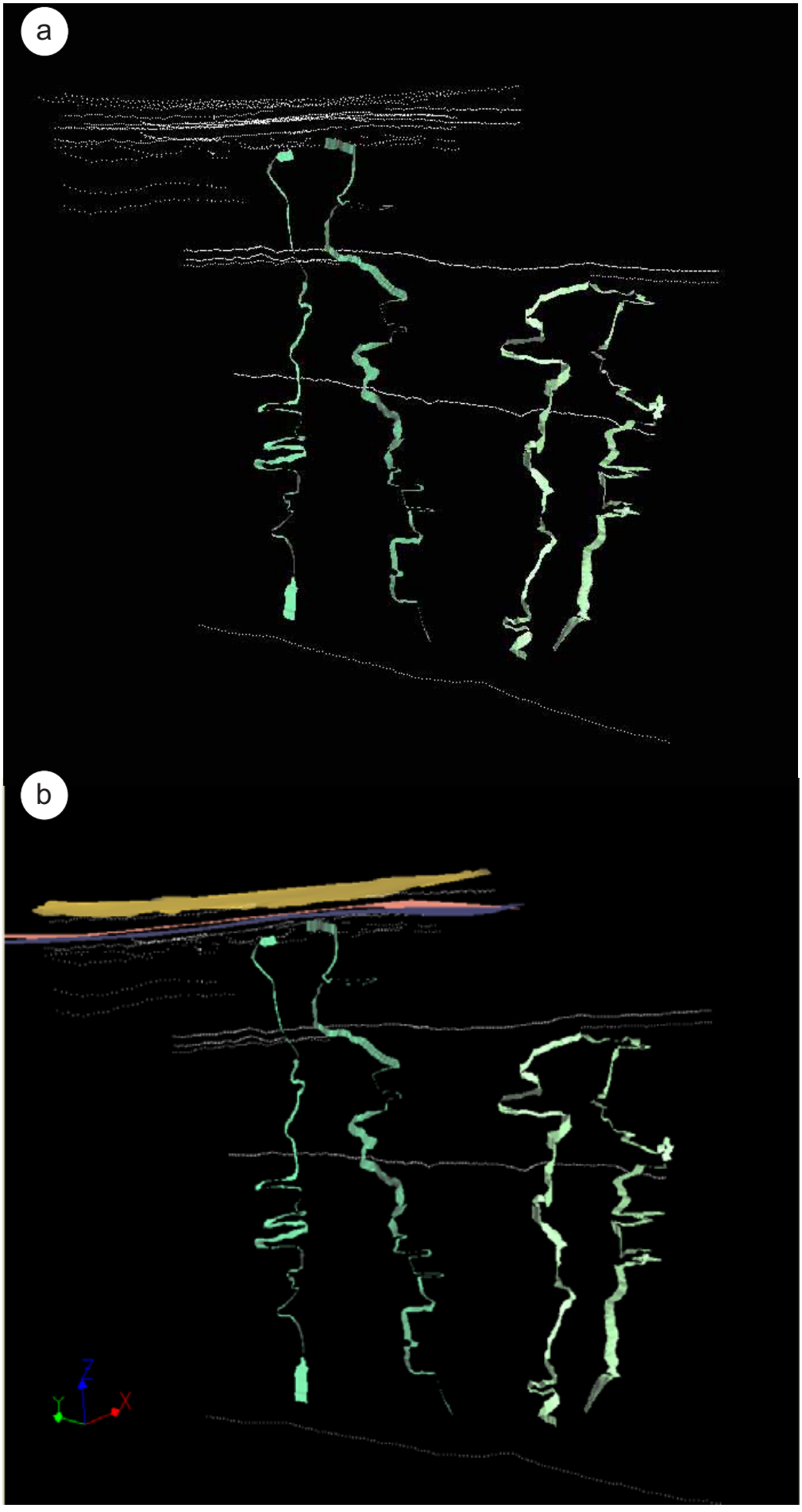
a
b
Z
Y
X

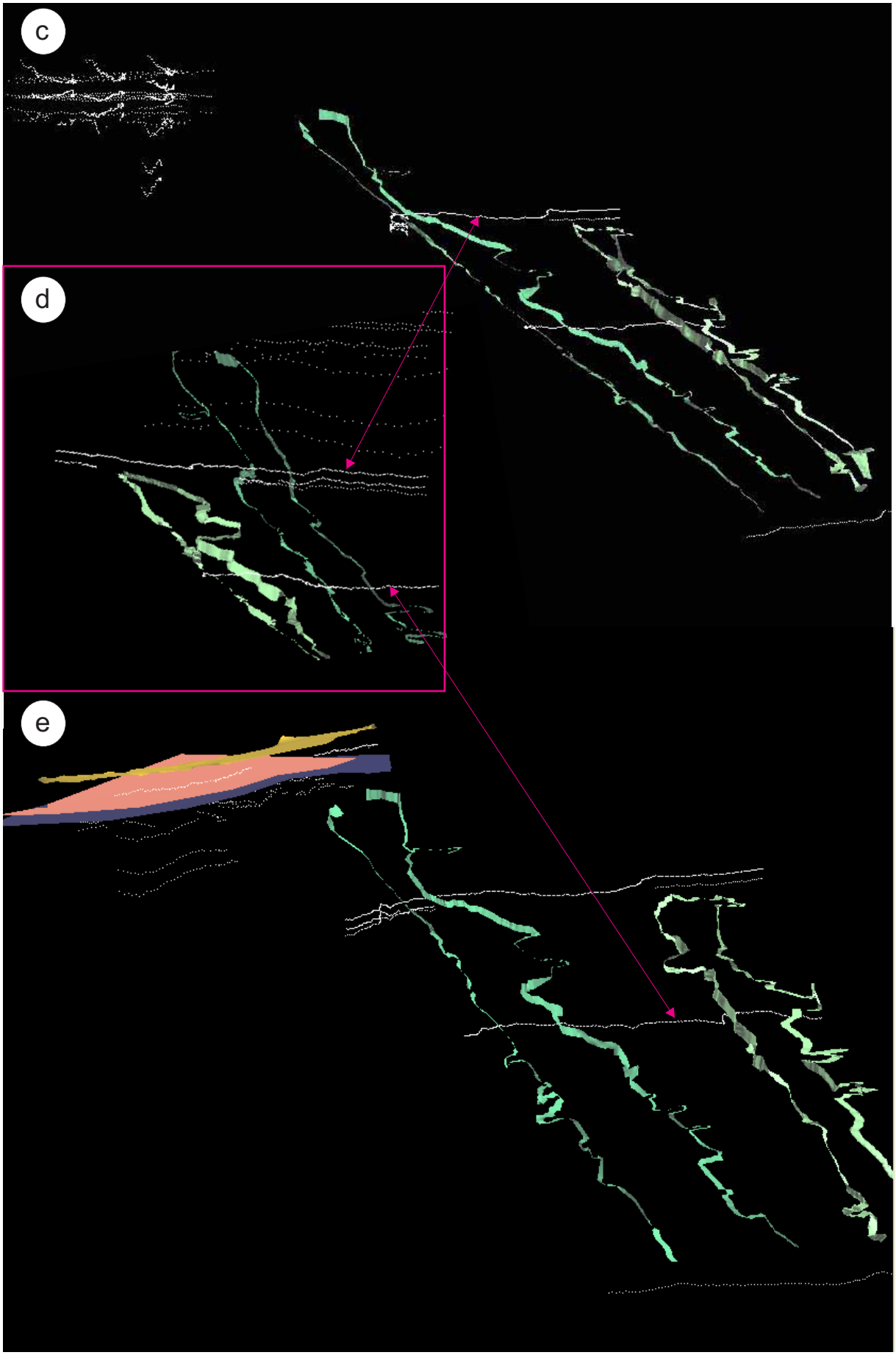
c
d
e

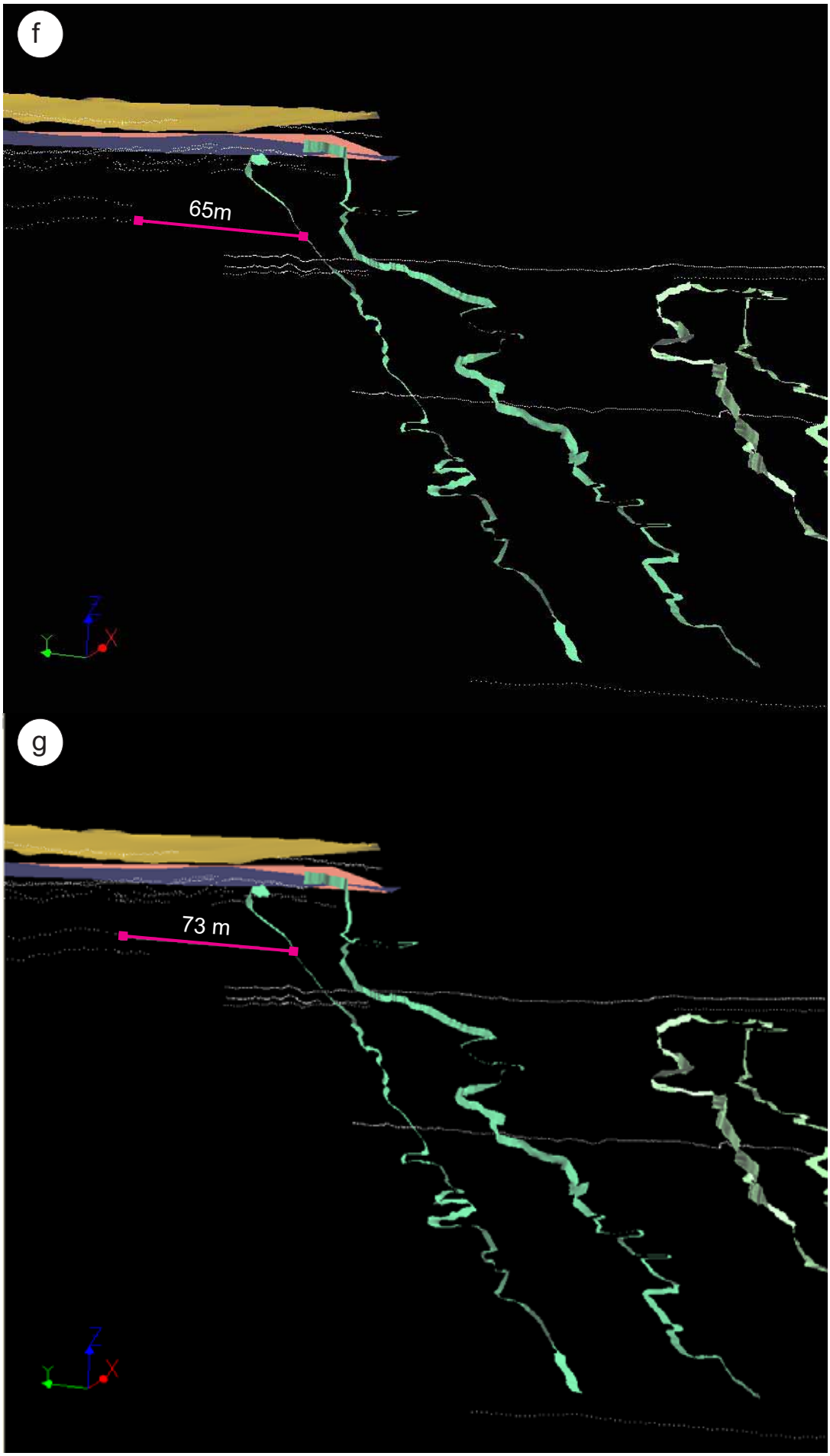
f
65m
Z
Y
X
g
73 m
Z
Y
X

6.- Conclusions

This study highlights the importance of introducing new techniques into the study of carbonate rocks, particularly paleocave systems. The conjunction of outcrop databases and GPR data provides spatial constaints for the assessment of geological heterogeneity.

This chapter documents the workflow to the construction of a diagenetically conditioned 3D model. Virtual outcrop was used from the start of the process —manually digitizing geological entities and extraction of datasets— to the final stages of the integration of the model into the photorealistic environment.

These modern techniques are versatile because the information is globally stored in a virtual environment as a "virtual library" of easy access where the information can be managed and displayed in line with different needs.

The GPR technique provides useful information about the penetration of the karst along the Upper Permian Capitan platform-margin. The estimation of the penetration distance is over 70 metres towards the north.

Given the evolution model of the paleokarst system (Chapter 4) and given our field observations, the paleokarst system is dimensionally much more pronounced throughout the southern margin of the platform.

Chapter 6
Diagenetic history of Rattlesnake Canyon

Abstract:

The Rattlesnake Canyon paleokarst system is genetically linked to syndepositional faulting in carbonate strata of the Upper Permian Capitan platform, Guadalupe Mountains, New Mexico. The paleokarst filling sequence in Rattlesnake Canyon consists of platform-derived sediments with abundant siliciclastic sediments and intercalations of fine carbonate sediment.

Dolomitization is massive in the host rock and coexists with calcite cements within the paleokarst area. The dolomitized paleokarst infills underwent different diagenetic episodes of replacement, multiphased dolomite cementation, dedolomitization and calcite precipitation. Replacive dolomite is recognized as a product of dolomitization of the early limestone and of siliciclastic sediments in karst affected areas. Timing of onset of replacement dolomitization is interpreted to be very early and the process continued during shallow burial when limpid vug-filling dolomite occluded part of the early porosity created by the karst. This evidence is supported by isotopic data and trace element composition, reinforcing the early dolomitization model by reflux proposed for the area (Melim, 1991; Melim and Scholle, 2002).

Two patterns of cementation are identified in the Rattlesnake Canyon paleokarst: vug-filling dolomite cements, and sulphate-replacing dedolomites and calcites (^{13}C depleted) as fracture fills and filling anhydrite moulds.

Dolomite cementation is observed through a multiphased textural evolution sequence generating dolomite frameworks. Coarse rhombs of sucrosic dolomite bounded by thin limpid corticles of bright luminescent dolomite overgrowths are also observed in zones of porosity enhancement. The clusters of sucrosic dolomites are often cemented by a later limpid dolomite cement phase totally occluding intercrystal porosity. Dolomite cements exhibit bright luminescences under CL and several hairline zones are recognized revealing a zonation array. The early pattern of dolomite cementation is restricted to minor disrupted zones preserved from faulting and from late diagenetic modification in fracture networks.

Dedolomitization was limited to areas open to high circulation of fluids such as fracture zones and probably interconnected vugs. Dedolomite cements are extremely heterogeneous in CL exhibiting diverse cement zones with different luminescences. Zone 1 (Dd1) corresponds to a bright orange dedolomite. Zone 2 exhibits darker orange dull luminescences (Dd2) and Zone 3 (Dd3) is non luminescent and presents calcite mineralogy without any observable ghosts of former dolomite. Spar calcite (Cc1) occurs as a fracture-fill component in larger and probably interconnected paths for oxygenated fluids. Some dedolomite and spar $\delta^{13}C$ values are low (reaching -15 ‰ PDB), outside the range of meteoric diagenesis, suggesting an increase in CO_2 contents and parental fluids linked to BSR.

Dickite cementation is found in fracture zones and cavity fills in areas of high dissolution associated with the dedolomite cements.

Dedolomites and spar cements with low $\delta^{13}C$ values are related to microbial oxidation of the hydrocarbons whereas thermal spar has typical $\delta^{18}O$ isotopic values of hydrothermal activity. Dedolomites and calcite cements are made up of non-ferroan and dull to non-luminescent cements indicative of moderately oxic environments, whereas indurated dolomite frameworks and void-filling dolomite consist of ferroan and bright cements, suggesting suboxic environments.

Dedolomite and spar cements are interpreted to be late diagenetic products and are closely related to the hydrocarbon charge of the basin. During uplift, siliciclastic diagenesis generated clay cementation and Fe migration, resulting in iron oxyhydroxides formed by oxidation and supergene enrichment within the paleokarst. Secondary leached porosity was extensively formed in many intervals during freshwater diagenesis. The varying ratios of mixing with fluids of different origin (evaporite dissolution, meteoric flushing and HC recharge) probably led to the dedolomitization and precipitation of light $\delta^{13}C$ calcite.

A coarser calcite (^{18}O depleted) overlying dedolomite cements and occluding late secondary porosity is attributed to Miocene hydrothermal activity in the region.

Early burial vug-filling dolomite sealed great part of the early vuggy porosity. Late diagenesis exploited early fracture networks modifying early syngenetic karst features and contributing intensively in the sealing of secondary porosity.

Chapter 6

Diagenetic history of Rattlesnake Canyon

1.- Introduction

The Guadalupe Mountains have been the subject of numerous studies concerning facies architecture (Ward et al, 1986), sequence stratigraphy (Borer and Harris, 1991), early fracturation and karst development (Koša, 2003; Koša and Hunt, 2005, 2006), mechanisms of the Capitan platform dolomitization (Melim and Scholle, 2002) and its diagenetic history (Hill, 1996, Melim, 1991; Melim and Scholle, 2002; Scholle et al, 1992). Koša and Hunt (2006) documented the relationship between early diagenetic karst alterations in syndepositional faults although the mechanisms of dissolution that promoted karst enhancement continue to be poorly understood. Moreover, the relationships between the late diagenetic events and the evolution of paleokarst systems have not yet been studied. Rattlesnake Canyon provides an excellent scenario to study the early fracture control on the karst development and offers great potential for unraveling its diagenetic evolution.

The present study seeks to (i) document a variety of early and late cements and constrain them into a paragenetic sequence using geochemical data and petrographic observations, (ii) investigate the nature of the fluids that circulated through the Capitan platform margins between the Upper Permian and the Quaternary period, (iii) discriminate between early dissolution and cementation processes (and its by-products), and late dedolomitization and cementation processes associated with the Tertiary uplift, and (iv) validate that the paleokarst system localizes major heterogeneity given that it underwent multiple and complex diagenetic episodes with mixed parental fluids of diverse origin (meteoric, hydrothermal and CO_2 rich fluids related to hydrocarbon migration).

2.- Materials and methods

Field and petrographic observations demonstrated that the processes affecting both faults are identical. The diagenetic study was therefore carried out using mainly samples of Fault N. These samples give a satisfactory overview of the karstic processes in the Rattlesnake Canyon paleokarst through its diagenetic history. A total of 87 samples from Fault N and adjacent carbonate host rock were examined at visu and 111 thin sections were obtained for examination by conventional petrography (Fig. 6.1).

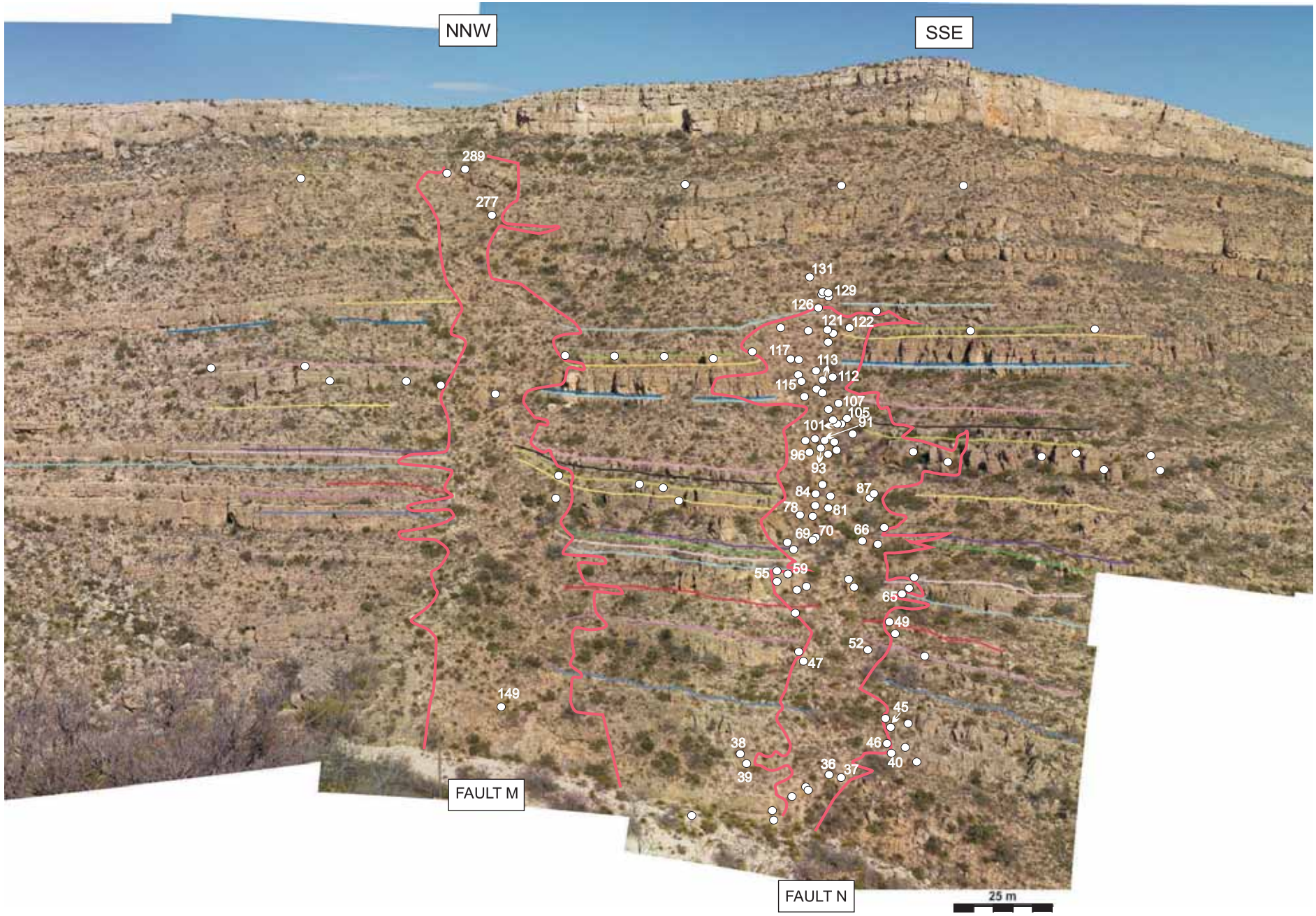

Fig. 6.1. Samples location (white spots). The location of the samples studied in this chapter is indicated by the numbered white spots in the figure. Pink lines represent the limits of the karst damage zones. Stratigraphic surfaces are correlated by the coloured lines.

Thick sections (250 μm) were used for observation by cathodoluminescence (CL) in order to sample individual cement generations for oxygen and carbon stable isotope analysis. Polished thick sections were examined using a Technosyn Cold Cathode Luminoscope model 8200 MkII with operating conditions of around 15kV beam energy, 260 mA beam current and 0.05 Torr vacuum.

Mineralogical identification and description were based on transmitted light microscopy, scanning electron microscopy (SEM), CL, X-ray diffraction (XRD) and infrared spectroscopy (FTIR).

XRD analyses for the bulk and cement carbonate samples were performed with a Bruker D-8 Advance diffractometer. Analytical conditions: Cu radiation, 40kV and 40mA, primary Göbbel mirror and energy dispersive SOL-X detector, range (2θ) between 4° and 60° with a step scan of 0.05°, 3s per step of measuring time. Spectra were evaluated by using the Diffrac.Suite™ software, and the mineral compounds were identified (when present) by using the PDF database.

Dolomite stoichiometry (M% $CaCO_3$) was calculated by using the relationship between calcium content and d[104] spacing (Goldsmith and Graf, 1958) and by applying the equation of Lumsden (1979) to the measured d[104] spacing.

Dickite mineralogical identification was determined with powdered samples by XRD using an INEL CPS-120 diffractometer with capillary samples and by Fourier transform infrared (FTIR) spectrometry.

FTIR spectra were recorded in the absorbance mode using a ABB Bomem FTLA device. FTIR spectrometer was set to give undeformed spectra. The resolution was 4 cm-1 in the 400–4000 cm-1 analyzed range.

Coloured carbonate karst sediments were dissolved using Na-EDTA and the insoluble residue (a concentrate of siliciclastics and iron oxides) was analyzed by XRD and transmission electron microscopy (TEM). The samples for transmission electron microscopy (TEM) were observed and analyzed in a Hitachi H 800- MT and a JEOL 2100. In order to characterize the iron oxides, a small amount of the sample suspension was dropped onto a mesh carbon-coated copper grid which was then allowed to dry in air.

The chemical composition of the dedolomite cements, the replacive dolomite and the thermal spar of the karst were compared using electron microprobe analysis (Cameca Camebax SX-50) at Serveis Científico-Tècnics de la Universitat de Barcelona (SCT-UB) calibrated with different natural carbonates and oxides of certified composition.

Fifty-two thick sections and hand samples were selected to obtain microsamples for stable C and O isotope and trace element analyses. Ninety-eight powder microsamples of various diagenetic phases were obtained using a Merchantek microdrill for C and O isotope analysis.

Moreover, powder samples from hand samples were obtained with a dentist's drill. The carbonate powders were reacted with 100% phosphoric acid at 70ºC. Isotope composition ($\delta^{13}C$ PDB, $\delta^{18}O$ PDB) of carbonate microsamples (about 60 µg) was analyzed with a Kiel preparation device online assembled to a MAT 252 IRMS. Analytical precision explained as sigma was better than 0.02 for C and 0.06 ‰ for O. Isotopic standards used as reference were NBS-19 in both cases. Carbon and oxygen isotope compositions are expressed in the text as PDB. The term PDB was suppressed to facilitate reading. The term SMOW in the text refers to the isotopic composition of parental fluids.

Some cements, host rock carbonates and karst sediments were analyzed for selected trace elements using Inductively Couple Plasma spectrometry (ICP). Eighty-six powder samples for ICP analyses were obtained using a low speed dental drill assembly. Ca, Mg, Sr, Zn, and Na were determined using ICP-MS and Fe using ICP-OES. Chemical element quantification was performed with a Perkin-Elmer Elan 6000 ICP-mass spectrometer. Powdered samples were reacted with high purity HNO_3 40% for twenty minutes. The standards to make the calibration curves were obtained from NIST commercial prepared solutions (1000 to 10.000 mg/L).

Measurements of total organic carbon (TOC) and of elemental C/N ratios were made by high-temperature combustion using a Carlo Erba 1108 CHNS-O analyser. A total of 11 duplicated samples were attacked with HCl 4M and subsequently dried to quantify organic carbon content. Instrumental detection limits are 0.5 µg for both C and N.

Ultraviolet fluorescence microscopy was used to study the presence and disposition of the hydrocarbon fluid inclusions in the calcite cements.

3.- Microfacies

Examination of thin sections of the paleokarst filling revealed that the filling sequence was made up of siliciclastic sandstones and siltstones as well as carbonate sediments. Major detrital fractions are identified as breccia matrices and as infills of vertical fractures. Siliciclastics mainly fill the open porosity created by the fault growth and the paleokarst collapses. Fine grain supported carbonate textures are rich in peloids and display diversity of cements filling voids and fractures. Fenestral and stromatolite structures (Fig. 6.2, Sample 117) are the only organic indicative textural structures recognized.

A variety of cements have been identified in thin sections and are summarized in Table 6.1. Planar-c dolomite is mainly identified as void and biomoulds infills (Fig. 6.3, Plate 1: d). Dolomite scalenoehedral dog-tooth crystals line cavities and display bright red luminescences under CL (Fig. 6.4: d). Bladed dolomite crystals are also identified as lining cavities (Fig. 6.3, Plate 1:b). Dolomite cements show limpid crystals and are mostly preserved in vugs. Isopachous early marine cements are found lining cavities and defining textures totally replaced by dolomite with bright yellow luminiscences identical to the replacive dolomite

luminescence. Dolomicrite to planar-s dolomite mosaics often show rhombohedra coloured cores and trace the karst affected areas (Fig. 6.3, Plate 1:a). These textures do not seem to be infills but subproducts of alteration within the karst areas with diffuse diagenetic contacts with the unaltered host rock. Peloidal and clotted micrite are commonly associated with these coloured cements and frequently show thrombolitic textures typical of clotted micrite aggregates. Spar and dedolomite cements are abundant in areas of enhanced dissolution.

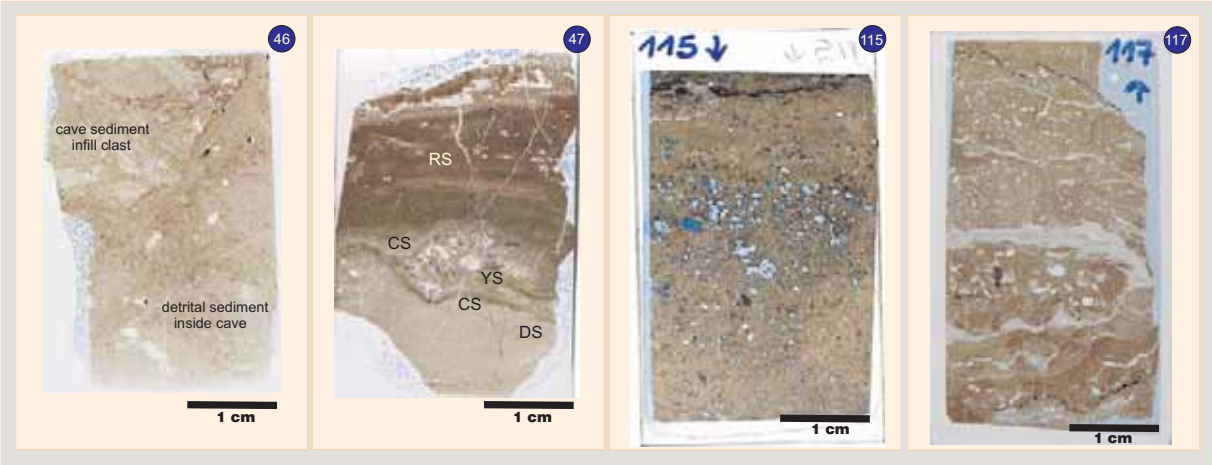

Fig. 6.2. From left to right: scanner images of thin sections. **Sample 46**: Reworked clast at the top of the section in contact with detrital sediment. Sample from the paleocave area. **Sample 47**: Stratigraphy of karst sediments. Detrital sediment at the base (DS), fine carbonate sediment (CS) with a dissolution cavity lined by yellow sediment (YS). **Sample 115**: Siliciclastic fracture fill at the uppermost fracture zone of Fault N. **Sample 117**: Cave infill at the top of Fault N. Density of cryptalgal void fenestrae is higher at the top of the section.

3.1. - Dolomite components

Dolomitization is massive in the host rock and coexists with calcite cements within the paleokarst area. The dolomitized paleokarst infills underwent different diagenetic episodes of replacement, multiphased dolomite cementation, dedolomitization and calcite precipitation. Replacive dolomite is recognized as a product of dolomitization of the early limestone and of siliciclastic sediments in karst affected areas. Most of this replacive dolomite forms planar-s dolomicrite mosaics with turbid cores.

3.1.1.- Dolomite cements

Dolomite cementation is observed through a multiphased textural evolution sequence generating dolomite frameworks. Coarse rhombs bounded by thin limpid corticles of bright luminescent dolomite overgrowths are also observed in zones of porosity enhancement (planar-e or sucrose dolomite, Fig. 6.3, Plate 1:h). The clusters of sucrosic dolomites are often cemented by a later limpid dolomite cement phase totally occluding intercrystal porosity. When these overgrowths are observed under CL, several hairline zones are recognized revealing a zonation array (Fig. 6.4: a). The whole pattern of cement generations is herein referred to as dolomite

cements which are also recognized as filling voids and moulds. Dolomite cements exhibit bright luminescences, sometimes displayed as sector zonations (Fig. 6.4: c2).

The nature of syntaxial overgrowths and of pore-filling dolomite cements probably represents transient pore fluids since both exhibit bright luminescences and a limpid appearance and only differ in their colour luminescences.

Cement	Fig.	Composition	Habit or Fabric	Dimensions	Interpretation
Planar-s	6.3. Plate 1a	Dolomite	Polymodal mosaic often coloured	150-250 μm 750 μm-4 mm	Shallow burial cements
Planar-c Dog tooth Bladed	6.3. Plate 1d. 6.4. d.2 6.3. Plate 2b	Dolomite	Drusy in cavities Scalenohedral Coarse acicular	Lenght up to 2 mm Widht up to 1 mm	Shallow burial cements
Planar-e	6.3. Plate 1h	Dolomite	Euhedral to sub-euhedral often coloured	100-500 μm	Shallow burial cements
Isopachous	6.3. Plate 1d	Aragonite (dolomitized, aragonite traces preserved)	Fibrous rims	2-100 μm	Marine phreatic-marine vadose aragonite cements
Micritic cement	6.3. Plate 1 c and e	Neomorphic low-Mg calcite entirely dolomitized	Meniscus Rim	8-10 μm	Marine vadose cement
Dolomicrite	6.3. Plate 2a	Dolomite	Mosaic of anhedral crystal often coloured	4-10 μm	Early diagenetic formation
Blocky	6.3. Plate 1 f and g	Major calcite	Spar	120μm- 1 cm	Freshwater phreatic Dedolomites Hydrothermal
Peloidal- Clotted micrite	6.3. Plate 1g	Microcrystalline calcite Dolomite	Peloidal and clotted micrite aggregates	<1 mm	Bacterial related Dedolomitisation
Dickite	6.3. Plate 2a 6.4. d.2	Alumino-silicate	Booklets	1-10 μm	Authigenic precipitation probably related to an hydrothermal event (Hill,1996)

Table 6.1. Description and interpretation of the cements observed within karst areas.

3.1.2.- Replacive dolomite

Replacive dolomite appears homogeneous with bright yellow luminescence under CL becoming homogenously red luminescent when the distance from the karst affected area is increased. Replacive dolomite has a high detrital content with feldspar and quartz clasts that are often dissolved and scarce mica. Under transmitted light the karst replacive dolomite often appears as dolomicrite mosaics of anhedral crystals with turbid cores. Carbonate marine sediments (Fig. 6.2, Sample 47) occur within the karst, but in a smaller proportion than the siliciclastic infills. A large number of mud components of these marine sediments are micrite, peloids and thrombolitic structures. Typically this carbonate is beige but can also be red or yellow stained. Green and black colours are observed in stromatolite structures that contain a large amount of iron oxides.

The relationship between replacive turbid dolomite, syntaxial overgrowths and pore-filling dolomite cements can be fitted into a temporary sequence which probably starts with a replacement episode. The core of the dolomite rhombohedra includes turbid dolomicrite relicts preserved as irregular forms that could have undergone corrosion or replacement. The similarities between the cores and later syntaxial overgrowth suggest a possible replacement of the cores during the formation of crystal cortices. It follows that later stages of syntaxial fringes were precipitated, competing and intergrowing during textural coarsening (Fig. 6.4: b). The early sucrosic texture was finally sealed by the pore-filling dolomite occluding porosity.

3.1.3.- Dolomite stoichiometry

Dolomites from Rattlesnake Canyon are highly stoichiometric (Table 6.2). Crystal stoichiometry ranges between 49.2 mol % $CaCO_3$ in the paleokarst zones and 49.7 mol % $CaCO_3$ in the adjacent host rock.

Component	Range	Mean	n
Replacive dolomite	48.63-50.40	49.48	35
Adjacent host rock	49.23-51.37	49.69	14
Unaffected host rock	49.47-50.18	49.74	3
Dolomite cement		49.40	1
Dedolomite	48.70-49.67	49.28	3

Table 6.2. Dolomite stoichiometry expressed by mol% (M%) $CaCO_3$.

3.2.- Dedolomite and calcite components

Spar calcite is commonly found as blocky spar cement filling voids as well as fracture porosity (Fig. 6.3, Plate 1: f, g). CL reveals that spar calcite shows 3 different luminescent subzones identified as Dd1, Dd2 and Dd3 (Fig. 6.4: f, g and h). This sequence contains dedolomites and calcite cements. Dd1 is often corroded by Dd2 (Fig. 6.4: f). Dd2 is strongly zoned and often corroded by Dd3 (Fig. 6.4: h2). Dd3 is dark red dull to non-luminescent. Dd1 and Dd2 are regularly associated with dickite cements (Fig. 6.4: d2). Dd2 appears frequently as an intermediate phase from Dd1 to Dd3 or vice versa. In the areas where the sequence starts from Dd1 there is a subsequent gradation from Dd1 to Dd2 and Dd3.

CL observations reveal rhombohedra calcite pseudomorphs and calcitized rhombs after dolomite within the calcite mosaics (Fig. 6.3, Plate 1: f; Fig. 6.4: f).

Fig. 6.3

Plate 1

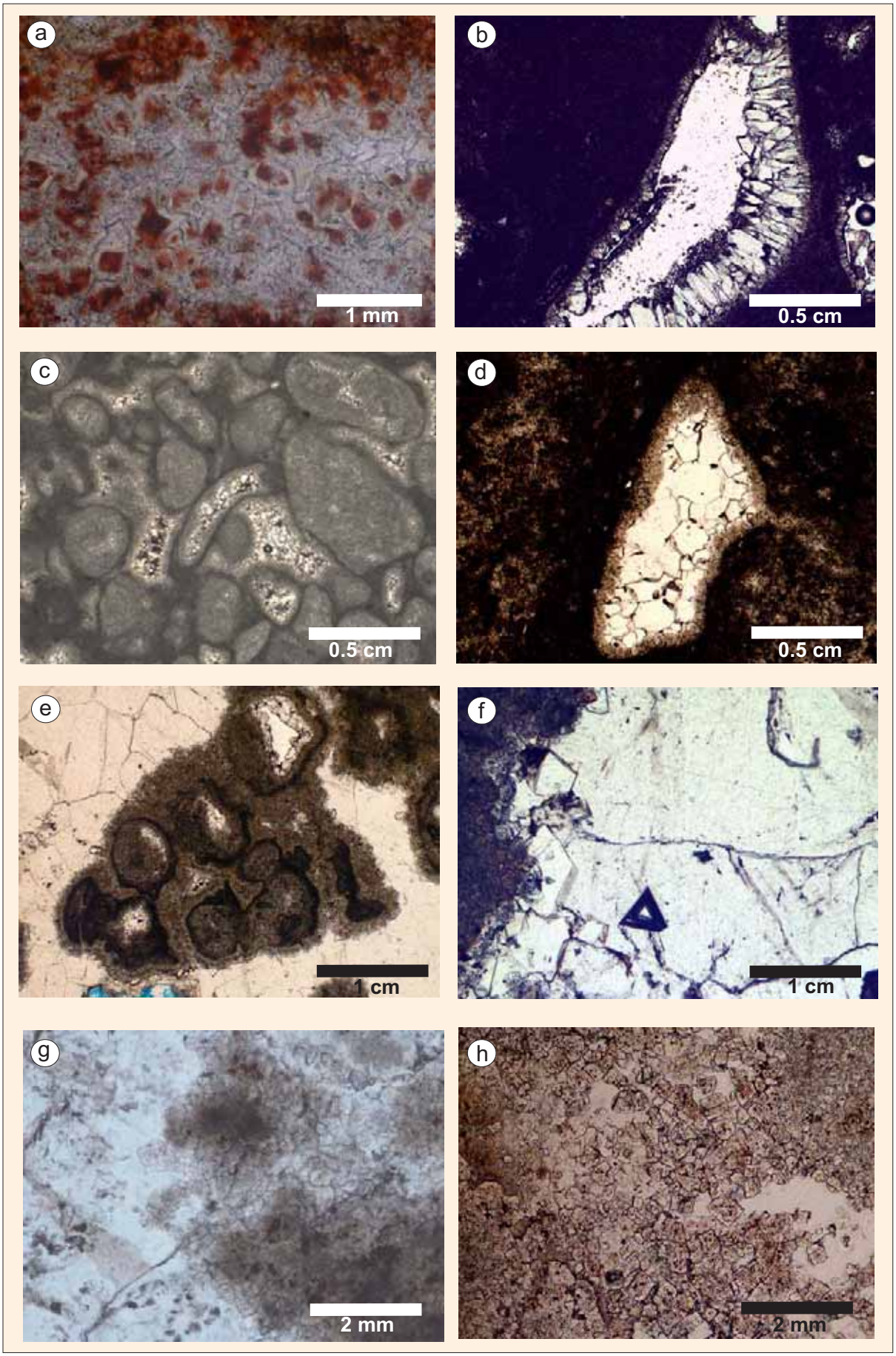

Fig. 6.3 Plate 2

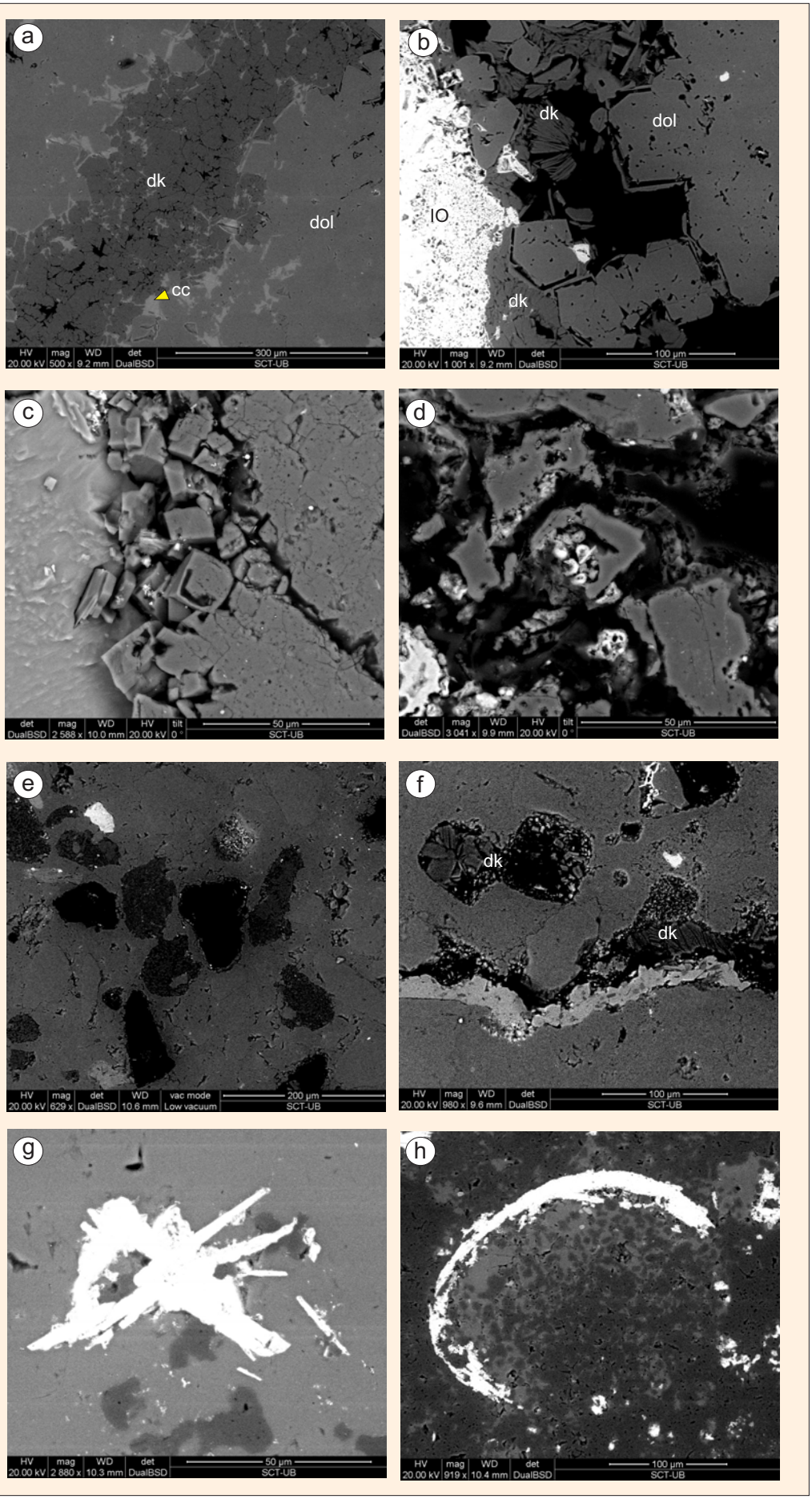

Fig. 6.3. **Plate 1**: Conventional petrography images of karst sediments and cements. Situation of the samples is shown in Fig. 6.1. a) Planar-s dolomite. Equigranular mosaic with nucleated red rhombohedra. Sample 55. b) Bladed dolomite cement filling karst cavity. Sample 84. c) Ooid lithoclasts in a grainstone sample. The internal structure of components is often dissolved inside karst domains. Dark micritic meniscus sediment is subtly preserved. Sample 36. d) Isapachous fibrous cement lining common cavity. Sample 70. e) Ooid grapestone. Internal ooid dissolution is observed. sample 66. f) Calcitized rhomb of dolomite within a late spar cement. Sample 96. g) Clotted to peloidal dolomitized karst sediment. Sample 103. (Fallen block). h) Planar-e dolomite. Euhedral to subeuhedral rhomboehedra dolomite growth create significant porosity. Sample 55. **Plate 2**: Scanning electron microscopy images of karst sediments and cements. Situation of the samples is shown in Fig. 6.1. a) Dickite cement filling fracture porosity. Note dedolomitized edges of rhombohedra crystals at the fracture contact. (dk: dickite, cc: calcite, dol: dolomite). sample 46. b) Rhombohedra dolomite crystals exhibit dissolution pores and dedolomitized rims. (dk: dickite, IO: iron oxides, dol: dolomite). Sample 46. c) Etched section. Dedolomitization reflected by dissolution pores and tubes in the outer zones and inner cores of rhombohedra. Sample 149. e) Siliciclastic grains dissolved. The light grain at the upper left part of the photograph has been identified by EDS as a Ti silicate. Sample 129. f) Dickite booklets filling cavities. Sample 49. g) Fibrous iron oxide. For the morphology and the yellow colour of the sample it is identified as goethite. Sample 69. h) Iron oxides preserve former mould structures. Sample 69.

It follows that cements Dd1, Dd2 and Dd3 probably resulted from dedolomitization. Dedolomitization was limited to areas open to high circulation of fluids such as fracture zones and probably interconnected vugs.

Calcite isolated cements (Cc1) are dark dull brown to non-luminescent and usually occur as fracture and solution pipe fills (Fig. 6.4: e) as well as filling anhydrite moulds (Fig. 6.8: a and c). This phase does not appear to be in contact with dedolomites but appears as a single product occluding porosity. Cc1 resembles Dd3 since both are homogeneous in CL and display similar luminescences. However, it is interpreted as another component since it is always isolated from the dedolomite sequence.

3.3.- Clay cements

Dickite cementation is found in fracture zones and cavity fills in areas of high dissolution associated with the dedolomite cements. Dickite displays some well developed booklets (Fig. 6.3, Plate 2: b, f) and was identified by X-ray powder diffraction and by infrared spectrometry. Dickite is also found partially filling porosity caused by dissolution of feldspar grains (Fig. 6.3, Plate 2: e, f).

Melim (1991) reported a correlation between kaolinization and the amount of siliciclastics, suggesting a derivation from feldspars. Dickite booklets are both stained with iron oxides and totally limpid. It may therefore be inferred that the clay genesis has continuity in time, predating and postdating the iron diagenesis.

Fig. 6.4

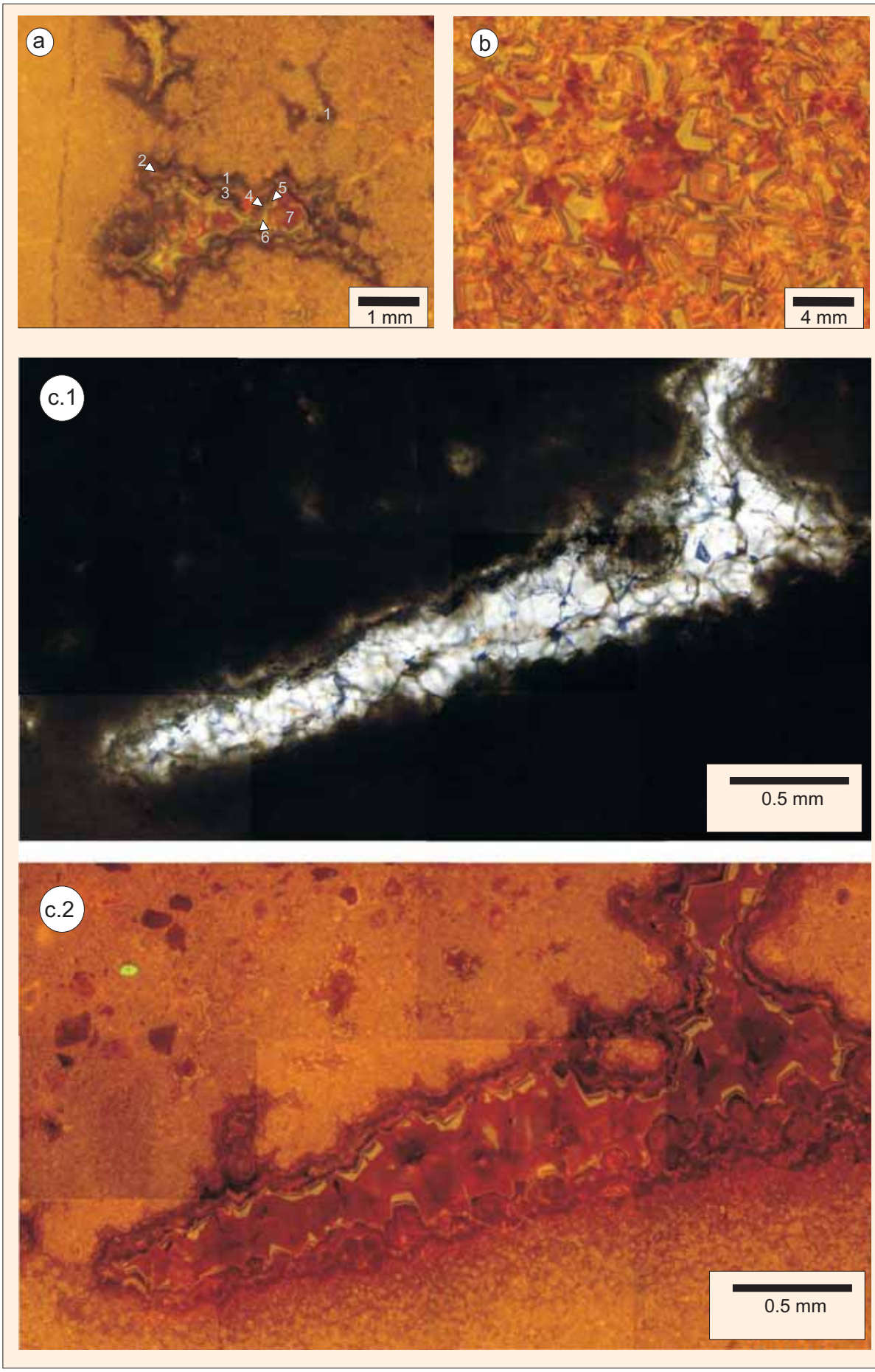

Fig. 6.4

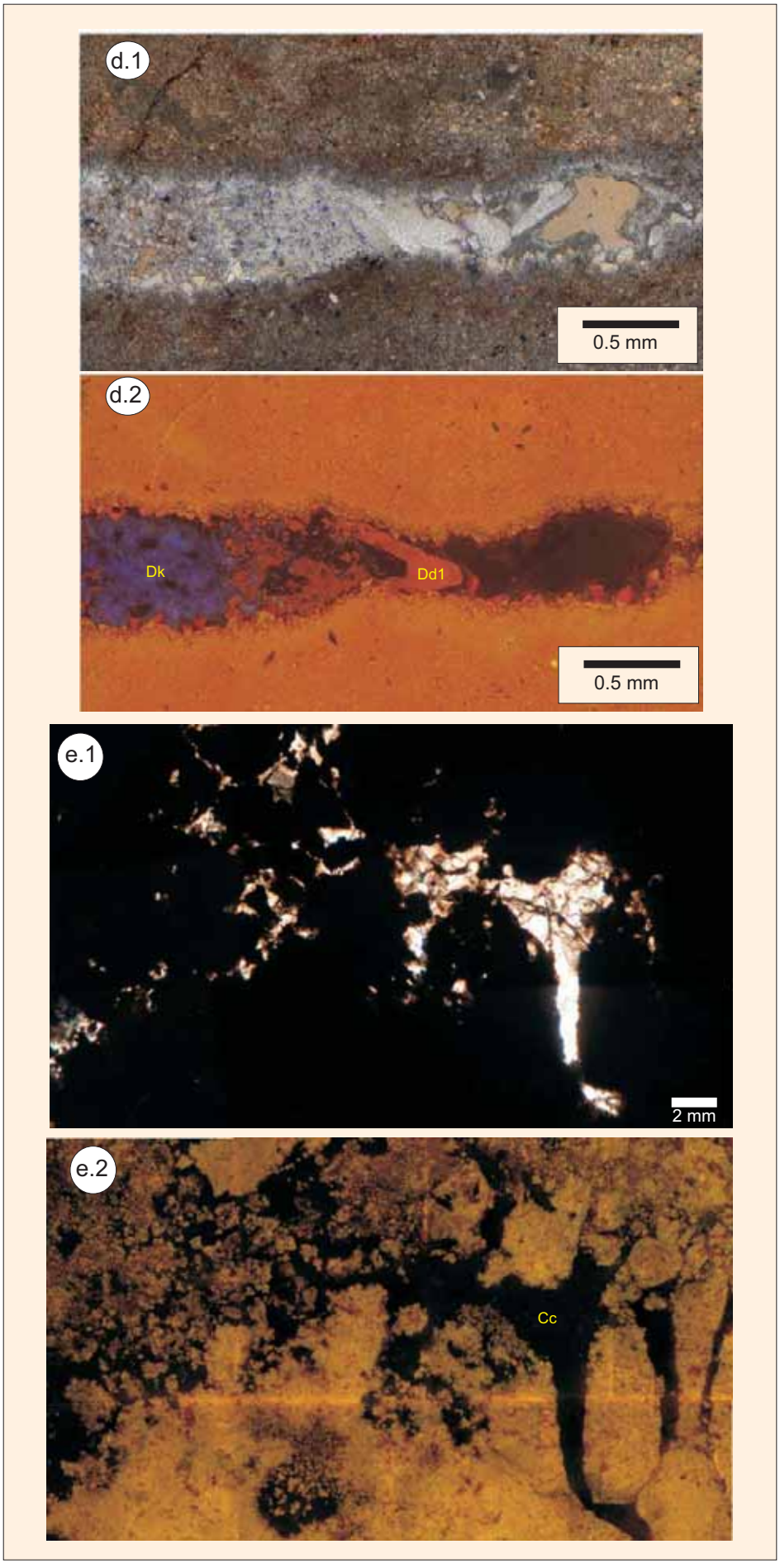

Fig. 6.4

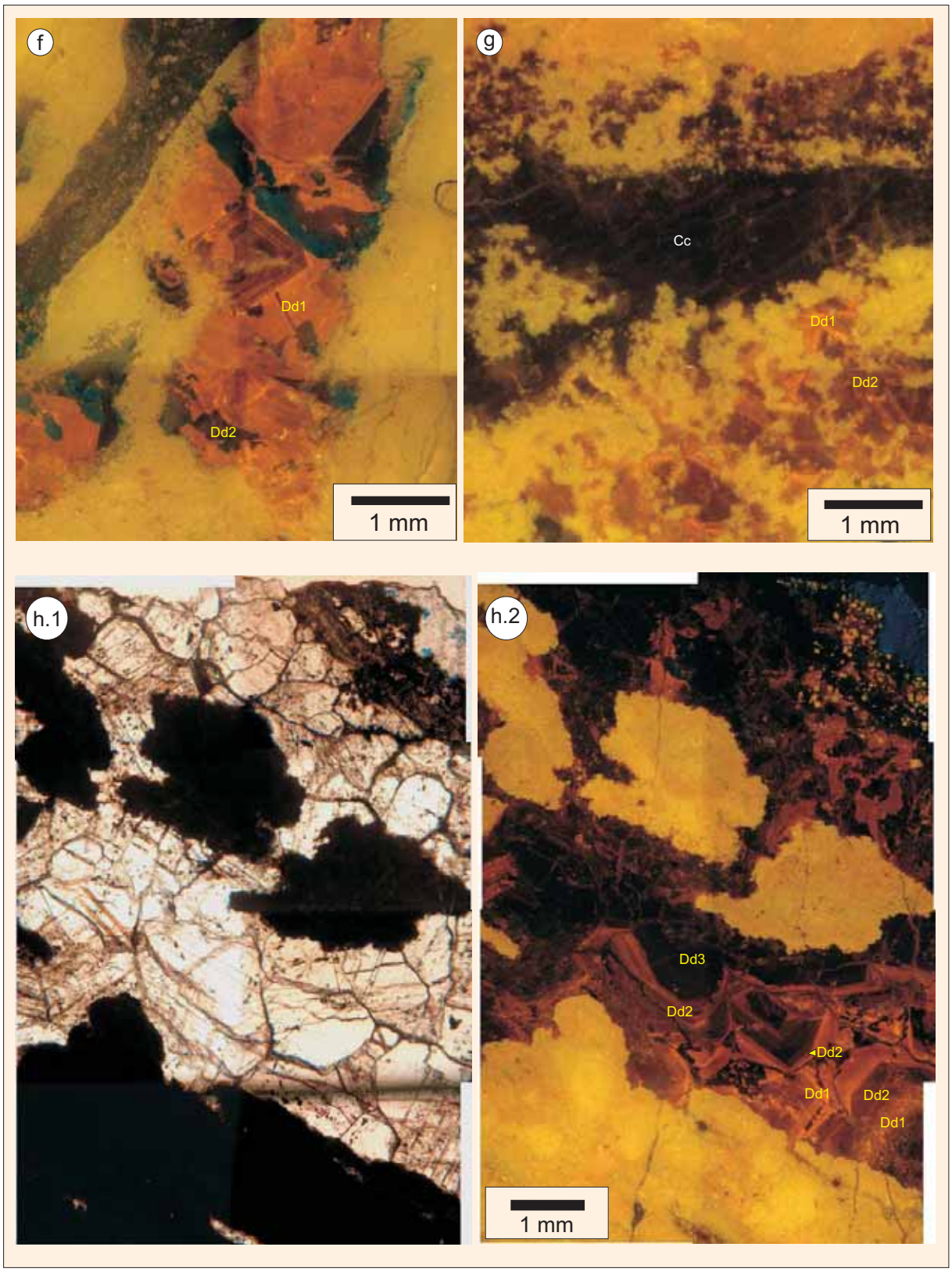

Fig. 6.4. Cathodoluminescence patterns of cementation. Early cementation sequences are shown in photographs a, b and c. Late cementation sequences are shown in photographs d, e, f, g and h. a) Multicyclic void lining syntaxial overgrowths. At least 6 cycles are recognized starting from non-luminescent phase 1 to bright luminescent cements 6 and 7. Sample 93. b) Detail image of the multicyclic overgrowths in dolomite rhombohedra and intercrystal porosity. Sample 101. c) Parallel ligh (c.1) and CL photomosaic (c.2) of the multicyclic void lining cement sequences. Sample 93. Continued on next page.

Fig. 6.4. d) Upper photograph is shown in parallel light (d.1) and the lower photograph shows CL luminescence (d.2). Solution cavity filled with clear dolomite cement. Dolomicrite matrix show homogenous orange-yellow luminescence. Dickite cement (blue) corrodes a prior generation of dedolomite cement (Dd1). Dogtooth cement is also observed at the rims of the cavity. Sample 66. e.1 and e.2) Solution pipe structures filled with non-luminescent calcite spar (Cc1). Sample 113. f) Fracture zoned cement with dedolomite Zone 1 (Dd1) highly corroded by dedolomite Zone 2 (Dd2) which exhibits rhombohedra ghosts of former dolomite. Sample 59. g) Fracture filled with calcite (Cc1) and towards the bottom of the photograph preserved vugs with graded bright dedolomite (Dd1) to dull dedolomite (Dd2). Sample 65. h.1 and h.2) Parallel light and CL photomosaic. Note the gradation from Dd3 to the top of the photograph to Dd1 at the bottom and an intermediate and complex pattern of cycles in the zone of mixing fluids. Sample 66.

3.3.1.- Identification of dickite. XRD Analyses and FTIR Analyses.

The XRD pattern of powdered dickite is shown in Fig. 6.5. Individual dickite pockets show mixtures with calcite.

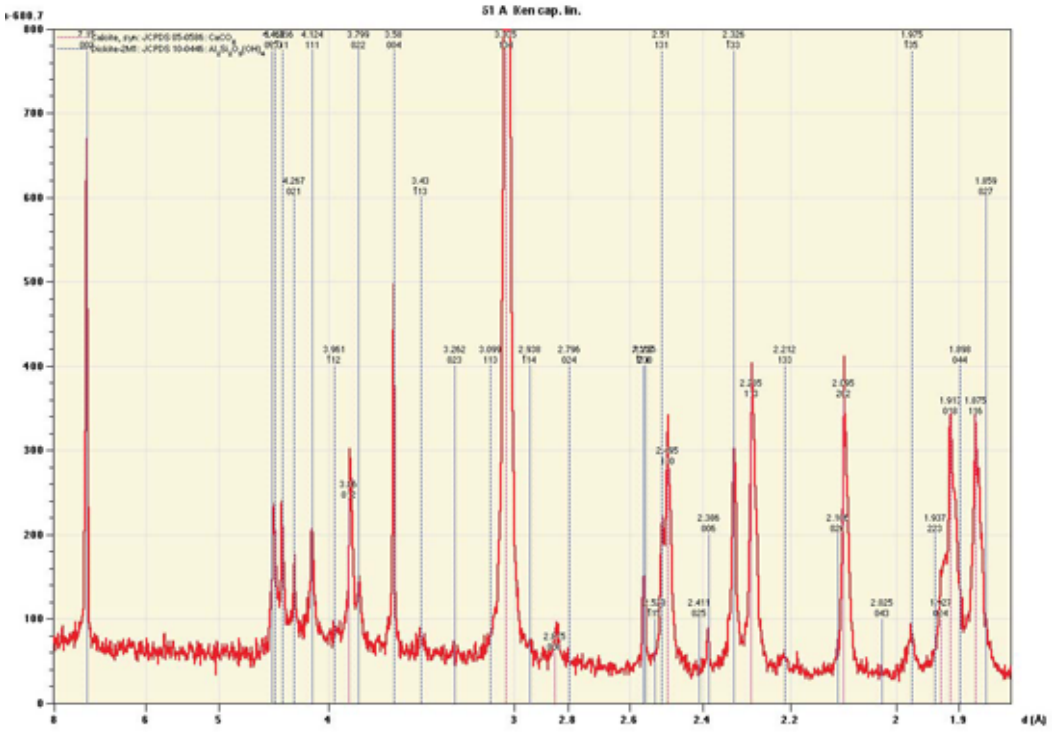

Fig. 6.5. XRD spectra of dickite with mixture of calcite cement.

An accurate distinction between kaolinite and dickite can be achieved employing FTIR spectroscopy by assessing the position and relative intensity of the OH-stretching bands in the 3600–3700 cm^{-1} region of the IR spectrum. The FTIR spectrum of the clay fraction in Rattlesnake Canyon is characteristic for dickite (Fig. 6.6a). The FTIR spectra of dickites formed at different burial depths (Beaufort et al., 1998) are shown together with the studied dickite spectrum (Fig. 6.6b). Rattlesnake dickite sample exhibits strong absorption at 3621 cm^{-1} and two medium-strong absorption bands at 3652 and 3703 cm^{-1} and is analogous to the 3500 m depth dickite of Beaufort et al. (1998).

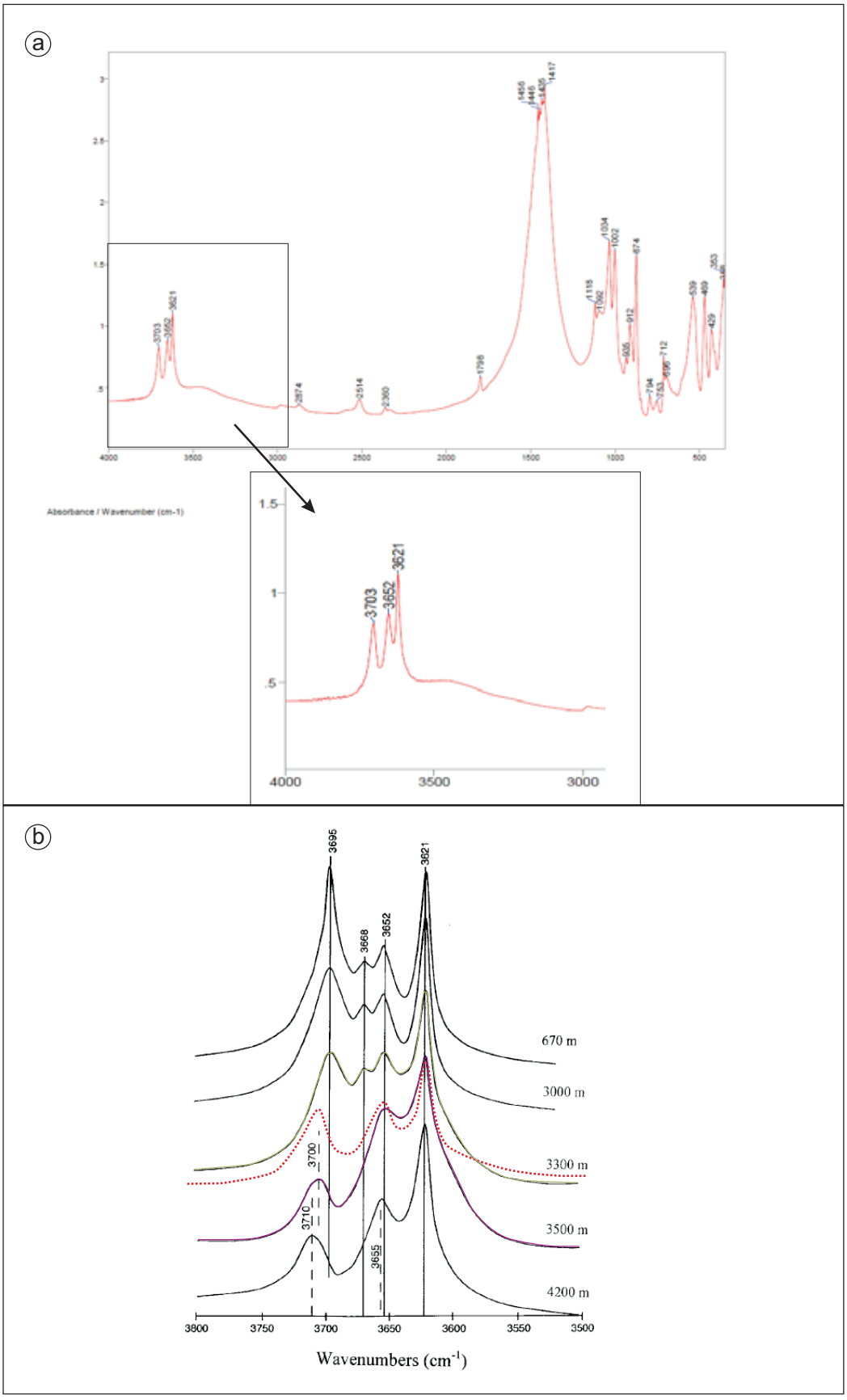

Fig. 6.6. a) FTIR spectra of dickite. The characteristic FTIR band for the identification of dickite is expanded. b)The FTIR spectrum of dickite of different burial depths described by Beaufort et al. (1998). The spectra of the studied sample in Rattlesnake Canyon is superimposed (red dotted line). The position of the peaks of the studied sample match with a dickite formed at 3500 m.

3.4.- Skeletal components

Skeletal components observed in karst sediments are scarce. Only calcareous red algae are found as intraclasts in the karst areas. Accessory grains identified as benthic foraminifers, fusulinids, bioclasts of sponges and oysters may be present.

3.5.- Non-skeletal components

Pisoids, as common constituents, and coated grains were identified in paleokarst sediments. Pisoids are massive in some stratigraphic levels of the host rock succession.

Earlier studies in the area have linked the formation of pisoids to the development of carbonate shoals in the shelf crest (Esteban and Pray, 1983). Pisoids are now present in karst brecciated areas as reworked clasts. Mud-intraclasts originated from the reworking of earlier consolidated mud.

Quartz and corroded feldspar grains display angular to sub-angular morphologies (Fig. 6.2, Sample 115) and represent the siliclastic fraction. Accessory grains are apatite and zircon.

Sutured contacts are often observed in ooid grainstones as products of compaction. At least two generations of stylolization are recorded (Fig. 6.7). Dolomite stylocummulates along microstylolites do not cross-cut dolomite cemented vugs. Dolomite was cross-cut by a later generation of clay stylocumulates. Geopetal infills are also detected in a few specimens.

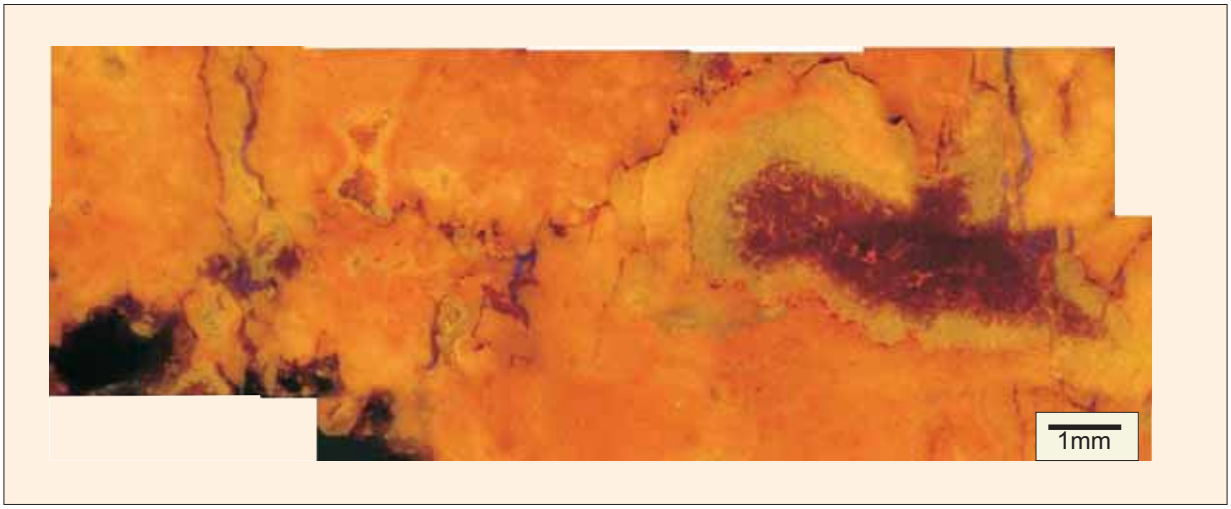

Fig. 6.7. Stylolites are cemented by the same red luminescent generation as dolomite vug filling cements. On the right of the photograph: Clay stylocumulates cross-cut dolomite cements and thus postdate dolomitization.

3.6.- Evaporite pseudomorphs

Some "T shaped" anhydrite crystal moulds, which are characteristic of anhydrite replacement fronts (stair-steps morphologies (Fig. 6.8: a, b and c)), are observed by petrography (Murray, 1960). Lath decussated and broken shaped anhydrite fabrics are overlain by the porphyroblastic fabrics (Fig. 6.8: d, e and f).

In carbonates, anhydrite tends to nucleate in organic-rich allochems, such as shells, peloids, ooids and algal stromatolites, and can be an early diagenetic product precipitated by capillary brines in the organic rich sediments.

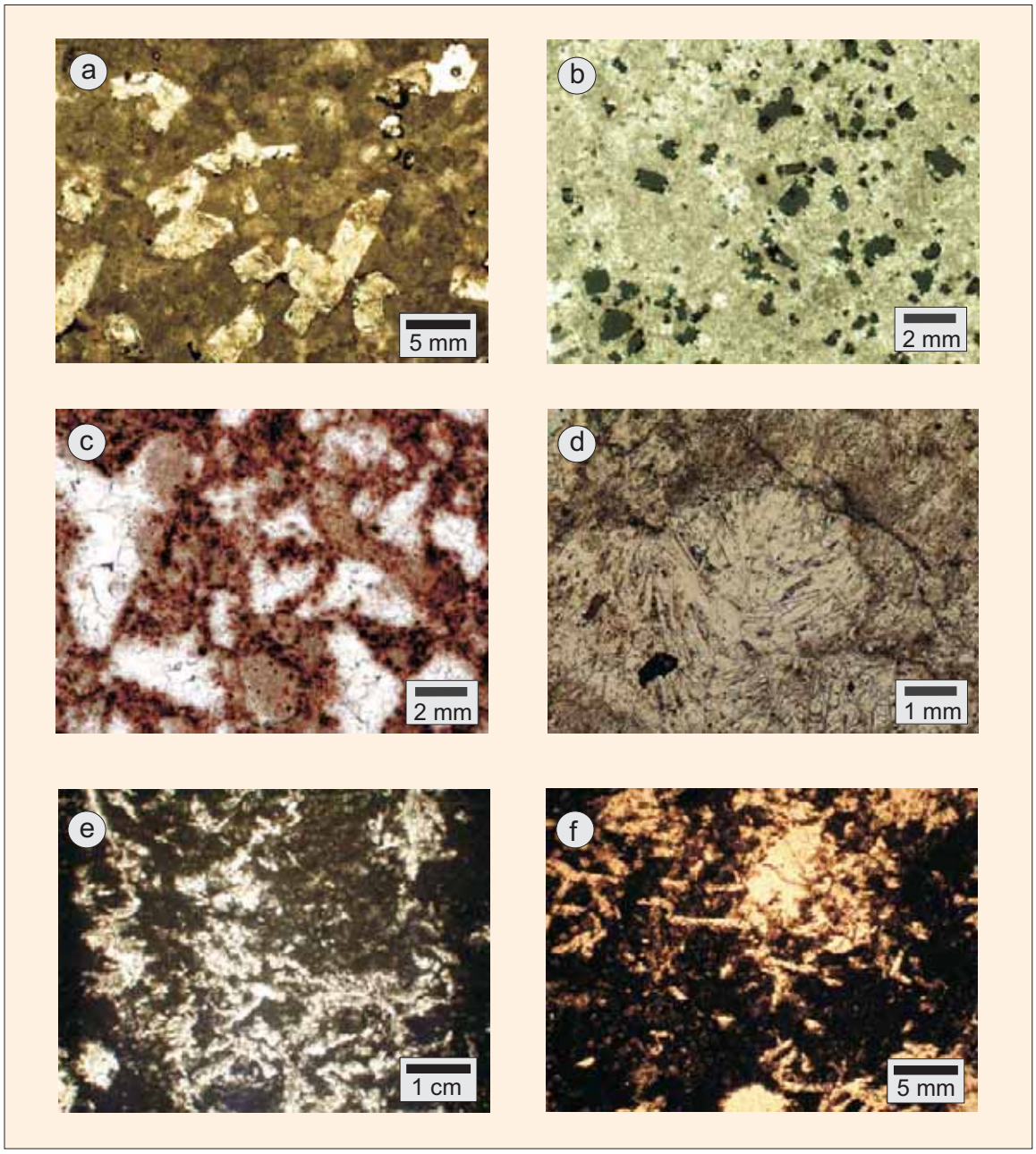

Fig. 6.8. Fabrics of the pseudomorphs after evaporites in Rattlesnake Canyon. a) Porphyroblastic anhydrite (stair-step morphologies) replaced by calcite. Sample 113. b) Dissolved anhydrite crystals. Sample 112. c) Replacement of porphyroblastic anhydrite crystals with corroded crystal boundaries and floating in a clotted texture of iron oxide stained masses. Sample 107. Continued on next page.

Fig. 6.8. d) Decussate anhydrite fabrics replaced by carbonate. Sample 73 (non in situ sample). e and f) Decussate prismatic fabricswith lath shaped replacement anhydrite crystals. It is difficult to interpret if the original phase mineral was made up of radiated aggregates of gypsum or displacive anhydrite. Samples 39 and 38.

Measurements of total organic carbon (TOC) in the karst infills resulted in concentrations of organic matter under the limit of detection.

4.- Coloured karst products

Coloured sediments are distinctive at outcrop scale within the paleokarst owing to the presence of iron oxides. These sediments do not seem classic infills since they do not exhibit sharp contacts in relation to the host rock. The contact observed in the field is diffuse, only detectable by a change of colour and a chemical gradation to an iron oxide enrichment fraction. The texture of these sediments differs from that of the host rock in that it shows abundant well zoned crystallized rhombohedra and preserved cement overgrowths. Examination under SEM confirms the presence of dolomite overgrowths that generate zoned rhombohedra as well as crystal pits (Fig. 6.3, Plate 2: a,b, c). SEM reveals that homogeneous replacive dolomite (yellow under CL) shows hollow dolomite rhombs. Many intracrystalline pits are preferential sites for the emplacement of iron oxides often appearing as pseudomorphs after pyrite (Fig. 6.9).

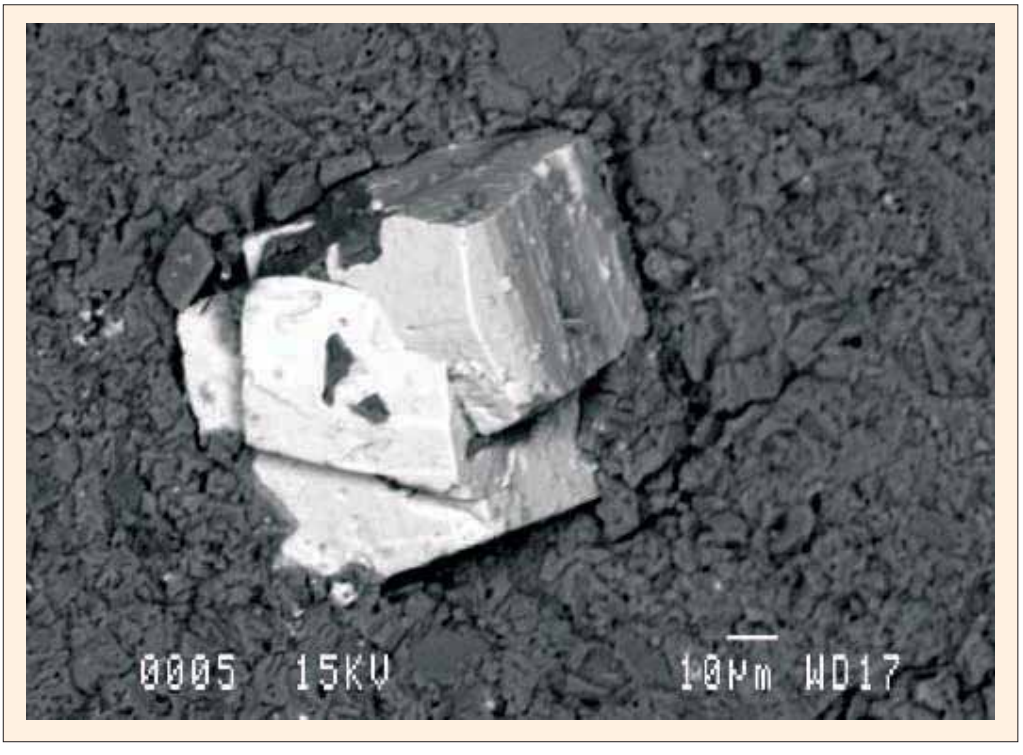

Fig. 6.9. Backscattered image of pyrite pseudomorph. The striated faces are typical of the precursor pyrite.

Coloured sediment admixtures of iron oxides and oxihydroxides may result from dedolomitization (Henrich and Zankl, 1986). The thrombolitic fabric of these sediments may also be indicative of dedolomitization. Petrographic evidence of dedolomitization in the paleokarst infills is only detected by SEM at micrometre scale and by CL observations as external rhombohedra rims that are totally dolomitized and as dolomite rhombohedra ghosts in spar mosaics.

Iron oxides and oxyhydroxides display close relations between dolomite rhombohedra pits and zones where dolomite and calcite patches coexist (Fig. 6.3, Plate 2: d, g). The yellow infills detected in the field show a large amount of poikilotopic calcite that includes iron hydroxides. Disperse fibrous and well crystallized hydroxides are commonly found in zones of intense dedolomitization and are thus localized in large calcite patches, whereas massive iron oxides tend to be found in zones of minor dedolomitization and minor calcite precipitation.

4.1.- Iron oxides

The precipitation of iron oxides (a group name for iron oxyhydroxides and oxides) such as goethite and hematite from ferryhydrite in aqueous media has been well documented (Fischer and Schwertmann, 1975), Jambor and Dutrizac, 1998). Ferrihydrite is always poorly crystalline or disordered. Thus, ferrihydrite is usually accompanied by a descriptive qualifier such as "2-line" ferrihydrite or "6-line" ferrihydrite according to its X-ray diffraction peaks. Ferrihydrite is rarely preserved in ancient samples because it commonly transforms into hematite on ageing, and to goethite in the presence of solutions containing Fe^{2+} (Jambor and Dutrizac, 1998). The transformation of ferrihydrite to hematite (at pH 7-8) and to goethite (at pHs 4 and 12) was experimentally observed at 24ºC (Schwertmann and Murad, 1983). Goethite precipitation reaches the highest rate when maximum activity of Fe(III) as $Fe(OH)^{2+}$ and $Fe(OH)^{4-}$ is attained at pH 4 and 12, respectively, whereas hematite precipitation coincides with the minimum activity of Fe(III) ions in solution at pH 8. These results suggest that goethite is formed from ferrihydrite by dissolution whereas hematite tends to be formed by internal rearrangement and dehydration within the ferrihydrite aggregates.

Factors which favor hematite formation from "2-line" ferrihydrite" over that of goethite have already been studied (Dousma et al, 1979; Schwertmann and Murad, 1983; Cornell and Giovanoli, 1987; Cornell and Schwertmann, 2003). At a pH close to zpc (zero point of charge), ferrihydrite is probably associated with its solubility minimum and this low solubility favours hematite formation versus goethite which tends to form via solution. The introduction of sulphate into the system promotes hematite formation and that of goethite on the addition of alkalis at high pH. In the ferrihydrite system, aluminium suppresses goethite, favouring hematite formation, and manganese inputs promote ferrihydrite dissolution, facilitating goethite formation.

Cornell and Schwertmann (2003) have reported the commonest habits of both hematite and goethite crystals using TEM, XRD and Mössbauer spectroscopy, and have documented

the differences in crystal morphologies and sizes according to different pH and temperature ranges. Hematite crystals are commonly rhombohedral, platy and rounded. Hematite grown from ferrihydrite in aqueous systems at temperatures <100ºC frequently forms hexagonal or subrounded plates with {001}. Goethite crystals display a wider range of morphologies depending on pH and temperature changes. The faster the growth and/or the larger the amount of impurities, the higher the growth rate of the acicular crystals. At an alkaline pH around 12, intensive hydrolysis promotes twinning of the goethite crystals. These goethite crystals grown in alkaline media commonly consist of parallel subunits called domains. Multidomainic crystals often display irregular ends with a series of well developed {210} faces. Multidomainic goethites are promoted by high ionic strength and low temperature (<40ºC). When the aluminium substitution increases in alkaline solutions, the multidomainic character decreases (Schulze and Schwertmann, 1984; Mann et al, 1985). Goethite twins usually consist of several "star-shaped" branches. Nucleation of twinned goethites in contrast to acicular habits occurs within ferrihydrite aggregates in the early stages of iron oxide precipitation. Star-shaped twins are only produced at high pH. The well defined faces of the goethite crystals could result from a retarded crystallization in the presence of silicium cations. Goethite grown in the presence of Si formed larger crystals (tens to hundreds of nm) whose shape varied from acicular to multidomainic (Glasauer et al, 1999).

The formation of pyrite via sulphate reduction bacteria (SRB) is well known despite several gaps in our knowledge. SRB consumes sulphate releasing H_2S as a by-product of metabolism. Whenever free Fe^{2+} cations are present in the environment, they can react and form FeS. Sulphate and organic matter as well as salinity and hydrostatic pressure are the main control factors of SRB activity (Jørgensen, 1982; Edenborn et al, 1987; Westrich and Berner, 1988). The rate of sulphate reduction decreases with the decline of carbon input, and is constrained at temperatures below 100 ºC (Trudinger, 1979; Canfield and Thamdrup 1994; Machel et al, 1995). Low to moderate salinities also favour microbial sulphate reduction, which takes place under anoxic conditions and concentrations of H_2S not exceeding 5% (Machel et al, 1995; Peters and Fowler, 2002). Sulphate can be derived from evaporite brines (pore water) and/or from the dissolution of solid calcium sulphate, either gypsum or anhydrite. The major sources of organic compounds are crude oil, microbial methane, thermogenic gas and/or gas condensate. The conversion of pyrite to iron oxides could be due to the infiltration of oxygenated meteoric waters during the uplift. Telogenetic alterations related to uplifting can also give rise to kaolinization of feldspars (Garcia et al., 1998; Morad et al., 2000).

4.2.- Iron oxides in the Rattlesnake Canyon samples

The variety of crystalline forms of iron oxides and oxihydroxides in Rattlesnake Canyon detected by SEM and TEM suggests different mechanisms for the generation of the coloured paleokarst infills. Hematite (α-Fe_2O_3) and goethite (α-FeOOH) were identified in different proportions in the coloured karst samples from Rattlesnake Canyon. Subsequent analysis confirmed that red samples contained mainly hematite whereas yellow samples were

characterized by the presence of goethite. These coloured samples comprise karst infills of both, fracture caves and stratabound caves (see Chapter 4 for field description). Their study and analysis deserves special attention because their crystal morphologies and chemical nature are a reflection of their conditions of formation in the geological environment. Microbial textures, which are usually associated with stromatolitic laminae, are rare and are mainly preserved in the uppermost parts of the paleokarst, whereas iron oxides commonly display a clotted microstructure in the other parts. The intimate relationship between dolomite rhombohedra and these organically derived microstructures as well as iron oxide pseudomorphs after pyrite suggest that the dolomite rhombohedra were probably modified by bacterial sulphate reduction. Hollow dolomite rhombohedra observed under SEM could be attributed to dissolution driven by BSR. Iron oxide pseudomorphs after pyrite are found in the form of hematite, although well crystallized acicular goethite crystals do not rule out the possibility of two mechanisms for the origin of iron-bearing minerals: sulphate reduction and direct precipitation from ferrihydrite.

The proportion of hematite in the karstic infills of the Rattlesnake Canyon paleokarst is much higher than that of goethite. Hematite observed by TEM displays hexagonal plates with sharp crystal faces with an average size of 1 μm (Figure 6.10: a) with the exception of multidomainic hematite crystals in some aggregates with goethite (Figure 6.10: b). Despite the large number of of hematite crystals, goethite exhibits a wide range of crystal habits. Goethite crystals are smaller than those of hematite and range from tens to hundreds of nm. Goethite crystal shapes vary from acicular to multidomainic and even, in some areas, monodomainic goethite crystals are affected by hydrothermal alteration (Figure 6.10: d). This hydrothermal episode is linked to the origin of dickite in the area. Multidomainic goethite crystals grow preferentially in the directions of the crystallographic axes c and b, which is distinctive of goethite growth in alkaline conditions and low temperatures (Figure 6.10: c and f) (Lewis and Schwertmann, 1980). Star-shaped twinning are frequently reported as early stages of goethite precipitation under alkaline conditions (Cornell and Schwertmann, 2003) (Figure 6.10: e). The variety of goethite crystal shapes identified in Rattlesnake Canyon also helps us to constrain the conditions of precipitation of this mineral from ferrihydrite. The persistent hexagonal habit of hematite helps to constrain the conditions of precipitation of this mineral at low temperatures and pH around 7-8. The variability of crystal forms and twinning of goethite constrains the conditions of goethite precipitation at low temperatures and pH >10.

Hydrothermal alteration is also observed locally in isolated pockets and is well determined by the monodomainic plates of goethite with smooth boundaries (Figure 6.10: d). This type of crystal commonly reveals signs of hydrothermal activity and is a better indication of high temperature events than crystal habits of hematite under the same conditions.

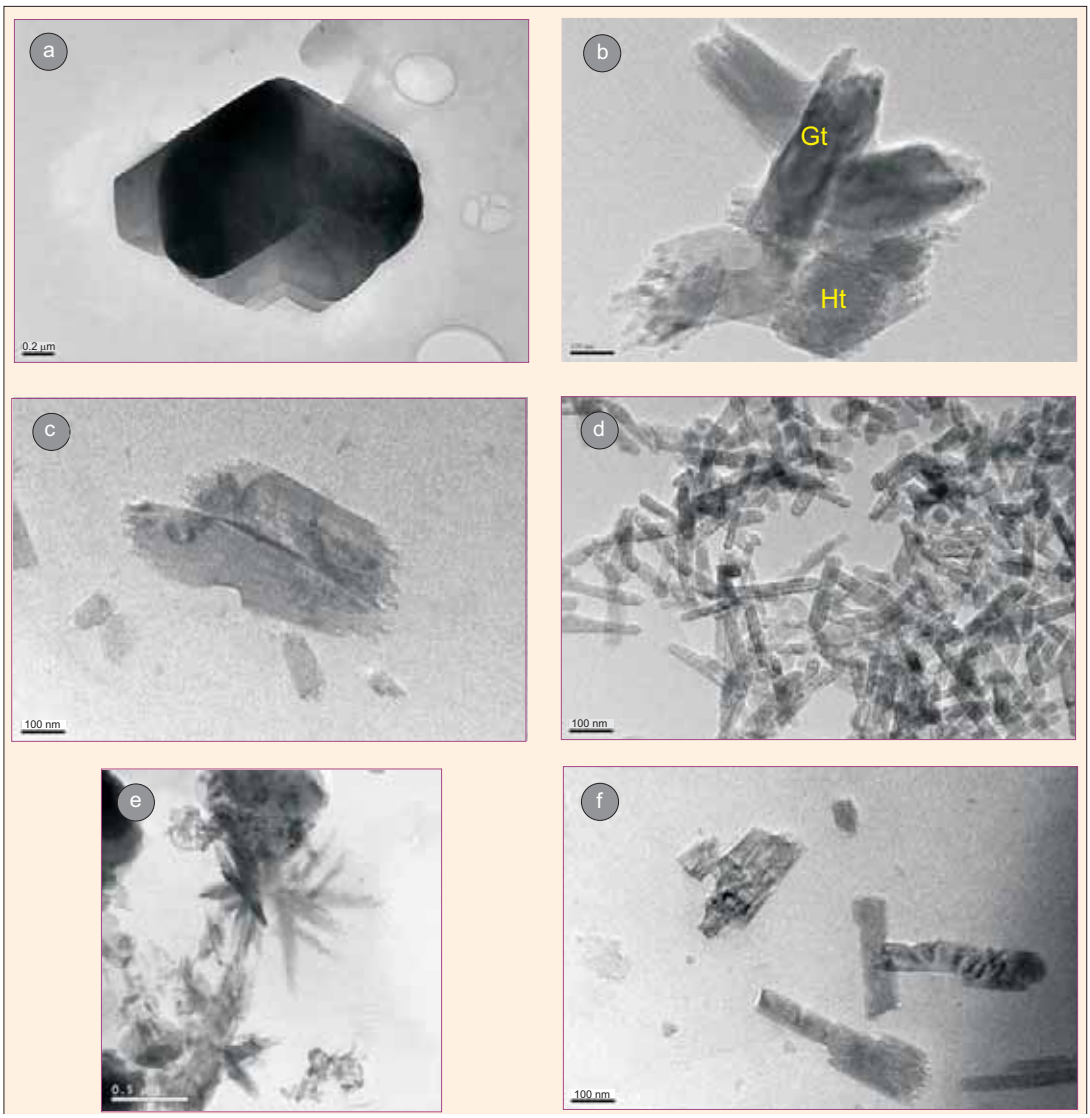

Fig. 6.10. TEM images of the iron oxides recognized within the Rattlesnake Canyon paleokarst infills. Situation of the samples is shown in Fig. 6.1. a)Hexagonal plates of hematite. Sample 81. b) Aggregate of plydomainic crystals of goethite (Gt) and hematite (Ht). Polydomainic hematite crystals have been reported from experimentaly precipitation from Al ferrihydrite at room temperature (Scwertmann et al, 2000). Sample 289. c) Polydomainic serrated crystals of goethite. Sample 289. d) Monodomainic goethite crystals commonly related with hydrothermal transformations. Sample 277. e) Star-shaped geoethite crystals. f) Multidomainic goethite crystals growth along c crystallographic axis but also increased width along b axis. Sample 289.

5.- Trace elements

5.1.- ICP data

Replacive dolomite samples within the karst and dedolomite fracture fills shows the following mean ICP concentration values, respectively: 1600 and 500 ppm Fe, 220 and 100 ppm Mn. Karst affected host rock has 130 ppm Mn. Karst dolomites show low Sr concentrations (~ 53 ppm Sr in average). Dolomite cements present higher Fe and Mn mean

concentrations (about 2220 and 270 ppm, respectively). In contrast, calcite cements have low mean concentrations of Fe (30 ppm) and Mn (70 ppm).

5.2.- Microprobe results

Microprobe analysis was used to analyse Fe and Mn contents (sometimes under the limits of detection) of the dull spar cements, the dedolomite cements and the thermal spar. These components show Fe concentrations ranging from 100 ppm to 0 ppm. By contrast, the replacive dolomite rhombohedra show concentrations exceeding one order of magnitude (1000 ppm Fe). Thermal spar has concentrations of Mn ranging from 100 to 300 ppm, similar to those analyzed by the same method in the dedolomite cements.

5.3.- Trace element distribution in Rattlesnake Canyon

Sr contents of the karst replacive dolomite are relatively low, ranging from 25 to 91 ppm. However, karst materials display a slight strontium increase in the non karstified host rock. Both coloured dolomite sediments and dedolomite cements present the highest strontium concentrations (54 and 84 ppm respectively) compared with 46 ppm of the unaffected karst carbonate. Sr contents are not significant in the adjacent host rock (Table 6.3).

Chemical analyses reveal that the concentration of Mn increases significantly in areas affected by karst dissolution. Dolomite cements also show high concentrations of Mn (269 ppm) compared with the unaffected host rock (42 ppm). Dispersion of Mn contents is high both in the karst and the adjacent karst affected areas. The process is therefore not homogenous but varies locally in the karst area (Table 6.3).

Na content generally decreases in the karst area due to dissolution. Dolomite and calcite cements are significantly depleted in Na whereas dedolomite and coloured dolomite sediments are rich in Na. The unaffected host rock exhibits the highest Na content (500 ppm).

A significant increase in Fe is detected in the karst area and in the dolomite cements. Fe shows high concentrations in the karst, but although its mean is not significant in the adjacent host rock, its dispersion is. Mn has a similar behaviour.

6.- Stable isotopes

Carbon and oxygen isotope compositions of bulk samples and individual microdrilled components range from -14.8‰ to +2.3 ‰ $\delta^{18}O$ and -15.6 ‰ to + 7.7 ‰ $\delta^{13}C$. Adjacent host rock dolomites range in $\delta^{13}C$ from +4.14 to +7.73 ‰ and in $\delta^{18}O$ from -0.58 to +2.37 ‰. Replacive dolomite within the paleokarst area show stable isotope values ranging in δ13C from -0.3 to +6.95 ‰ and in $\delta^{18}O$ from -5.02 to +2.04 ‰. The lowest values of $\delta^{13}C$ correspond to samples associated with stromatolitic structures with possible organic matter. Stable isotopes from void-filling dolomite and interpisoid cements in grainstones range in $\delta^{13}C$ from +3.25 to +7.21 ‰ and in $\delta^{18}O$ from -3.14 to +1.78 ‰. Stable isotopes from calcite

	Avg Sr (ppm)	Range	σ	Avg Mn (ppm)	Range	σ	Avg Na (ppm)	Range	σ
Karst replacive dolomite n = 34	54	(25-91)	15.53	215	(55-432)	102.40	427	(216-1240)	204.23
Calcite cements n = 7	68	(48-85)	13.11	88	(3-194)	55.32	198	(58-498)	139.06
Dolomite cements n = 4	36	(28-45)	6.98	269	(44-531)	127.42	140	(46-285)	89.55
Dedolomite cements n = 6	84	(53-139)	26.54	106	(12-215)	72.31	354	(77-895)	307.11
Adjacent Host Rock n = 31	44	(15-92)	22.05	133	(21-510)	113.04	401	(161-897)	200.79
Unaffected Host Rock n = 6	46	(36-73)	12.23	42	(26-68)	13.22	506	(289-738)	164.91
	Avg Zn (ppm)	Range	σ	Avg Fe (ppm)	Range	σ			
Karst replacive dolomite n = 34	18	(8-58)	11.98	1620	(486-6390)	1075.02			
Calcite cements n = 7	8	(6-10)	1.37	30	(8-85)	24.16			
Dolomite cements n = 4	10	(8-11)	1.28	2220	(774-4190)	1479.98			
Dedolomite cements n = 6	17	(8-38)	10.05	495	(34-1390)	505.60			
Adjacent Host Rock n = 31	13	(7-40)	6.58	702	(173-1480)	395.22			
Unaffected Host Rock n = 6	27	(9-99)	32.29	731	(442-1250)	271.54			

Table 6.3. Trace element composition of the studied components.

in voids and fracture fillings inside the paleokarst area range in $\delta^{13}C$ from -15.64 to -0.42 ‰ and in $\delta^{18}O$ from -9.80 to -4.22 ‰. Stable isotopes from dedolomite correspond to altered dolomite cements described above and range in $\delta^{13}C$ from -14.03 to +4.69 ‰ and in $\delta^{18}O$ from -10.97 to -6.95 ‰.

Stable isotope values for the marine Yates formation fall within the box in Fig. 6.11. Although most values of the replacive dolomite and adjacent host rock fall within the field of marine Yates (Hill, 1996), a notable feature in the plot is the slight deviation of the dolomite cements towards more negative values of oxygen and constant carbon values. The majority of the stable isotope values of the calcite and dedolomite cements that precipitated in the karst tend to encompass the most negative isotopic values of both carbon and oxygen. As regards the cements, three subzones were identified in the dedolomite cements in accordance with its luminescence, and plotted separately following a sequence. Zone 1 in dedolomites (Dd1) shows low negative carbon and oxygen values whereas Zones 2 and 3 (mixed because of the impossibility of separation by microsampling) tend to move progressively towards more negative values (Fig. 6.11).

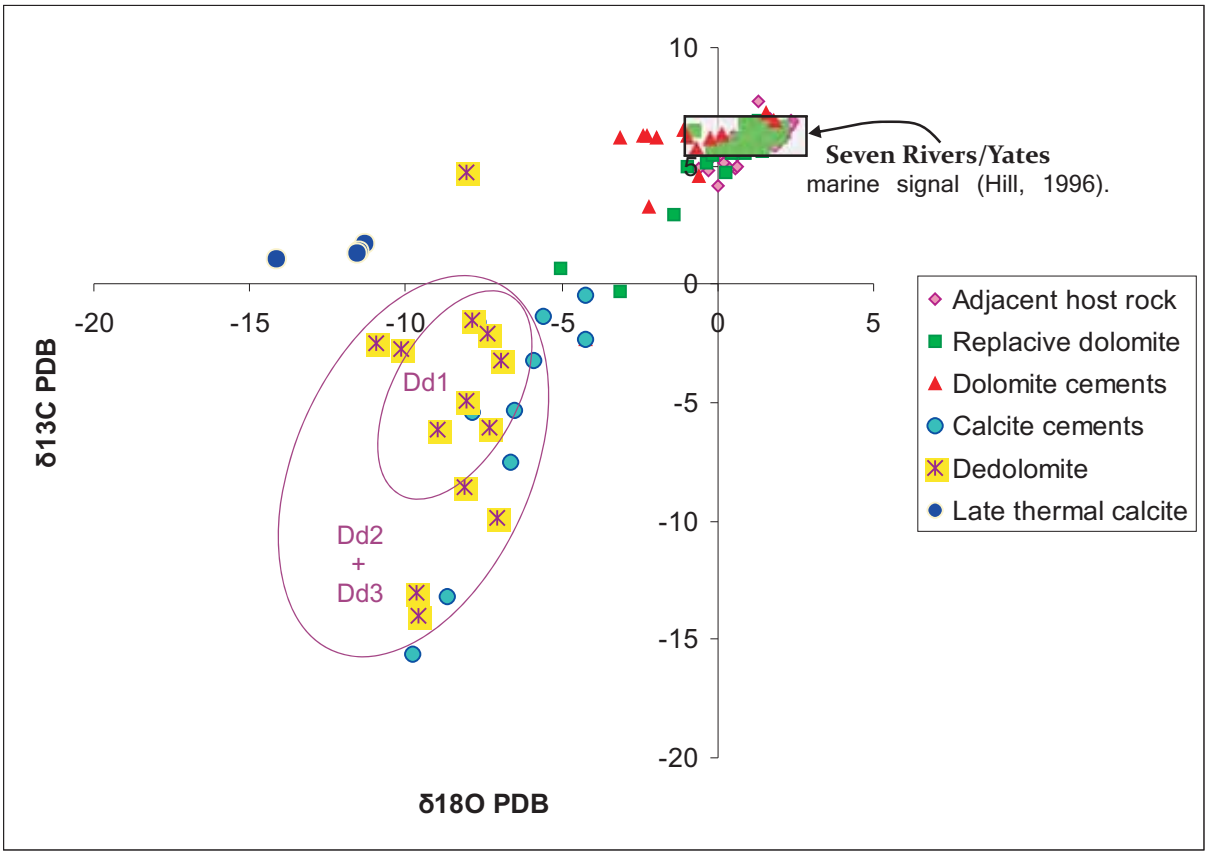

Fig. 6.11. Oxygen and carbon stable isotopes for individual components from Rattlesnake Canyon samples. The samples display a classic trend of mixing between brine, marine and meteoric values. Dedolomite subzones (Dd1, Dd2 and Dd3) indicate increasing meteoric ratios from Dd1 to Dd3. Karst cements underwent progressive water-rock interactions. Seven Rivers-Yates carbon-oxygen isotopic values reported by Hill (1996) are enclosed in the black box. Adjacent host rock values include the carbonate non-karstic host rock samples whereas replacive dolomite values comprise the dolomitic samples within the karst zone.

7.- Patterns of cementation in relation to hydrogeological regimes

Cementation patterns differ markedly from zones of isolated vugs to fracture zones. Sequences of cementation in areas of restricted circulation show multiple and numerous stages of cementation as syntaxial overgrowths, whereas in higher-rate dissolution areas (usually fracture zones) cementation is significantly constant and always associated with corrosion events.

The limited range of the karst cements identified in the samples from Rattlesnake Canyon contrasts with the complexity of their arrangement. However, we can infer that the patterns of cementation are mainly controlled by Eh and, to a lesser extent, by pH fluctuations, which were basically controlled by the paleo-hydrogeological regimes.

7.1.- Dolomite cements

Syntaxial overgrowths and pore-filling dolomite are best developed when forming sucrosic dolomite and when lining cavities that overlie the early replacive dolomite before the sequence is completed (Fig. 6.3, Plate 1: h). These cements totally occlude porosity in vug-filling sequences and when forming indurated dolomite frameworks (Fig 6.4: b). Syntaxial overgrowths are very well preserved in samples located at the top of the karst where they have been preserved from faulting. Nevertheless, they can be found in the karst, in non fractured and/or brecciated areas involving a more restricted circulation of fluids and presumably indicating cementation from pore waters. Syntaxial overgrowths and pore-filling dolomite cements contain multiple luminescent zones that have well defined contacts and lack evidence of dissolution episodes. The latest bright yellow and red episodes detected by CL seem to be repeated regularly throughout the karst affected area within isolated vugs of the same characteristics (Fig 6.4: a, c2). The first stage of precipitation seems to involve a dull episode that is not everywhere preserved. This CL pattern shows dolomite mineralogy. The stable isotope signal of this sequence of cementation is represented by the dolomite cements in Fig 6.11 which shows a slight shift towards lighter values of $\delta^{18}O$ when compared to the constant range of values of the replacive and adjacent host rock.

The complicated CL patterns of the dolomite cements show cyclicities of cement precipitation. The cycles display regular and sharp borders with no dissolution episodes but fluctuations in Eh. Cement overgrowths and pore-filling dolomite cements that are mainly bright luminescent suggest evolving reducing conditions for the parental fluid. Red dolomite cements overlie yellow cements and display complicated patterns of sectorial zonations, indicating an increase in reducing conditions given the ferroan nature of the last dolomite cement. The pattern seems to follow the petrographic sequence of Choquette and Hiatt (2008), which explains the textural evolution of dolomite in the shallow-burial environment. The sequence accounts for the initial coarsening of dolomite owing to the growth of the corticles around the nuclei followed by the cement overgrowth which confers a solid architecture to

the rock texture. The process ends with the final occlusion of the pore system by the same cementation process (Fig. 6.12).

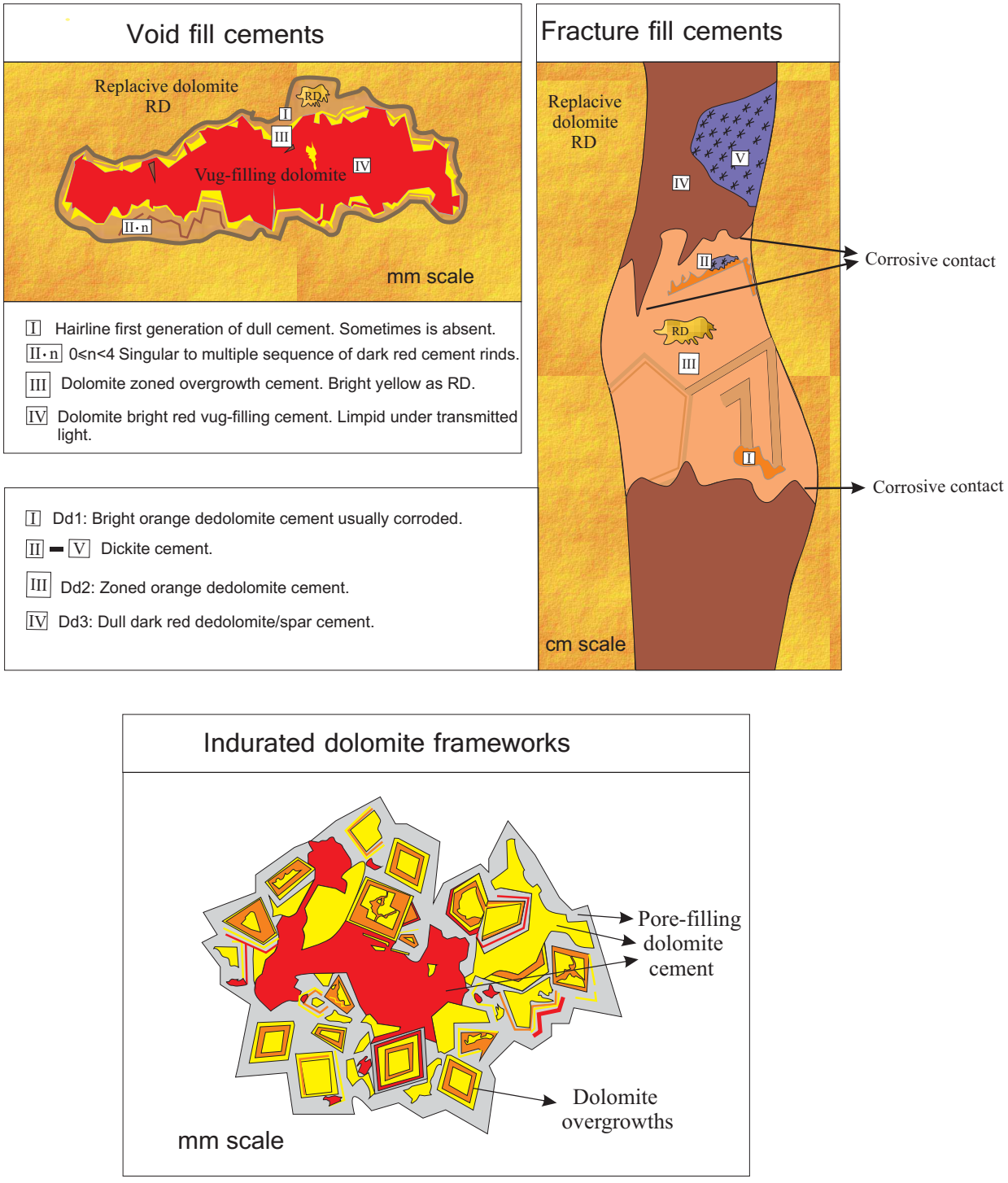

Fig. 6.12. Cathodoluminescence model of the sequences of cementation observed in voids, fractures and pore-filling cements. Void filling cements start with different dolomite rinds and overgrowths with bright luminescences to end up with a blocky bright red vug-filling cement totally occluding the porosity . Fracture fill cements are made up of three different generations of dedolomite cements I, II and IV(Dd1 Dd2 and Dd3 in the text). Calcite content (>50% wt) increases from I to IV in the fracture fill sequence. Indurated dolomite frameworks originate from textural maturation of sucrosic dolomites resulting in limpid planar-s to nonplanar-a (transitional) textures under transmitted light.

This pattern shares some features with the replacive Dolomite B and its associated dolospar documented by Melim (1991). Petrographic descriptions are fairly similar to those of Melim despite the greater abundance of these cements in the Rattlesnake Canyon samples. By contrast, the Fe content of Melim's samples (forereef setting) differs from that of the dolomite cements reported in the present study. Moreover, an isotopic shift to more depleted $\delta^{18}O$ (~ 2 ‰) is also detected in both locations. Dolomite overgrowths configure a solid architecture, providing indurated dolomite frameworks with multiple overgrowths evolving to pore-filling cement sequences. Thus, the pattern with multiple and repetitive cycles of the same luminescence is herein interpreted as a complete evolving transitional sequence of former multiphased sucrosic dolomite to dolomite pore-filling cements. The zoned rhombohedra commonly show turbid cores with luminescences identical to those of replacive dolomite, which indicates growth by accretion of cortices from remnants of the former replacive dolomite. The pore-filling cements show a probable correlation with cortical stages and appear limpid under transmitted light.

7.2.- Calcite and dedolomite cements

The sequence of precipitation in the fracture zones is dominated by calcite and dedolomite cements and differs from the indurated dolomite frameworks and void-filling dolomite. Calcite is usually found associated with goethite in yellow stratabound karst infills. These areas are related to interpreted halocline paleopositions which gave rise to mosaic breccia deposits beneath fracture zones, indicating high dissolution rate areas (Chapter 4). Two types of cement generations are distinguished in fracture zones by their luminescence patterns and correspond to mosaics of dedolomite cements. Dickite is usually present in the corroded contacts of these zones, and corroded carbonate is attributed to acidic conditions linked to kaolinite/dickite precipitation. Dedolomite is extremely heterogeneous in CL exhibiting diverse cement zones with different luminescences. Zone 1 (Dd1) corresponds to a bright orange dedolomite. Zone 2 exhibits darker orange dull luminescences (Dd2) and Zone 3 (Dd3) is non luminescent and presents calcite mineralogy without any observable ghosts of former dolomite.

All these zones are arranged in a complex pattern of sector and concentric zonations that clearly reflect changes in fluid composition. There is evidence of corrosion at the contacts of the zones, suggesting fluctuating levels in calcite saturation during calcitization and precipitation of dull to non luminescent calcite cement. Dedolomites show partial replacement of the former dolomite mineralogy (>50% calcite). The isotopic composition of these cements undergoes a decreasing trend of $\delta^{18}O$ and $\delta^{13}C$, indicating an increase in water-rock ratios towards more depleted values.

A first generation of dolomite cements is interpreted to be altered to dedolomites by the action of meteoric fluids possibly mixing with dissolved sulphates. The input of the meteoric

fluids led to an imbalance of the Eh conditions, producing the transition to Dd2 and Dd3 as the fluid became diluted and showed progressive calcitization.

Cc1 occurs as a fracture-fill component in larger and probably interconnected paths for oxygenated fluids.

Dedolomites and calcite cements are made up of non-ferroan and dull to non-luminescent cements indicative of moderately oxic environments, whereas indurated dolomite frameworks and void-filling dolomite consist of ferroan and bright cements, suggesting suboxic environments. The relationship between both cementation sequences was not detected in any sample as they did not show any clear cross-cutting or petrographic association that could define their paragenetical evolution. The shift of the dolomite cements towards more depleted values of $\delta^{18}O$ would reveal precipitation of these cements during shallow burial, indicating a temperature increase between the replacive dolomite and the dolomite cements. These sequences are shown in Figure 6.12. Dedolomitization is confined to open flow areas and dark dull to non-luminescent calcite to areas of meteoric flushing. The contacts between subzones of the dedolomite cements are sharp, displaying concentric and sectoral zonations with evidence of dissolution between contacts.

7.3.- Dickite cements

The kaolinite domain is restricted to sandstones buried at <2000 m and these are gradually replaced by dickite below 2500 m. The temperature, in addition to the large water/rock ratio, enhances the development of dickite (Whitney, 1990) and, as a result, increases petrophysical porosity and permeability, favouring kaolinite 'dickitization' (Kisch, 1983). Conversely, high values of hydrocarbon saturation inhibit the kaolinite-to-dickite reaction when compared with samples of the same depth interval inside the water zone, where 'Dickitization' developed without restriction (Lanson et al., 2002).

Dickitization of kaolinite is a dissolution-precipitation process that occurs in pore waters with low $a K^+/a H^+$ ratio; otherwise illite forms (Ehrenberg et al, 1993). Low $a K^+/a H^+$ ratio in pores can be achieved through the input of acids derived from organic matter. CO_2, H_2S and organic acids resulting from the microbial oxidation of the hydrocarbons at shallow depths can create reducing, slightly acidic conditions conducive to feldspar dissolution. Subsequently, this process may lead to the conversion of illitic clays to kaolinite.

Kaolinite-to-dickite transformation has usually been described as a high temperature reaction with the result that many authors have therefore ascribed dickite to burial diagenesis or hydrothermal activity (Ehrenberg et al.,1993; Parnell et al., 2000; Parnell, 2004; Lanson et al., 2002; De Bona et al, 2008). The paragenetic time of dickite in the Guadalupe Mountains is still unknown although the dickite studied in Rattlesnake Canyon is always found postdating dissolution episodes and unequivocally associated with feldspar diagenesis (Fig.6.3, Plate 2: e, f). Because thermal coarse spar postdates dedolomite/calcite sequences associated with

dickite, it is interpreted that dickite formation results from hydrothermal alteration of former kaolinite. Dickite is also found coated with red Fe oxide in some areas, indicating that Fe mobilization was partially coeval with the clay genesis (Fig. 6.13). Kaolinite in Rattlesnake Canyon is thought to form as a consequence of transitional acidic conditions, interrupting the precipitation of the dedolomite/calcite sequence in high-rate dissolution areas. Corroded boundaries of Dd2 and Dd3 thus originated during intermittent episodes of hydrocarbon recharge. Subsequent Miocene hydrothermal activity facilitated the kaolinite-to-dickite polymorphic reaction. This is why dickite is not associated with the coarser thermal spar; rather it is a product of the alteration of former clays. The preservation of the booklets is also an indicator of shallow depth conditions associated with thermal pulses along the faults.

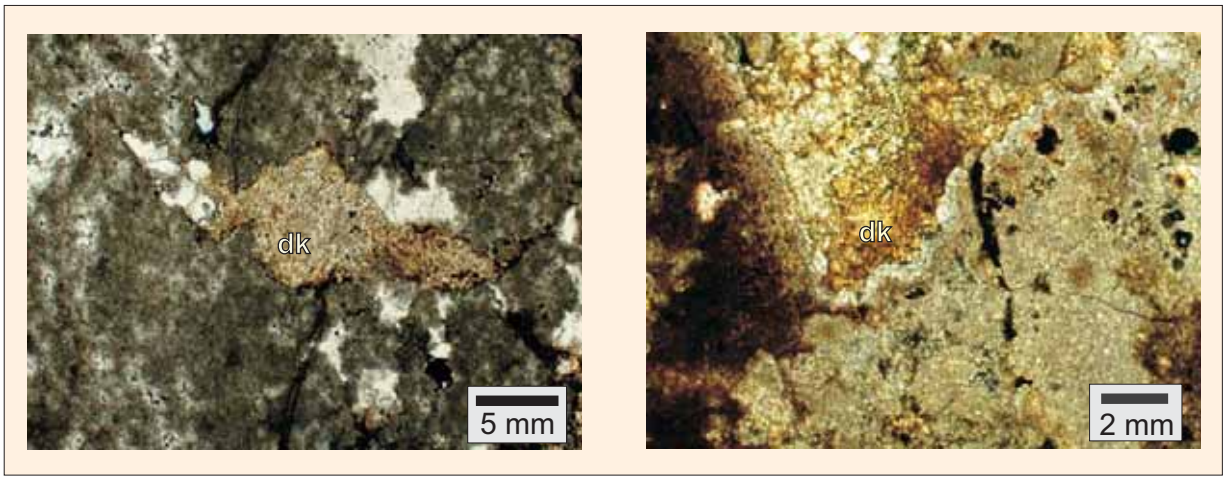

Fig. 6.13. Dickite cement (dk) stained by iron oxides.

In Rattlesnake Canyon, dickite cements are regularly associated with dedolomite cements and spar, which present hydrocarbon inclusions. Thus the patterns of zonations that result from Eh transitions are interpreted to be linked with microbial activity owing to the presence of hydrocarbons. Primary and secondary fluid inclusions contain hydrocarbon (Fig. 6.14), thereby indicating that these cements are coeval with the hydrocarbon recharge. The same characteristics play a role in the distribution of hydrocarbon fluid inclusions in the coarser thermal spar. Although thermal spar is not associated with dickite cements, it shows the same range of trace element values of the dedolomite/calcite sequences (Appendix 2, Table II). The main differences between these two types of cements lie in the size of the thermal spar crystals (up to cm), which are significantly coarser, and in its isotopic signal, which clearly differs from the lower $\delta^{13}C$ and $\delta^{18}O$ values of the dedolomite/spar cements. In addition, thermal spar does not display poikilotopic textures embedding iron-bearing oxides. Dedolomites and spar cements with low $\delta^{13}C$ values are related to microbial oxidation of the hydrocarbons whereas thermal spar has typical $\delta^{18}O$ isotopic values of hydrothermal activity. Another criterion for the discrimination between dedolomites and thermal spar is based on petrographic observations: thermal spar is regularly recognized overlying dedolomite sequences.

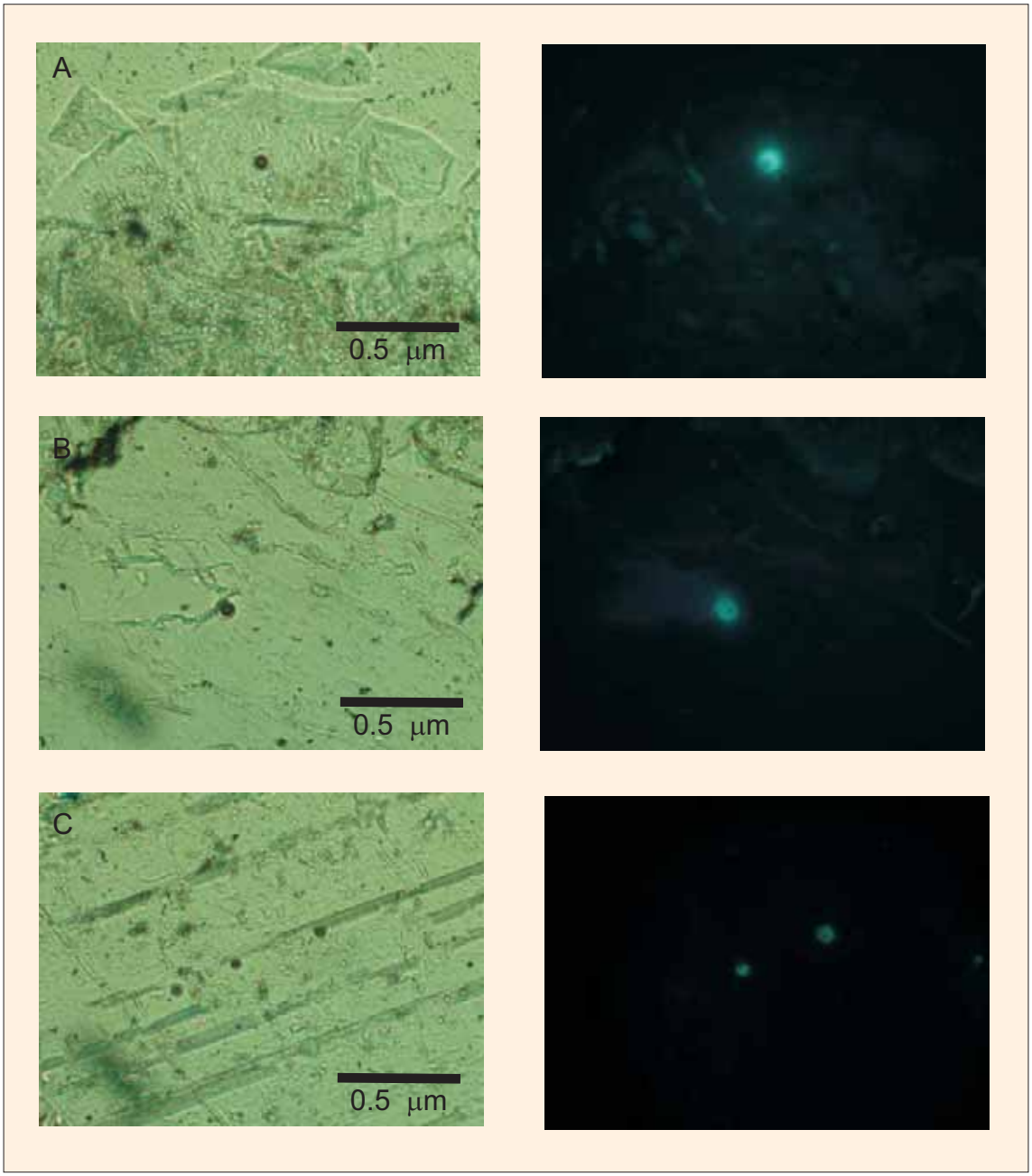

Fig. 6.14. Hydrocarbon-bearing fluid inclusions of the carbonate cements (thermal spar and calcite). The inclusions show two phases of probably oil and gas. Hydrocarbon fluid inclusion in the calcite cement of photograph A appear to be as primary origin, whereas in C the alignment pattern suggests secondary origin for the trail of the thermal spar. The photographs on the right show the UV radiation characteristic for the entrapment of organic matter.

7.3.1.- Indirect indicators for the formation temperature of dickite.

The hydroxil-stretching band in the infrared spectra of the dickite identified in Rattlesnake Canyon shows maximum peaks at 3703, 3652 and 3621 cm^{-1} (Fig. 6.6). The position of the studied dickite peaks is compatible with the model of Beaufort et al. (1998) for a maximum burial depth of 3500 m. Thus, we can estimate a minimum temperature for dickite formation of approximately 100 ºC (assuming 30ºC/km) not produced by an increase in burial depth but

by hydrothermal fluids. Considering that Yates karstified Formation underwent a maximum burial depth close to 750 m, in accordance with the subsidence curve of the zone (Fig. 6.15), we can propose a temperature close to 100ºC at this depth. This temperature is sufficient for the complete transformation kaolinite-dickite, which normally occurs at temperatures over 75ºC. Within the 2500- 4000 m depth range, this reaction is fed by detrital feldspar and mica dissolution and is accelerated when accompanied by hydrocarbon fluids (Lanson et al., 2000).

8.- Paragenesis

Assuming that karst initiation took place during eodiagenesis (Chapter 4), early limestone and siliciclastics filled the karst sequence during its development. Geochemical results show that the karst sediments and cements underwent enrichment in Mn, Fe and K. Enrichment of Fe and K consists respectively of mineral precipitation of iron oxides and dickite cement whereas Mn is incorporated into the carbonate structure. Meteoric leaching releases Fe, and Mn from the siliciclastics and from the dissolution of the early replacive dolomite.

The early replacive dolomite was modified or replaced by subsequent processes of cementation by reducing pore waters. This is deduced from CL observations that show early replacive dolomite within the karst with homogeneous bright yellow luminescence owing to its Mn content. Mimetic replacement of the early marine cements indicates that this process took place before the inversion from aragonite to calcite, or from low magnesium calcite to high magnesium calcite. The non-karst-affected host rock show bright red luminescences. Thus, the karst displays a positive anomaly in Mn probably generated by episodes of reducing pore fluid cementation and modification of the replacive dolomite presumably during mesodiagenesis as stylolites are cemented by the same ferroan dolomite cements (Fig. 6.7). Replacive dolomite cores are bounded by syntaxial overgrowths during the construction of indurated dolomite frameworks (Fig. 6.4: b). These dolomite cements have lower Sr and Na concentrations (Table 6.2), which suggests an origin unrelated to the Ochoan evaporites dissolution but sets them in an early shallow stage of the diagenetic history in line with the textural evolution of Choquette and Hiatt (2008). There is some uncertainty about the time when evaporites began to dissolve but some authors have dated this dissolution episode to the Tertiary uplift (Melim, 1991; Scholle et al, 1992). Maximum burial occurred towards the end of the Permian and the area remained quiescent until the Tertiary uplift (Fig 6.15). Constraining syntaxial overgrowth and limpid dolospar precipitation to the burial history leads to the formation of these cements in the Upper Permian at shallow depths because the area underwent a maximum estimated burial of 1 km. The $\delta^{13}C$ values of these cements suggest that there were no significant amounts of organic matter during this phase. The carbon signal was buffered by the Yates dolomitization.

Sulphate-reducing bacteria (SRB) by-products now oxidized are recognized as iron oxide pseudomorphs after pyrite and as poorly crystallized framboid-like morphologies embedded within dolomite crystals (Fig. 6.3, Plate 2: d). The pattern on the dolomite crystals reveals hollow

dolomite that could reflect the dissolution of the dolomite sulphate inclusions. Release of the sulphate coupled with the hydrocarbon emplacement probably created a suitable environment for sulphate-bacteria reduction. This could account for the coloured dolomite rhombohedra cores confined to dolomite rhombohedra pits when observed by SEM. Some peaks of S in EDS spectra are recognized in samples with stromatolitic structures and pyrite pseudomorphs with pseudo-spherules occupying dolomite pores. Furthermore, the pattern of the dedolomite cementation observed by CL and trace element content suggest relatively sharp and cyclic transitions of Eh from sub-oxic to moderately oxic conditions. In line with these observations, the sequence is interpreted as a progressive evolution towards a more hydrous oxic media with associated calcitization. Release of Fe from the former carbonates and siliciclastics is associated with kaolinitization when the area was charged by hydrocarbons. Release of Fe from the acid leaching of the siliciclastic fraction and from the former carbonates would be favourable for iron-oxide precipitation and oxidation. This episode could occur during the regional uplift where the entrance of oxygenated meteoric water possibly mixed with CO_2 rich fluids triggered by the migration of the hydrocarbon in the area. The varying ratios of mixing with fluids of different origin (evaporite dissolution, meteoric flushing and HC recharge) probably led to the dedolomitization and precipitation of light $\delta^{13}C$ calcite.

Iron hydroxy-oxide (goethite) and oxide (hematite) precipitation postdates the syntaxial and pore-filling dolomite cementation since these oxides are emplaced within dolomite pores and are found cross-cutting dolomite crystals as well as occupying intercrystalline positions (Fig 6.3, Plate 2: d). Hematite can be precipitated by a neutral and slightly basic fluid (pH 7-8) whereas multidomainic goethite is known to precipitate by more basic fluids in a pH range from 8-12 (Cornell and Schwertmann, 2003). The close petrographic relationship of goethite and calcite reveals that goethite precipitated when the fluid was buffered by a high concentration of CO_3^{2-}. The presence of goethite with well-developed crystal faces indicates that goethite crystals grew followed by poikilotopic calcite precipitation (Figure 6.3, Plate 2: g). Given that part of the hematite does not result from pyrite oxidation, hematite could also have formed by direct precipitation with goethite in aggregates (Fig 6.10: b).

The characterization of high and low temperature iron hydroxide crystalline forms points to the fact that precipitation of iron oxy-hydroxides ended before the cessation of hydrothermal activity. None of the coarse thermal calcites contain any iron oxy-hydroxide but some of the identified dedolomites and calcites embed well crystallized acicular forms of goethite (Fig. 6.3, Plate 2: g). Iron mobilization therefore occurred during the charge of the hydrocarbons and was probably connected with the acid leaching of siliciclastics and kaolinitization. Precipitation of goethite occurred during basic conditions as indicated by the multidomainic crystalline forms and was thus associated with dedolomite/spar cementation. Hematite crystals embedded in the dolomite rhombohedra could be products of oxidation of precursor sulphate-reduction pyrite.

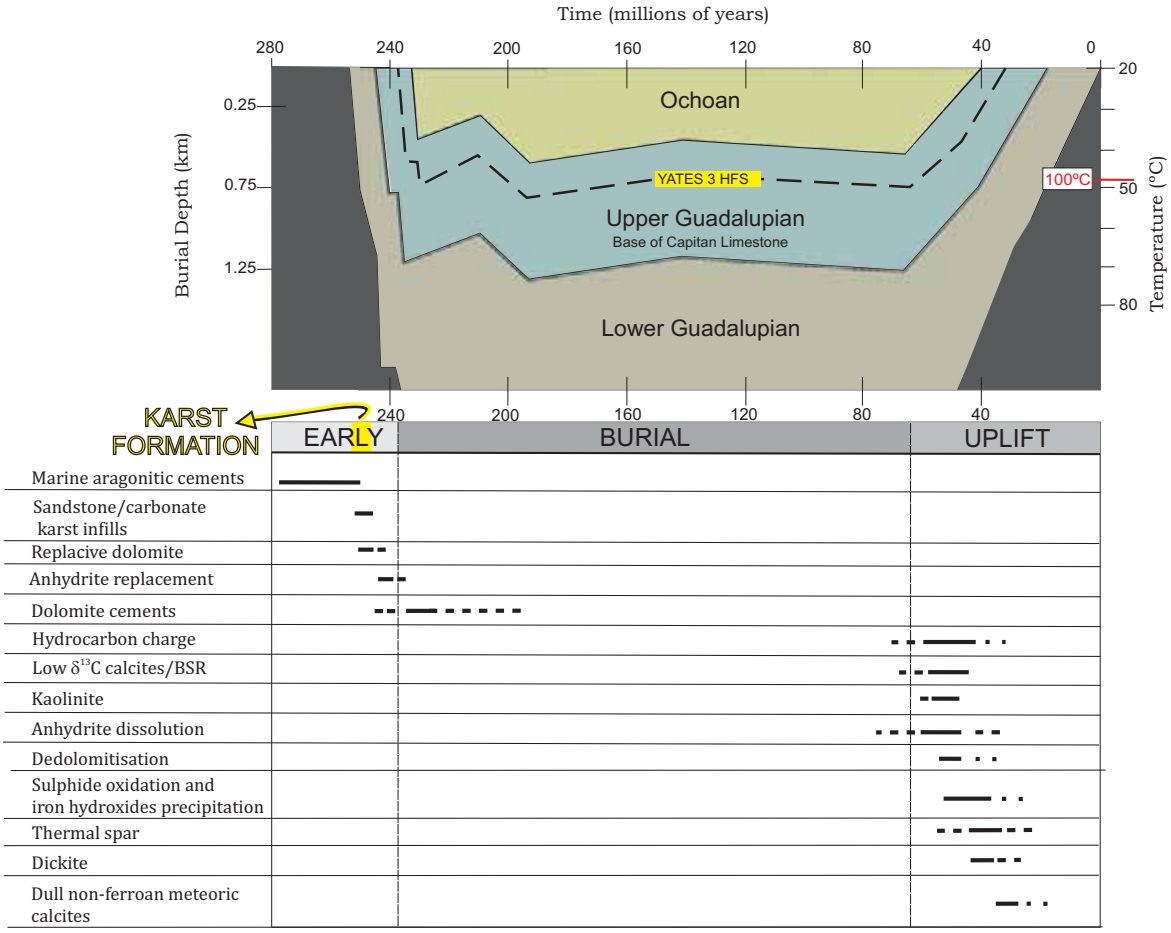

Fig. 6.15. Paragenetic sequence. The sequence is represented together with the burial and thermal history of the Noethwestern Shelf region of the Delaware Basin. The diagram is adapted from Hill (1996). Burial depths are calculated from PDB-04 well thicknesses based on Scholle et al. (1992). Yates 3 HFS subsudence curve is inferred from the total thickness of the Upper Guadalupian stratigraphic section. Temperatures assume modern geothermal gradients (± 5ºC). Temperatures during Permian to Cretaceous presumably were higher and could underwent a significant increase triggered by the volcanic intrusion during the Tertiary. The thermal gradient increased during the uplift phase in the Tertiary and temperaure of 100ºC during that time is indirectly deduced by the FTIR peaks position of the studied dickite according to the burial curve of Beaufort et al. (1998).

9.- Mechanisms for dedolomitization

It is commonly suggested that dedolomitization is related to flushing of meteoric waters and dissolution of gypsum/anhydrite (Goldberg, 1967; Folkman, 1969; Warrak, 1974; Hanshaw and Back, 1979; Back et al., 1983; Lee and Harwood, 1989; Kenny, 1992; Bischoff et al., 1994; Arenas et al., 1999; Sanz-Rubio et al., 2001; Fu et al., 2008).

The low $\delta^{13}C$ values of the dedolomite (until - 15‰ in the study area) could be interpreted as resulting from fresh groundwater mixed with CO_2, H_2S and organic acids derived from bacterial sulphate reduction (BSR) (Deines et al., 1974; Sanz-Rubio et al., 2001). Moreover, sulphate solubility is enhanced by a factor of 1.56 when coupled with the dedolomitization reaction, and presumably its rate of dissolution is also accelerated (Bischoff et al., 1994).

In Rattlesnake Canyon, dedolomitization of the dolomite cements might have diminished or ceased when sulphates were completely removed or when there was no longer significant invasion of meteoric waters into the paleokarst. The preferential occurrence of dedolomite along fractures and adjacent areas as fracture/void-filling calcite indicates that dedolomitization initiated along the fractures. These fractures might have acted as permeable conduits to channel the groundwater that was under-saturated with respect to dolomite. With progressive dedolomitization, the dolomite cements may be completely calcitized. Generally, dedolomitization is not fabric-selective. However, the permeability and porosity of the precursor dolomite appears to have influenced the degree of dedolomitization locally.

Upon uplift, meteoric-derived fluids dissolved the replacive sulphate and precipitated calcite cements in the resultant porosity. CL and trace element geochemistry show that these cements are zoned, and that different CL zones correlate well with iron and manganese geochemical changes, indicating a gradual increase in oxygenation of the precipitating fluids through time.

10.- Trace element behaviour and composition of parental fluids

The slight enrichment in Sr of the replacive dolomite and the dedolomites may be interpreted according to three hypotheses. The first hypothesis concerns early diagenesis in a rock-buffered system from high Sr/Ca fluids derived from the aragonite-calcite transformation (Harris and Matthews, 1968; Land, 1973; Banner, 1995; Budd, 1997; and Swart and Melim, 2000). Petrographic observations concluded that this process was uncompleted given the local preservation of isopachous dolomitized marine cements. The second hypothesis implies that the dissolution of sulphates rich in Sr such as primary anhydrite is a source of Sr incorporation into the system. The time when sulphate dissolution occurred is difficult to constrain, but according to the stair-step calcite that filled pseudomorphs after anhydrite, it can be postulated that dissolution occurred before the late meteoric calcite cementation. The third hypothesis suggests that Sr input to the system is due to the dissolution of carbonates and siliciclastics. This option seems more likely although it is not possible to confirm that there is covariance of the insoluble residue with the amount of Sr in the samples. This is because the selected samples have little or no insoluble residue. Petrographic evidence of dissolution of feldspar was found in several samples (Fig. 6.3, Plate 2: e, f), lending support to this hypothesis and to the entry of Mn to the system. Sr enrichment is not sufficiently significant to rule out a possible influence of a partial release of Sr promoted by the dissolution of aragonite in early dolomitization.

Mn appears to be present in the fluid from the early stages of dolomititzation. The extensive mobilization of Mn has created a positive Mn anomaly in all the karst materials. Mn follows the same trend as Fe. In Rattlesnake Canyon we observed high Fe concentrations in the karst replacive host rock and a progressive decrease in dedolomite and calcite cements. However, the adjacent host rock does not contain much Fe oxides although it does have high

concentrations of Mn incorporated into its carbonate structure. Meteoric calcites contain a range of 2-200 ppm of Mn but insignificant Fe concentrations. It is therefore believed that in the redox conditions for the precipitation of calcite, Mn was still dissolved in the fluid while the Fe oxides had precipitated. The main source of Mn is thought to be the leaching of siliciclastics. SEM shows that Fe oxides are located in the porosities of the replacive dolomite crystals and not in its structure. No evidence of manganese oxide was found except isolated Mn crusts at the top of the Fault M. Therefore, Mn was incorporated into the crystal structure of dolomite. Na and Sr contents in the replacive dolomite suggest an early dolomitization model by reflux with subsequent recrystallization. Incorporation of Mn and Fe into carbonates is mainly controlled by the Eh, and to a lesser extent, by the pH of the precipitating fluid (Garrels and Christ, 1965; Frank et al, 1982). Dolomite cements are ferroan with relatively high Mn^{2+} contents and thus dolomitization might have ocurred in the presence of reducing fluids (Wong and Oldershow, 1981; Reinhold, 1998). All this suggests Mn enrichment during stabilization or early recrystallization by moderately to significantly reducing pore waters in a closed system in a shallow burial environment.

Sr content tends to rise and Na contents have a wide range of dispersion in the dedolomites. The increase in Sr is thought to have occurred due to the late dissolution of the sulphates which resulted in partial dedolomitization along fracture zones. Sr decreases significantly in calcite cements and indicates that sulphate dissolution gradually comes to an end. Na undergoes a sharp drop and both, Sr and Na contents, confirm that the fluid that precipitated the late calcites was basically meteoric.

CL homogenization of the replacive matrix may be a distinctive feature of recrystallization. Replacive matrix yellow luminescence, due to its Mn content, is repeatedly observed in the CL cyclicities of the indurated dolomite frameworks. Pore waters with moderate salinities in a burial environment lead to reducing conditions that favour Mn incorporation and the production of characteristic yellow luminescences.

Carbon and oxygen stable isotopy shows that dolomite cements experiment a decrease in the oxygen signal of the early carbonate in a regime of low water/rock ratio. Meanwhile, SEM reveals that early dissolution processes did in fact affect the cores and not the rims of the rhombohedra. Thus, it follows that the recrystallization involved multiple small dissolution-precipitation processes in a relatively closed system and in equilibrium with the pore waters presumably during an early phase of the mesodiagenesis.

The range of $\delta^{18}O$ values is best explained by varying degrees of recrystallization, which can also be viewed as varying water/rock ratios. A preliminary approach to the temperature of precipitation of the cements can be made using the $\delta^{18}O$ of today's meteoric water, seawater, and evaporated brines owing to the antecedents of reflux dolomitization in the area. Assuming -6.3‰ SMOW as an approximate value of δ18O for rainwater in the region (Hill, 1996), and taking -9.80‰ as an approximation for the meteoric calcite end member (Appendix 2, Table III), the temperature of precipitation turns out to be about 26 °C, using the Friedman and O'Neil (1977) temperature fractionation equation. This temperature is consistent with

a surface temperature and with shallow depths. At the other end of the spectrum, taking brine water with $\delta^{18}O$ of about +2‰ SMOW, the temperature of crystallization would be 78 °C. CL luminescences of these calcites are dull and and do not correspond to the bright luminescence of typical hydrothermal calcite.

Using the same calculations for the highest values of $\delta^{18}O$ for the calcite cements (-2.2‰) leads to a temperature of calcite precipitation from meteoric fluids of -7ºC and 48ºC by a brine of +2‰ SMOW. Considering these data alone, it cannot be said that these calcites precipitated from only one fluid. Calcite $\delta^{13}C$ values are fairly negative and do not rule out a possible influence of meteoric waters mixed with brines in different proportions.

Extending these calculations to dolomite cements using the temperature fractionation equation by Fritz and Smith (1970), the highest values of $\delta^{18}O$ for the dolomite cements (1.78‰ PDB) lead to the conclusion that this heavy $\delta^{18}O$ dolomite is precipitated from concentrated brines around 2-3‰ SMOW.

11.- Evaporite diagenesis

Evaporitic sediments tend to dissolve readily when they are exposed to freshwater meteoric diagenesis. Dissolution of sulphates can also be produced through BSR often accompanied by the precipitation of carbonates with low isotopic carbon signals. Such a process is active when sulphate is in contact with hydrocarbon or when sulphate coexists with significant amounts of organic matter (Dessau et al, 1962; Davies and Kirkland, 1970; McKenzie, 1985).

The replacement of sulphates by carbonates is a common process although its recognition is not always evident. Two possible mechanisms have been proposed for the replacement of sulphates by carbonates: Bacterial reduction of the sulphate and Sulphate dissolution by bicarbonate-bearing waters (Pierre, 1986; Pierre and Rouchy, 1988). A complete replacement can obliterate the original structures of the former evaporitic sediment. Moreover, the replacement carbonates may reproduce concretionary or radial microfabrics which can be confused with speleothems. Anhydrite preferentially nucleates within the organic-rich cores, and subsequent dissolution produces hollow dolomite crystals or intracrystalline porosity. Thus, anhydrite commonly replaces allochems and the replacement of such anhydrite generally produces biomoulds. Some ferruginous biomoulds probably replaced former anhydrite moulds, which indicates that Fe mobilization postdates evaporite dissolution (Fig. 6.3, Plate 2: h). Dissolution of these crystals produced voids with angular and stair-step outlines which were later occluded by equant spar calcite (Fig. 10: a and b). These rectilinear stair-step moulds, which are attributed to former displacive porphyroblastic anhydrite crystals, are very common in the upper interval of the paleokarst sequence fill. The main evaporite fabrics recognized in the paleokarst sediment differ from mixed fabrics of anhydrite and show prismatic-elongated to grain and equidimensional fabrics of porphyroblastic anhydrite towards the top of the paleokarst fill sequence. According to Ortí and Rosell (1981), decussated prismatic fabrics with split and broken lath-shaped replacement anhydrite crystals entail some compaction

whereas porhyroblastic equidimensional fabrics could be attributed to the presence of halite. In general, lath decussated type-fabric has been ascribed to shallow burial conditions (Kasprzyk and Ortí, 1998).

Sulphate dissolution had already begun when freshwater percolated through the karst promoting meteoric diagenesis and precipitation of late dull calcites. Unless evaporite dissolution started very early during synsedimentary karstification due to early meteoric diagenesis, it is reasonable to assume that it was mainly triggered by BSR and continued during uplift, reinforced by meteoric flushing.

Iron oxide pseudomorphs after pyrite were encountered filling hollow dolomite pores, and hollow dolomite textures are common in many evaporite-associated units (Folk, 1968).

In line with these observations it is suggested that most anhydrite was emplaced diagenetically during and following early dolomitization as blocky porphyroblasts and lath felted fabrics. The change in the fabric might be attributed to increasing salinity, indicating a change to more arid conditions during the paleokarst filling given that Ortí and Rosell (1981) associate this fabric type with halite.

The best Permian reservoirs contain intercrystalline porosity with pores created by dissolution of anhydrite and grains.

12.- Diagnostic criteria for the characterization of early dolomitization and late dedolomitization and calcite cementation

The timing of replacement dolomitization is interpreted to be early and confined from subsurface to shallow burial by the following lines of evidence:

- The dolomite cements show different cement generations when observed under CL.
- The replacive dolomite shows yellow luminescence identical to the yellow cement generation observed in the dolomite cements.
- The replacive dolomite is Mn enriched and the dolomite cements are ferroan. Mn and Fe are incorporated into the dolomite crystal lattice under reducing pore water conditions in the burial environment.
- The fact that no replacement dolomite occurs within the pseudomorphs of evaporite crystals suggests that the dolomitization replacement took place earlier than the dissolution of evaporite minerals.
- Stylolites growing from the dolomite cemented cavities are commonly cemented by the same cements that filled the cavities (Fig. 6.7).

• Dolomite is not found overlying the dedolomite/spar cements.

• The indurated dolomite frameworks recognized in the study area are equivalent to the ones defined by Choquette and Hiatt (2008) and ascribed to shallow burial conditions of formation.

• Shallow burial modification is preferred to near-surface modification due to the presence of non-planar crystal boundaries (Fig. 6.3, Plate 1: d) in the dolomite mosaics.

• Lower $\delta^{18}O$ isotopic values for the dolomite cements are thought to be caused by an increase in temperature corresponding to conditions of shallow burial.

Dedolomite and spar cements are interpreted to be late diagenetic products and are closely related to the hydrocarbon recharge of the basin. During uplift, siliciclastic diagenesis generated clay cementation and Fe migration, resulting in iron oxyhydroxides formed by oxidation and supergene enrichment within the paleokarst. Secondary leached porosity was extensively formed in many intervals during freshwater diagenesis. Evidence for the timing of these processes is provided below:

• Spar cements show lower concentrations of Fe, suggesting the involvement of meteoric fluids.

• Dedolomites and spar cements contain hydrocarbon fluid inclusions. These fluid inclusions occupy primary and secondary positions indicating coeval precipitation of these cements with the HC charge. Statistical analysis for their distribution is not possible because of the limited data.

• Kaolinitization generally forms after feldspar and mica in the presence of low pH meteoric water and is common during exhumation (Lanson et al., 2002).

• Dedolomites are regularly associated with dickite cements, which are frequently coated by iron oxyhydroxides.

• Some of the dedolomite and spar $\delta^{13}C$ values are low (reaching -15 ‰ PDB), outside the range of meteoric diagenesis (Fig. 6.11), suggesting an increase in CO_2 contents. Their parental fluids might therefore be linked to BSR.

• Oxyhydroxides cross-cut the massive dolomite.

• SEM reveals hematite pseudomorphs after pyrite (Fig. 6.9) and the presence of spherules resembling framboid structures. These structures are embedded in the pores of hollow dolomite rhombohedra.

• Thrombolitic structures coated with iron oxides are also observed and interpreted as resulting from dedolomitization.

• Goethite crystals with well developed crystal faces were trapped during poikilotopic calcite growth (Fig 6.3, Plate 2: g).

• Dedolomite/spar fracture and void fills are post-compactional.

• Spar calcite is recognized filling evaporite moulds.

13.- Spatial assessment of HC migration in the Capitan platform margins

Thermal coarse spar is considered to postdate dedolomite cementation since it overlies dedolomite/spar sequences. Thermal spar also traps HC fluid inclusions but does not exhibit poikilotopic textures. Positive $\delta^{13}C$ isotopic and extremely low $\delta^{18}O$ (-11 — -14‰) values suggest an interval of late hydrothermal diagenesis in Rattlesnake Canyon.

Spars I, II and III were described by Mruk (1989) in McKittrick Canyon. Dd1 and Dd2 show similarities (when observed under CL luminescence and zonation) with Spar I and Spar II, respectively, although Dd2 $\delta^{13}C$ values are much lower than the ones of Spar II. Spar II was interpreted as a thermal spar by Mruk (1989) in accordance with its low $\delta^{18}O$ isotopic values (from -11.5 to -13.9 ‰) and fluid inclusion homogenization temperatures (~70-80ºC). Accordingly, it may be assumed that the diagenetic sequence recognized by Mruk (1989) in the carbonate facies of the McKittrick Canyon is not affected by the hydrocarbon migration since it presents higher $\delta^{13}C$. Thus, the diagenetic sequence in McKittrick Canyon obeys a meteoric diagenetic environment (Spar I) interrupted by a hydrothermal event (Spar II) and finally completed by the precipitation of Spar III, which could have precipitated from mixed hydrothermal and meteoric fluids. By contrast, in Rattlesnake Canyon the hydrocarbon signal is captured in the Dd2 and Dd3 cements. Dd2 and Dd3 cementation phases are followed by the thermal spar. These observations raise one important question: Does the same cement phase reproduce different diagenetic conditions in the two canyons? The same paragenetic sequence as in the forereef facies of McKittrick Canyon is detected in Rattlesnake Canyon but is interrupted by the hydrocarbon charge during the time of Dd2 cementation. This period corresponds to the thermal Spar II cementation in McKittrick Canyon. Hydrothermalism is structurally controlled and preferentially developed along fracture zones or sealed by massive and homogeneous lithofacies in non fracture zones. It seems that no barriers could have paralyzed hydrothermal flux along the faults studied because of the similarity of the depositional facies of the Capitan platform, the distance between the two canyons (~ 30 km), and the fact that Rattlesnake Canyon is faulted. However, no fluid inclusions were found to corroborate the foregoing hypothesis.

In order to spatially assess the range of hydrocarbon migration in the Capitan margin platform, we compared the isotopic signals of the cements in the different canyons of the carbonate system. On the basis of the available data, Fig. 6.16 shows that the limits between meteoric diagenesis and BSR diagenesis lie in Rattlesnake Canyon. Slaughter Canyon cements do not record the isotopic signature of BSR although it is not possible to rule out that this

process did not occur there. Koša's data (2003) were obtained from bulk sampling and were probably contaminated by the heavy signal of the replacive dolomite. Thus, we can conclude that hydrocarbon migration seems to be confined to the paleokarst faulted areas of the backreef, especially in Yates unit. These areas include Dark Canyon, Rattlesnake Canyon and probably Slaughter Canyon.

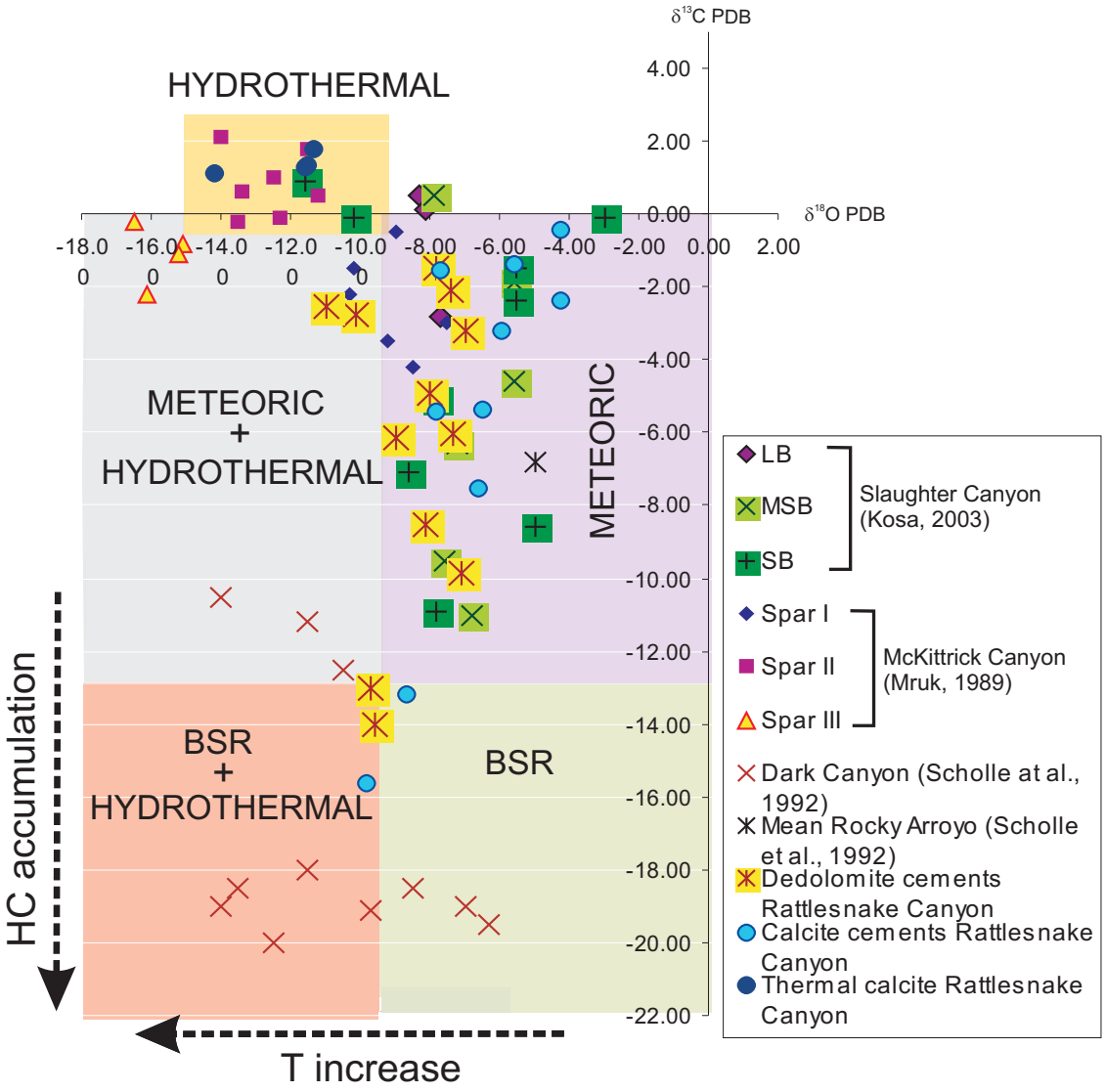

Fig. 6.16. Compilation of the stable isotope data of the diagenetic cements of the different canyons in the area limiting the Capitan platform margins.This work supplies a new interpretation for the origin of the different cements involucrating different parental fluids and processes (discussed in the text).

14.- Conclusions

The mixed carbonate-siliciclastic Yates unit has proved to be a good reservoir in the Guadalupe Mountains although hydrocarbon accumulation in the backreef karstified Yates in Rattlesnake Canyon was interrupted by late Tertiary diagenetic events. The Rattlesnake Canyon paleokarst filling sequence localizes considerable evaporite diagenesis triggered and controlled by the Upper Permian synsedimentary karst development. The paleokarst potential reservoir structure, which proved ineffective, was forced by the dedolomitization and hydrothermal cementation that ocurred during uplifting.

The dolomitized Rattlesnake Canyon paleokarst infills underwent different diagenetic episodes of replacement, multhiphased dolomite cementation, dedolomitization and calcite precipitation.

Two patterns of cementation were identified in the Rattlesnake Canyon paleokarst: dolomite cements filling voids, and sulphate-replacing dedolomites and calcites (^{13}C depleted) as fracture fills and filling anhydrite moulds. Dolomite cementation is observed in voids through a multiphase textural evolution sequence generating dolomite frameworks. Syntaxial overgrowths and pore-filling dolomite are best developed when associated with sucrosic dolomite and when lining cavities, overlying the early replacive dolomite. The sequence is in line with the Choquette and Hiatt (2008) cementation pattern attributed to shallow burial conditions.

Spar calcite is commonly found as blocky spar cement mainly filling fracture porosity. Under CL, spar calcite shows three luminescent subzones: Dd1, Dd2 and Dd3. These subzones probably resulted from dedolomitization as suggested by the occurrence of dissolution fabrics in dolomite and by the presence of dolomite relicts such as calcitized rhombs after dolomite and floating dolomite relicts within dedolomite mosaics.

Calcite (Cc1) as a single product, with no ghosts of calcitization, is encountered as fracture-fills, solution pipe fills and within anhydrite moulds.

A coarser calcite (^{18}O depleted) overlying dedolomite cements and occluding late secondary porosity is attributed to Miocene hydrothermal activity in the region.

Dedolomites and spar cements contain hydrocarbon fluid inclusions. The distribution of these fluid inclusions indicates coeval precipitation of these cements with the Tertiary hydrocarbon charge of the basin.

Anhydrite was probably emplaced diagenetically as blocky porphyroblasts and lath felted fabrics during and following early replacive Yates dolomitization. The change in the fabric might be attributed to increasing salinity, indicating a shift to more arid conditions during paleokarst filling.

A significant increase in Fe and Mn is perceived in the karst area. Fe is mobilized and precipitated as iron oxides whereas Mn is incorporated within the karst replacive dolomite. Dedolomite and calcite cements display non-ferroan and dull to non-luminescent cements indicative of moderately oxic environments, whereas indurated dolomite frameworks and void-filling dolomite show ferroan and bright cements indicative of suboxic environments. Dedolomite and calcite cements show progressive depletion of iron and manganese directly linked to uplifting and increasing volumes of meteoric waters.

Coloured sediments within karst are due to the presence of iron oxides. The yellow infills detected in the field, show an abundance of poikilotopic calcite which includes well crystallized acicular goethite crystals. SEM reveals hollow dolomite with numerous intracrystalline pits as preferential sites for the emplacement of hematite pseudomorphs after pyrite. Two mechanisms are proposed for the origin of iron-bearing minerals in the paleokarst: sulphate reduction and direct precipitation from ferrihydrite.

Dickite cementation is found in fracture zones and recognized as cavity fills in areas of high dissolution. It is regularly associated with the dedolomite cements. Given that dickite booklets are found stained with the iron oxides as well as in a limpid form, the clay genesis is inferred to have continuity in time, predating and postdating the iron diagenesis.

The pattern of the dedolomite cementation observed by CL in combination with the TEM observations of iron oxides and trace element analysis suggests fluctuating pH conditions and the following processes:

» dickite tansformation of former kaolinite derived from the leaching of siliciclastics at acid pH during mixing of hydrocarbon and hydrothermal fluids.

» dedolomitization confined to fracture zones associated with iron oxide precipitation at basic pH and with relatively sharp and cyclic transitions of Eh from suboxic to moderately oxic conditions based on the complex array of zonations of these cements.

Chapter 7

Paleokarst reservoir properties: characterization, spatial distribution and diagenetic modification

Abstract:

Three stratigraphic horizons were selected to study the lateral expansion of the karst impact on the carbonate host rock. These levels display grain supported textures but different reservoir properties (pisolitic grainstones and fusulinid packstone/grainstones). The horizons that were vertically displaced by faulting growth during karsting show higher permeabilities than the uppermost horizon that was deposited practically fossilizing the system. The pisolitic level deposited during Upper Yates 3 shows major expansion over 40 metres from fault boundaries and major permeability values confined to karst boundaries and solution enhanced zones with mouldic and vuggy porosity. Lower Yates 3 fusulinid packstone/ grainstone also underwent synfault movement and localizes major intraparticle porosity and very high permeability values thought to have occurred as a result of episodes of early karst dissolution. The upper pisolitic level deposited during the final stages of karsting (Upper Yates 4) shows the lowest lateral expansion (only few metres) and the lowest permeability values and present mainly interparticle depositional pore types. The differences reveal that karst development rather than depositional textures determined the petrophysical properties of the host rock.

Late diagenetic cementation during the uplift led to clay cementation and dedolomitization preferentially along fracture zones within the paleokarst sequence, resulting in a significant permeability reduction. The lateral pores of the carbonate host rock are less modified preserving much dolomite cemented vugs with high rates of intercrystalline and vuggy porosity. Although high poroperm values are still linked to fracture and breccia porosities around fault boundaries, the lateral poroperm heterogeneity shows that lens dissolution processes contributed significantly to the expansion of the system.

This study contributes to a better understanding of lateral heterogeneity distributions in karst affected carbonate platforms unlike most studies that focus on vertical subsurface heterogeneity.

Chapter 7

Paleokarst reservoir properties: characterization, spatial distribution and diagenetic modification

1.- Introduction

Paleokarsts have been broadly recognized as an important type of hydrocarbon reservoir (Kerans, 1988; Loucks, 1999; Wang and Al-Aasm, 2002). Reservoir characterization in these types of systems focuses on the complexity of spatially predicting heterogeneity. In addition, working with ancient carbonate reservoir facies increases the possibility that multiple diagenetic imprints have strongly modified the early depositional pore features.

Petrophysical properties of sedimentary rocks are influenced by porosity, permeability, velocity and density; these properties are partly controlled by facies characteristics which in turn are related to depositional processes. Syndepositional faulting played a major role in the development of vertical paleocaves in Rattlesnake Canyon. By contrast, matrix properties of the carbonate host rock regulated the extent of the stratabound caves in Rattlesnake Canyon, which reinforces the scientific interest in studying the horizontal variability of poroperm values along the graben system.

The results presented here are of interest as an example of qualitative characterization of the pore types in a carbonate paleokarst system. Moreover, the studied oucrop appears particularly suitable for quantifying the horizontal propagation of the karst system and analyzing its effects through the carbonate host rock properties. Preliminary diagenetic studies are necessary for discriminating between early intraparticle and vuggy cementation distributions and late cementation patterns. Analyzing the impact of late diagenetic fluid flows onto these early pore type distributions has been the key to understanding the evolution of the petrophysical properties of the system.

The aim of this study is to describe, characterize and quantify the reservoir properties of the Upper Permian host rock carbonates of the Rattlesnake Canyon paleokarst system. This study also seeks to analyze the controls of the karst system on the spatial distribution of the reservoir properties and to evaluate the role of diagenesis in the evolution of porosity and permeability.

2.- Methodology

A total of 89 1-inch plugs were drilled from rock samples. Grain density measurements were also obtained for the plugs (Appendix 2). Porosity and permeability of plug samples from three stratigraphic horizons were analyzed at Reservoir Laboratories AS in Stavanger. Air permeability gas values reported are Klinkenberg-corrected nitrogen permeabilities measured with confining pressure of 20 bar. Rock samples were collected from the outcrop at horizontal intervals of 5 m, focusing on the trace of three selected stratigraphic horizons. Thin-section porosity was impregnated with blue-dyed epoxy for visualization of pore types.

Liquid and air permeability was measured in each plug. The absence of significant variations between these two values enabled us to use both for this study. Air permeability values were mainly used for the construction of regression plots as well for determining the main statistical parameters. Whenever liquid permeability values are used this is commented upon in the text.

3.- Facies

The depositional environments of the platform margins that host the paleokarst system include shallow open subtidal, tidal flats, restricted peritidal and open shoal facies (Figure 3.4).

Three specific stratigraphic horizons were chosen to provide the data set for poroperm analysis. The lower horizons chosen, which are cut by the two studied faults (M and N), underwent vertical displacement simultaneously with paleokarst development. The upper selected horizon was deposited fossilizing the system and thus it presents a slight faulting displacement (Fig. 7.1). Analysis of the horizontal variations along these three specific horizons can supply information about the impact of the karst development on the host rock for subsequent comparison with the petrophysical properties of the host rock in the final stages of karsting.

The stratigraphic levels chosen are made up of (i) Pisolitic Dolograinstone and (ii) Dolopackstone with fusulinids to Dolograinstone.

1) Pisolitic Dolograinstone (Middle and Upper levels)

Description: This facies was extensively encountered as massive metre scale thick levels overlying shallow subtidal and peritidal marine facies. Its microscopic fabric is made up of pisoids in a grainstone texture. The Upper level forms part of the Upper Yates 4 Formation whereas the middle pisolitic level forms part of the Upper Yates 3 Formation.

This facies represents a supratidal environment.

2) Dolopackstone with fusulinids to Dolograinstone (Lower level)

Description: Grey weathering, dm- to m-thick beds mark this facies in the field. The microfacies of the fusulinid packstone is characterized by fusulinids associated with peloids and micritised grains. Dolomite cement growth is common in inter- and intraparticle pore space. This facies is most abundant in the lower interval of the logged section. The texture of this facies varies from packstone to grainstone throughout the graben system appearing as fusulinid packstone in the footwall of Fault N and as fusulinid grainstone in the graben section and in the footwall of Fault M. The variability of the texture was regulated by the energy of the environment removing the mud when the environment had more active hydrodynamics.

Intraclast-peloid grainstone is common towards the top of the level. Intraclasts are frequent and have predominantly rounded shapes. These facies also contain some ooids and peloids. The intergranular space is filled with fine sediment or cement. The facies can be described as a bioclastic-peloidal grainstone. Locally fenestral fabrics are detected. The fenestral structures are characteristic features for upper intertidal to supratidal environments. This graded level forms part of the Lower Yates 3 Formation.

It is therefore interpreted as a gradual transition from subtidal open shelf deposits to intertidal facies from base to top.

4.- Pore types

Pore types and cement morphology were analyzed to understand porosity–permeability relationships in Rattlesnake Canyon. The description of pore types is organized in this work according to Lønøy's classification (2006).

Lønøy (2006) organized a pore-type classification for carbonate rocks based on sedimentological and diagenetic characteristics. The classification scheme includes 20 pore type classes, including interparticle, intercrystalline, intraparticle, mouldic and vuggy porosity as well as mudstone microporosity. In addition, the classification also considers pore sizes and porosity distributions. Lønøy's classification can be accepted as a combination of the classifications of Choquette and Pray (1970) and Lucia (1983, 1995 and 1999). However, Lønøy's (2006) classification system approaches a higher degree of correlation between porosity and permeability based on R^2 values for porosity/permeability crossplots. Thereby, this new system of pore type classification offers more reliable rates to predict the relationships between porosity and permeability.

The three main elements in Lønøy's pore-type classification are:

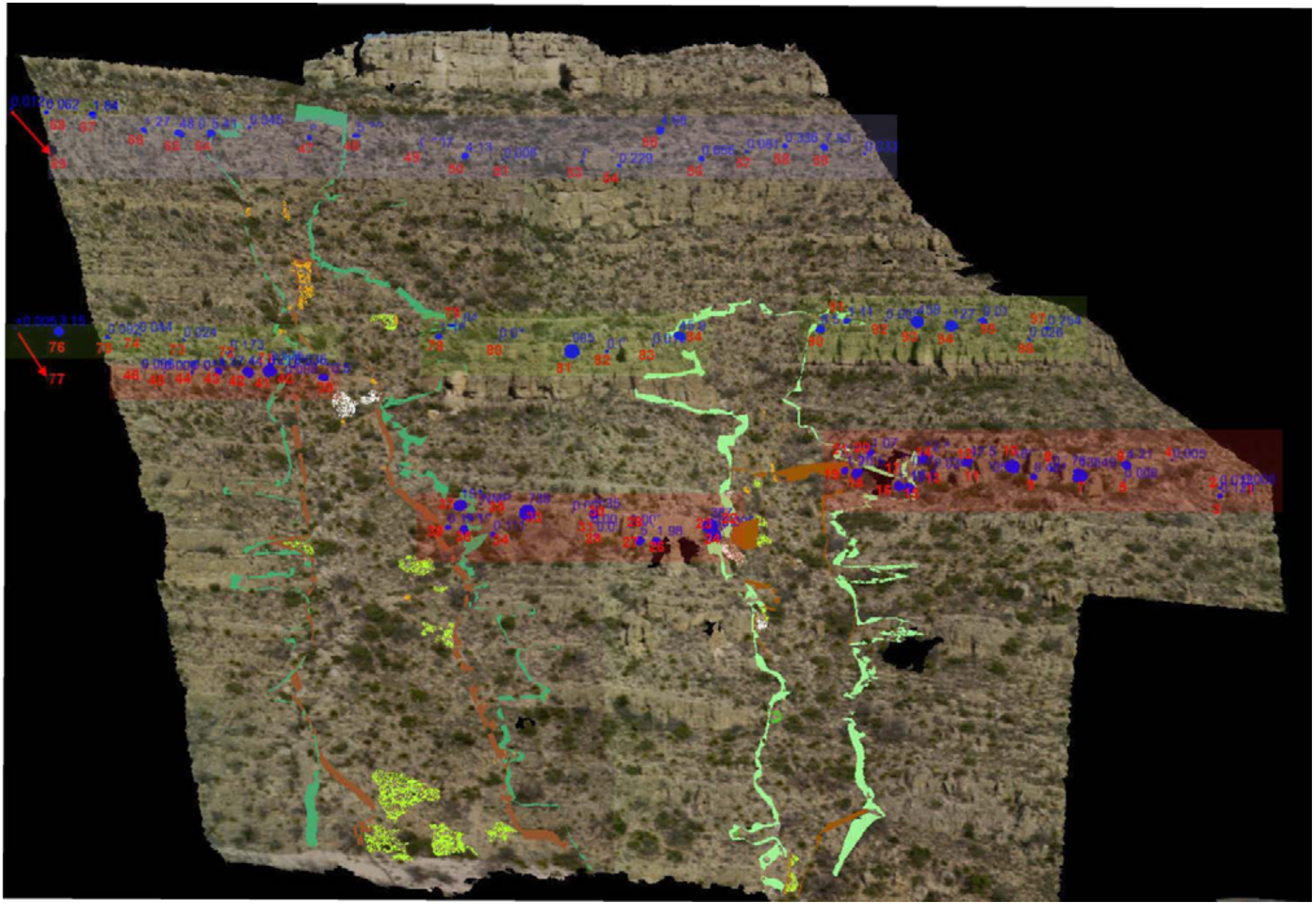

Fig. 7.1. Stratigraphic horizons chosen for poroperm sampling. Green surfaces represent the limits of karst damage zones and brown surfaces the limits of the paleocave zones.

» *Pore size*. The influence of pore size on permeability (and consequently rock fabrics) was highlighted by both Archie (1952) and Lucia (1983, 1995 and 1999). However, Lucia used grain size and sorting to separate pore-type classes. But since cements commonly occlude pore space and reduce pore throats, the relation between pore size and grain size is indirect and often incorrect. This may explain the wide range and scatter of data in all of Lucia's pore-class fields. As for Lønøy's classification, pore sizes of the different classes vary with pore type and are not based on other published classifications. They are instead visually determined.

» *Pore type*. Six main pore types were defined: (1) interparticle, (2) intercrystalline, (3) intraparticle, (4) mouldic, (5) vuggy and (6) mudstone microporosity. The first five pore types are based on those defined by Choquette and Pray, whereas the last one is new. Lønøy distinguishes between interparticle pores and intercrystalline pores whereas Lucia brings these two pore types together. Lønøy (2006) points out significant differences in permeability trends between intercrystalline and interparticle porosity, which allows us to analyze the role of the cementation and dolomitization processes.

» *Porosity distribution*. In line with Choquette and Pray (1970) the porosity distribution was subdivided into *uniform* and *patchy* subclasses. Patchy porosity distributions lead to best connected pathways for fluid flow, resulting in higher permeability values than uniform porosity distributions. Patchiness is often related to secondary dissolution and/or selective cementing during diagenesis.

Table 7.1 illustrates Lønøy's new porosity classification system and codification of pore types used in this chapter. The definitions for the six main pore types used agree with those of Choquette and Pray.

Interparticle porosity is defined as porosity occurring between grains (intergrain) (Choquette and Pray, 1970; Lønøy, 2006). Interparticle pores are commonly primary in origin, but may also be formed by secondary dissolution of cements or matrix.

Intercrystalline porosity is the porosity between crystals that may be of either primary or secondary origin (Lønøy 2006). If of secondary origin, intercrystalline pores may be associated with calcite recrystallization or dolomitization. Patchy intercrystalline pore distribution is normally related to patchy cementation controlled by the depositional setting.

Intraparticle pores are pore spaces occurring within grains, either of primary origin or formed through the decay of organic material in carbonate skeletons (Lønøy 2006).

Mouldic pores are secondary pores formed by the selective, complete or partial dissolution of constituent grains or crystals (Lønøy, 2006). Mouldic macropores are commonly formed through dissolution, and their porosity distribution is controlled by both diagenesis and depositional setting.

Vuggy pores are secondary pores that are not fabric selective and originated by dissolution enlargement of an existing pore or combination of pores whose origin can no longer be identified (Choquette and Pray, 1970; Lønøy, 2006). The vuggy pores studied by Lønøy mostly fall into Lucia's (1983, 1995and 1999) touching-vug pore system and are interconnected.

Mudstone micropores may be defined as interparticle or intercrystalline pores, but are not grouped with these pore types because of the extremely small size of the pores. The pore structure is variable. Mudstone microporosity includes both true chalks and chalky microporosity. Chalk micropores are primary in origin. Chalky micropores are not related to chalk, but the pore structure is similar.

Pore Type	Pore Size	Pore Distribution	Pore Fabric
Interparticle (1)	Micropores (10 - 50 μm) (11)	Uniform	Interparticle, uniform micropores
		Patchy	Interparticle, patchy micropores
	Mesopores (50 - 100 μm)	Uniform	Interparticle, uniform mesopores
		Patchy	Interparticle, patchy mesopores
	Macropores (>100 μm) (13)	Uniform	Interparticle, uniform macropores
		Patchy	Interparticle, patchy macropores
Intraparticle (2)			Intraparticle
Mouldic (3)	Micropores (<10 - 20 μm) (1)		Mouldic micropores
	Macropores (>20-30 μm) (2)		Mouldic macropores
Intercrystalline (4)	Micropores (10 - 20 μm) (11)	Uniform	Intercrystalline, uniform micropores
		Patchy	Intercrystalline, patchy micropores
	Mesopores (20 - 60 μm)	Uniform	Intercrystalline, uniform mesopores
		Patchy	Intercrystalline, patchy mesopores
	Macropores (>60 μm) (13)	Uniform	Intercrystalline, uniform macropores
		Patchy	Intercrystalline, patchy macropores
Vuggy (5)			Vuggy
Mudstone microporosity (6)	Micropores (<10 μm)		Tertiary chalk
			Cretaceous chalk
		Uniform	Chalky micropores uniform
		Patchy	Chalky micropores patchy

Table 7.1. Porosity classification system from Lønøy (2006). Numbers are used to codify the different pore types for visualization in the 3D model (Fig. 7.5), e.g.: 1.13 refers to macrointerparticle porosity, 3.13: macromouldic porosity, 4.13: macrointercrystalline, 4.11: microintercrystalline.

5.- Pore types in Rattlesnake Canyon

Pore types in Rattlesnake Canyon are classified according to Lønøy (2006) and codified by numbers in relation to pore type, pore size and pore fabric (Table 7.1). Examination of plugs made it possible to assign main pore types and subordinate pore types for each sample

and integrate the information into the photorealistic model (Fig. 7.2). The distribution of pore types differs in each stratigraphic level. Mouldic porosity is abundant in the lower level, especially in the fusulinid packstones and grainstones. Intercrystalline and vuggy porosity is significant in the middle level. In the upper level, by contrast, the pisolitic lithofacies show abundant interparticle porosity.

Solution enhanced intraparticle porosity is also common in the lower bioclastic level (Fig. 7.3: Sample 41). It occurs frequently as small pore spaces within fusulinid grains. Many of the pores observed in this level are diagenetically altered by reducing cement or enhancing dissolution of the particles. More than 50% of the total porosity in this level is classified as mouldic porosity.

In the middle level intraparticle is the main porosity category although vuggy and mouldic porosity are common porosity subtypes. Vugs exhibit centimetric sized irregular shapes that do not conform to any grain type (Fig. 7.3: Sample 80). Elevated permeability values are associated with both vuggy and mouldic porosity (Fig. 7.3: Sample 93). Intraparticle porosity constitutes more than 30% of the total porosity in this level and most of the intraparticle porosity is associated with vuggy and mouldic porosity.

Interparticle porosity is by far the most abundant porosity type in the upper level. Primary interparticle porosity is often sealed by dolomite cement and is less solution enhanced. This type of porosity constitutes more than 70% of the total porosity in this level. The presence of dickite cement in fractures markedly reduces the permeability values (Fig. 7.3: Sample 58).

Fracture and breccia porosity are recognized throughout the study area. Fracture pore space is regularly filled with dickite cements. The abundance of both fracture and breccia porosity decreases as the distance from the karst boundaries is increased. For this reason, the role of these porosity types is not significant in the analysis of the lateral poroperm heterogeneity as they are restricted to the fault areas.

6.- Quantitative variations on petrophysical data

Petrophysical data measured from plugs were used to assess the texture-related variability of reservoir properties and the identification of the karst effects onto the host rock properties. Table 7.2 illustrates the poroperm characteristics of the different dolomite lithofacies in the three stratigraphic levels.

Grouping the data by horizons facilitates the analysis of the variability of petrophysical data based on karst development. Although some of the textures are identical or very similar grain dominated textures, the mean permeability values differ considerably (Table 7.2). This is evidence that karst development determine stronger the petrophysical properties of the host rock rather than the inherited depositional rock texture.

The upper and middle levels tend to have higher permeability means than the less karst affected higher level. The lower level exhibits extremely high permeability values with

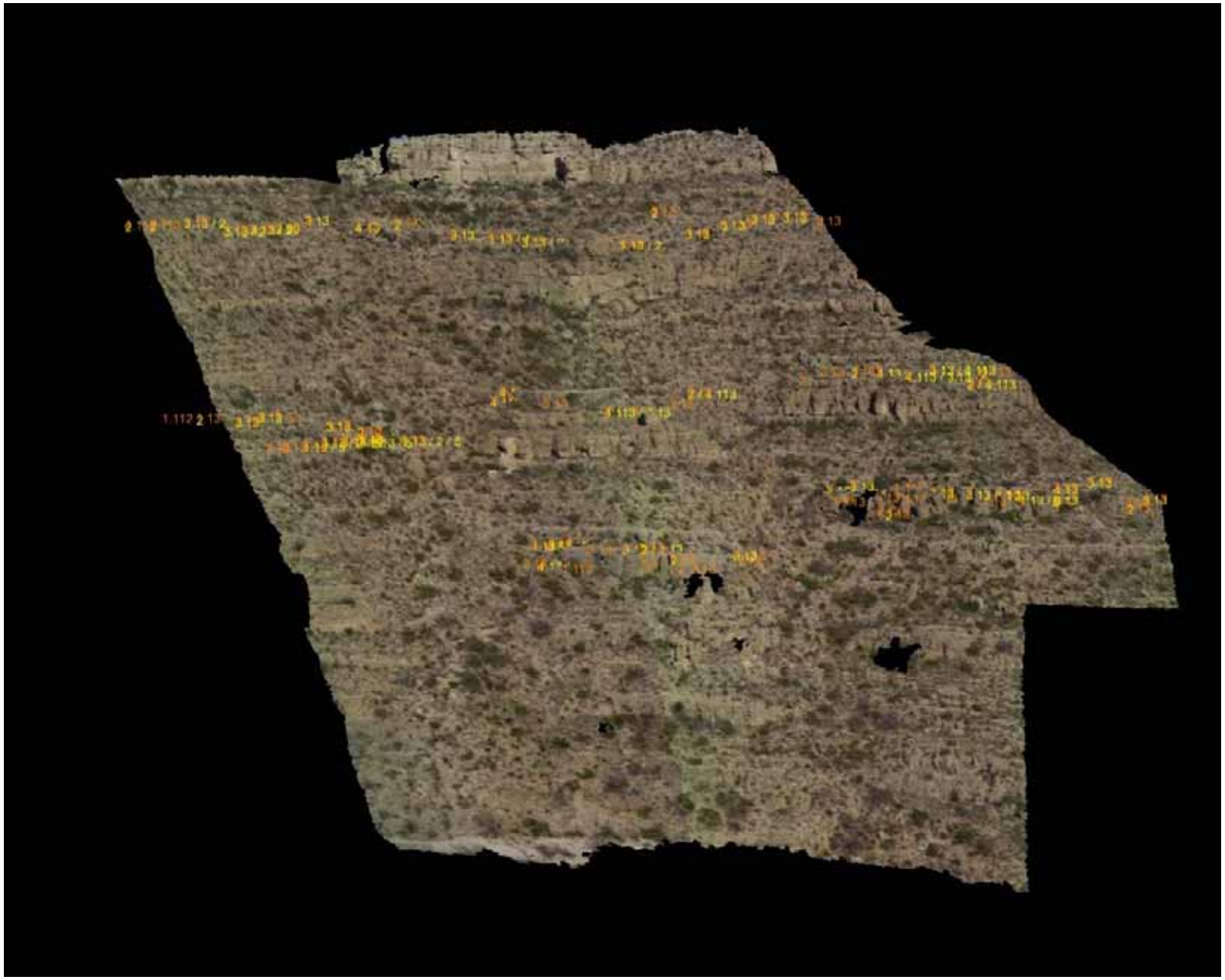

Fig. 7.2a. Integration of code pore types into the 3D model. See Table 7.1 for code type description.

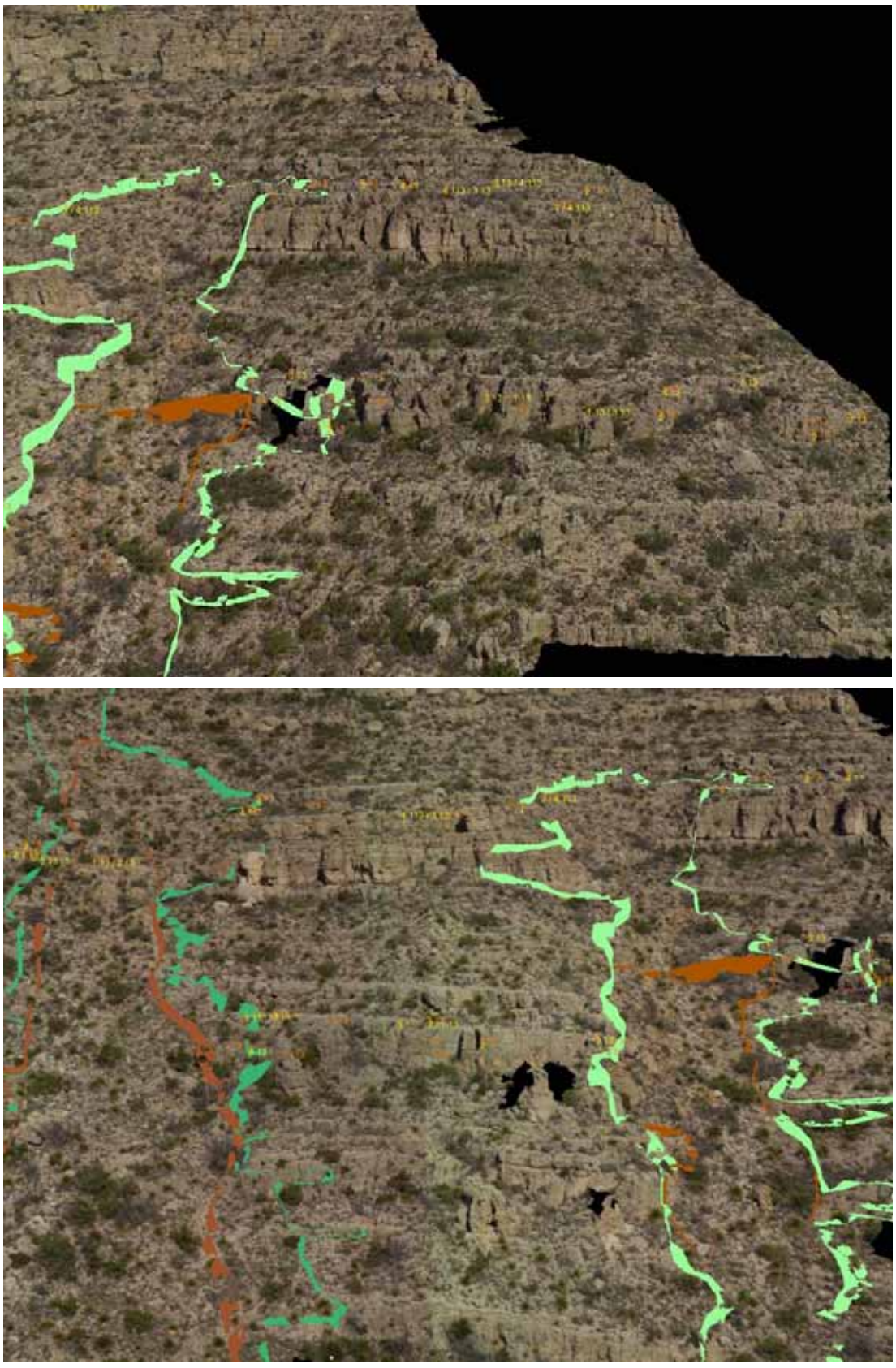

Fig 7.2b. Detail images. Main pore types are expressed by orange colours whereas subordinate pore types are codified by yellow numbers. The codification is based on Lønøy's classification (2006). The first number indicates pore type: (1) interparticle, (2) intraparticle, (3) mouldic, (4) intercrystalline and (5) vuggy.

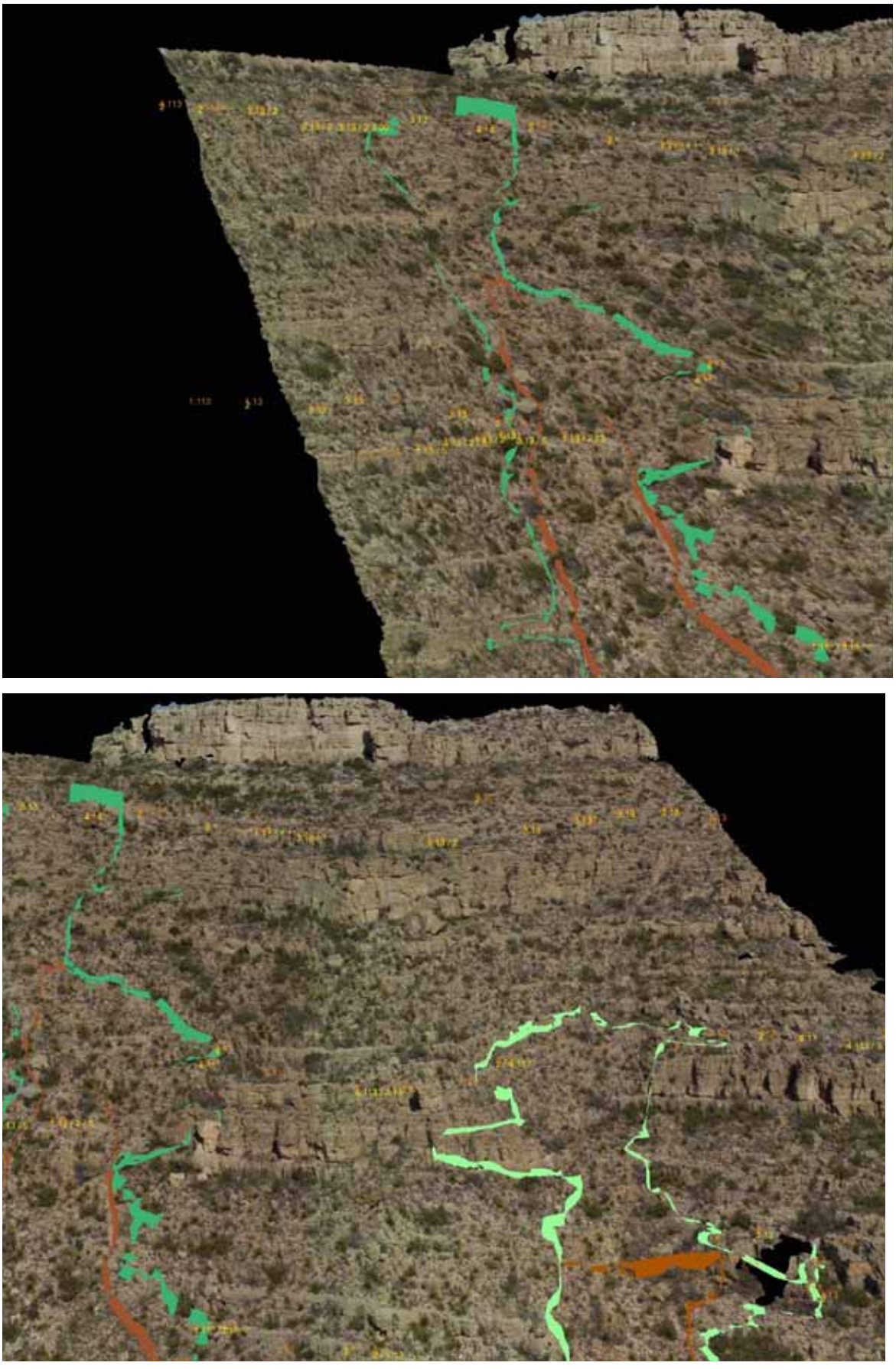

Fig 7.2b. Detail images.

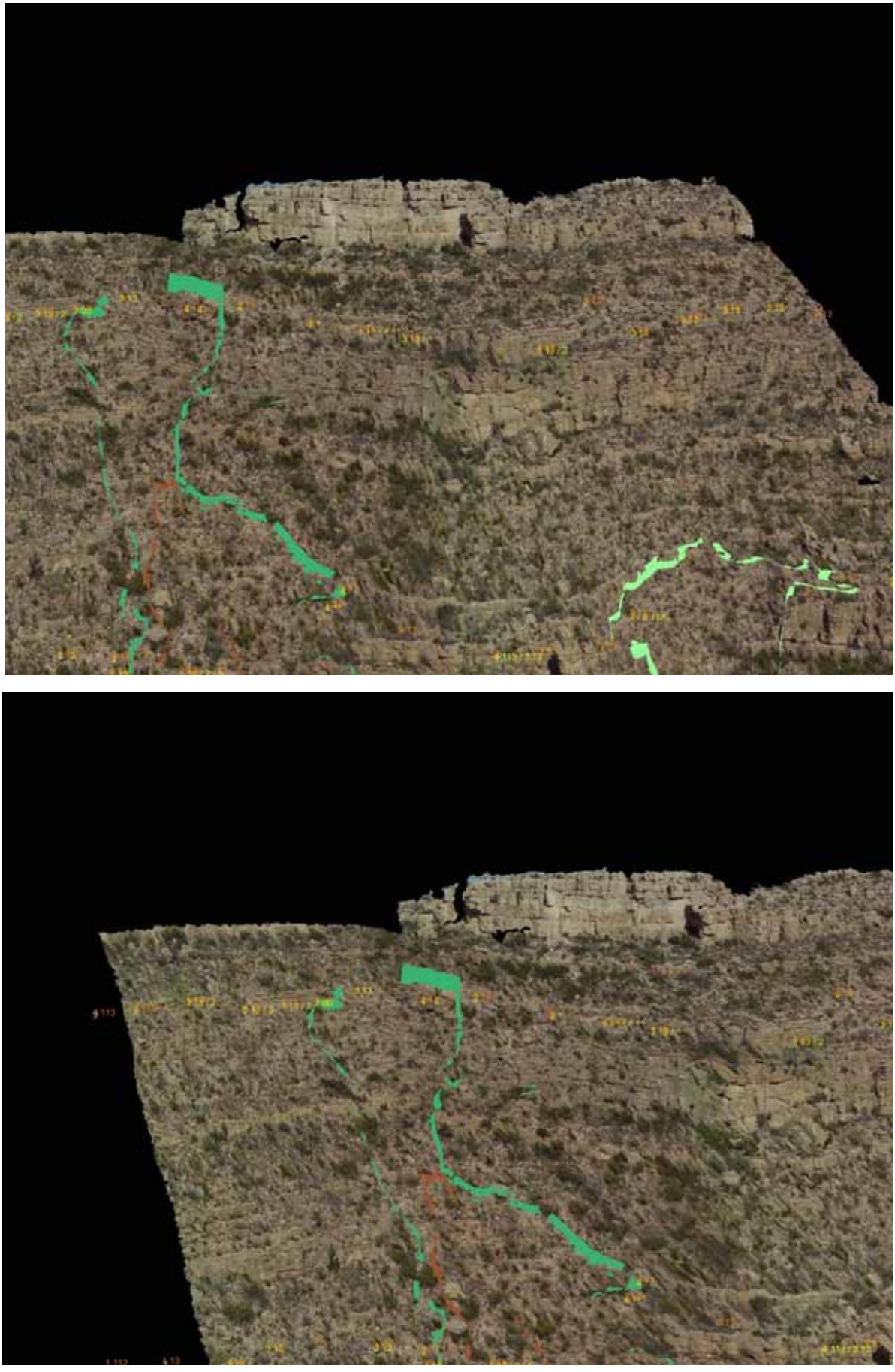

Fig 7.2b. Detail images.

arithmetic means of hundreds of milidarcies (511 and 135 mD) and the middle level shows a very high permeability arithmetic mean value of 77 milidarcies. By contrast, the upper level with the same rock fabric type as the middle level presents a much lower mean permeability value of 5 milidarcies.

Given the previous pore type qualitative characterization, it may be argued that intraparticle and intercrystalline or vuggy porosity sensu lato are the pore types that lead to higher permeability values in Rattlesnake Canyon.

	Arithmetic mean		Geometric mean		
	Porosity (%)	Perm. (mD)	Porosity (%)	Perm. (mD)	R^2
Fusulinid packstone / grainstone	8.07	510.79	6.43	0.57	0.49
Bioclastic-peloidal grainstone	8.98	134.68	7.55	2.91	0.59
Pisoid grainstone	6.95	76.56	6.06	0.75	0.51
Pisoid grainstone /packstone "Upper level"	6.81	4.89	5.98	0.57	0.50

Table 7.2.Statistical parameters of each carbonate texture according to the means of porosity and permeability. Coefficients of determination (R^2) correspond to exponential regression straight lines that better fit each group of samples (Fig 7.4).

7.- Porosity-Permeability relationships

Porosity-permeability cross-plots for carbonate rocks usually display a wide scatter and this is also the case of the Rattlesnake Canyon petrophysical data. The permeability vs. porosity crossplots presented in Figure 7.4 show the trends associated with each level. The correlation coefficients (R^2) vary from 0.49 to 0.59.

According to the regression trends (for porosity values greater than 10%) both pisoids and grainstone lithologies present moderate to very high permeability values. By contrast, fusulinid packstone/grainstones start reaching moderate permeability values from 15% of porosity values. Although the pisoid and fusulinid textures have coarser grain lithologies that tend to supply very high interparticle primary depositional porosities, the diagenetic mechanism affecting the middle level seems much more effective for maximizing permeability. The middle pisolitic level records higher values for permeability for a larger range of porosities

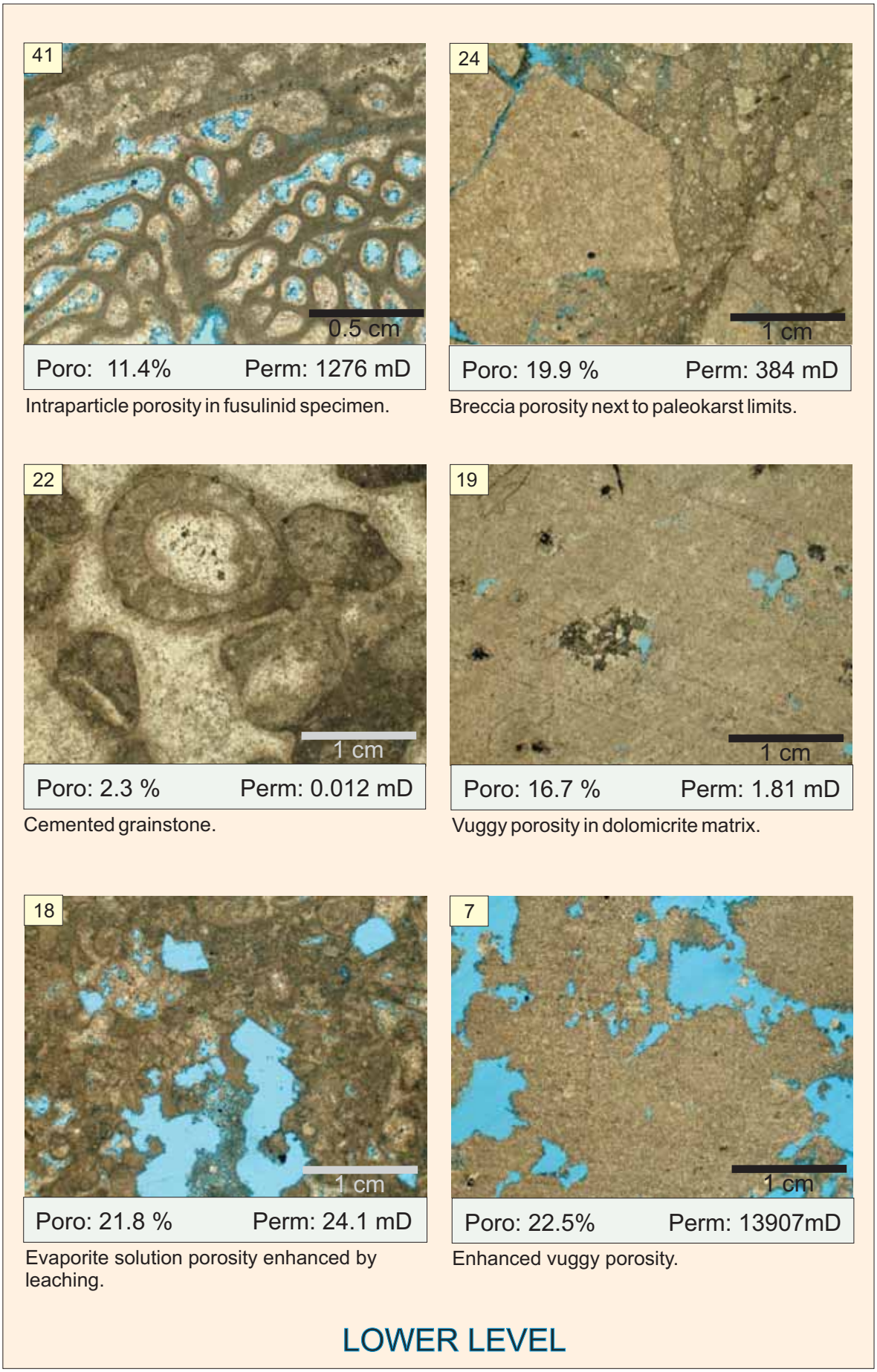

Fig 7.3. Pore types in each stratigraphic level studied.

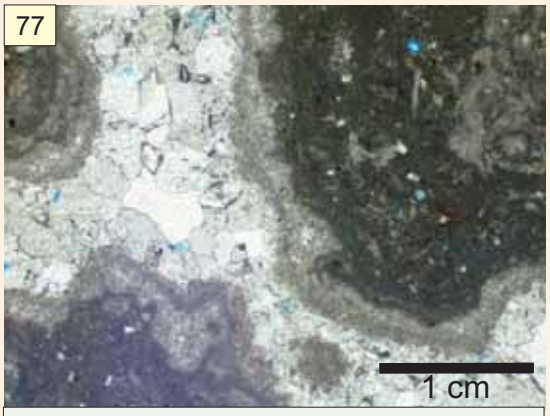

Poro: 2.5 % Perm: 0.01 mD

Interparticle porosity occluded by dolomite cements.

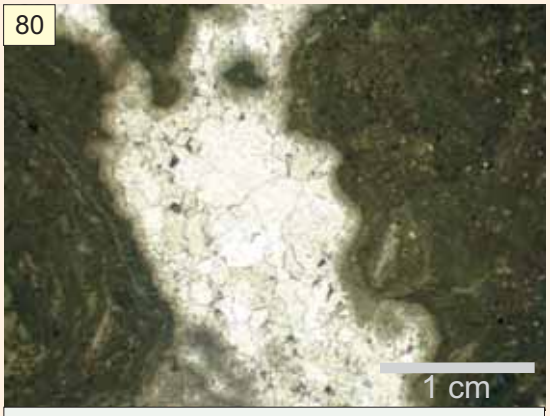

Poro: 2.8 % Perm: 0.018 mD

Primary porosity filled with dolomite cement.

Poro: 18.4 % Perm: 1047 mD

Fracture porosity.

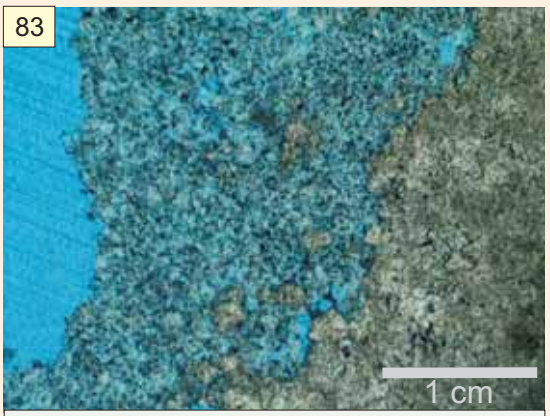

Poro: 4.5 % Perm: 0.035 mD

Permeability systematically decreases when dickite cement is present.

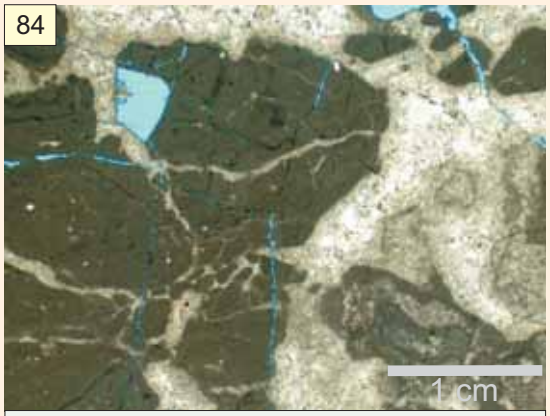

Poro: 11.2 % Perm: 52.8 mD

Breccia porosity cemented and cut by a later generation of fracture porosity.

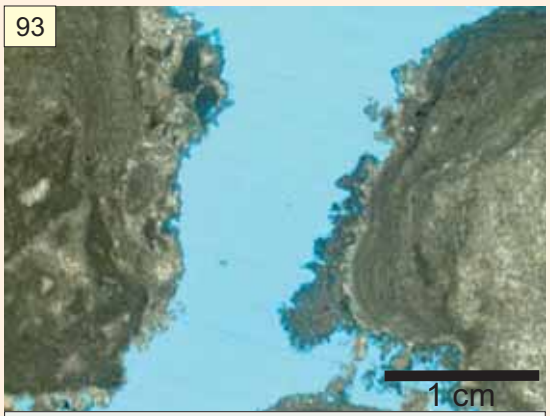

Poro: 7.3 % Perm: 489 mD

Corrosion of the fine matrix results in open interparticle porosity.

MIDDLE LEVEL

Fig 7.3. Pore types in each stratigraphic level studied.

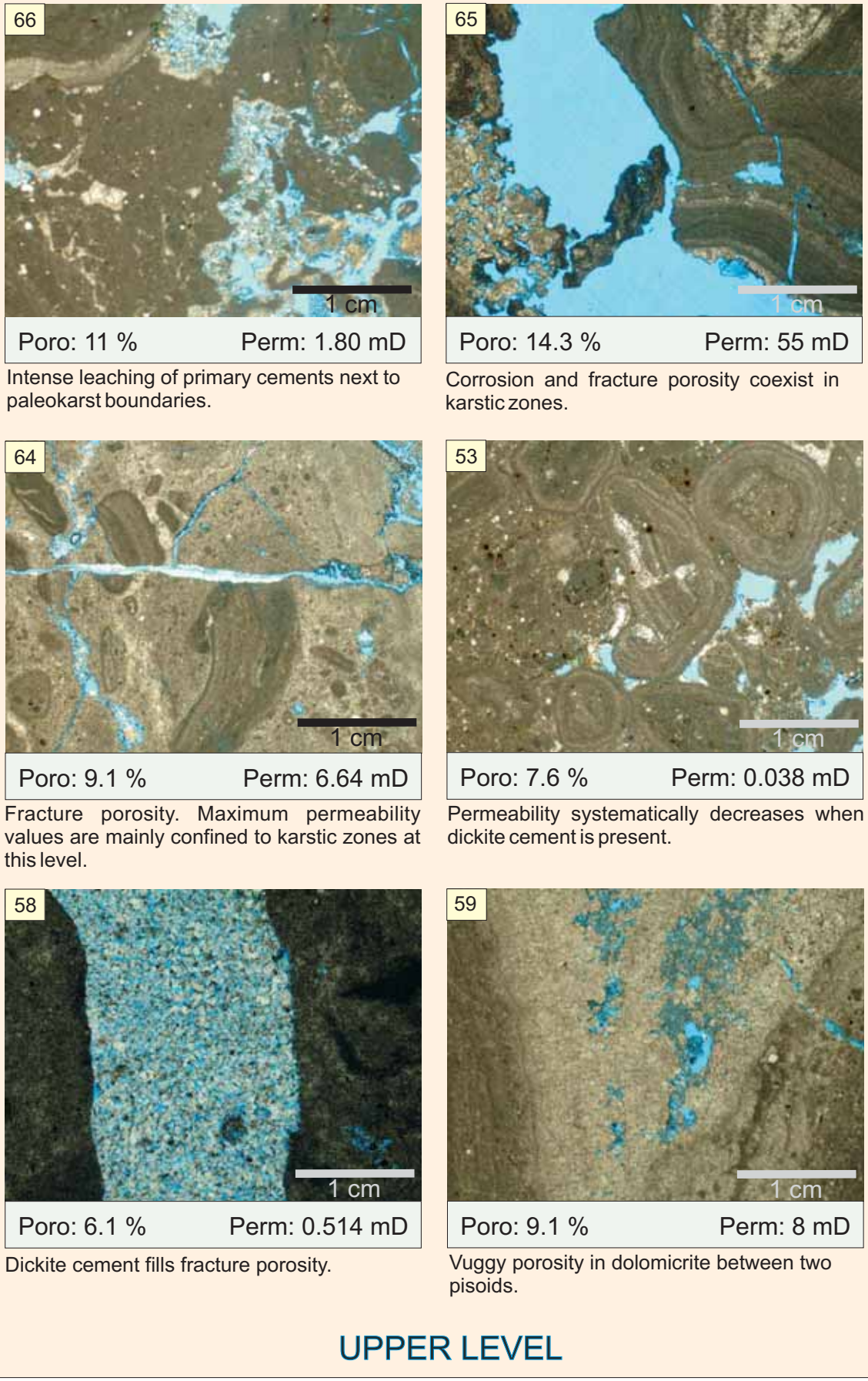

Fig 7.3. Pore types in each stratigraphic level studied.

than the upper level. The fusulinid level records the maximum permeability values (>10000 mD) although dispersion is higher.

The spatial distribution of these samples must be analyzed in order to examine the dispersion of the permeability values. The spatial distribution may supply some insights into whether or not the mechanism for enhancing permeability is structurally controlled. The examination of cement types that occlude the pores is also necessary for determining the grade of diagenetic modification.

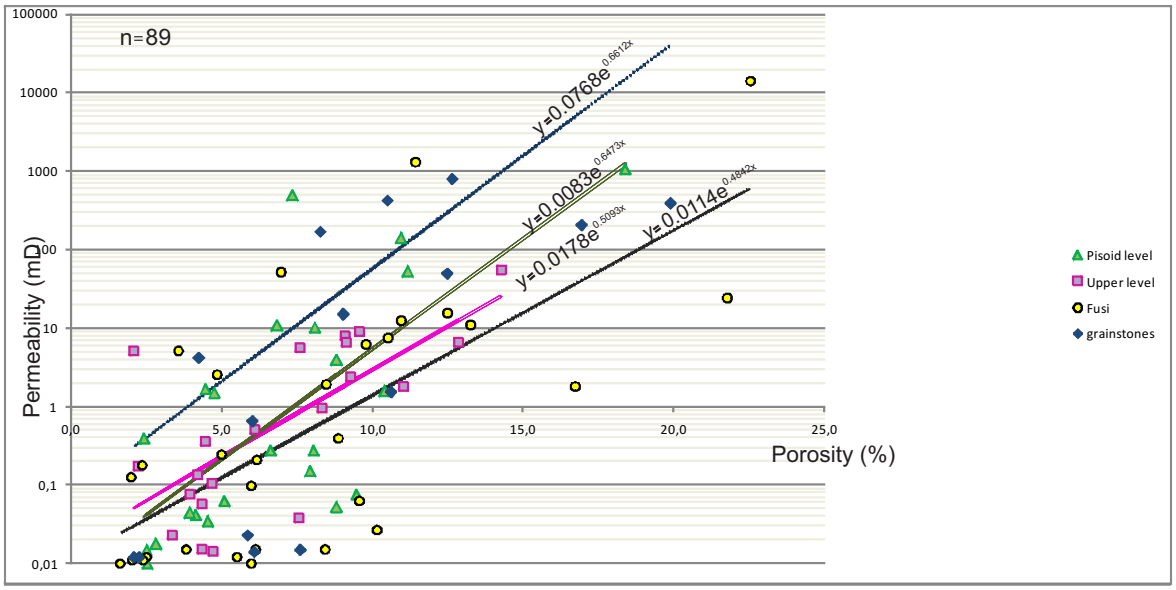

Fig. 7.4. Cross-plots of porosity versus permeability according to rock textures of the different horizons. The straight lines correspond to exponential regression lines for each of the carbonate textures at each selected level. The coefficients of determination (R2) for each regression line are shown in Table 7.2

8.- Spatial distribution of reservoir properties

The position of the poroperm samples has been orthogonally projected along lines at different heights in order to analyze the distribution poroperm values as a function of the distance from the karst modified fault boundaries (Fig. 7.5).

Fig.7.6 shows the plots of porosity and permeability vs. distance to karst modified fault boundaries.

- ***Lower level.***

As stated above, the lower level displays a great dispersion of values. In this level, it is regularly observed that porosity values covary with permeability values with the exception of few samples (i.e. Sample18) that record moderate to high porosities and low values of

permeability. Given the location of these samples next to the karst boundaries, high permeability values are expected. Examination of these samples reveals the presence of solution enhanced evaporite moulds. This could account for the reduction of permeability given that cementation, particularly by anhydrite, is the dominant mechanism of porosity destruction in carbonate reservoirs (Southwood and Hill, 1995). The remaining open pore space could have resulted from the late dissolution of the evaporite minerals, and thus, indicates that porosity in these samples is secondary and did not contribute to fluid flow during karst development (Fig 7.3: Sample 18).

Generally samples near karst boundaries record high values of both porosity and permeability. The high porosity values correspond to fracture and breccia porosity types genetically related to karsting. Unexpectedly, Sample 22 appears as a tight dolomite cemented grainstone with very low values of both porosity and permeability (Fig 7.3: Sample 22). With an increase in the distance from fault limits, permeability values tend to decrease with few exceptions (i.e. Sample 7) (Fig 7.3: Sample 7). In general, the petrophysical karst impact onto host carbonates expands laterally about 20 metres in this level.

- ***Middle level.***

In this level, porosity values covary well with permeability values. The wide range of higher permeability values (> 40%) is confined between 5 to 12% of porosity values.

There is no clear pattern vs. the fault distance. It seems that poroperm values oscillate along the stratigraphic level with weaker fault control. Karst boundaries record both high and low levels of permeability and porosity values remain fairly constant along the stratigraphic level ranging between 5—10 %.

Examination of the samples in this level reveals that cementation plays a significant role in sealing porosity, giving rise to ineffective permeability paths. In zones of tight cementation, permeability decreases considerably. Major permeability values are confined to karst boundaries and solution enhanced zones which result in intercrystalline and vuggy porosity zones. These irregular pores are centimetre sized and are originated by crystal dissolution as well as by mud sediment leaching (Fig 7.3: Sample 93).

The lateral modification of the carbonate host in this level is more pronounced and expands to over 40 metres from the fault boundaries.

- ***Upper level.***

This level is the least affected level by karst processes since it is slightly displaced by faulting and does not localize lateral extensions of stratabound caves (Fig. 7.1).

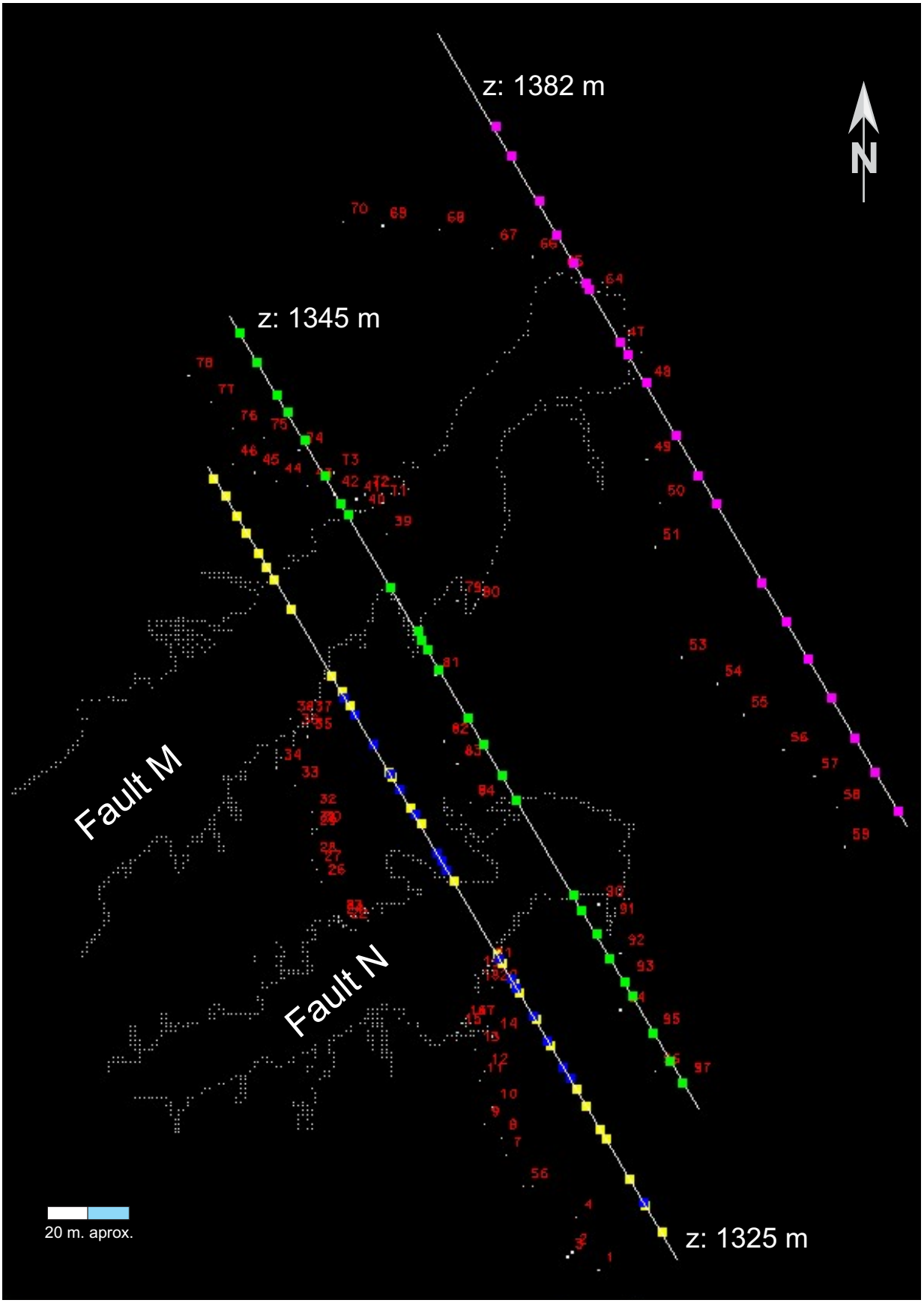

Fig. 7.5. Map view of the two faults (M and N) with the limits of the paleokarst and the location of the poroperm samples. An orthogonal projection of the position of the samples onto lines of different elevations has been done in order to plot the poroperm values versus the distance from the paleokarst limits (Fig. 7.3).

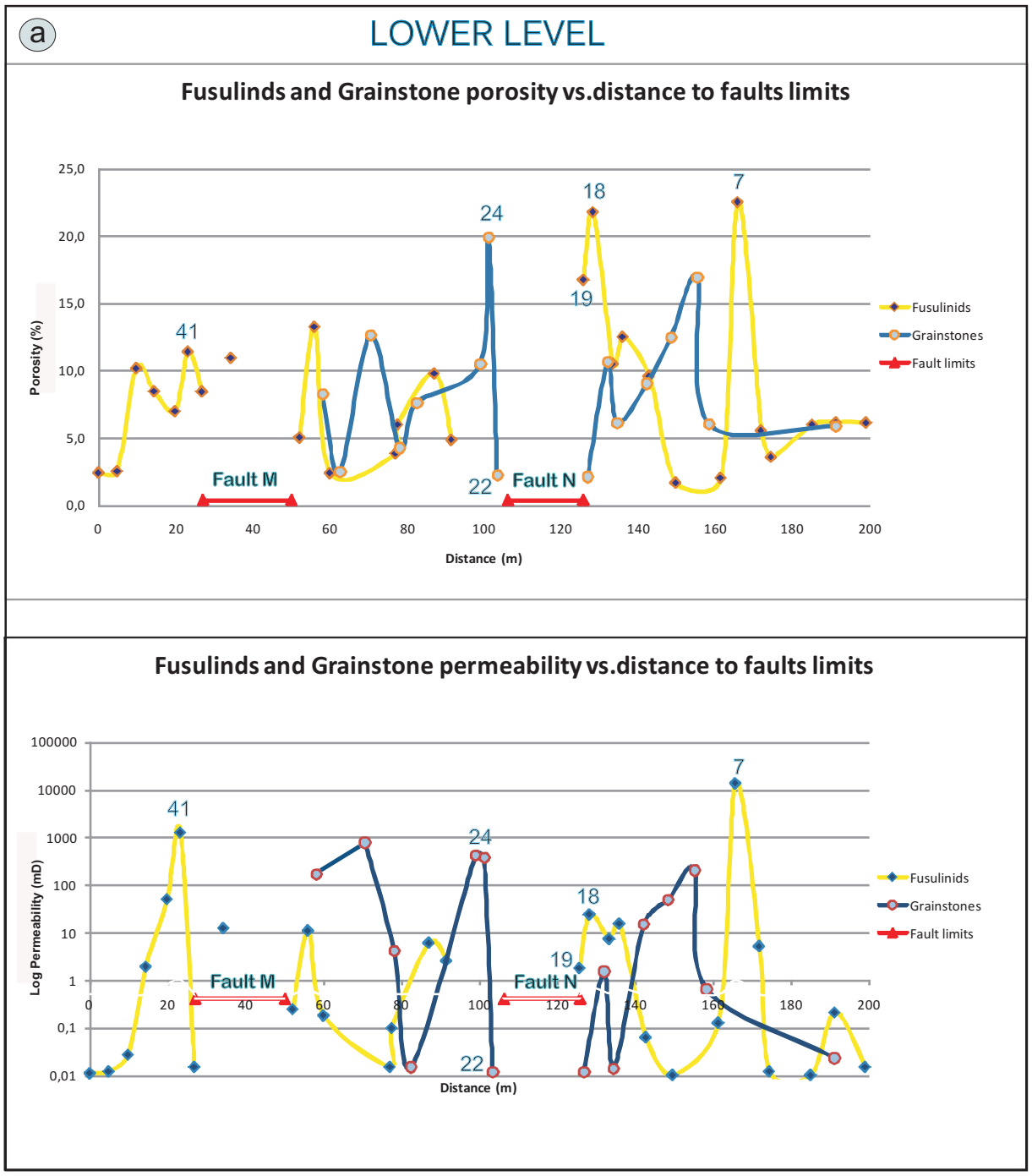

Fig. 7.6a. Crossplot of the poroperm values of the lower level versus distance to solution-modified fault boundaries.

Porosity and permeability are limited to a lower range of values in the upper level. Generally the permeability values in this level do not exceed tens of milidarcies and most values of porosity fall between 5 — 10%. The leaching of the interparticle dolomicrite is less pronounced in this level (Fig 7.3: Sample 59) and high amounts of dickite cements occluded pores and fracture porosity.

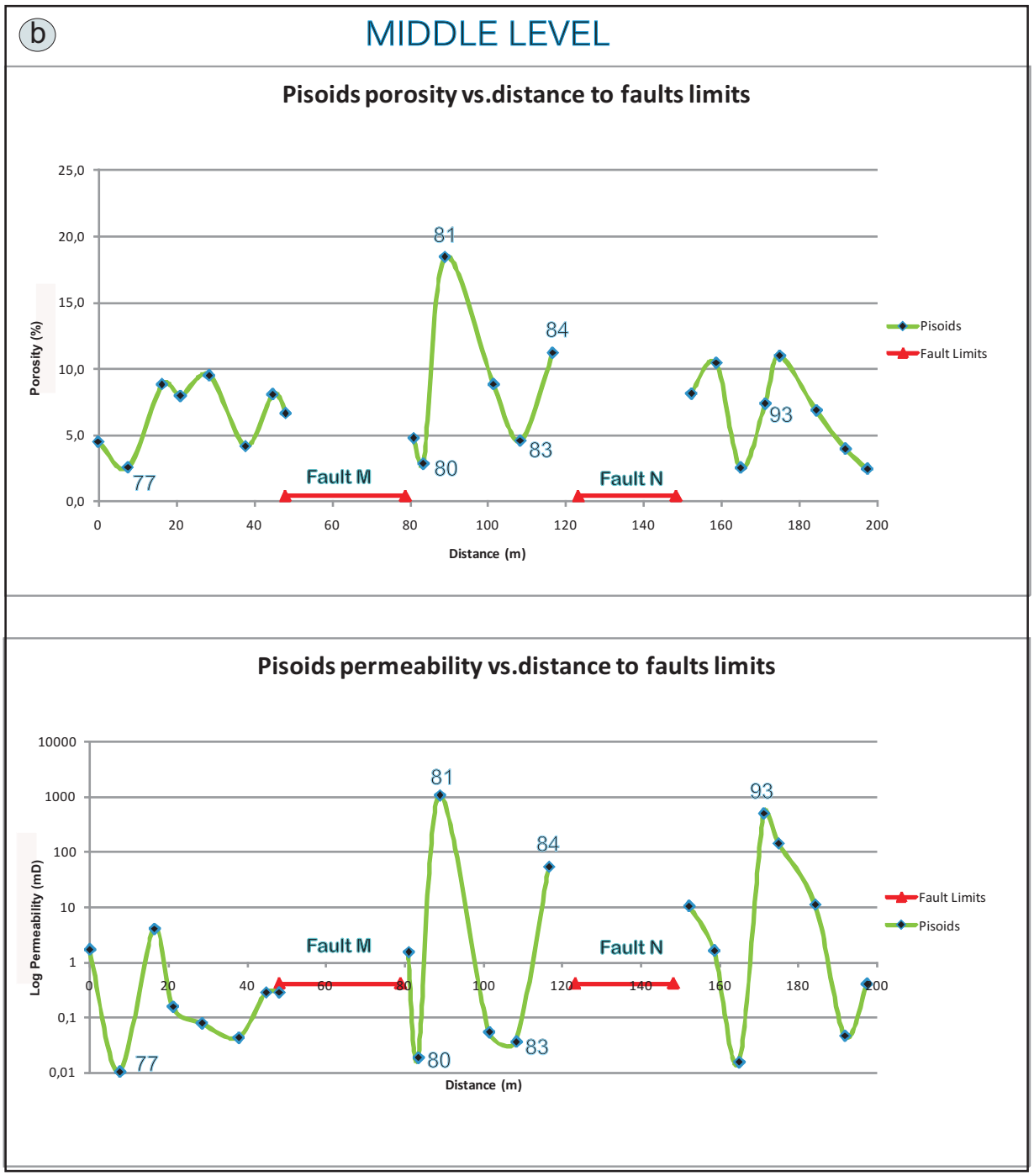

Fig. 7.6b. Crossplot of the poroperm values of the middle level versus distance to solution-modified fault boundaries.

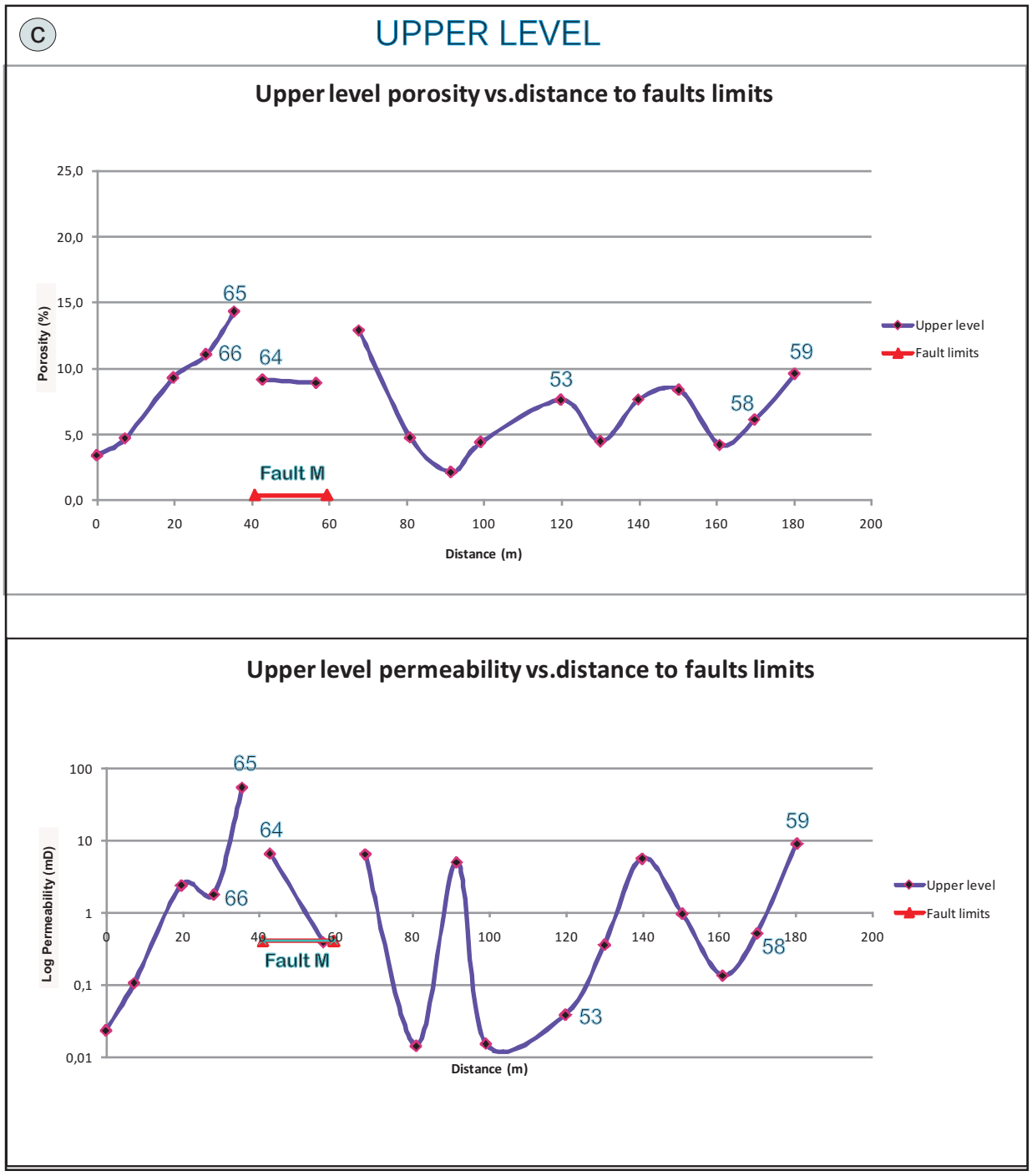

Fig. 7.6c. Crossplot of the poroperm values of the upper level versus distance to solution-modified fault boundaries.

The lateral variations of petrophysical properties in the upper level are restricted to few metres from the fault M boundaries towards the NNW and follow an oscillating pattern of low porosity and permeability values towards the SSE.

9.- Diagenesis and reservoir quality

Primary pore space is usually diagenetically modified, especially in Paleozoic systems. Since diagenesis exerted a significant control over the evolution of reservoir properties, it is essential to analyze the local impact of cementation vs. dissolution in Rattlesnake Canyon. The diagenetic sequence of Rattlesnake Canyon comprises different diagenetic episodes (Chapter 6) which can be summarized as:

1) Early marine cementation.

2) Replacive dolomitization.

3) Episodes of dissolution which could cyclically alternate with episodes of dolomitization. These processes were responsible for the generation of mouldic and intercrystalline porosity.

4) Anhydrite formation. Anhydrite emplacement was nearly syndepositional because of the anhydrite displacive fabrics identified in the paleokarst filling sequence.

5) Dolomite cementation. Dolomite cements are found lining moulds of leached carbonate grains. After replacive dolomitization, waters supersaturated with respect to dolomite were able to seep into the platform in a shallow burial environment, precipitating dolomite cements. This mechanism was responsible for the late sealing of primary porosity.

6) Alteration and dissolution of anhydrite. This process was interpreted to have resulted from oxidation of hydrocarbons and BSR.

7) Dedolomitization and kaolinite and calcite cementation associated with the HC charge and the meteoric flushing of the platform.

8) Hydrothermal phase responsible for the precipitation of the coarse spar.

The last three events are concomitant with uplifting and flushing of meteoric water. The variation in calcite/dedolomite isotopic values is attributed to the mixing of fluids of diverse origin (Fig. 6.16). Hydrocarbon charge and its associated processes coupled with the hydrothermal episode led to the main late diagenetic alterations that sealed secondary porosity.

9.1- Dissolution

The main episodes of dissolution in Rattlesnake Canyon are genetically related to the depositional setting as well as to the karst development. The influence of the karst system in the generation of porosity is evidenced by the large volume of pores concentrated close to the system. Early dissolution resulted in the generation of mouldic, intercrystalline and vuggy pores. Much of this leaching is thought to have occurred during the development of the karst system as a result of the infiltration of fresh-waters during sea-level lowstands in a mixing environment. Early fracture networks proved to be good conduits for the fluid flow since fracture boundaries are solution modified. The intervals with pervasive dolomite cementation,

which are frequent in the karst-damage area, are indicators of the spatial distribution of primary porosity due to karst development. In fact, the zones where these dolomite cements are present were also effective in later dedolomitization preferentially initiated along fractures.

The late diagenetic episodes modified the original reservoir properties of the system and also entailed episodes of corrosion. The acidic conditions resulting from the hydrocarbon oxidation led to the episodes of corrosion in the dedolomite sequence and to clay cementation. These cementation episodes reduced the primary porosity and permeability of the system.

9.2.- Cementation

Dolomitization exerts a considerable influence on poroperm values (Purser *et al*., 1994; Machel, 2004) and can enhance or reduce porosity depending on the mode and timing of dolomitization (Mazzullo, 1992). Early dolomitization is frequently associated with anhydrite precipitation, a process that commonly has a negative effect on reservoir quality.

Increased anhydrite cementation is observed in the uppermost parts of the paleokarst filling sequence. The muddy matrix poroperm samples containing displacive anhydrite have lower poroperm values in Rattlesnake Canyon. However, the number of anhydrite-cemented samples is not enough to establish a clear relationship between this cement type and the reservoir quality. Most samples analyzed came from the adjacent host rock, and anhydrite is solely detected within the paleokarst filling sediments.

The higher volume of cements (calcite and dickite) occluding porosity were precipitated during late telogenetic conditions (Chapter 6). During these conditions, the fracture-controlled system was probably reactivated supplying effective flow networks as evaporite dissolution increased. A major preservation of the early dolomite cementation, especially in the grainstone facies, is observed with the increase in distance from the faults.

Many pisolitic poroperm samples are affected by further calcite cementation that occludes the remaining pore space. The latest thermal event is considered to be the largest cementation episode that caused the occlusion of the remaining pore space, which probably originated after evaporite dissolution.

According to Lambert (1983), the average porosity and permeability values of the Yates formation are 9.74% and 10.79 mD. In the light of our findings, the Rattlesnake Canyon karst system clearly modified the reservoir properties, giving rise to significantly higher permeability values.

10.- Conclusions

Karst development had a much greater effect than the inherited depositional rock textures on the petrophysical properties of the host rock in Rattlesnake Canyon.

Mouldic, intraparticle and vuggy porosity are the pore types that result in higher permeability values.

Major permeability values are confined to karst boundaries and are linked to fracture and breccia porosity. The lateral expansion of the dissolution processes reveals a large presence of solution enhanced intercrystalline and vuggy pores.

Major lateral heterogeneity is associated with pisolitic shelf crest facies in a level that was vertically displaced by faulting. This together with the absence of late lateral diagenetic modifications indicates that the best reservoir properties in the carbonate host rock originated during syndepositional faulting.

The original poroperm heterogeneities were mainly inherited from the syndepositional karst development but were subsequently modified during diagenetic processes. Dolomite cements sealed most of the vuggy porosity that originated because of early dissolution. During late telogenetic conditions there were different episodes of corrosion associated with the hydrocarbon charge. As a result, dickite cementation and dedolomitization brought about partial sealing of porosity and significant reduction of permeability especially in fracture areas. Laterally, modification of dolomite cements is minor and high permeabilities are attained. The last hydrothermal episode led to high volumes of calcite cementation that sealed the major porosity created by evaporite dissolution.

Chapter 8
General discussion

The Rattlesnake Canyon paleokarst system constitutes an example of an extremely well preserved ancient system that has proved effective in the creation and the retention of early porosity and permeability. Since eogenetic conditions generated good reservoir properties, a thorough understanding of the initial hydrogeological, fracture and depositional controls is essential for application to analogue reservoirs. Paleokarst field-sized analogue models based on three-dimensional data from outcropping examples are poorly documented, and their associated dissolutional processes as well as their evolution continue to be little understood.

The potentially important factors in early karsting for review and discussion in an overview of regional diagenetic implications include: (i) the depositional environment and syndepositional faulting and (ii) the regional and local hydrodynamics.

The depositional textures do not seem to strictly control the distribution of solution cavities. The stratabound karstic features developed in the halocline or mixing zone are generated by freshwater-saline mixing and controlled by synfaulting with interplay of sea-level variations. These factors should be considered in the classic hydrogeological model of the Carbonate Island.

The particular location of the system in the platform margins and the hydrogeological regime that favoured the formation of freshwater lens have proved useful in determining karst timing. Karsting in Slaughter Canyon has been regarded as syndepositional on the basis of the paleokarst filling sequence and synsedimentary faulting patterns (Koša, 2003, 2006). In Rattlesnake Canyon, restoration of faults M and N shows that stratabound caves are horizontally aligned in each step of restoration. This is a good indicator of the generation of porosity in specific horizons associated with paleohalocline positions. The generation of these stratabound paleocaves was controlled by the syndepositional faulting resulting in abandoned and reused stratiform passages presumably developed during stillstands (Chapter 4: Fig 4.9). The final pattern of mixing dissolution is difficult to decipher without restoration of the faults because faulting produces migration of the former halocline positions. Nevertheless, after restoration the correlation of these levels is precise: beginning at the top of Yates 2 and continuing until the Upper Yates 4 (Chapter 4: Fig. 4.9). According to this interpretation,

the most intense period for stratabound cave formation is during the deposition of Yates 3. During the Yates 3 cycle a shallowing upward trend for the paleohalocline position suggests that the lens gradually thinned towards the top of the sequence. This trend together with the detection of displacive anhydrite moulds at the top of the paleokarst filling sequences suggests that the reduction of the lens coincides with a change to arid conditions during highstands. The system was then confined to coastal sabhkas at the top of the cycles and this type of dissolution ended during arid conditions at the top of Yates 4. As a result, the Rattlesnake Canyon system can be analyzed as a composite karst system.

Halocline dissolution occurred via bedding-plane dissolutional conduits that promoted vuggy and intercrystalline pore types which concentrated along the lateral stratabound caves and extended towards the host rock. Vug-dolomite cements and progressive textural modification towards dolomite frameworks may be proportionally indicative of the degree of early permeability that promoted the cavernous system. The shallow burial dolomite cements sealing this karst derived porosity is compatible with precipitation from mesosaline waters under slightly reducing conditions based on stable isotopy and trace element geochemistry. Pore-filling dolomite was precipitated within cavities conditioned by the remaining porosity after dolomite replacement and minor early evaporite dissolution. In these lateral areas, this shallow burial cementation stage seemed to have been completed and was less diagenetically modified by later meteoric flushing of the platform during uplifting. By contrast, in the paleocave zones (much more disrupted and fractured), diagenetic modification is strong, indicating that porosity and permeability were significant and effective in fluid flow during the Tertiary. Moreover, dissolution of evaporites by inflow of meteoric water into the system probably enhanced fluid flow, creating new porosity through the connected cavernous system.

The absence of a normal marine fossil assemblage and the presence of anhydrite at the top of the cycles in the paleokarst filling sequence suggest that the system culminated in an evaporitic depositional environment, leading to considerable thinning of the freshwater lens.

Substracting the volume of the dolomite vug-filling cements and dolomite frameworks precipitated under shallow burial conditions can provide a quantitative approach of the early porosity of the system. Because the system is strongly modified by later diagenetic events in the paleocave areas and in the preserved fracture networks at the top of the karst damage zones, it is much more difficult to predict reservoir porosity in these areas. However, local permeability might have been high, especially along fractures, allowing concentrated solutions to escape after evaporite dissolution, thereby contributing extensively to the creation of secondary porosity.

From the fracture fills recognized (dedolomite/calcite cements associated with dickite) it may be assumed that permeability trends were conditioned by the early fracture networks and by the breccia porosity in the most chaotic areas of the paleocave zones. Fracture density and distribution is well determined in the system. The estimation of quantitative volumes of karst porosity in the brecciated areas is much more difficult to predict since siliciclastic

diagenesis is not limited to occluding porosity but has also modified early depositional textures involving feldspar dissolution.

Bottrell et al, (1991) argued that bacterially mediated early S redox reactions contributed significantly to the development of porosity in freshwater-saline mixing zones in carbonate aquifers. These authors documented the presence of crusts containing pyrite and/or gypsum in the mixing zone of Cousteau's Blue Hole, North Andros, Bahamas. The association of pyrite with bacterial sulphate reduction (BSR) was based on mass and isotopic analyses of S species. BSR was interpreted to occur near the base of the freshwater-sea water mixing zone, generating a 1m thick brown coloured level approximately 10 m below the top of the mixing zone. Sulphur redox reactions were associated with an overall rise in carbonate corrosion by increasing pCO_2 and by the oxidative generation of protons where this could be decoupled from the production of HCO_3 alkalinity.

Similarly, early BSR could have existed in the karstic lateral extensions of the Rattlesnake Canyon paleokarst system. These S redox reactions could have generated a pattern of stratiform corrosion, preventing the sealing of porosity given that the system did not facilitate cementation without having a buffering effect associated with high HCO_3 alkalinity values. The preservation of this stratiform corrosion distribution reproduces accurately the geometry of the paleo-mixing zone or halocline through the coloured levels recognized in the field. However, their original products, which could be associated with an early episode of BSR, were strongly modified or removed from the system. There is no evaporite relict in the paleokarst system and evidence of former pyrite can only be inferred from some S peaks detected in EDS spectra and from the resemblance to framboid structures of some of the hematite aggregates (Chapter 6: Fig. 6.3: Plate 2:d). Thus, this hypothetical early BSR episode cannot be verified by stable isotopes since the late diagenetic episodes strongly modified or dissolved early products.

The main factors that control pyrite formation and the duration of BSR processes are well documented by Machel (2001):

1) - Concentration of H_2S. When the inhibitory H_2S concentration is reached (>5-10 %) BSR stops.

2) - Limitation of organic matter.

3) - Low T and shallow environments which commonly facilitate H_2S diffusion into the overlying oxygenated zones and where molecular O_2 is transported advectively into BSR zones.

The first case is the least probable to have occurred in Rattlesnake Canyon since high permeability values in these zones suggest the generation of an open conduit system which inhibited buffering with the subsequent carbonate precipitation.

Organic matter in blue holes can be supplied by sporadic inputs of incoming tides.

The shallow environment probably restricted the volumes of pyrite in these zones since oxygenated zones might be easily reached by diffusion or advection in a shallow highly permeable system.

Several processes could have caused pyrite precipitation including syndepositional to early diagenetic BSR or telogenetic weathering also associated with BSR. In our system the isotopic signal of BSR is recorded in the calcites associated with the Tertiary uplift. Since calcites replaced early evaporites and since their replacement is not easy to decipher, they often seem to occupy primary positions and can be mistakenly associated with these early BSR episodes. The presence of primary HC fluid inclusions in these calcites as well as their association with large amounts of corroding dickite cements facilitated their constraint to a secondary telogenetic stage of diagenesis.

Siliciclastic diagenesis is similarly attributed to the telogenetic domain where the acidic conditions of the HC derived fluids mixed with meteoric waters percolating through the platform promoted the generation of abundant kaolinite cements and Fe oxyhydroxides sometimes trapped within the poikilotopic calcites. The large amount of carbonate cements (dedolomite, calcite and thermal spar) precipitated during late diagenetic episodes suggests that the system acted as a closed system as cementation increased and/or dissolution was more significant allowing high alkalinity conditions. The association of goethite with calcite mosaics indicates decay in pH and therefore a pronounced buffering, inducing carbonate cementation. Synsedimentary faulting and early mixing zone dissolution provided effective early permeability networks, creating porosity and inhibiting massive early carbonate cementation. The late evaporite dissolution provided secondary porosity followed by progressive episodes of cementation. In line with this, we could link the reduction of connectivity with the ineffectiveness of the intended reservoir and hydrocarbon entrapment.

Thus, the paragenetic sequence discussed in Chapter 6 could also include a probable episode of early BSR in the mixing zone that would generate significant reservoir porosity in oscillating mixing zones on the time scale of single sea-level stillstands. Since dolomitization occurs in the area in a diagenetic realm of surface and shallow burial, the close relationship between framboid pseudomorphs of former pyrite and dolomite rhombohedra can be a reliable indicator of an early episode of BSR.

If this early BSR episode had occurred, it would necessarily have taken place in the water column. Thus, the stratabound caves indicate former zones of shallow phreatic sulphate reduction horizons not associated with any exposure. This scenario increases the difficulty of exactly predicting sea-level paleopositions since the position of the halocline is therefore a relative indicator of paleosea-level positions. The thickness of the halocline can oscillate between about 1 metre and few tens of metres in caves in similar settings (Moore et al, 1992; Stoessell, 1995). However, the thickness of the lens is mainly conditioned by three factors: the amount of freshwater recharge, eustacy and the rate of water agitation. The position of the halocline is located below sea level when recharge is a significant input in the system.

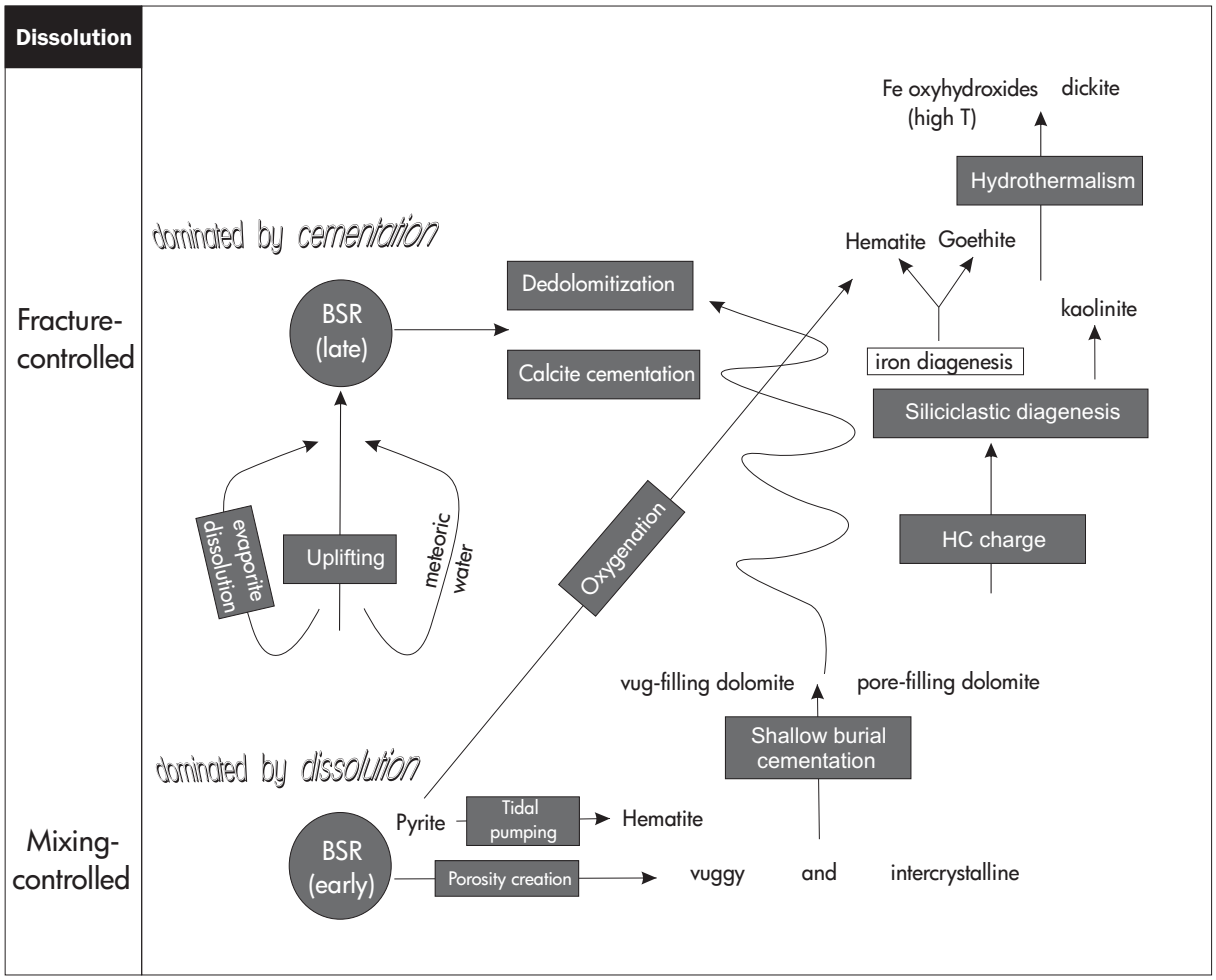

Fig. 8.1. Early and late bacterial sulphate reduction processes and their relationship with the paragenetical sequence and the type of dissolution.

Lowstands favour freshwater recharge in wet or semiarid climates. Hubbert (1940) showed that the interface is deeper under dynamic conditions than under static conditions.

Given these factors, we suggest that there was a gap between the position of the halocline and the position of the sea-level. The length of this gap was much more pronounced during the early stages of the Yates 3 cycle, probably because of a significant sea-level fall and freshwater recharge. Ye and Kerans (1996) suggested that the amplitude of 4th –eustatic cycles within the Yates Formation range between 15-50 m whereas Borer and Harris (1991) estimated a range varying between 8-12 m. The position of the oldest lens in the restoration step of the top of Yates 2 far exceeds 50 m, corroborating the existence of this gap (Chapter 4: Fig.9:a). As the system evolved during Yates 3 we found a progressive reduction of the freshwater lens and a reduction between the distance of the halocline and the absolute sea-level position. At the top of Yates 3 we suggest that recharge was insignificant and climatic conditions were arid owing to the presence of evaporite moulds at the top of the cycle. Similarly, we found evaporite moulds at the top of Yates 2, suggesting a composite karst system despite the absence of younger stratabound caves in the outcrop. As Fault N was formed during

Yates 3 deposition, it is thought that the densely fractured graben system played a major role in concentrating fluid flow along fracture paths, boosting recharge effectiveness which enhanced matrix dissolution.

Since the base of the water lens was therefore located below sea level, recharge might have been more significant than expected. Koša (2003) suggested that recharge was scarce in the area due to the aridity of paleoclimate conditions and the absence of stratiform dissolution in Slaughter Canyon. The older similar stratiform karst pattern in the paleokarst of San Andres Formation indicated a transition from arid conditions during sea level highstands to semiarid wetter conditions during lowstands (Craig, 1988; Tinker et al., 1995). Despite the time gap between the Leonardian and the Capitanian paleokarst systems, we suggest parity for the mechanisms of both systems under similar climatic conditions.

Since early dissolution is controlled by sea-level variations with the interplay of faulting, the spatial distribution of porosity and permeability could be effectively predicted along specific stratigraphic horizons if we had a sound knowledge of the dimensions of eustatic sea level falls. Nevertheless, a good prediction can be inferred at the top of the cycles when the system was constrained to a sabhka environment during highstands.

The construction of the 3D model initially sought to limit two zones (the paleocave zone and the karst damage zone) based on the lithofacies distribution and on the geometry of the karst affected zones. With subsequent diagenetic studies we are able to refine these restrictions and argue that these zones also reflect two different patterns of diagenesis. The early mixing pattern of diagenesis is retained along the stratabound areas of the karst-damage zone which localize high permeability values at present. The fracture zones preserved from faulting at the top of the karst damage areas and the brecciated paleocave areas have been massively cemented, occluding secondary porosity and sealing the system. These diagenetic patterns are spatially well fixed into the domains of the irregular surfaces, although the early diagenetic pattern could be extended few metres towards the host rock in line with the poroperm values of synfaulting levels (Chapter 7).

Modelling these zones constitutes an excellent method to spatially constrain diagenetic domains and establish relationships between diagenetic trends and early depositional zones affected by mixing dissolution. The 3D model served to spatially restrict the most chaotic zones with fracture controls. Constraining spatially these domains in detailed outcrop scale can prove effective in reservoir prediction in analogue reservoir cases.

Given the in-depth study of the diagenetic processes during the karst evolution we can assume, on the basis of the available isotopic signal of the calcite and dedolomite products, that the late diagenetic fluids exerted a regional influence throughout the Capitan Reef Complex. However, the hydrocarbon migration was confined to the paleokarst faulted areas of the backreef in the Yates unit of Dark Canyon, Rattlesnake Canyon and probably Slaughter Canyon. Because of the lack of early mixing porosity features reported in these areas and because of the lack of isotopic data of vug-filling dolomite cements, the extent of the early

mixing dissolution process cannot be generalized to these canyons. Nevertheless, the karst features in these three canyons have significant similarities: the timing of the syndepositional faulting, the morphology of the caves and the nature of the karst infills.

Limitations of the study and suggestions for future work

This detailed study provides a comprehensive understanding of the evolution of the paleokarst system and the associated dissolutional and cementation processes that regulated the reservoir properties. Despite the scientific and industrial contribution to the knowledge and reservoir characterization of paleokarst systems, the study does not cover the scale required for interpreting and characterizing petroleum reservoirs. Further research is warranted to fill this gap.

The 3D paleokarst model of Rattlesnake Canyon has substantial limitations as it represents surfaces that do not have structural control, especially the karst damage zone limiting surfaces but do have matrix control in stratabound dissolution zones. The penetration of the karst alteration is difficult to predict owing to the heterogeneity of the system and to the lack of subsurface data in depth, which prevents us from assessing the penetration of the karst below 20 metres from the platform top. The model is tightly constrained to the outcrop geometry of the karstic alterations, assuming that the pattern of dissolution is continuous in zones of 1.5 m of extent. Uncertainties in modelling diagenetic surfaces reflect the multi-scale heterogeneity of the system and the difficulty of tracing fluid paths. The continuity of the model is difficult in subsurface and could be achieved by reducing the degree of spatial precision, i.e. constraining the boundaries to interruptions in the continuous trace of radar signals. This should certainly result in incrementing the constant ranges to more than 1.5 m and in reducing the accuracy of dip domains.

Microthermometry of the primary hydrocarbon rich fluid inclusions in calcites could reveal homogenization temperatures and salinities of the fluids operating during that time.

The incorporation of the data into a reservoir model with fluid simulations would be useful for assessing conductivities along vertical fracture networks and along the lateral levels of enhanced dissolution. These types of models proved very effective in the design of production strategies in analogous systems. To simulate early poroperm conditions in the karstic lateral levels, substraction of dolomite cements of the stratabound caves is recommended since these zones remained open until shallow burial when they were occluded by the vug-filling dolomite cements and the indurated dolomite frameworks.

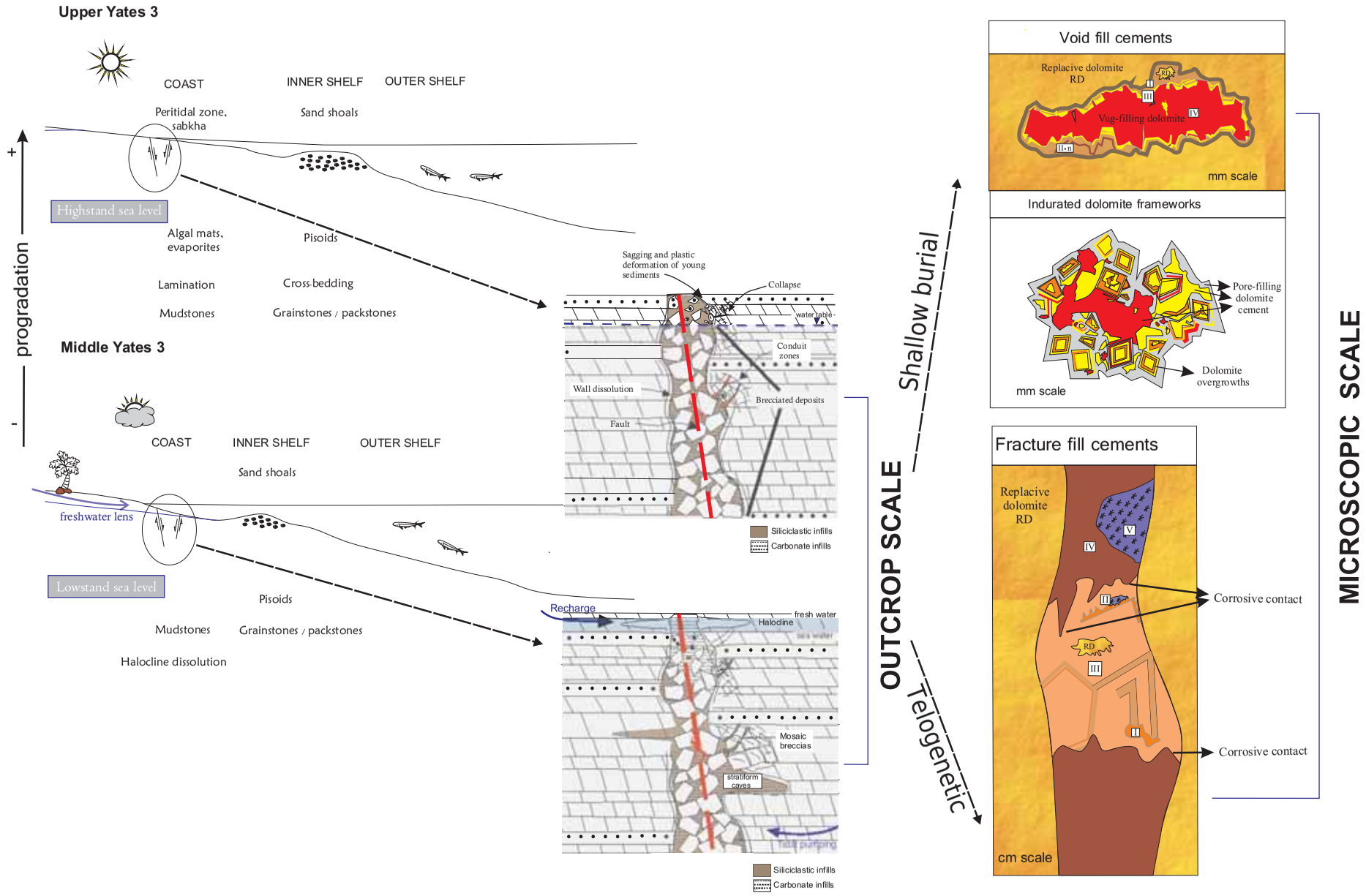

Fig. 8.2. Multi-scale heterogeneity of the system. Sea-level variations during the progradational tendency of Yates 3 originated two dissolutional mechanisms of dissolution generating vertical fracture fluid flows and stratabound caves. Both mechanisms evolved differently during diagenetic modification producing two different patterns at microscopic scale.

Chapter 9
Conclusions

This thesis adresses the relationships between syndepositional faulting and karst development in the Capitan platform margins in Guadalupe Mountains, New Mexico, USA. The thesis supplies information relative to these relationships by the study of two solution-modified syndepositional faults (M and N) in Rattlesnake Canyon. This scenario has resulted successful for deciphering the sequence of karst development and for establishing its controls. Depositional, fracture and diagenetic controls on karst development created distinct geometries of karst alterations. A 3D paleokarst model was built to represent the spatial paleokarst heterogeneity and to determine the extent of the penetrative system. The study also offers new insights into the diagenetic evolution of the system that controlled the modification of the reservoir properties.

Evidence of early speleogenesis recognized in the field

∘ Early syndepositional fracture networks are solution-modified and contain reworked clasts with evidence of corrosion on their boundaries.

∘ Abundant reworked clasts within fracture fills and brecciated deposits of the paleokarst sequence fill are derived from carbonate levels of the host rock.

∘ Fracture fills and the paleokarst sequence fill are dolomitized with the exception of calcite cements whose timing is often unclear in the field.

Spatial distribution of karst geometries and distinction of karst zones

∘ Two distinctive dissolutional geometries are recognized: a vertical continuous pattern and sub-horizontal separate horizons emerging from the fault boundaries.

∘ The vertical dissolution pattern mimics and enlarges the geometry of both faults and is attributed to fracture/fault cave development.

∘ The sub-horizontal pattern of dissolution concentrates along specific stratigraphic horizons of the host rock with no stratigraphic correlation. This dissolution pattern is termed stratabound dissolution in this study and is responsible for the creation of stratabound caves or passages.

∘ At the top of the paleokarst sequence fill, where this sequence is preserved from faulting, the trace of the stratabound passages can be followed towards the inner parts of the faults. In these areas stratabound caves cross-cut the paleokarst sequence fill providing evidence that stratabound dissolution postdates vertical dissolution.

∘ Two zones are defined and mapped in this study in terms of paleokarst facies distribution and the degree of host rock disruption: the paleocave zone and the karst-damage zone.

» **The paleocave zone** delimits the ancient space of the cave and contains areas of major collapse. Chaotic breccia deposits are abundant in this zone.

» **The karst damage zone** encompasses the paleocave zone and includes a zone of minor host rock disruption such as stratabound caves and fracture fills.

Mechanisms for karst formation

∘ The mechanism of fracture/fault karst formation is attributed to fracture-controlled channelized fluid flow.

∘ After restoration of fault displacement from the top of Yates 2 until Upper Yates 4, the stratabound passages appear aligned for each step of restoration. This suggests that the mechanism of stratabound dissolution may be attributed to syngenetic karst development under the controls of the hydrogeologic model of Carbonate Islands.

∘ The presence of mosaic breccias immediately below fracture areas associated with stratabound caves suggests that the sub-horizontal diffuse flow responsible for stratabound dissolution was probably enhanced by its connectivity to the sub-vertical fracture-controlled channelized flow.

Timing of the Rattlesnake Canyon karst

∘ Restoration of both faults point to stratabound caves as possible indicators of the paleo-halocline position during the deposition of theYates Formation.

∘ The most productive period for the generation of these stratabound caves appears to be during the deposition of Yates 3 according to the restoration method.

Speleogenesis in Rattlesnake Canyon

- Pre-stratabound speleogenesis can be characterized by:
  - (I) **Fracture-controlled dissolution**. Corrosion in syndepositional extensional fractures caused solution enlarged fractures restricted in metre scale zones.
  - (II) **Cave breakdown**. Corrosion is localized along fracture and bedding surfaces with outcrop areas of tens of metre scale. Paleoflow must have been channelized along numerous fractures and dilated bedding surfaces. Mosaic breccias result from this process.
  - (III) **Vertical open passage-cave floor**. Corrosion is locally extensive along passage walls as paleoflow must have diffused along open passages. The gravitational karst component is significant with an extension of tens of metres. Chaotic breccia deposits result from this stage.

- Syn-stratabound speleogenesis:
  - (IV) **Strata sagging** processes and the presence of mosaic breccia deposits are related to halocline corrosion. Corrosion at this stage produces new porosity and bending of the overlying sandstones as a result of plastic deformation of low-competence materials. Formation of new porosity allows rotation of the clasts accentuating the formation of mosaic breccia deposits.

- Incipient post-stratabound reactivation of the karst system is characterized by a matrix selective dissolution process. No gravitational karst component is associated with this flow driven dissolution process. Yellow patchy vugs are products of this stage that can illustrate how initial dissolution could have initated.

3D paleokarst model

- The 3D paleokarst model reproduces the spatial distribution of the paleokarst facies and the irregular boundaries of the paleocave and karst-damage zones.

- A complex workflow was designed for the construction of these surfaces which is detailed in Chapter 5.

- The penetration distance of the paleokarst system was determined using GPR profiles. The system penetrates over 70 metres towards the north into the platform.

Diagenesis

∘ The dolomitized Rattlesnake Canyon paleokarst infills underwent different diagenetic episodes of replacement, multhiphased dolomite cementation, dedolomitization and calcite precipitation.

Two patterns of cementation were identified in the Rattlesnake Canyon paleokarst: dolomite cements filling voids, and sulphate-replacing dedolomites and calcites (^{13}C depleted). Dolomite cementation is observed in voids and is interpreted as a multiphase textural evolution sequence generating dolomite frameworks under shallow burial.

∘ Dedolomitization is detected by the occurrence of dissolution fabrics in dolomite and by the presence of dolomite relicts such as calcitized rhombs after dolomite and floating dolomite relicts within dedolomite mosaics. Dedolomitization was preferentially initiated along fractures based on dedolomite cement distribution.

∘ Calcite cements are encountered as fracture-fills, solution pipe fills and within anhydrite moulds.

∘ Dedolomites and spar cements contain hydrocarbon fluid inclusions. The distribution of these fluid inclusions indicates coeval precipitation of these cements with the Tertiary hydrocarbon charge of the basin.

∘ Dedolomite and calcite cements show progressive depletion of iron and manganese directly linked to uplifting and increasing volumes of meteoric waters.

∘ Coloured sediments within karst are due to the presence of iron oxides. The yellow infills detected in the field show an abundance of poikilotopic calcite which includes well crystallized acicular goethite crystals. SEM reveals hollow dolomite with numerous intracrystalline pits as preferential sites for the emplacement of hematite pseudomorphs after pyrite, especially in the stratabound cave levels. Two mechanisms are proposed for the origin of iron-bearing minerals in the paleokarst: sulphate reduction and direct precipitation from ferrihydrite

∘ Dickite resulted from tansformation of former kaolinite because of the leaching of siliciclastics at acid pH during mixing of hydrocarbon and hydrothermal fluids during late diagenesis.

Reservoir characterization

∘ Major permeability values are attained in the karst lithofacies.

∘ The lateral expansion of the stratabound dissolution processes reveals a large presence of solution enhanced mouldic and vuggy pores.

∘ Major lateral heterogeneity is associated with pisolitic shelf crest facies in a level that was vertically displaced by faulting. This together with the absence of late lateral diagenetic

modifications indicates that the best reservoir properties in the carbonate host rock originated during syndepositional faulting.

∘ The original poroperm heterogeneities were mainly inherited from the syndepositional karst development but were subsequently modified during diagenetic processes.

∘ Dickite cementation and dedolomitization brought about partial sealing of porosity and significant reduction of permeability especially in fracture areas. Laterally, modification of dolomite cements is minor and high permeabilities are attained.

References

Adams, J.E., Rhodes, M.L.,1960. Dolomitization by seepage reflux. AAPG Bull., 44 , 1912–1920.

Amthor, J.E., Friedman, G.M., 1991. Dolomite–rock textures and secondary porosity development in Ellenburger Group carbonates (Lower Ordovician), west Texas and southeastern New Mexico. Sedimentology 38, 343–362.

Archie, G.E., 1952. Classification of Carbonate Reservoir Rocks and Petrophysical Considerations. AAPG Bulletin 36 (2), 278–298.

Arenas, C., Alonso Zarza, A.M., Pardo, G., 1999. Dedolomitization and other early diagenetic processes in Miocene lacustrine deposits, Ebro Basin (Spain). Sedimentary Geology 125, 23–45.

Aydin, A., 2000. Fractures, faults, and hydrocarbon entrapment, migration and flow. Marine and Petroleum Geology 17 (7), 797–814.

Baceta, V.P. Wright, Pujalte,V., 2001. Palaeo-mixing zone karst features from Palaeocene carbonates of north Spain: criteria for recognizing a potentially widespread but rarely documented diagenetic system. Sedimentary Geology 139, 205– 216.

Baceta, V.P., Wright, S.J., Beavington-Penney, S.J., Pujalte, V., 2007. Palaeohydrogeological control of palaeokarst macro-porosity genesis during a major sea-level lowstand: Danian of the Urbasa–Andia plateau, Navarra, North Spain. Sedimentary Geology 199, 141–169.

Back, W., Hanshaw, B.B., Plummer, L.N., Tahn, P.H., Rightmire, C.T., Rubin, M.,1983. Process and rate of dedolomitization: mass transfer and 14C dating in a regional carbonate aquifer. Geol.Soc. Am. Bull. 94, 1415–1429.

Bailey, W.R., Manzocchi, T., Walsh, J.J., Keogh, K., Hodgetts, D., Rippon, J., Nell, P. A. R., Flint, S., Strand, J. A., 2002. The effect of faults on the 3D connectivity of reservoir bodies: a case study from the East Pennine Coalfield, UK. Petroleum Geoscience 8, 263–277.

Baker, G.S., Jordan, T.E., Pardy, J., 2007. An Introduction to Ground Penetrating Radar (GPR). In: Baker, G.S. and Jol, H. M. (Eds), Stratigraphic Analyses using GPR. The Geological Society of America, Special Paper 432. Colorado, USA. 1–18.

Banner, J.L., 1995. Applications of the trace element and isotope geochemisty of strontium to studies of carbonate diagenesis. Sedimentology 45 (2), 805–824.

Beaufort, D., Cassagnabere, A., Petit, S., Lanson, B.,1998. Kaolinite-to-dickite reaction in sandstone reservoirs. Clay Minerals 33, 297–316.

Bebout, D.G., Kerans, C. (Eds.), 1993. Guide to the Permian Reef Geology Trail, McKittrick Canyon, Guadalupe Mountains National Park, West Texas. Bur. Econ. Geol. Univ. Texas, Austin, Guidebook 26, 46 pp.

Bellian, J.A, Kerans, C, Jennette, D.C., 2005. Digital outcrop models: Applications of terrestrial scanning Lidar technology in stratigraphic modeling. Journal of Sedimentary Research 75, 2, 166–176.

Bischoff, J.L., Julià, R., Shanks, W.C., Rosenbauer, R.J., 1994. Karstification without carbonic acid: bedrock dissolution gypsum-driven dedolomitization. Geology 22, 995–998.

Borer, J.M., Harris, P.M., 1991. Lithofacies and cyclicity of the Yates Formation, Permian Basin: implications for reservoir heterogeneity. American Association of Petroleum Geologists Bulletin 75, 726–779.

Bosák, P., Ford, D.C., Glazek, J., Horácek, I. (Eds.), 1989. Paleokarst: A Systematic and Regional Review. Elsevier, Amsterdam, 728 pp.

Bottrell, S.H., Smart, P.L., Withaker, F., Raiswell, R., 1991. Geochemistry and isotope systematics of sulphur in the mixing zone of Bahamian blue holes. Applied Geochemistry 6, 97–103.

Budd, D.A., 1997. Cenozoic dolomites of carbonate islands; their attributes and origin. Earth-Science Reviews 42, 1–47.

Budd, D.A., Vacher, H. L., 1991. Predicting the thickness of fresh-water lenses in carbonate paleo-islands. Journal of Sedimentary Petrology 61 (1), 43–53.

Cabello, P., Falivene, O., López-Blanco, M., Howell, J., Arbués, P., Ramos, E., 2011. An outcrop-based comparison of facies modelling strategies in fan-delta reservoir analogues from the Eocene Sant Llorenç del Munt fan delta (NE Spain). Petroleum Geoscience 17, 65–90.

Canfield D.E., Thamdrup, B., 1994. The production of 34S-depleted sulfide during bacterial disproprtionation of elemental sulfur. Science 266, 1973–1975.

Carew, J.L., Mylroie, J.E., 1995. Quaternary tectonic stability of the Bahamian Archipelago: evidence from fossil coral reefs and flank margin caves. Quaternary Science Reviews 14, 145–153.

Choquette, P.W., Pray, L.C., 1970. Geologic Nomenclature and Classification of Porosity in Sedimentary Carbonates. AAPG Bulletin 54 (2), 207–250.

Choquette, P.W., Hiatt, E.E., 2008. Shallow-burial dolomite cement: a major component of many ancient sucrosic dolomites. Sedimentology 55, 423–460.

Cornell, R.M., Giovanoli, R.,1987. Effect of manganese on the transformation of ferrihydrite into goethite and jacobsite in alkaline media. Clays and Clay Minerals 35, 11–20.

Cornell, R.M. and Schwertmann, U, 2003. The iron oxides. 2nd ed., Wiley-VCH; 613 pp.

Craig, D.H., 1988. Caves and other features of Permian karst in San Andres Dolomite, Yates field reservoir, west Texas. In: James, N.P., and Choquette, P.W. (Eds.), Paleokarst. New York, Springer-Verlag, pp. 342-363.

Craig, D.H., 1990. Yates and other Guadalupian (Kazanian) oil fields, U. S. Permian Basin. Geological Society, London, Special Publications 50, 249–263.

Crysdale, B.L., 1987. Fluid inclusion evidence for the origin, diagenesis and thermal history of sparry calcite cement in the Capitan Limestone, McKittrick Canyon, West Texas. Master's Thesis. Universiy of Colorado, Boulder, CO, 78 pp.

Davis, J.L., Annan, A.P., 1989. Ground penetrating radar for high resolution mapping of soil and rock stratigraphy. Geophysical Prospecting 37, 531–551.

Davis, J.B., Kirkland, D. W., 1970. Native sulfur deposition in the Castile Formation, Culberson County, Texas. Economic Geology 65, 107–121.

Dawers, N.H., Anders, M.H., Scholz, C.H., 1993. Growth of normal faults: Displacement-length scaling. Geology 21, 1107–1110.

De Bona, J., Dani, N., Ketzer, J. M., De Ros, L. F., 2008. Dickite in shallow oil reservoirs from Recôncavo Basin, Brazil: diagenetic implications for basin evolution. Clay Minerals 43, 213–233.

Deines, P., Langmuir, D., Harmon, R.S., 1974. Stable carbon isotope ratios and the existence of a gas phase in the evolution of carbonate ground waters. Geochimica et Cosmochimica Acta 38, 1147–1164.

Dessau, G., Jensen, M.L., Nakai, N., 1962. Geology and isotopic studies of Sicilian sulfur deposits. Economic Geology 57, 410–438.

Dickerson, P. W., 1985. Evidence for Late Creataceous-early Tertiary transpression in Trans-Pecos Texas and adjacent Mexico. In:. Dickerson, P. W. and Muehlberger, W. R (Eds.), Structure and tectonics of Trans-Pecos Texas, West Geol. Soc., Guidebook Publ., pp 185–194.

Dickerson, P.W., Muehlberger, W.R., 1985. Structure and tectonics of Trans-Pecos Texas. Midland, TX, West Texas Geological Society Publication 85-81, pp. 278.

Dousma,J., den Ottelander, D., de Bryn, P.L., 1979. The Influence of Sulfate Ions on the Formation of Iron (III) oxides. Journal of Inorganic and Nuclear Chemistry 41, 1565–1568.

Dreybrodt, W., 2000. Equilibrium chemistry of karst water in limestone terranes. In: A.A. Klimchouk, A.A., Ford, D.C., Palmer, A.N., Dreybrodt, W., (Eds), Speleogenesis. Evolution of karst aquifers: National Speleological Society, Huntsville, Ala., pp. 126–135.

Edenborn, H.M., Silverberg N., Mucci A., Sundby B., 1987. Sulphate reduction in deep coastal marine sediments. Marine Chemistry 21, 329–345.

Ehrenberg, S.N., Aagaard, P., Wilson, M.J., Fraser, A.R., Duthie, D.M.L., 1993. Depth-dependent transformation of kaolinite to dickite in sandstones of the Norwegian continental shelf. Clay Minerals 28, 325–352.

Erdlac, Jr,R.J., 1993. Small-scale structures in the Guadalupe Mountains region; implication for Laramide stress trends in the Permian basin. In: D.W. Love, J.W. Hawley, B.S. Kues, J.W. Adams, G.S. Austin and J.M. Barker (Eds.), Carlsbad Region, New Mexico and West Texas, New Mexico Geological Society, 44th Annual Field Conference, pp.167–174.

Esteban, M., Pray, L., 1983. Pisoids and pisolite facies (Permian), Guadalupe Mountains, New Mexico and west Texas. In: Peryt,T. (Ed.),Coated Grains, Berlin, Springer-Verlag, p. 503-537.

Falivene, O., Cabrera, L., Muñoz, J.A., Arbués, P., Fernández, O., Sáez, A., 2007. Statistical grid-based facies reconstruction and modeling for sedimentary bodies. Alluvial palustrine and turbiditic examples. Geologica Acta 5 (3), 199–230.

Fernández, O., Muñoz J.A., Arbués, P., Falivene, O., Marzo, M., 2004. 3-D reconstruction of geological surfaces: an example of growth strata and turbidite systems from the Ainsa basin (Pyrenees, Spain). AAPG Bull 88, 1049–1068.

Fischer, A.G., Sarnthein, M., 1988. Airborne silts and dune-derived sands in the Permian of the Delaware Basin. Journal of Sedimentary Petrology 58, 637–643.

Fischer, W.R. and Schwertmann, U., 1975. The formation of hematite from amorphous iron-(III) hydroxide. Clays and Clay Minerals 23, 33–37.

Folk, R.L., 1968. Petrology of Sedimentary Rocks. Hemphill Publishing Company, Austin.

Folk, R.L., Siedlecka, A., 1974. The ”Shizohaline” environment: its Sedimentary and Diagenetic Fabrics as Exemplified by Late Paleozoic Rocks of Bear Island, Svalbard. Sedimentary Geology 11, 1–15.

Folkman, Y., 1969. Diagenetic dedolomitization in the Albian-Cenomanian Yagur dolomite on Mount Carmel (northern Israel). Journal of Sedimentary Petrology 39, 380–385.

Ford, D., 1988. Characteristics of Dissolutional Cave Systems in Carbonate Rocks. In: N. P. James and P. W. Choquette (Eds.), Paleokarst, Springer Verlag, New York, pp.1–21.

Ford D.C., Williams P.W. 1989. Karst Geomorphology and Hydrology. Springer, London: Unwin Hyman.

Franco, A.L., 1973. Deposition and diagenesis of the Yates Formation, Guadalupe Mountains and Central Basin Platform. Unpublished Master’s thesis. Texas Tech University, Lubbock, TX, 68 pp.

Frank, J.R., Carpenter, A.B., Oglesby, T.W., 1982. Cathodoluminescence and composition of calcite cement in the Taum Sauk Limestone (Upper Cambrian), Southeast Missouri. Journal of Sedimentary Petrolology 52, 631–638.

Frank, E.F., Mylroie, J.M., Troester, J.W, Alexander, Jr., E.C., Carew, J.L., 1998. Karst development and speleogenesis, Isla de Mona, Puerto Rico. Journal of Cave and Karst Studies 60(2), 73–83.

Friedman I., O’Neil J. R., 1977. Compilation of stable isotope fractionation factors of geochemical interest. In: Fleischer, M., (Ed.), Data of Geochemistry 6th Edition, Government Printing Office, Washington, D.C.

Fritz, P., Smith, D.G.W.,1970. The isotopic composition of secondary dolomites. Geochimica et Cosmochimica Acta 34, 1161–1173.

Frost, E.L., Kerans, C., 2009. Platform-margin trajectory as a control on syndepositional fracture patterns, Canning Basin, Western Australia. Journal of Sedimentary Research 79, 44–55.

Fu, Q., Qing, H., Bergman, K.M., 2006. Paleokarst in Middle Devonian Winnipegosis mud mounds, subsurface of south-central Saskatchewan, Canada. Bulletin of Canadian Petroleum Geology 54 (1), 22–36.

Fu, Q., Qing, H., Bergman, K.M. and Yang, C., 2008. Dedolomitization and calcite cementation in the Middle Devonian Winnipegosis Formation in Central Saskatchewan, Canada. Sedimentology 55, 1623–1642.

Garber, R.A., Grover, G.A., Harris, P.M., 1989. Geology of the Capitan shelf margin — subsurface data from the northern Delaware Basin. In: Harris, P.M., and Grover, G.A., (Eds.), Subsurface and Outcrop Examination of the Capitan Shelf Margin, Northern Delaware Basin. Tulsa, OK, SEPM Core Workshop No. 13, pp. 3–271.

Garcia, A.J.V., Morad, S., De Ros, L.F., AL-Aasm, I.S., 1998. Paleogeographical, paleoclimatic and burial history controls on the diagenetic evolution of Lower Cretaceous Serraria sandstones in Sergipe-Alagoas Basin, NE Brazil. In: Carbonate Sedimetation in Sandstones (Ed. By S. Morad), Spec. Publ. Int. Assoc. Sediment., 26, pp 107–140.

Garrels, R.M., Christ, C.L., 1965. Solutions, Minerals and Equilibria: New York, Harper and Row, 450 pp.

Given, R.K., Lohmann, K.C., 1986. Isotopic evidence for the early meteoric diagenesis of the reef facies, Permian reef complex of west Texas and New Mexico. Journal of Sedimentary Petrology, 56, 183–193.

Glasauer, S.M., Friedl, J., Schwertmann, U., 1999. Properties of goethites prepared under acid and basic conditions in the presence of silicate. Journal of Colloid and Interface Science 216, 106–115.

Goldberg, M., 1967. Supratidal dolomitization and dedolomitization in Jurassic rocks of Hamakhtesh Hagatan, Israel. Journal of Sedimentary Petrology 37, 760–773.

Goldsmith, J., Graf, D. L., 1958. Relation lattice constant and composition of the Ca-M carbonates. American Mineralogist 43, 84–101.

Gonzalez, L.A., Ruiz, H. L., Taggart, B. E., Budd, A. F., Monell, V., 1997. Geology of Isla de Mona, Puerto Rico. In: Vacher, H.L., Quinn, T. M. (Eds.), Geology and Hydrogeology of Carbonate Islands. Developments in Sedimentolgy, vol. 54. Elsevier, pp. 183–216.

Guidry, S.A., Grasmueck, M., Carpenter, D.G., Gombos, A.M., Bachtel S.L., Viggiano, D.A., 2007. Karst and Early Fracture Networks in Carbonates, turks and Cicos islands, British West Indies. Journal of Sedimentary Research 77 (6), 508–524.

Hanshaw, B.B., Back, W., 1979. Major geochemical processes in the evolution of carbonate-aquifer systems. Journal of Hydrology 43, 287–312.

Harris, W.H., Mattews, R.K., 1968. Subaerial diagenesis of carbonate sediments: efficiency of the solution-reprecipitation process. Science 160, 77–79.

Hayes, P.T., 1964. Geology of the Guadalupe Mountains, New Mexico, U. S. Geological Survey Professional Paper 446, 69 pp.

Henrich, R., 1984. Facies, dolomitization and karstification of lagoonal carbonates: Triassic of the Northern Alps. Facies 11, 109–156.

Henrich, R., Zankl, H., 1996. Diagenesis of Upper Triassic Wetterstein Reefs of the Bavarien Alps. In: Shroeder, J.H., Purser, B.H. (Eds.), Reef Diagenesis. Springer-Verlag, Berlin Heidelberg, Germany, pp. 245–268.

Hill, C.A., 1996. The Geology of the Delaware Basin, Guadalupe, Apache and Glass Mountains New Mexico and West Texas. Society of Economic Paleontologists and Mineralogists, Permian Basin Section, Special Publication, vol. 96–39.

Hill, C.A., 2000. Overview of the geologic history of cave development in the Guadalupe Mountains, New Mexico. Journal of Cave and Karst Studies 62 (2), 60–71.

Hubbert, M.K. 1940. The theory of ground-water motion. The Journal of Geology 48 (8), 785–944.

Hunt, D.W., Fitchen, W.M., Koša, E., 2002. Syndepositional deformation of the Permian Capitan Reef carbonate platform, Guadalupe Mountains, New Mexico, USA. Sedimentary Geology 154, 89–126.

Hunt, D.W., Blendiger, W., Labrana, G., 2009. 3-D Variability of the Upper Permian Capitan Carbonate Platform: New Insights from Subsurface and Outcrop Data. AAPG poster presentation. Denver. USA.

Hurley, N.F., 1989. Facies mosaic of the lower Seven Rivers Formation, McKittrick Canyon, New Mexico. In: Harris, P.M., and Grover, G.A.(Eds.), Subsurface and Outcrop Examination of the Capitan Shelf Margin, Northern Delaware Basin. Tulsa, OK, SEPM Core Workshop No. 13, pp. 325–346.

Jagnow, D.H., Jagnow, R.R., 1992. Stories from rocks: the geology of the Guadalupe Mountains, Carlsbad, Carlsbad Caverns–Guadalupe Mountains Association, 40pp.

Jambor, J.L., Dutrizac, J.E., 1998. Occurrence and constitution of natural and synthetic ferrihydrite, a widespread iron oxyhydroxide. Chemical Reviews 98, 2549–2585.

James, N.P., Choquette, P.W. (Eds.), 1988. Paleokarst. Springer, New York, 416 pp.

Jennings, J.N., 1985. Karst Geomorphology. Basil Blackwell, Oxford, 293 pp.

Jol, H.M., 2009. Ground Penetrating Radar: Theory and applications. Elsevier Science, Amsterdam, The Netherlands.

Jones, G.D., Whitaker, F.F., Smart, P.L., Sanford, W.A., 2002. Fate of reflux brines in carbonate platforms. Geology 30 (4), 371– 374.

Jørgensen B.B., 1982, Mineralization of organic matter in the sea bed – the role of sulphate reduction. Nature 296, 643–645.

Kasprzyk, A., Ortí, F., 1998. Palaeogeographic and burial controls on anhydrite genesis: a case study from the Badenian basin in the Carpathian Foredeep (southern Poland, western Ukraine).Sedimentology 45, 889–907.

Keith S. B., 1982. Paleoconvergence rates determined from K_2O/SiO_2 ratios in magmatic rocks and their application to Cretaceous and Tertiary tectonic patterns in southwestern North America. Geol. Soc. Amer. Bull., 93, 524–532.

Kenny, R., 1992. Origin of discontinuity dedolomite in the Martin formation (late Devonian, northern Arizona). Sedimentary Geology 78, 137–146.

Kerans, C., 1988. Karst-controlled reservoir heterogeneity in Ellenburger Group carbonates of West Texas. AAPG Bulletin 72, 1160–1183.

Kerans, C., 1989. Karst-controlled reservoir heterogeneity and an example from the Ellenburger Group (Lower Ordovician) of West Texas: The University of Texas at Austin, Bureau of Economic Geology Report of Investigations No. 186, 40 p.

Kerans, C., Fitchen, W.M., Gardner, M.H., Sonnenfeld, M.D., Tinker, S.W., Wardlaw, B.R., 1992. Styles of sequence development within uppermost Leonardian through Guadalupian strata of the Guadalupe Mountains, Texas and New Mexico. In: Mruk, D.H., and Curran, B.C., (Eds.), Permian Basin Exploration and Production Strategies: Applications and Sequence Stratigraphic and Reservoir Characterization Concepts. West Texas Geological Society, Symposium 92-91, pp. 1–7.

Kirkland-George, B., Longacre, S.A., Stoudt, E.L., 1993. Reef. In: Bebout, D.G., Kerans, C., (Eds.), Guide to the Permian Reef Geology Trail, McKittrick Canyon, Guadalupe Mountains National Park, West Texas. Tex. Bur. Econ. Geol., Guidebook, vol. 26, 23–31.

Kisch H.J.,1983. Mineralogy and petrology of burial diagenesis (burial metamorphism) and incipient metamorphism in clastic rocks. In: G. Larsen, G., Chilingar, G.V. (Eds.), Diagenesis in Sediments and Sedimentary Rocks 2. Developments in Sedimentology 25B, Elsevier, Amsterdam, pp 289– 494.

Klimchouk, A.B., 1996. Gypsum karst in the western Ukraine. In: Klimchouk A.B, Lowe D.J, Cooper A.H and Sauro U. (Eds.), Gypsum karst of the World. Int. Journal of Speleology Theme Issue 25 (3-4), 263–278.

Klimchouk, A.B. and Ford, D.C. 2000. Types of karst and evolution of hydrogeologic settings. In: Klimchouk, A., Ford, D.C., Palmer, A.N. and Dreybrodt, W. (Eds.), Speleogenesis: Evolution of karst aquifers. National Speleological Society, Huntsville, 45–53.

Kluth, C.F., Coney, P.J., 1981. Plate tectonics of the Ancestral Rocky Mountains. Geology 9 (1), 10–15.

Koša, E., 2003. Heterogeneity in the structure, diagenesis and fill of syndepositional faults in carbonate strata: Upper Permian Capitan Platform, Guadalupe Mountain mexicoMexico, USA. Unpublished Ph.D Thesis, University of Manchester, United Kingdom, 403 pp.

Koša, E., Hunt, D.W., 2005. Growth of syndepositional faults in carbonate strata: Upper Permian Capitan platform, New Mexico, USA. Journal of Structural Geology 27, 1069–1094.

Koša, E., Hunt, D.W., 2006. Heterogeneity in fill of karst-modified syndepositional faults and fractures: Upper Permian Capitan platform, New Mexico, USA. Journal of Sedimentary Research 76, 130–149.

Kupecz, J.A., Land, L. S., 1991. Late-stage dolomitization of the Lower Ordovician Ellenburger Group, West Texas: Journal of Sedimentary Petrology 61, 551–574.

Kupecz, J.A, Montanez, I.P, Gao, G., 1993. In: Rezak, R. and Lavoie, D.L. (Eds.), Carbonate Microfabrics. Springer-Verlag, New York Inc., pp. 187–194.

Lambert, S.J., 1983. Dissolution of Evaporites in and Around the Delaware Basin, Southeastern New Mexico and West Texas, SAND82-0461. Albuquerque, NM: Sandia National Laboratories.

Land, L.S., 1973. Holocene meteoric dolomitization of Pleistocene limestones, North Jamaica. Sedimentology 20, 411–424.

Lanson, B., Beaufort, D., Berger G., Baradat, J., Lacharpagne, J.C., 1996. Illitization of diagenetic kaolinite to dickite conversion series: late-stage diagenesis of the Lower Permian Rotliegend sandstone reservoir, offshore of the Netherlands. Journal of Sedimentary Research 66, 501–518.

Lanson, B., Beaufort, D., Berger, G., Bauer, A., Cassagnabere, A., Meunier, A., 2002. Authigenic kaolin and illitic minerals during burial diagenesis of sandstones: a review. Clay Minerals 37, 1–22.

Lee, M.R., Harwood, G.M, 1989. Dolomite calcitization and cement zonation related to uplift of the Raisby Formation (Zechstein carbonate), Northeast England. Sedimentary Geology 65, 285–305.

Lewis, D.G., Schwertmann, U., 1980. The effect of [OH] on the goethite produced from ferrihydrite under alkaline conditions. Journal of Colloid Interface Science 78, 543–553.

Longley, 1999. Differential compaction and its effects on the outer shelf of the Permian Capitan Reef Complex, Guadalupe Mountains, New Mexico. In: Saller, A.H., Harris, P.M.,

Kirkland, B.L, Mazzullo, S.J. (Eds.), Geological framework of the Capitan Reef, Society of Economic Paleontologists and Mineralogists, Special Publication 65, pp. 85–106.

Lønøy, A., 2006. Making Sense of Carbonate Pore Systems. AAPG Bulletin 90 (9), 1381–1405.

Loucks, R.G., 1999. Paleocave carbonate reservoirs: origins, burial-depth modifications, spatial complexity, and reservoir implications. AAPG Bulletin 83, p. 1795–1834.

Loucks, R.G., Mescher, P.K., McMechan, G.A., 2004. Three-dimensional architecture of a coalesced, collapsed-paleocave system in the Lower Ordovician Ellenburger Group, central texas. AAPG Bulletin 88 (5), 545–564.

Lucia, F.J., 1983. Petrophysical Parameters Estimated From Visual Descriptions of Carbonate Rocks: A Field Classification of Carbonate Pore Space. Journal of Petroleum Technology 216, 221–224.

Lucia, F.J., 1995. Rock-fabric / Petrophysical Classification of Carbonate Pore Space for Reservoir Characterization. AAPG Bulletin 79 (9), 1275–1300.

Lucia, F.J., 1999. Carbonate Reservoir Characterization. Springer-Verlag, Berlin, 226 pp.

Lumsden, D.N., 1979. Discrepancy between thin-section and X-ray estimates of dolomite in limestone. Journal of Sedimentary Petrology 49, 429–435.

Machel, H.G., 2001. Bacterial and thermochemical sulfate reduction in diagenetic settings. Sedimentary Geology 140, 143–175.

Machel, H.G., 2004. Concepts and models of dolomitization: a critical reappraisal. In: Braithwaite, C.J.R., Rizzi, G. and Darke, G. (Eds.), The geometry and Petrogenesis of Dolomite Hydrocarbon Reservoirs, Spec. Publ. Geol. Soc., 235, 7, pp 7–63.

Machel, H., G., Krouse, H., R., Sassen, R., 1995. Products and distinguishing criteria of bacterial and thermochemical sulphate reduction. Applied Geochemistry 10, 373–389.

Mann, S., Cornell, R.M., Schwertmann, U., 1985. The influence of aluminium on iron oxides: XII. High resolution transmission electron microscopic (HRTEM) study of aluminous goethites. Clay Mineralogy 20, 255–262.

Mazzullo, S. J.,Cys, J. M.,1977. Submarine cements in Permian boundstones and reef-associated rocks, Guadalupe Mountains, west Texas and southeastern New Mexico. In: Hileman, M.E. and Mazzullo, S. J. (Eds.), Upper Guadalupian Facies, Permian Reef Complex, Guadalupe Mountains, New Mexico and West Texas. Soc.Sed. Geology Perm. Bas. Sect. Spec. Pub. 77-16, pp.151–200.

Mazzullo, S.J., Bischoff, W.D., Hedrick, C.L.,1989. Stacked island facies in Tansill outer-shelf platform, Dark Canyon, Guadalupe Mountains, New Mexico. In: Harris, P.M., Grover, G.A. (Eds), Subsurface and Outcrop Examination of the Capitan Shelf Margin, Northern Delaware Basin. SEPM Core Workshop, 13, pp. 287–294.

Mazzullo, L.J., 1992. Significance of reservoir zonation in Silurian (Fusselman and Wristen) carbonates, Wells Field, Dawson County, Texas; Transactions Southwest Section - AAPG, Midland, Publ. 92-90, p. 27–37.

Mazzullo, S.J. ,1999. Paleoenvironments, cyclicity, and diagenesis in the outer shelf Tansill Formation in the Carlsbad Embayment (Dark Canyon), northern Guadalupe Mountains, New Mexico. In: Saller, A.H., Harris, P.M., Kirkland, B.L., Mazzullo, S. (Eds.), Geologic Framework of the Capitan Reef. SEPM Spec. Publ., 65, pp. 107–128.

McKenzie, J.A., 1985. Stable isotope mapping in Messinian evaporative carbonates of Central Sicily. Geology 13, 851–854.

McMechan, G.A., Loucks, R.G., Mescher, P., Zeng, X., 2002. Characterization of a coalesced,collapsed paleocave reservoir analog using GPR and well-core data. Geophysics 67, 1148–1158.

Meissner, F.F., 1972. Cyclic sedimentation in middle Permian strata of the Permian basin.In: Elam, J.G., and Chuber, S., (Eds.), Cyclic Sedimentation in the Permian Basin, second edition. Midland, TX, West Texas Geological Society Publication 72-60, pp. 203–232.

Melim, L.A., 1991. The origin of dolomite in the Permian (Guadalupian) Capitan Formation, Delaware Basin, West Texas and New Mexico: Implications for dolomitization models. Unpublished Ph.D thesis, Southern Methodist University, Dallas, Texas, USA, 199 pp.

Melim, L.A., Scholle, P.A., 2002. Dolomitization of the Capitan formation forereef facies (Permian, west Texas and New Mexico): seepage reflux revisited. Sedimentology 49, 1207–1227.

Melim, L.A., 2004. Mixing-zone diagenesis in the subsurface of Florida and the Bahamas. Journal of Sedimentary Research 74 (6), 904–913.

Moore, Y.H., Stoessell, R.K., Easley, D.H., 1992. Fresh-Water/Sea-Water Relationship Within a Ground-Water Flow System, Northeastern Coast of the Yucatan Peninsula. Ground Water 30 (3), 343–350.

Morad, S., Ketzer, J.M., Ros, L.F., 2000. Spatial and temporal distribution of diagenetic alterations in siliciclastic rocks: implications for mass transfer in sedimentary basins. Sedimentology 47, 95–120.

Mruk, D.H., 1989. Diagenesis of the Capitan Limestone, Upper Permian, McKittrick Canyon, West Texas. In: Harris, P.M., and Grover, G.A., (Eds.), Subsurface and Outcrop Examination of the Capitan Shelf Margin, Northern Delaware Basin. SEPM, Core Workshop 13, pp. 387–406.

Murray, R. C., 1960. Origin of porosity in carbonate rocks. Journal of Sedimentary Petrology 30,59–84.

Mylorie J.E., Carew, J.L., 1990. The flank margin model for dissolution cave development in carbonate platforms. Earth Surface Processes and Landforms 15, 413–424.

Mylroie, J.E., Carew, J.L., 1995. Karst development on carbonate Islands. In: Budd, D.A., Harris, P.M.,Saller, A., (Eds.), Unconformities and Porosity in Carbonate Strata, American Association of Petroleum Geologists, p. 55–76.

Mylroie, J.E, et al, 2001. Karst features of Guam in terms of a general model of carbonate island karst: Journal of Cave and Karst Studies, 63 (1), 9–22.

Mylroie, J.E., Mylroie J.R., and Nelson, C.N., 2008. Flank Margin Cave Development in Telogenetic Limestones of New Zealand. Acta Carsologica 37(1), 15–40.

Narr, W., Fischer, D., Harris, P.M., Heidrick, T., Robertson, B.T., Payrazyan, K., 2008. Understanding and Predicting Fractures at Tengiz – A Giant, Naturally Fractured Reservoir in the Caspian Basin of Kazakhstan. Search and discovery article adapted from oral presentation at AAPG Hedberg Conference, "Carbonate Reservoir Characterization and Simulation: From Facies to Flow Units," El Paso, Texas. http://www.searchanddiscovery.com/documents/2008/08041narr/images/narr.pdf.

Neal, A., 2004. Ground-penetrating radar and its use in sedimentology: principles, problems and progress. Earth-Science Reviews 66, 261–330.

Ortí, F., Rosell, L., 1981. Fábricas cristalinas de la anhidrita nodular y laminada. Acta Geológica Hispánica 16, 235–255.

Osborne, R.A.L., 2002. Cave breakdown by vadose weathering. International Journal of Speleology 31 (1/4), 37–53.

Osleger, D.A., 1998. Sequence architecture and sea-level dynamics of Upper Permian shelfal facies, Guadalupe Mountains, southern New Mexico. Journal of Sedimentary Research, Section B: Stratigraphy and Global Studies, 68, 327–346.

Osleger, D.A., Tinker, S.W., 1999. Three-dimensional architecture of Upper Permian high-frequency sequences, Yates-Capitan shelf margin, Permian Basin, USA. In: Harris, P.M., Saller, A.H., and Simo, J.A., (Eds.), Advances in Carbonate Sequence Stratigraphy — Application to Reservoirs, Outcrops, and Models. Tulsa, OK, SEPM Special Publication No. 63, pp. 169–185.

Palmer, R., 1986. The blue holes of South Andros, Bahamas. Cave Science 13 (1), 3–6.

Palmer, A.N., Palmer, M.V., 1989. Geological history of the Black Hills caves, South Dakota. National Speleologic. Society Bulletin, 51, 72–99.

Parnell, J., Baron, M., Boyce, A., 2000. Controls on kaolinite and dickite distribution, Highland Boundary Fault Zone, Scotland and Northern Ireland. J. Geol. Soc. London, 157, 635–640.

Parnell J., 2004. Kaolin polytype evidence for a hot- fluid pulse along Caledonian thrusts during rifting of the European Margin. Mineralogical Magazine 68, 419–432.

Parsley, M.J. and Warren, J.K., 1989. Characterization of an upper Guadalupian barrier-island complex from the middle and upper Tansill Formation (Permian), east Dark Canyon, Guadalupe Mountains, New Mexico. In: P.M. Harris and G.A. Grover (Eds), Subsurface and Outcrop Examination of the Capitan Shelf Margin, Northern Delaware Basin. SEPM Core Workshop, 13, pp. 279–286.

Peters, K.,E., Fowler, M.,G., 2002. Application of petroleum geochemistry to exploration and reservoir management. Organic Geochemistry 33, 5–36.

Pierre, C. and Rouchy, J.M., 1988. Carbonate replacements after sulfate evaporites in the middle Miocene of Egypt. Journal of Sedimentary Petrology 58, 446–456.

Plummer L.N., 1975. Mixing of sea water with calcium carbonate ground water. In : Whitten, E. H. T. (Ed.), Quantitative studies in geological sciences. Boulder, Colorado, Geological Society of America, pp. 219–236.

Pringle, J.K., Howell, J.A., Hodgetts, D., Westerman, A.R., and Hodgson, D.M., 2006. Virtual outcrop models of petroleum reservoir analogues: a review of the current state-of-the-art. EAGE. 33 technical article first break volume 24.

Purser, B.H., Tucker, M.E., Zenger, D.H. , 1994. Problems, progress and future research concerning dolomites and dolomitization. In: Purser,B.H., Tucker, M.E. and Zenger, D.H. (Eds.), Dolomites: A Volume in Honour of Dolomieu, Blackwell Scientific Publications, Oxford, pp.3–28.

Quinlan, J.F., 1978. Types of karst, with emphasis on cover beds in their classification and development. Unpublished PhD Thesis, Univ. of Texas at Austin, 323 pp.

Reinhold, C., 1998. Multiple episodes of dolomitization and dolomite recrystallization during shallow burial in Upper Jurassic shelf carbonates: eastearn Swabian Alb, southern Germany. Sedimentary Geology 121, 71–95.

Ronald K., Stoessell, R.K., 1995. Dampening of Transverse Dispersion in the Halocline in Karst Limestone in the Northeastern Yucatan Peninsula. Ground Water 33 (3), 366-371.

Saller, A.H., 1996. Differential compaction and basinward tilting of the prograding Capitan reef complex, Permian, west Texas and southeast New Mexico, USA, Sedimentary Geology 101, 21–30.

Saller. A.H., 2004. Paleozoic dolomite reservoirs in the Permian Basin, SW USA: stratigraphic distribution, porosity, permeability and production. In: Braithwaite C.J.R., Rizzi G., Darke G. (Eds.), The Geometry and Petrogenesis of Dolomite Hydrocarbon Reservoirs Geological Society. Special Publication. 235. pp. 309–323.

Sanz-Rubio, E., Sanchez-Moral, S., Cañaveras, J.C., Calvo, J.P., Rouchy, J.M., 2001. Calcitization of Mg-Ca carbonate and Ca sulphate deposits in a continental Tertiary basin (Calatayud Basin, NE Spain). Sedimentary Geology 140, 123–142.

Sarg, J.F., 1977. Sedimentology of the carbonate-evaporite facies transition of the Seven Rivers Formation (Guadalupian, Permian) in southeast New Mexico. In: Upper Guadalupian Facies,

Permian Reef Complex Guadalupe Mountains, New Mexico and West Texas, Field Conference Guidebook, 1977, Permian Basin Section- SEPM, Pub.77-16, p.451–478.

Sarg, J.F., 1981. Petrology of the carbonate-evaporite facies transition of the Seven Rivers Formation (Guadalupian, Permian) southeast New Mexico. Journal of Sedimentary Petrology 51, 73–96.

Sarg, J. F., 1988. Carbonate sequence stratigraphy. In: C. Wilgus (Ed.), Sea-Level Changes: An Integrated Approach. SEPM Special Publication No. 42, pp.155–181.

Sarg, J.F., 1989. Stratigraphy and sedimentology of the back-reef upper Queen-lower Seven Rivers strata, Goat Seep-Capitan reef complexes (middle-late Guadalupian, Permian), southeast New Mexico. In: Harris, P.M., and Grover, G.A., (Eds.), Subsurface and Outcrop Examination of the Capitan Shelf Margin, Northern Delaware Basin. Tulsa, OK, SEPM Core Workshop No. 13, pp. 347–352.

Schneider, R. V., Hinojosa, J. H., 1991. Tectonic history of southwestern New Mexico and southwestern Arizona – a thermal perspective (abs.): Geol. Soc. Am., Rocky Mountain section-South Central section, Alburquerque, NM, v.23, no 4, p. 90.

Scholle, P.A., Ulmer, D.S., Melim, L.A., 1992. Late-stage calcites in the Permian Capitan Formation and its equivalents, Delaware Basin margin, west Texas and New Mexico: evidence for replacement of precursor evaporites. Sedimentology 39, 207–234.

Schulze, D.G., Schwertmann, U.,1984. The influence of aluminium on iron oxides. X. Properties of Al-substituted goethites. Clay Mineralogy 19, 521–529.

Schwabe, S., Herbert, R.A., 2004. Black Holes of the Bahamas: what they are and why they are black. Quaternary International 121, 3–11.

Schwertmann, U., Murad, E., 1983. Effect of pH on the formation of goethite and hematite from ferrihydrite. Clays and Clay Minerals 31, 277–284.

Sealey, N.E., 1994. Bahamian Landscapes: an introduction to the geography of The Bahamas, Media Publishing, Nassau, Bahamas.

Sibley, D.F., 1982. The origin of common dolomite fabrics: clues from the Pliocene. Journal of Sedimentary Petrology 52, 1087–1100.

Sibley, D.F., 1991. Secular changes in the amount and texture of dolomite. Geology 19, 151–154.

Siegmund, H., Erdrmann B-D., 1994. Facies and diagenesis of some upper Proterozoic Dolomites of South China. Facies 31, 255–264.

Smart P.L., Dawans J.M., Whitaker F., 1988. Carbonate dissolution in a modern mixing zone. Nature 335, 811–813.

Smart, P.L., Palmer, R.J., Whitaker, F., Wright, V.P., 1988. Neptunian dikes and fissure fills: an overview and account of some modern examples. In: James, N.P., Choquette, P.W. (Eds.), Paleokarst. Springer, New York, pp. 149–163.

Southwood, D.A., Hill, W.O.R., 1995. The origin and distribution of porosity in the Zechstein Kalk (Upper Permian) of Hewett field, southern North Sea. Petroleum Geoscience 1, 289–302.

Stafford, K., Mylorie, J., Taborosi, D., Jenson, J., Mylorie, J., 2005. Karst development on Tinian, Commonwealth of the Northern Mariana Islands: Controls on dissolution in relation to the Carbonate Island Model. Journal of Cave and Karst Studies 67 (1), 14–27.

Strebelle, S., Payrazyan, K., Caers, J., 2002. Modeling a Deepwater Turbidite Reservoir conditional to seismic data using multiple-point geostatistics. Society of Petroleum Engineers Paper No. 77425, 10 pp.

Stringfield, V.T., Legrand, H.E., 1971. Effects on karst features on circulation water in carbonate rocks in coastal areas. Journal of Hydrology 14, 139–157.

Swart, P.K., Melim, L.A., 2000. The origin of dolomites in Tertiary sediments from the margin of Great Bahama Bank. Journal of Sedimentary Research 70, 738–748.

Tinker, S.W., 1998. Shelf-to-basin facies distributions and sequence stratigraphy of a steep-rimmed carbonate margin: Capitan depositional system, McKittrick Canyon, New Mexico and Texas. Journal of Sedimentary Research, 68, 1146–1174.

Tinker, S.W., Ehrets, J.R., Brondos, M.D., 1995. Multiple karst events related to stratigraphic cyclicity: San Andres Formation, Yates Field, West Texas. In: Budd, D.A., Saller, A.H., Harris, P.M. (Eds.), Unconformities and porosity in carbonate strata, Am. Assoc. Pet. Geol. Mem., vol 63, pp 213–237.

Tinker, S.W., Mruk, D.H., 1995. Reservoir characterization of a Permian giant: Yates field, west Texas. In: Stoudt, E.L., and Harris, P.M. (Eds.), Hydrocarbon Reservoir Characterization: Geologic Characterization and Flow Unit Modelling, Tulsa, OK, SEPM Short Course Notes No. 34, pp. 51–128.

Tóth, J. 1995. Hydraulic continuity in large sedimentary basins. Hydrogeology Journal 3 (4), 4–15.

Trudinger, P. A., 1979. The biological sulphur cycle. In: Trudinger, P. A., and Swaine, D. J. (Eds.), Biogeochemical Cycling of Mineral-Forming Elements. Elsevier Publishing Company, Amsterdam pp. 293–313.

Vacher, H.L., 1988. Dupuit-Ghyben-Herzberg analysis of strip-island lenses. GSA Bulletin 100 (4), 580–591.

Vacher, H.L., Mylroie J. E., 2002. Eogenetic karst from the perspective of an equivalent porous medium. Carbonates and Evaporites 17(2), 182–196.

Vacher, H.L., Quinn, T.M., 2004. Geology and Hydrogeology of Carbonate Islands. Elsevier, Amsterdam.

Walker, D.A., Golonka, J., Reid. A., Reid. S, 1995. The effects of Paleolatitude and Paleogeography on Carbonate sedimentation in the Late Paleozoic. In: Huc, A. Y. (Ed.), Paleogeography, Paleoclimate and Source Rocks. AAPG studies 40, pp. 133–155.

Wang, B., I.S. Al-Aasm, 2002. Karst-controlled diagenesis and reservoir development; example from the Ordovician main reservoir carbonate rocks on the eastern margin of the Ordos basin, China. AAPG Bulletin 86, 1639–1658.

Ward, R.F., Kendall, C., Harris, P.M, 1986. Upper Permian (Guadalupian) Facies and their Association with Hydrocarbons-Permian Basin, West Texas and New Mexico. AAPG Bulletin 70 (3), 239–262.

Warrak, M., 1974. The petrology and origin of dedolomitized veined or brecciated carbonated rocks, the cornieules, in the Fréjus region, French Alps. J. Geol. Soc. 130, 229–247.

Weissmann, G.S., Carle, S.F., Fogg, G.E., 1999. Three-dimensional hydrofacies modeling based on soil surveys and transition probability geostatistics. Water Resources Research 35, 1761–1770.

Westrich J.T., Berner R.A.,1988. The effect of temperature on rates of sulphate reduction in marine sediments. Geomicrobiology Journal 6, 99–117.

Whitaker, F., 1992. Hydrology, geochemistry and diagenesis of modern carbonate platforms in the Bahamas. Unpublished Ph.D. Thesis, University of Bristol, UK, 347 pp.

Whitaker, F.F., 1998. The Blue Holes of the Bahamas: An overview and introduction to the Andros Project: Cave and Karst Science 25, 53–56.

Whitaker, F., Smart, P.L., 1997. Groundwater circulation and geochemistry of a karstified bank–marginal fracture system, South Andros Island, Bahamas. Journal of Hydrology 197, 293–315.

Whitaker, F.F. and Smart, P.L., 1998. Hydrogeology, geochemistry and diagenesis of fracture blue holes, South Andros, Bahamas. Cave and Karst Science 25, 75–82.

Whitney G., 1990. Role of water in the smectite-to-illite reaction. Clays and Clay Minerals 38, 343–350.

Wigley T.L. and Plummer, L.N., 1976. Mixing of Carbonate Waters. Geochimica et Cosmochimica Acta 40 (9), 989–995.

Wilson, P., Hodgetts ,D., Rarity, F., Gawthorpe , R.L., Sharp, I.R, 2009. Structural geology and 4D evolution of a half-graben: New digital outcrop modeling techniques applied to the Nukhul half-graben, Suez rift, Egypt. Journal of Structural Geology 31, 328–345.

Wong, P.K., Oldershow, A., 1981. Burial cementation in the Devonian Kaybob reef complex, Alberta, Canada. Journal of Sedimentary Petrology 51, 507–520.

Wright, V.P., 1991. Palaeokarst: types, recognition, controls and associations. In: Wright, V.P., Esteban, M. and Smart, P.L. (Eds.), Paleokarsts and paleokarstic reservoirs. Postgraduate Research Institute for Sedimentology, University of Reading Contribution 152, pp. 56–88.

Xu, X., Aiken, C.L., Bhattacharya, J.P., Corbeanu, R.M., Nielsen, K.C., McMechan, G.A., Abdelsalam, M.G., 2000. Creating virtual 3-D outcrop. The Leading Edge 19, no. 2,197–202.

Ye, Q., Kerans, C.,1996. Reconstructing Permian eustasy from 2-D backstripping and its use in forward models. In: W.D. DeMis and A.G. Cole, (Eds.), The Brushy Canyon Play in Outcrop and Subsurface: Concepts and Examples, Society of Economic Paleontologists and Mineralogists, Permian Basin Section, Publication vol. 96–38, pp. 69–74.

Yilmaz, I.Ö., Altiner, D., 2006. Cyclic paleokarst surfaces in Aptian peritidal carbonate successions (Taurides, southwest Turkey): internal structure and response to mid- Aptian sea-level fall. Cretaceous Research 27, 814–827.

Yurewicz, D.A., 1976. Sedimentology, paleoecology, and diagenesis of the massive facies of the lower and middle Capitan Limestone (Permian), Guadalupe Mountains, New Mexico and west Texas. Unpublished Ph.D. dissertation, University of Wisconsin at Madison, Madison, WI, 278 pp.

Appendices

Appendix One

This appendix contains a compilation of field and microscope photographs of some of the samples studied in Fault N. These supplementary petrographic data show detailed cathodoluminescence petrography of cements and karst components by a representative selection of Fault N samples. This selection covers the karst sequence from the base to the the upper parts of the paleokarst damage zone.

Snapshots of the virtual outcrop are used to show the location of the samples in the field. The limiting karst damage and paleocave surfaces are also shown in these photographs as well as the scaled blue spots representing permeability values.

Hand samples and thick (250 μm) and thin (30 μm) sections are also displayed with the areas of the cathodoluminescence photomosaics marked.

Scanning electron microscopy (SEM) photographs show microstructure features of the karst microcavities and fractures.

Sample 45. Thin section: 45B.

Limiting the east border of the paleokarst. Fault N: lower part of the paleokarst sequence fill.

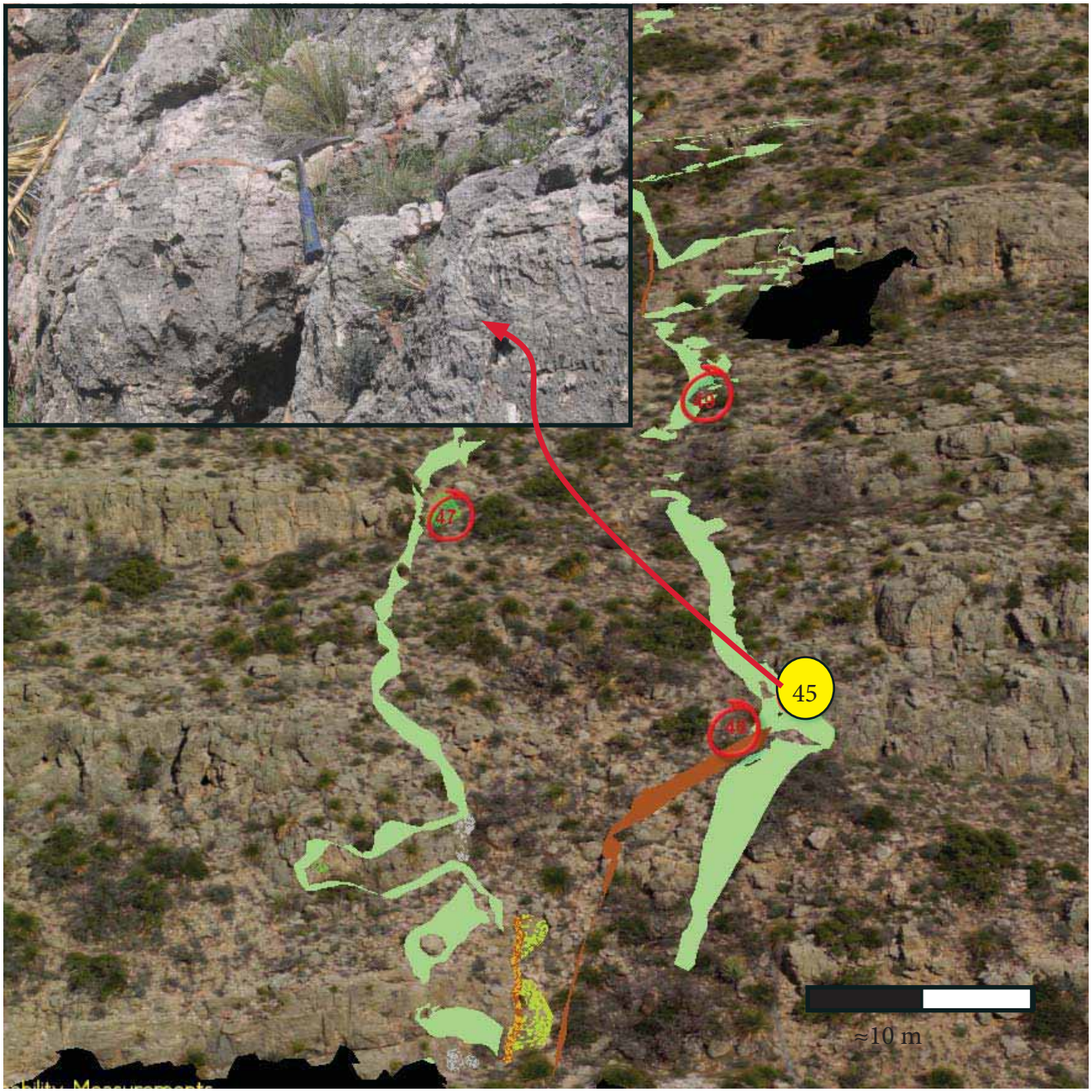

Location of the sample in the field.

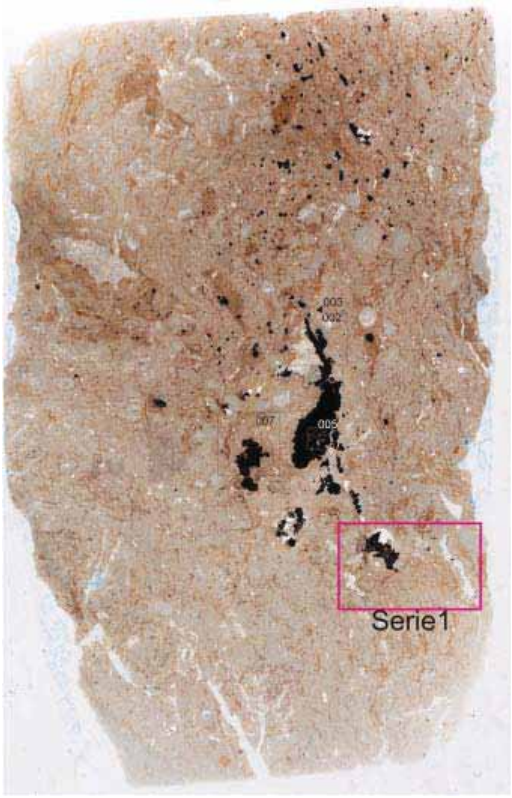

Photograph of the hand sample (above). Scanner of the thin section which shows the position of the SEM photographs and CL photomosaics (right).

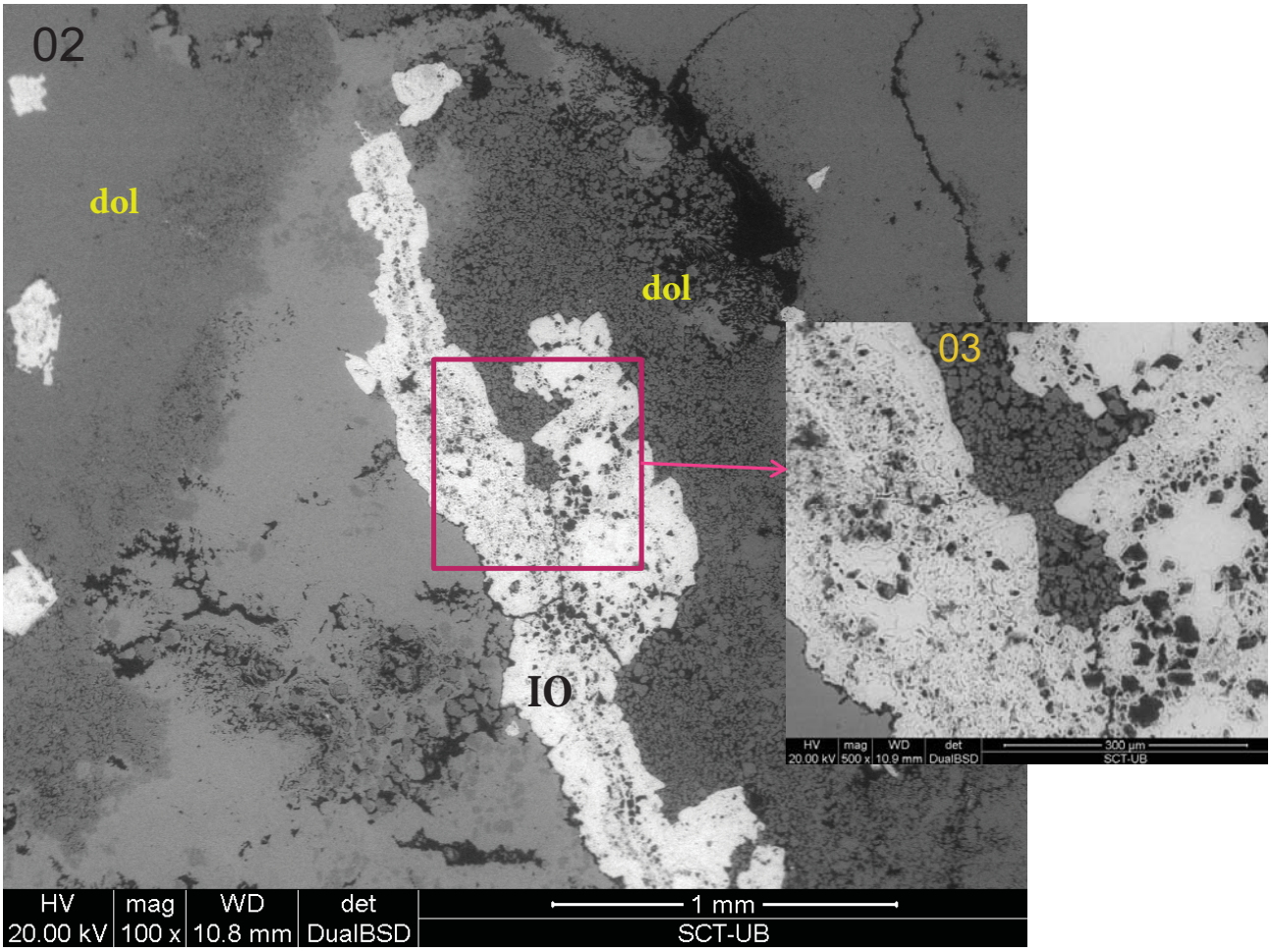

SEM images 02 and 03 (see areas in the scanner of the thin section). Remnants of dolomite (dol) embedded in massive hematite concretions. IO: Iron oxides.

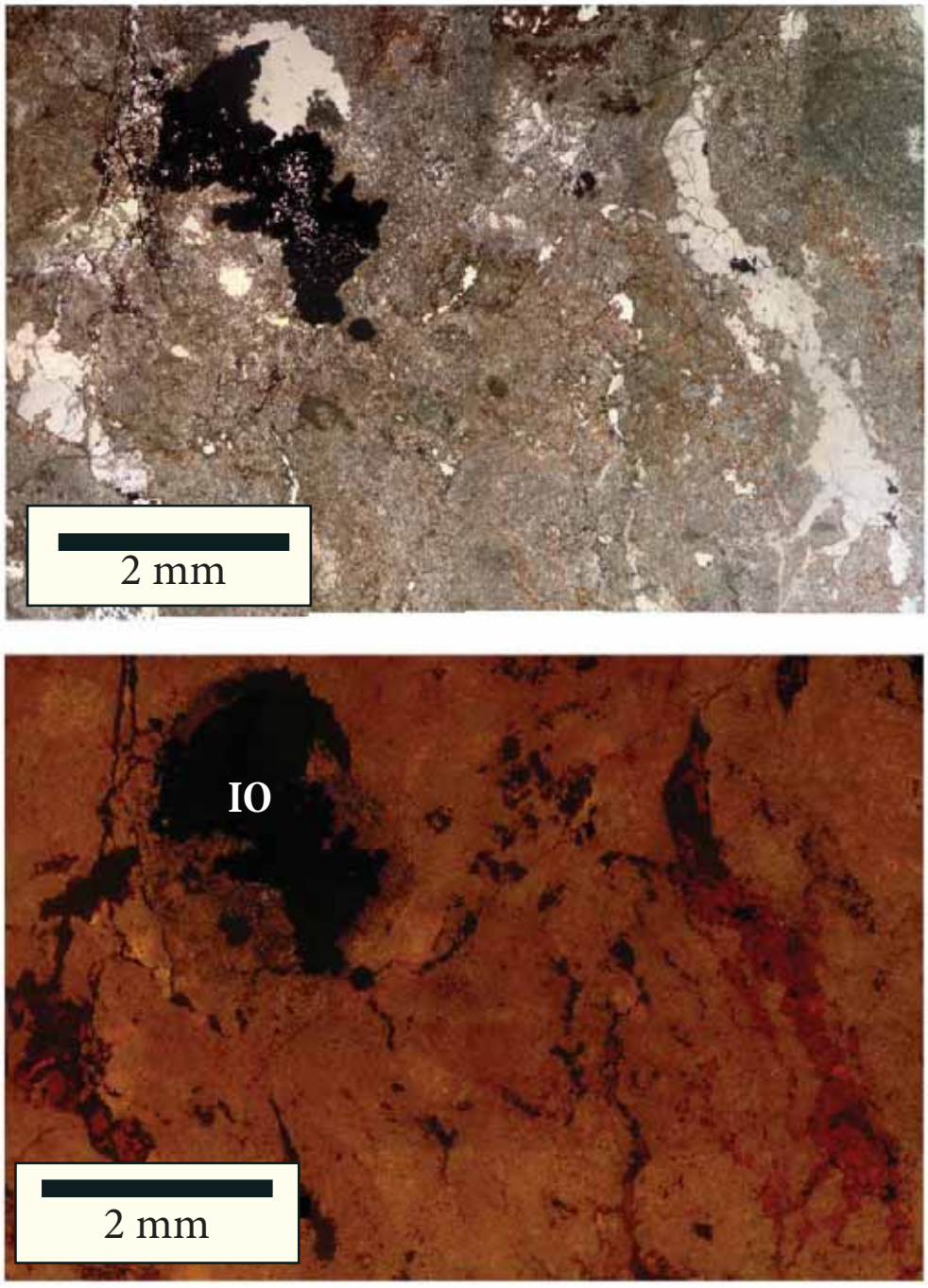

Serie1. CL photomosaic of the area shown in the thin section scanner. Iron oxide accumulation (IO) and dedolomite/calcite cemented microfractures.

Sample 46. Thin section: 46B

Adjacent to the eastern border of the paleocave area in a fracture zone. Fault N: lower part of the paleokarst sequence fill.

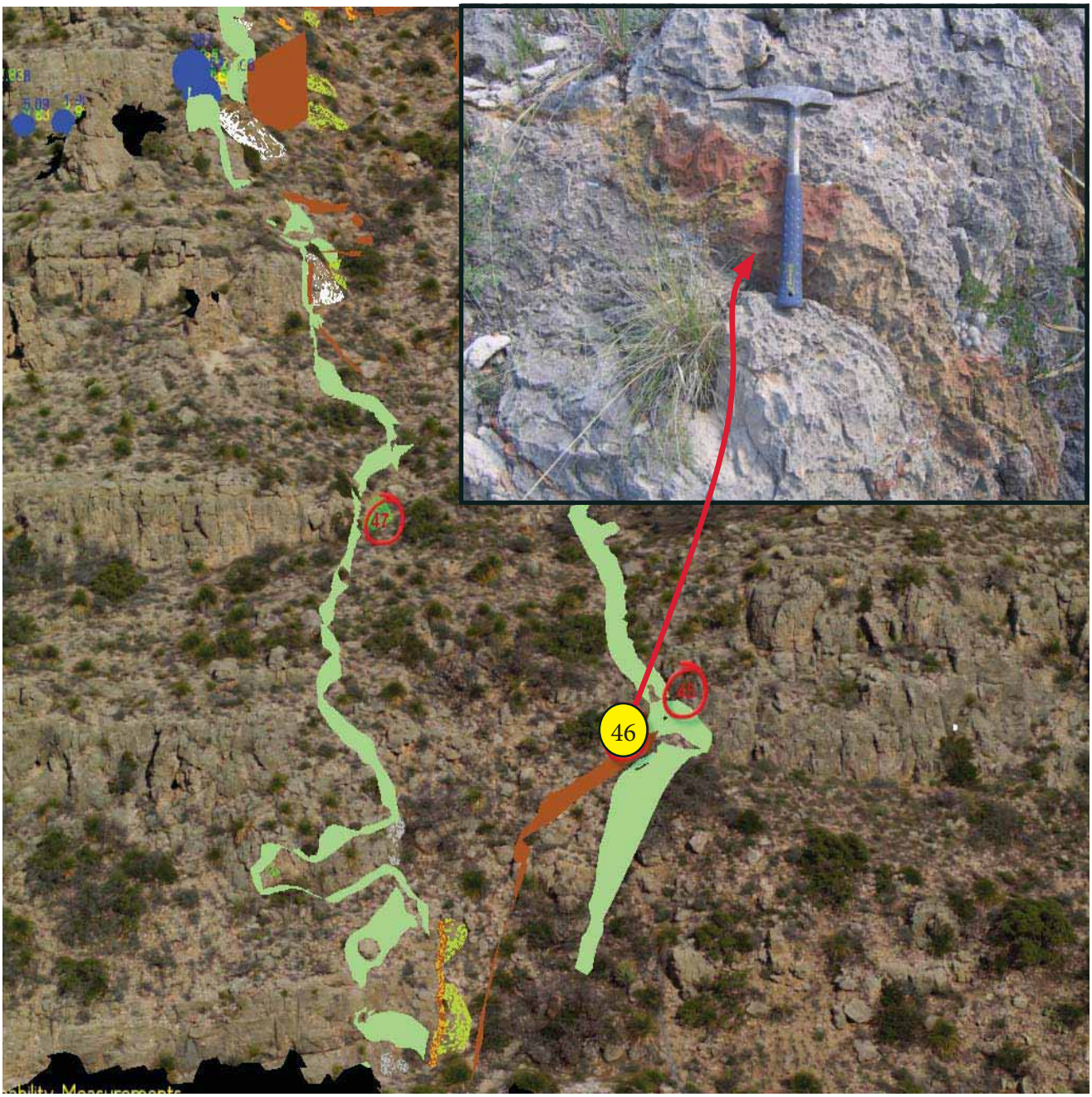

Location of the sample in the field.

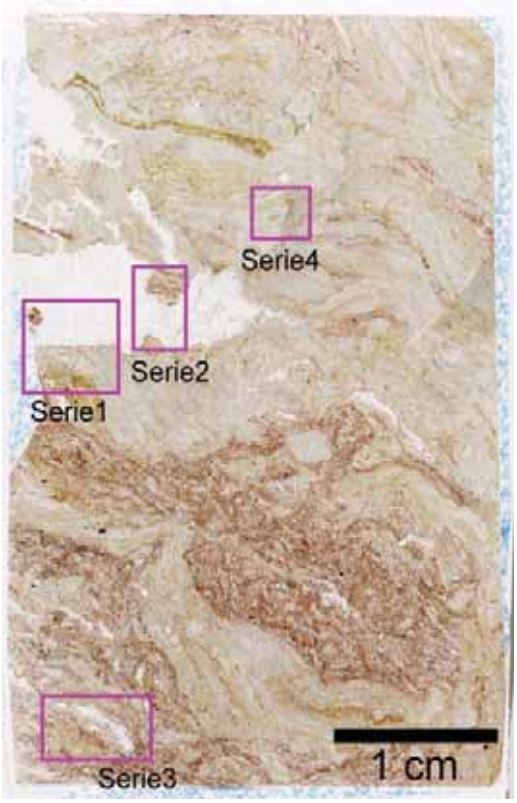

Just above: Photograph of the hand sample. At the right: Scanner of the thin section with the position of CL series.

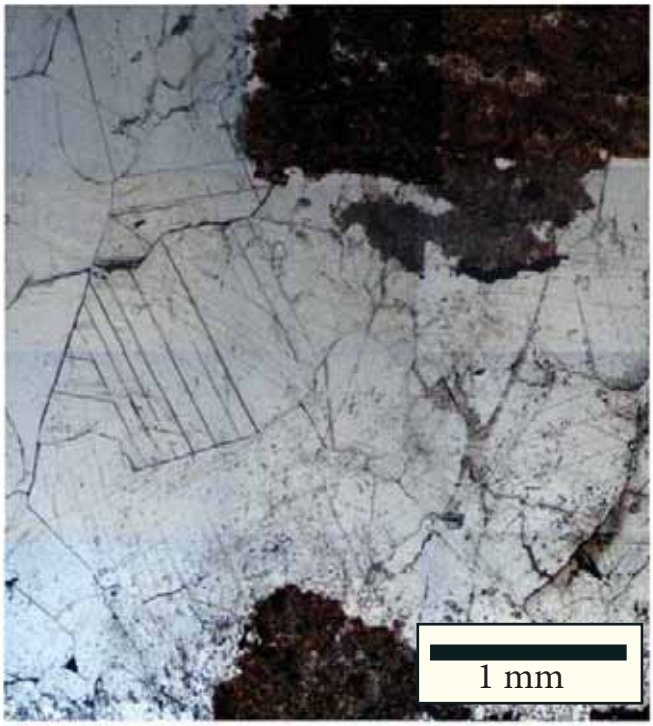

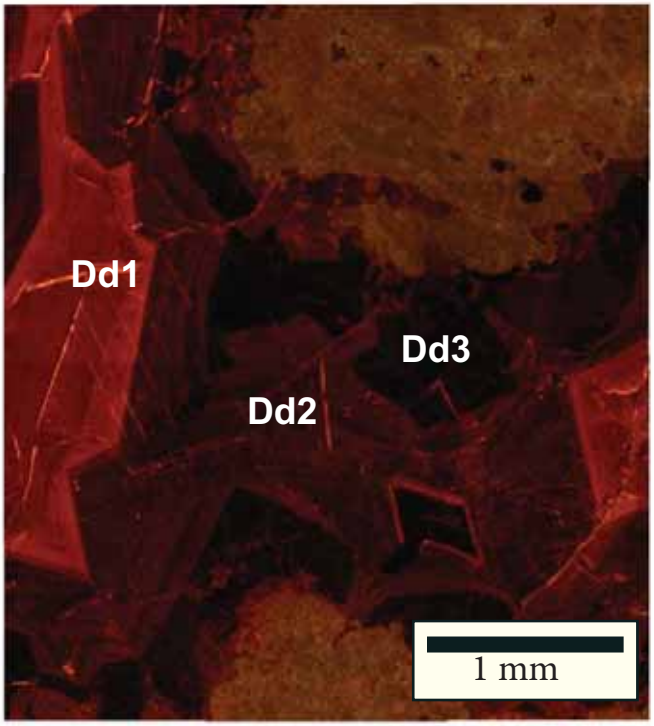

Serie 2. Dedolomite zoned crystals cementing porosity between two corroded masses of replacive dolomite. The three subzones (Dd1, Dd2 and Dd3) display different luminescences, trace element and isotope compositions.

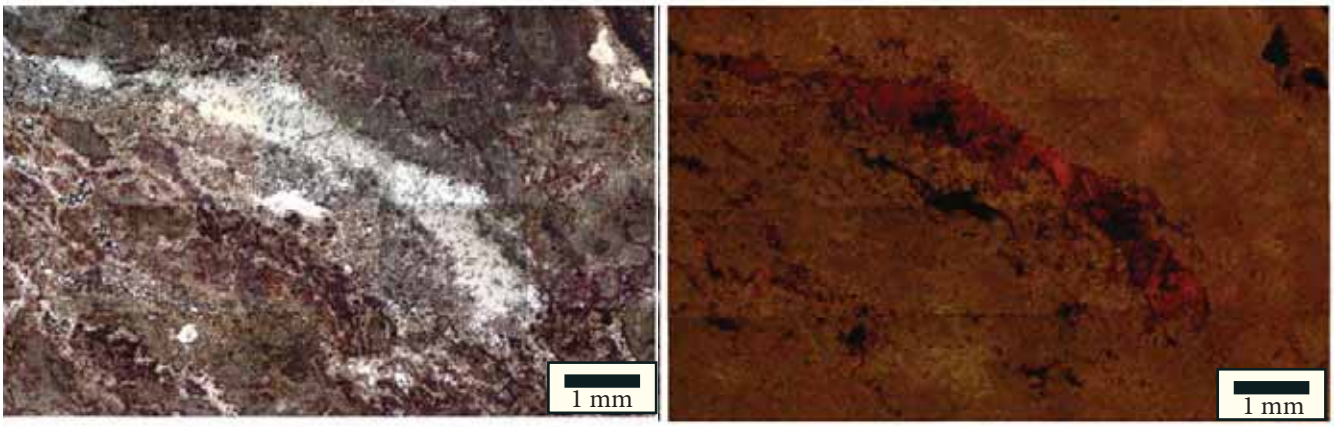

Serie 3. Dedolomite cemented cavity.

Serie 3. Dark insoluble residue along pressure-solution surfaces (stylocumulate: SC) The stylocumulate is cemented with dull calcite.

Sample 47. Thin sections 47A and 47B

Inside the paleocave zone. Below a chaotic breccia deposit. Fault N: lower part of the paleokarst sequence fill.

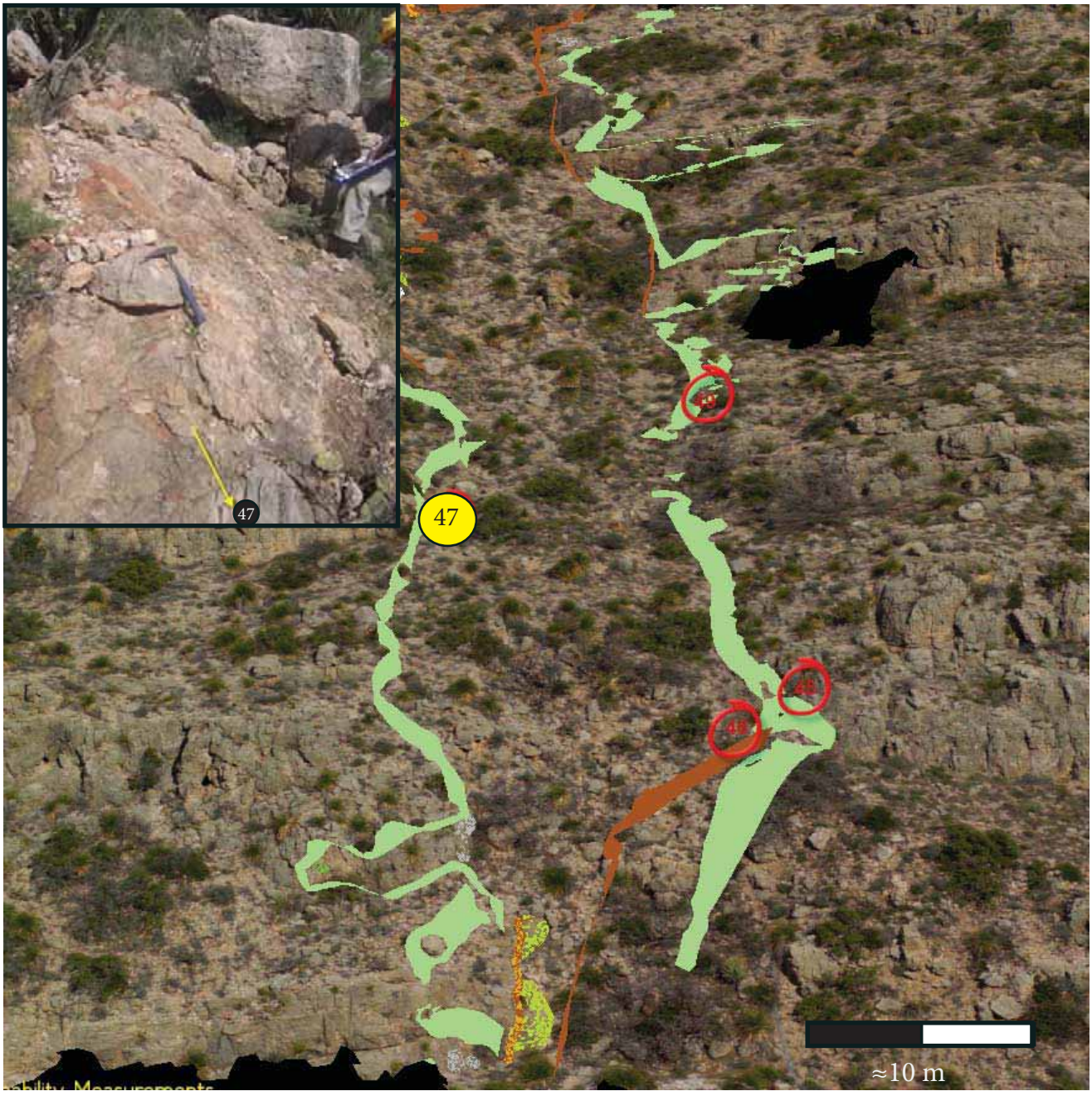

Location of the sample in the field.

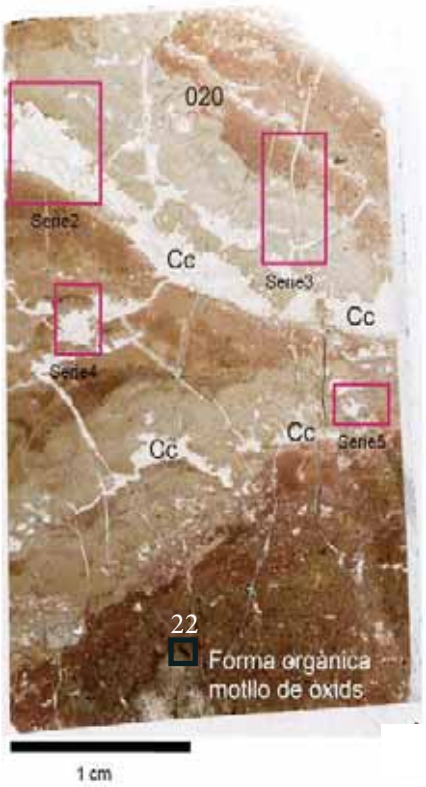

Just above: Photograph of the hand sample. At the right: Scanner of the 47A thin section with the position of CL photomosaics.

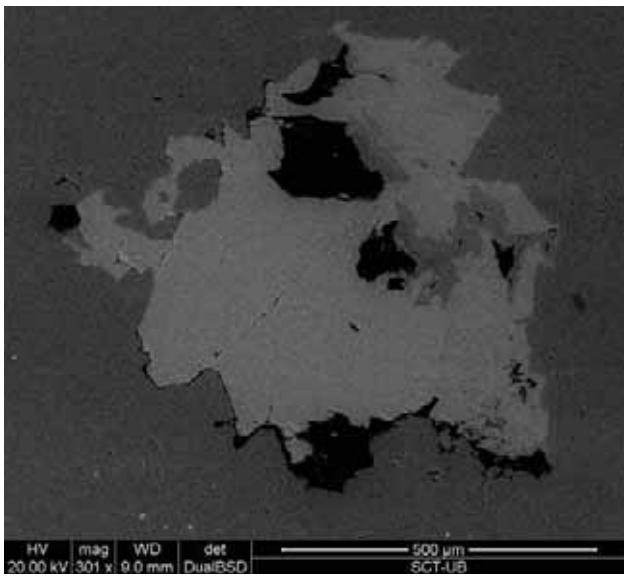

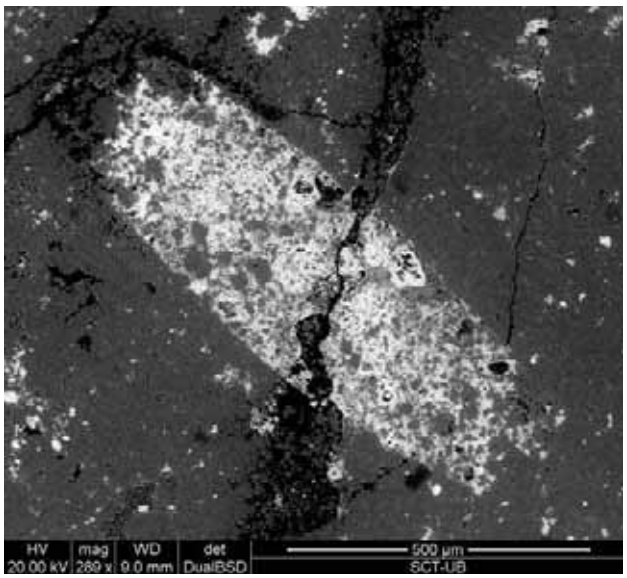

SEM images. Left: Calcite filled cavity (Photo 20). Right: Fractured hematite mould. Iron oxides probably replaced evaporites that nucleated organic rich structures and biomoulds (Photo 22). See area of the photographs in the thin section scanner.

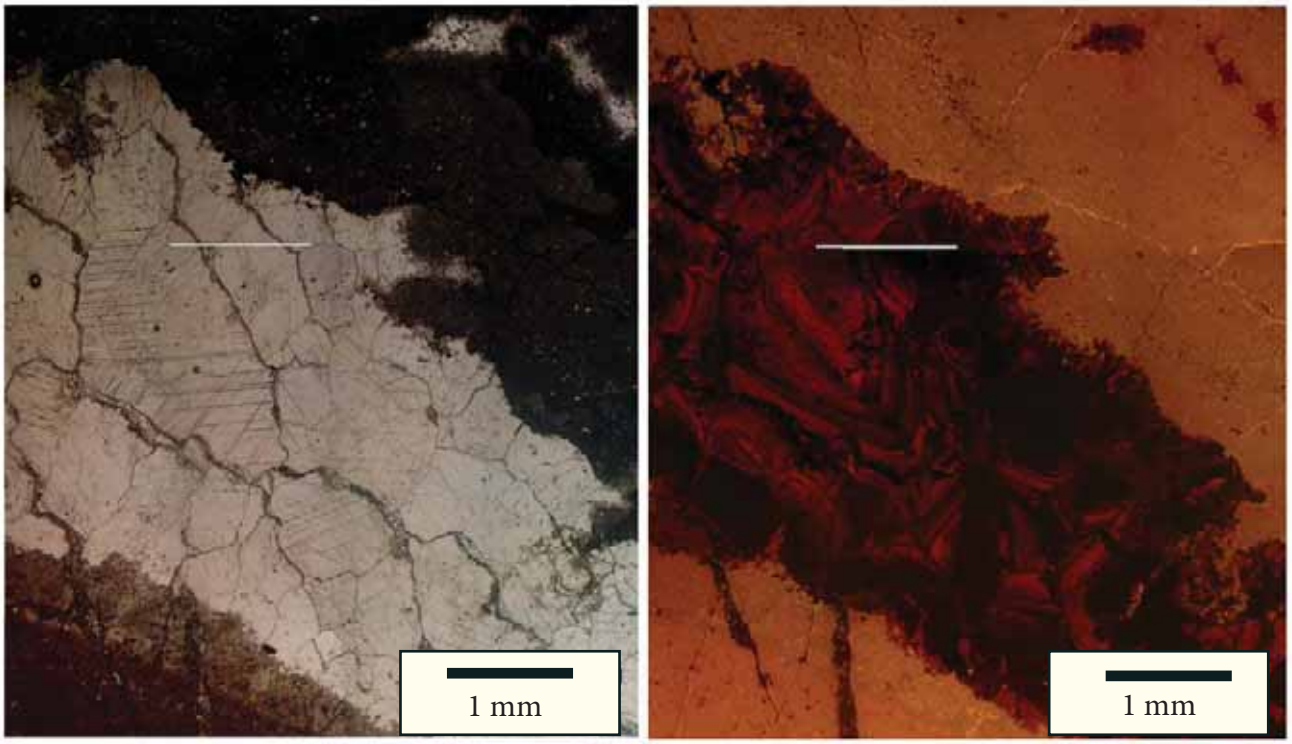

Serie 2. Dedolomitization along fractures.

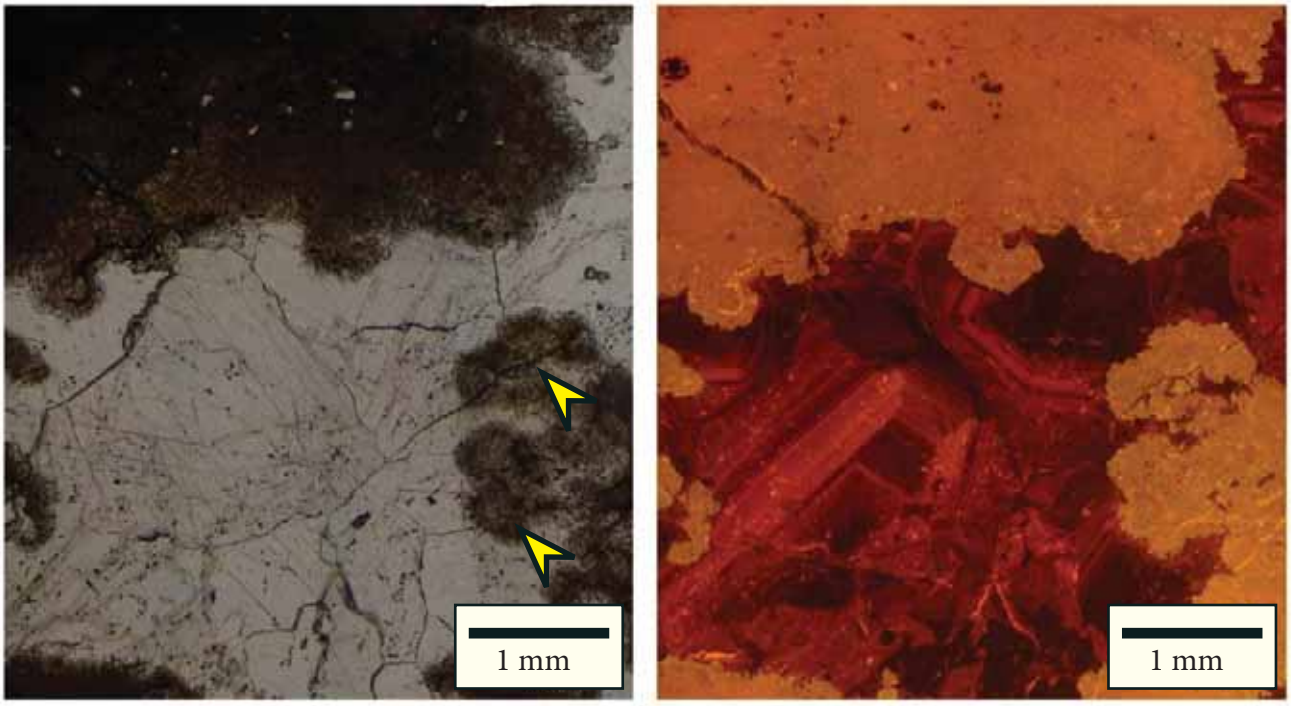

Serie 3. Dedolomite fracture fill cements exhibiting complex CL zonation. Crystal boundaries cut early relict dolomite masses (arrows) proving the replacement fabric of dedolomite.

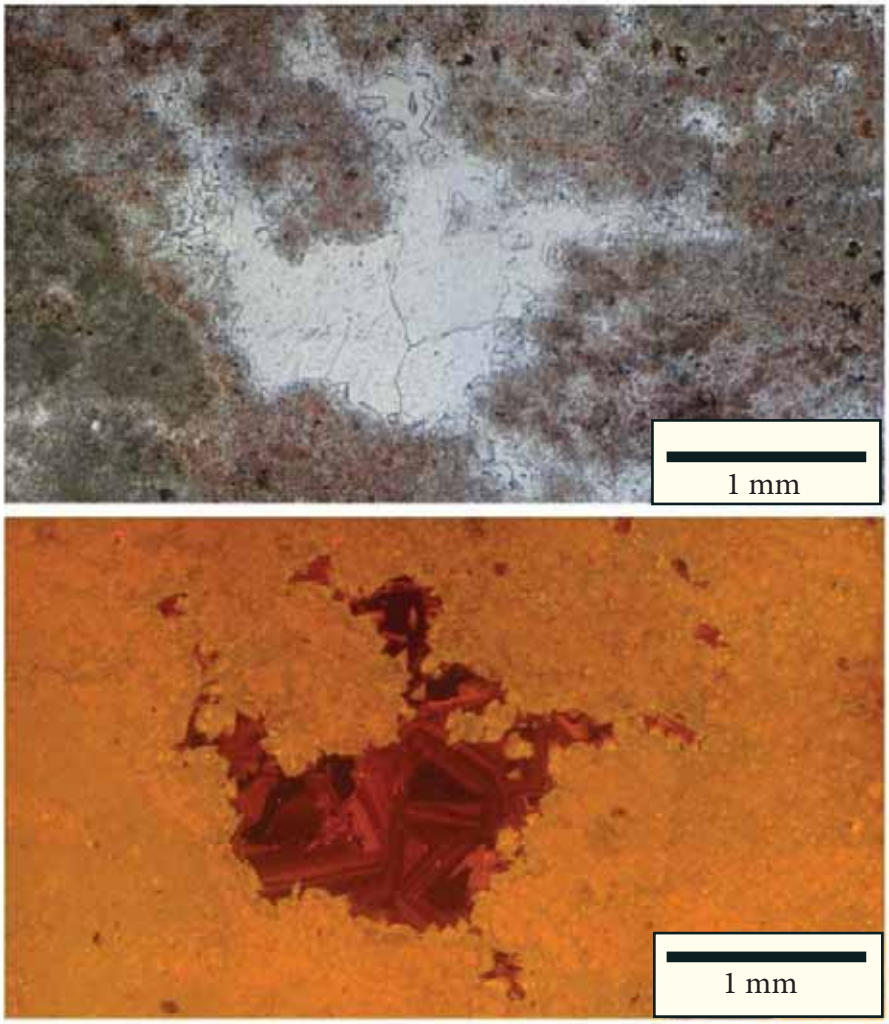

Serie 4. Vug-filling dedolomite in fracture area.

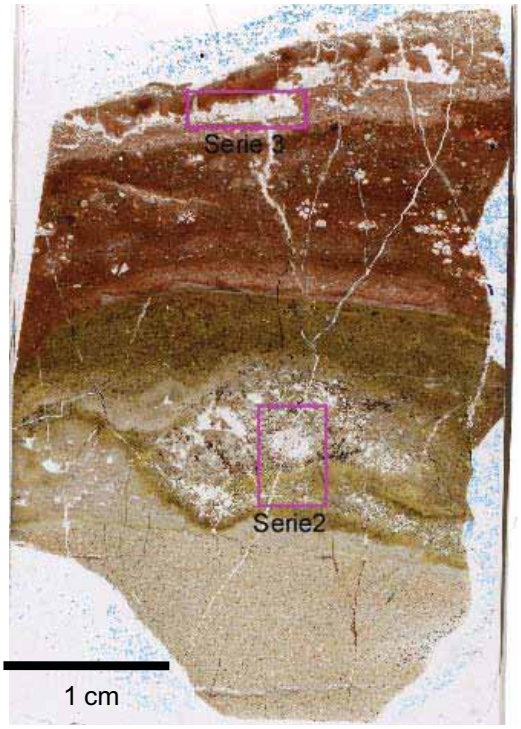

Scanner of the 47B thin section with the position of CL photomosaics.

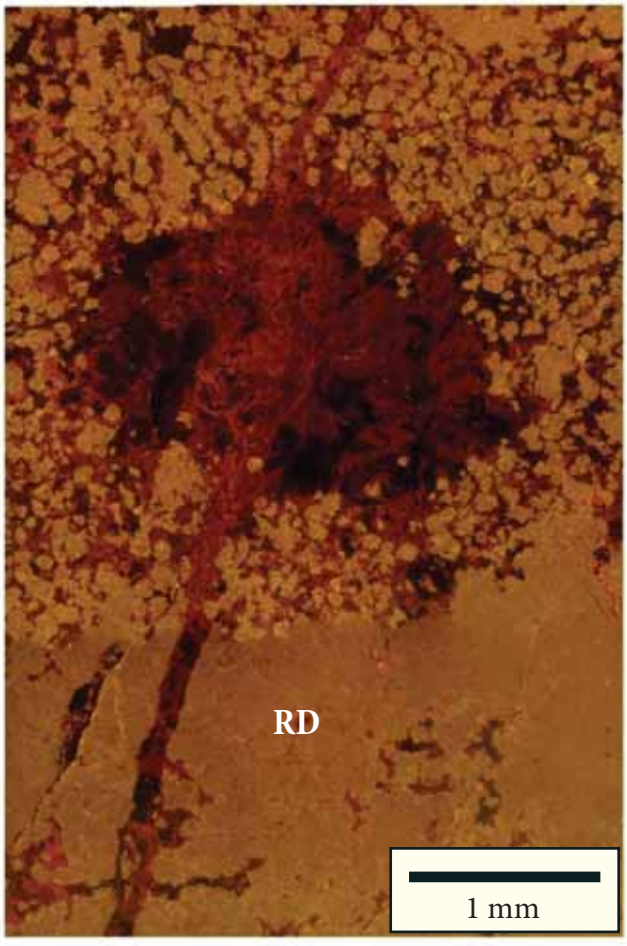

Serie 2. Late generation of dedolomite/calcite fracture fill and vug fill. Note the halo of sucrosic corroded dolomite with similar luminescence of the replacive dolomite (RD).

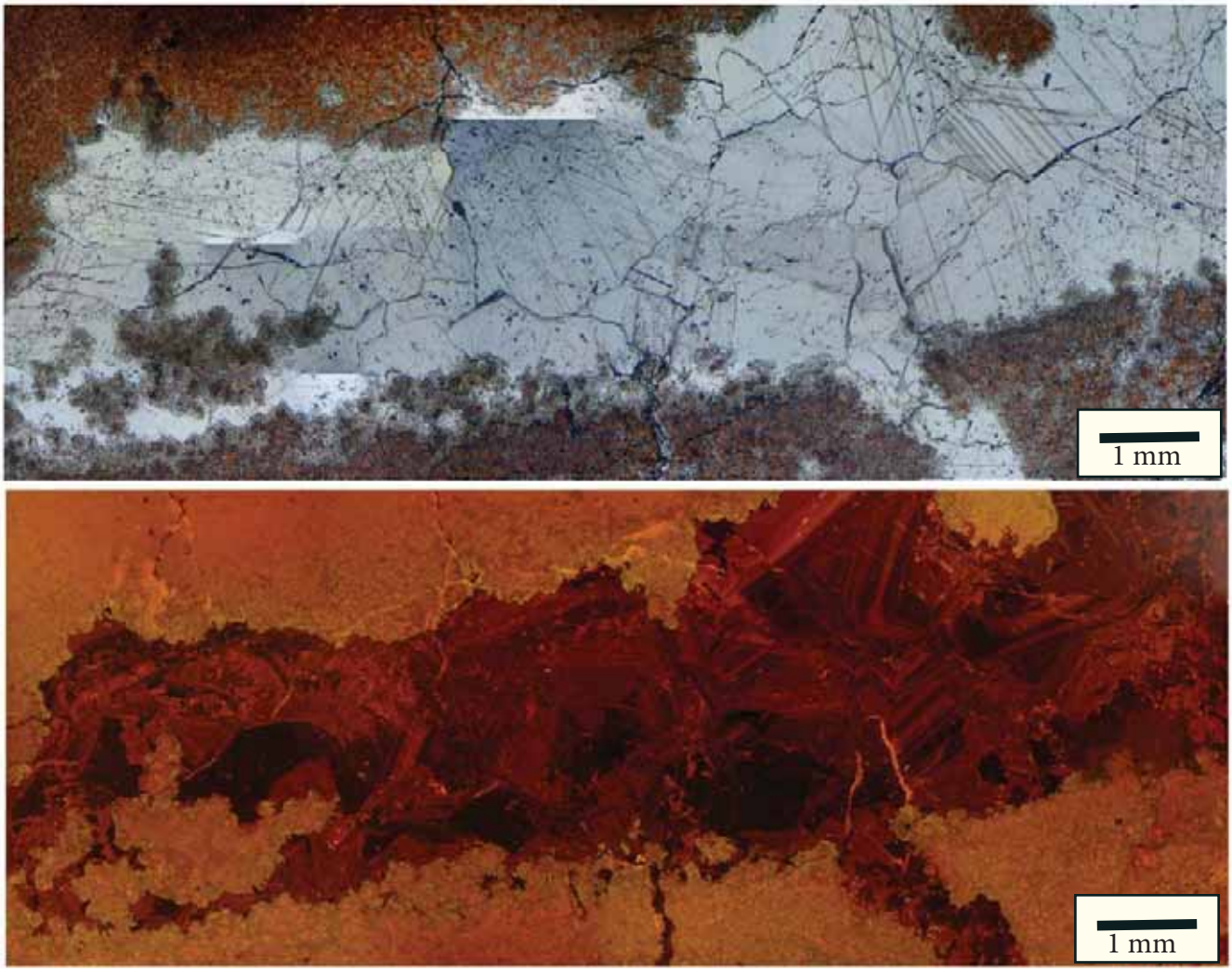

Serie 3. dedolomite mosaics with dolomite floating patches (left part of the photograph).

Sample 49. Thin section: 49A.

Host rock. External zone of the paleokarst. Fault N: lower part of the paleokarst sequence fill.

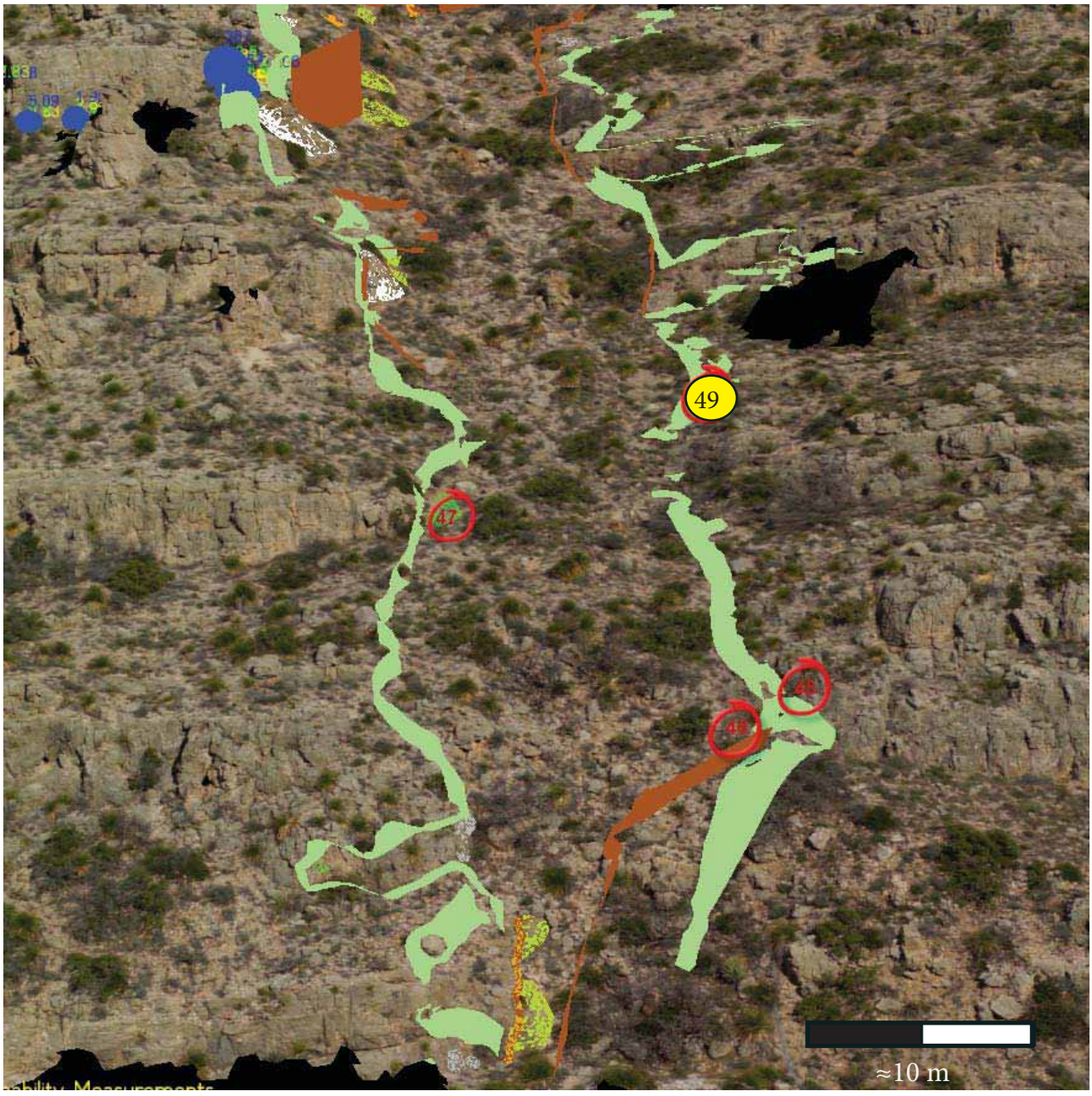

Location of the sample in the field.

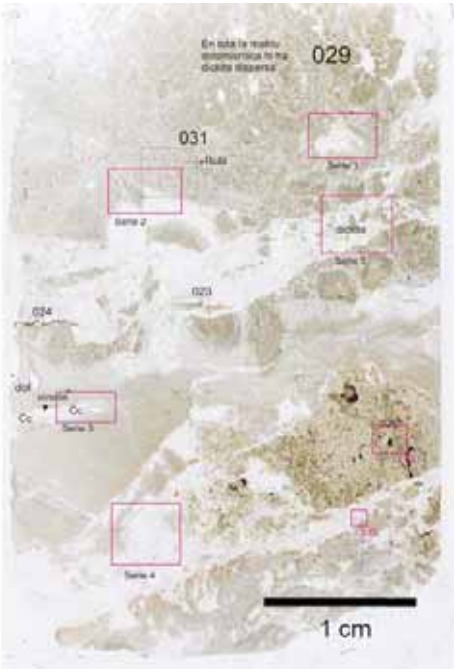

Just above: Photograph of the hand sample. At the right: Scanner of the thin section with the position of CL photomosaics.

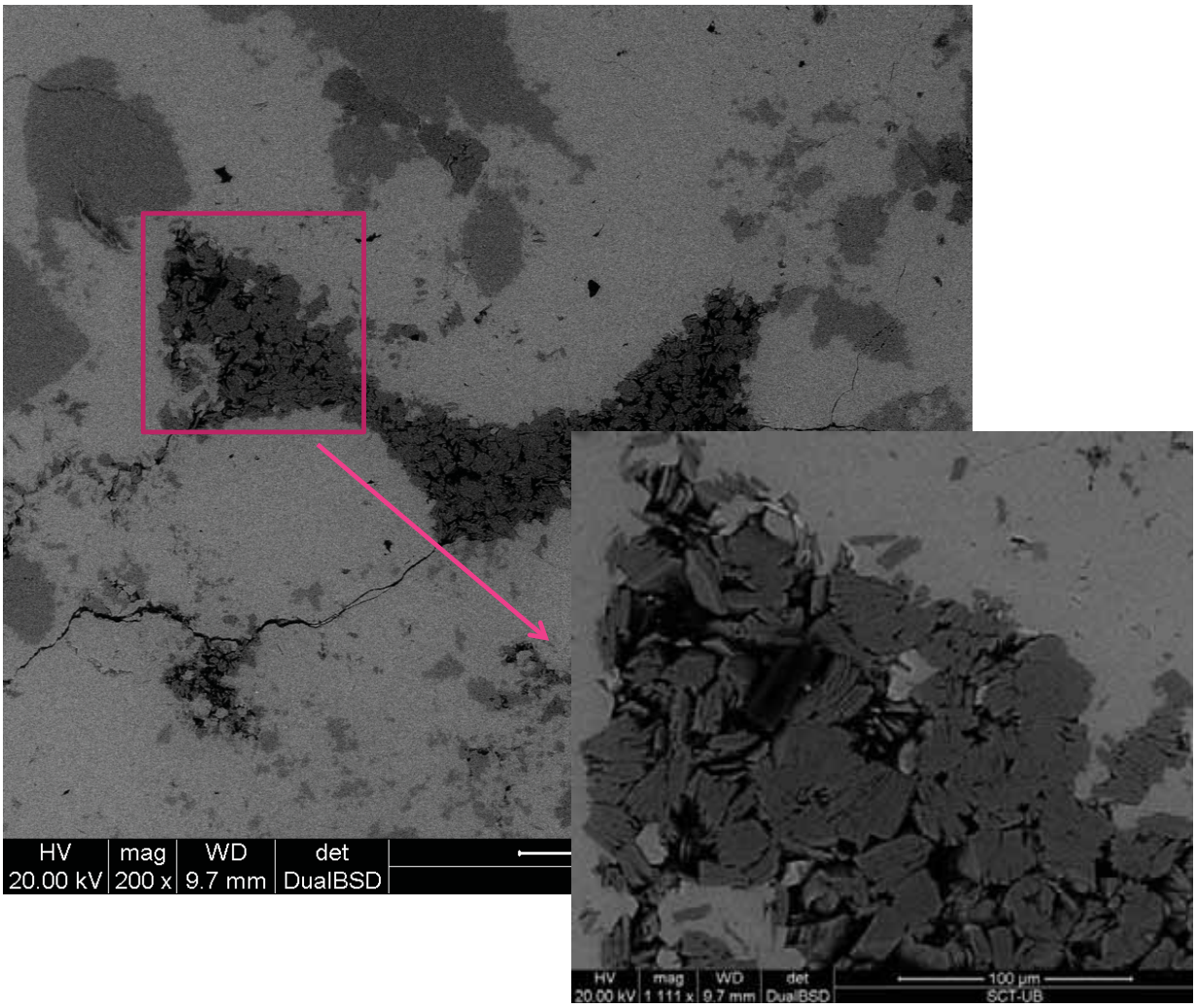

SEM image of vug filled with dickite.

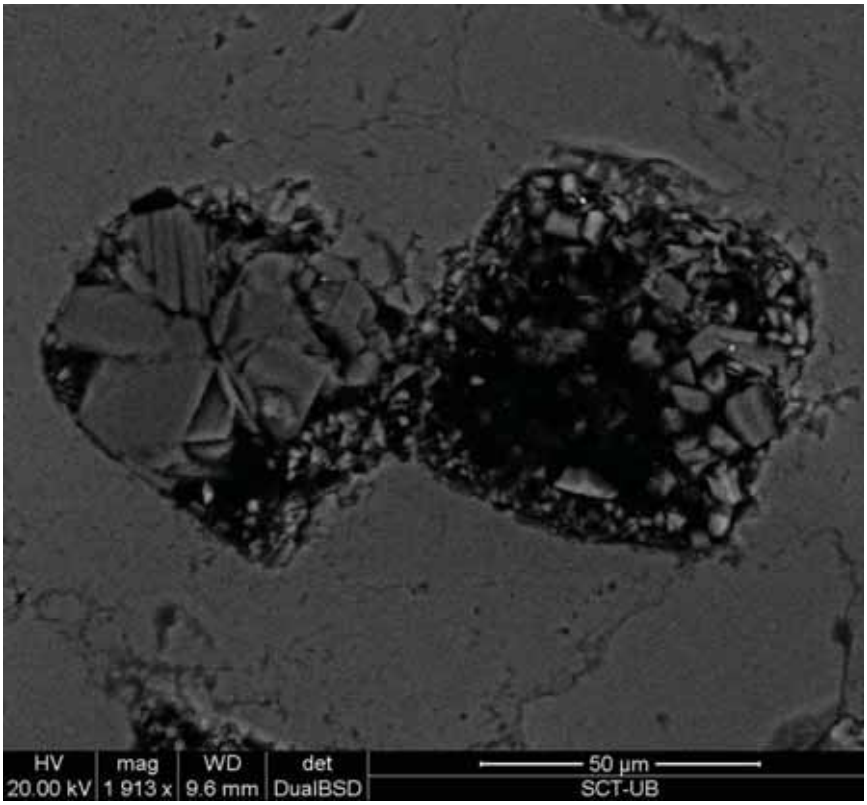

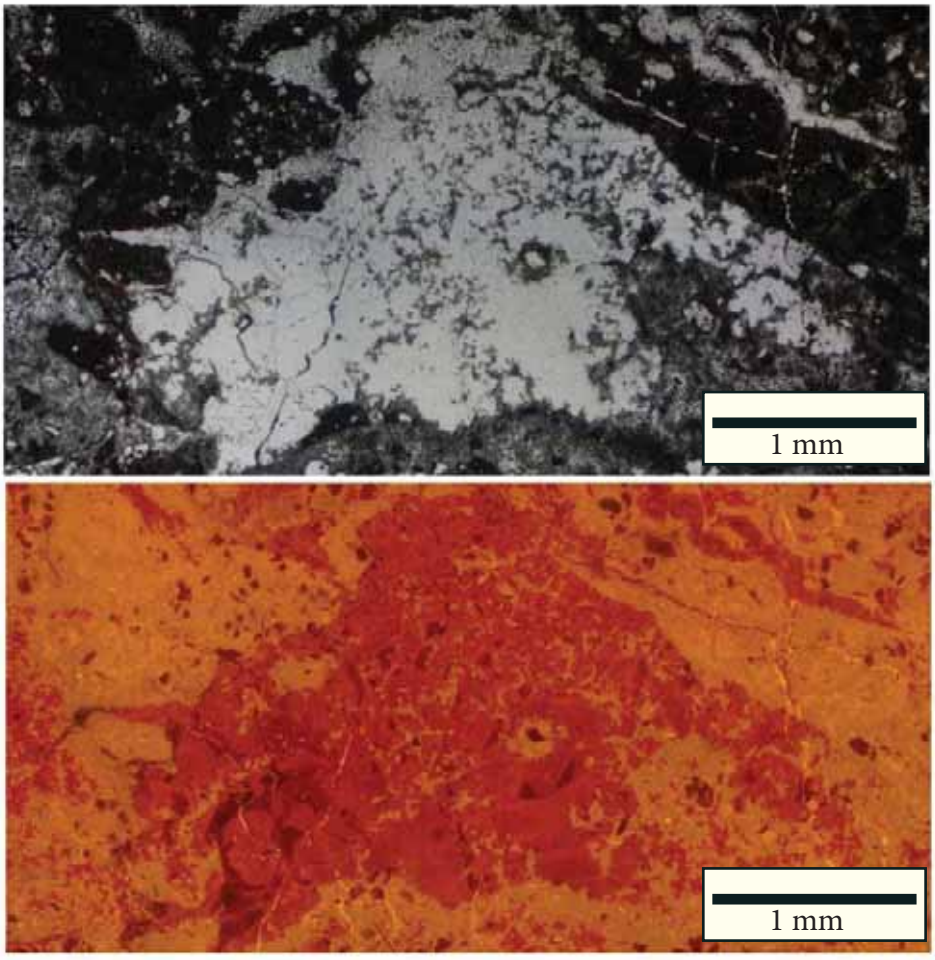

Top of the page: SEM image of dickite booklets within cavities of dissolved feldspars. Above: Serie 1. Dissolution fabric of vug- filling dedolomite.

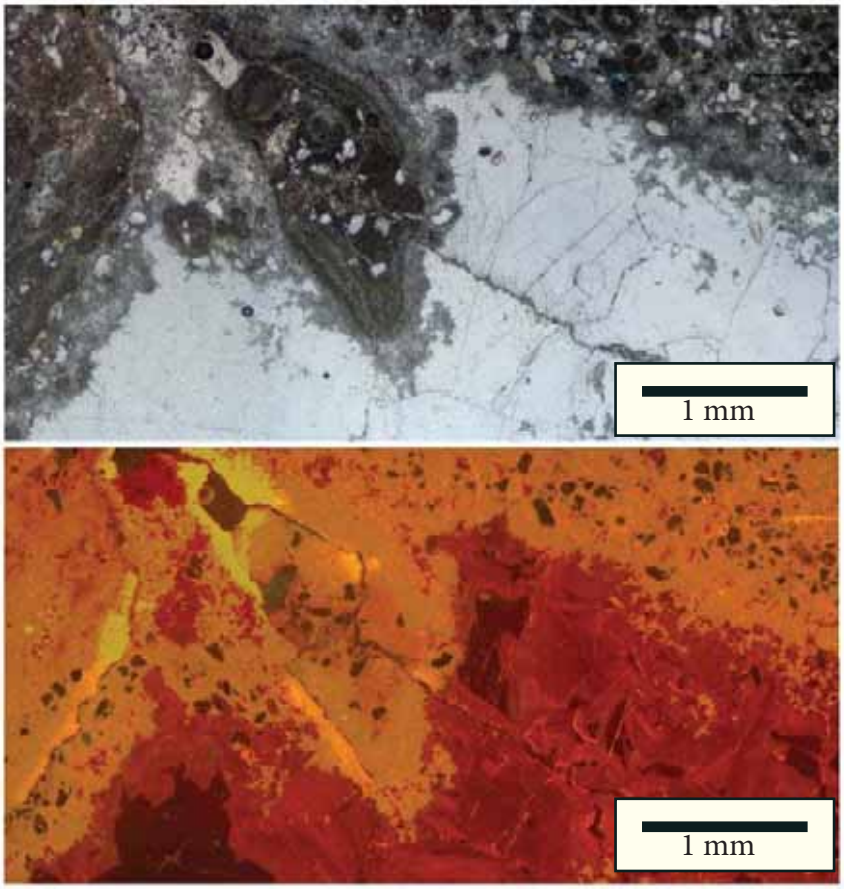

Serie 2. Dedolomite cement in a cavity after evaporite dissolution.

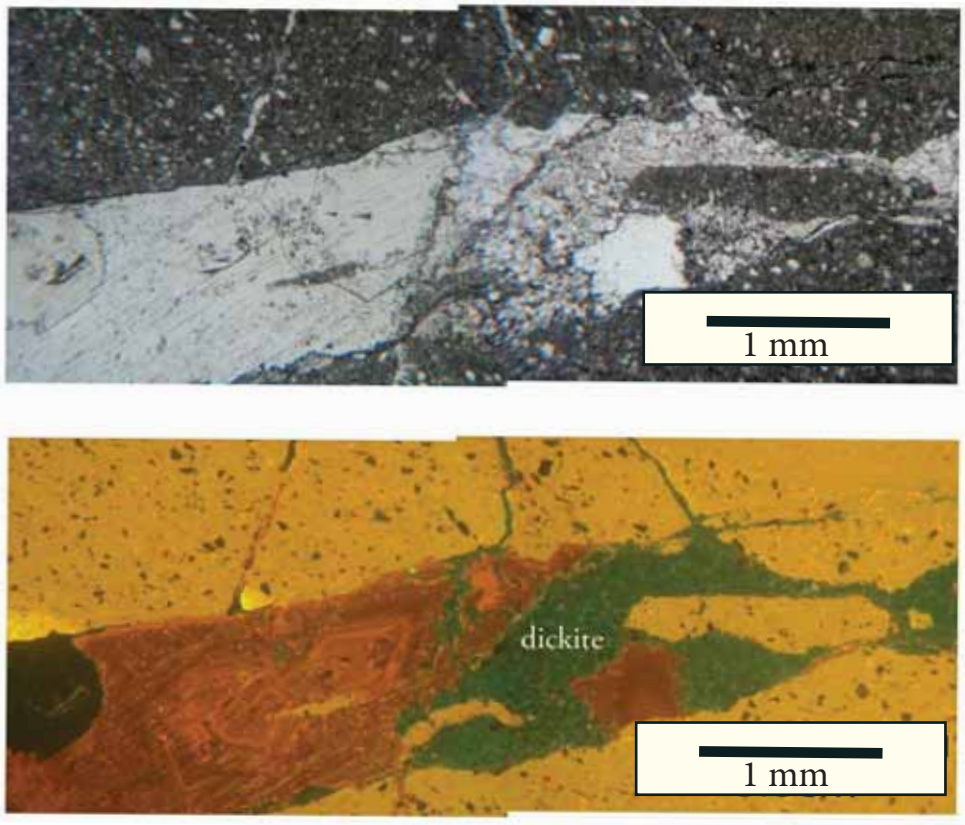

Serie 3. Fracture-fill dedolomite corroded and engulfed by dickite. Here dedolmite predates dickite. Dickite does not exhibit its characteristic blue luminescence in this photomosaic due to an error on the calibration of the CL device.

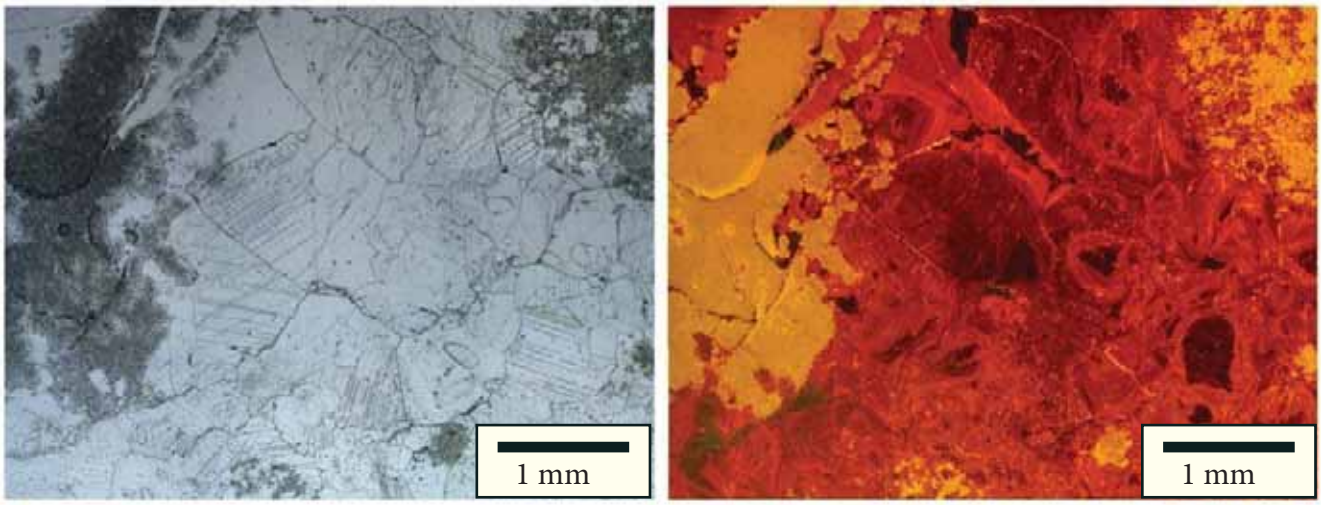

Serie 4. Detailed of the zonation array of the interpreted dedolomite.

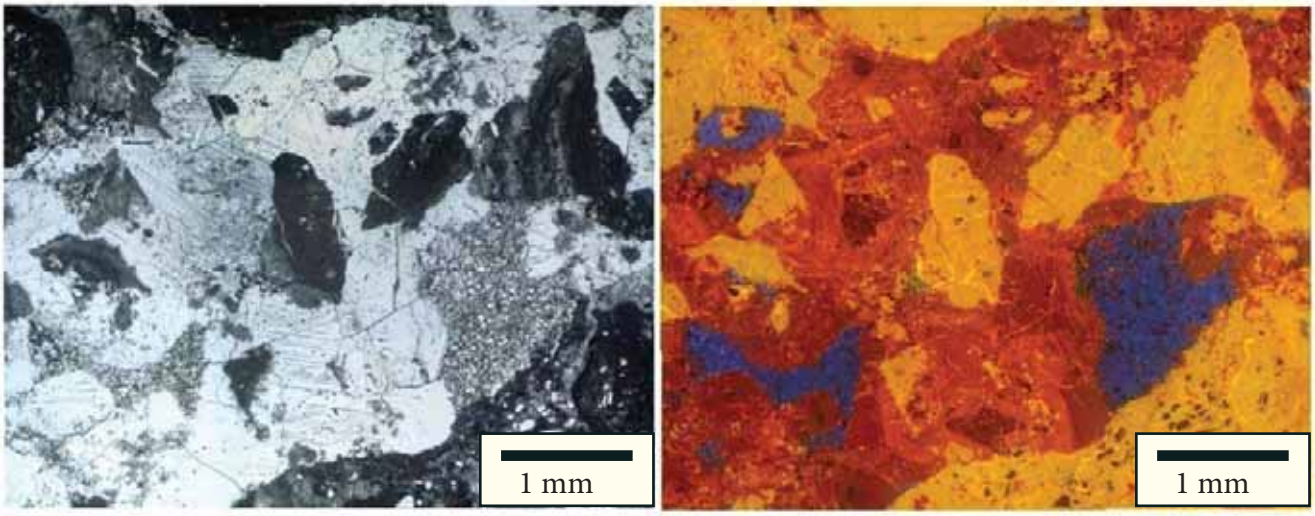

Serie 5. Floating dolomite angular clasts in a chaotic arrangement of dedolomite and dickite cements filling secondary porosity.

Sample 54.

Adjacent to the karst-damage zone. Fault N: middle part of the paleokarst sequence fill.

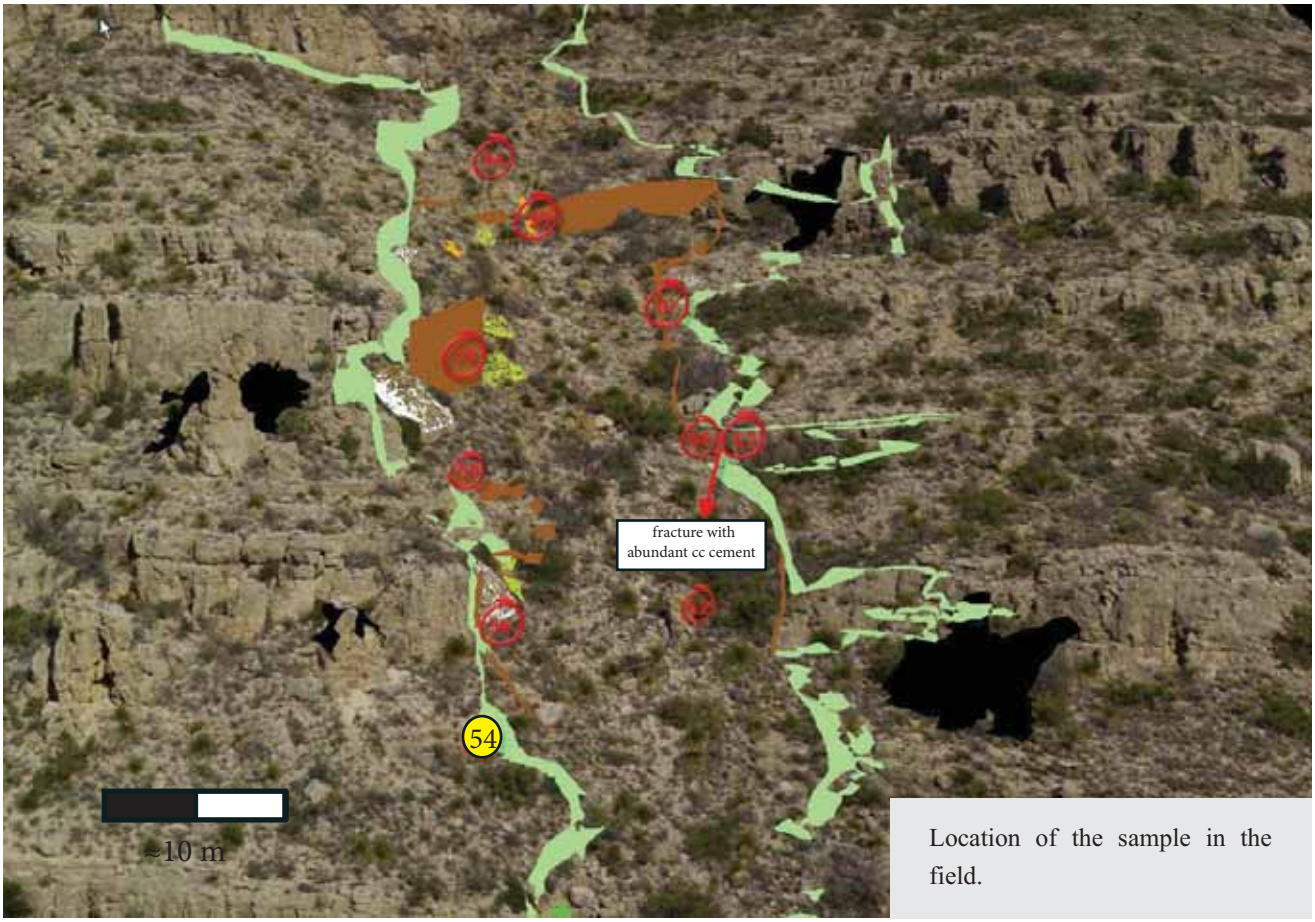

Location of the sample in the field.

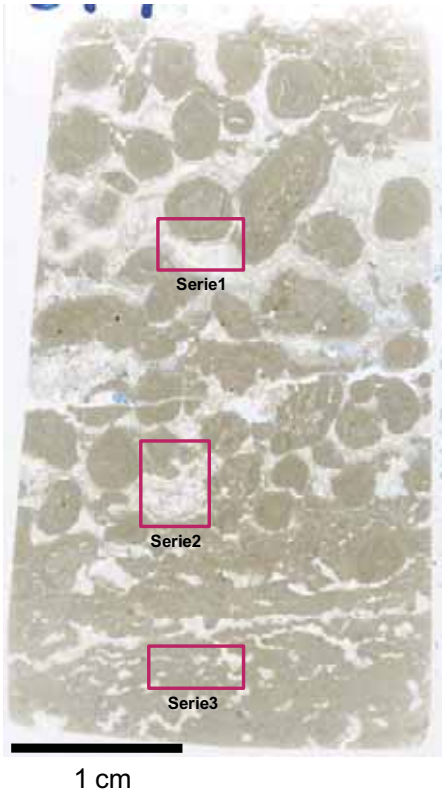

Just above: Photograph of the hand sample. At the right: Scanner of the thin section with the position of CL photomosaics.

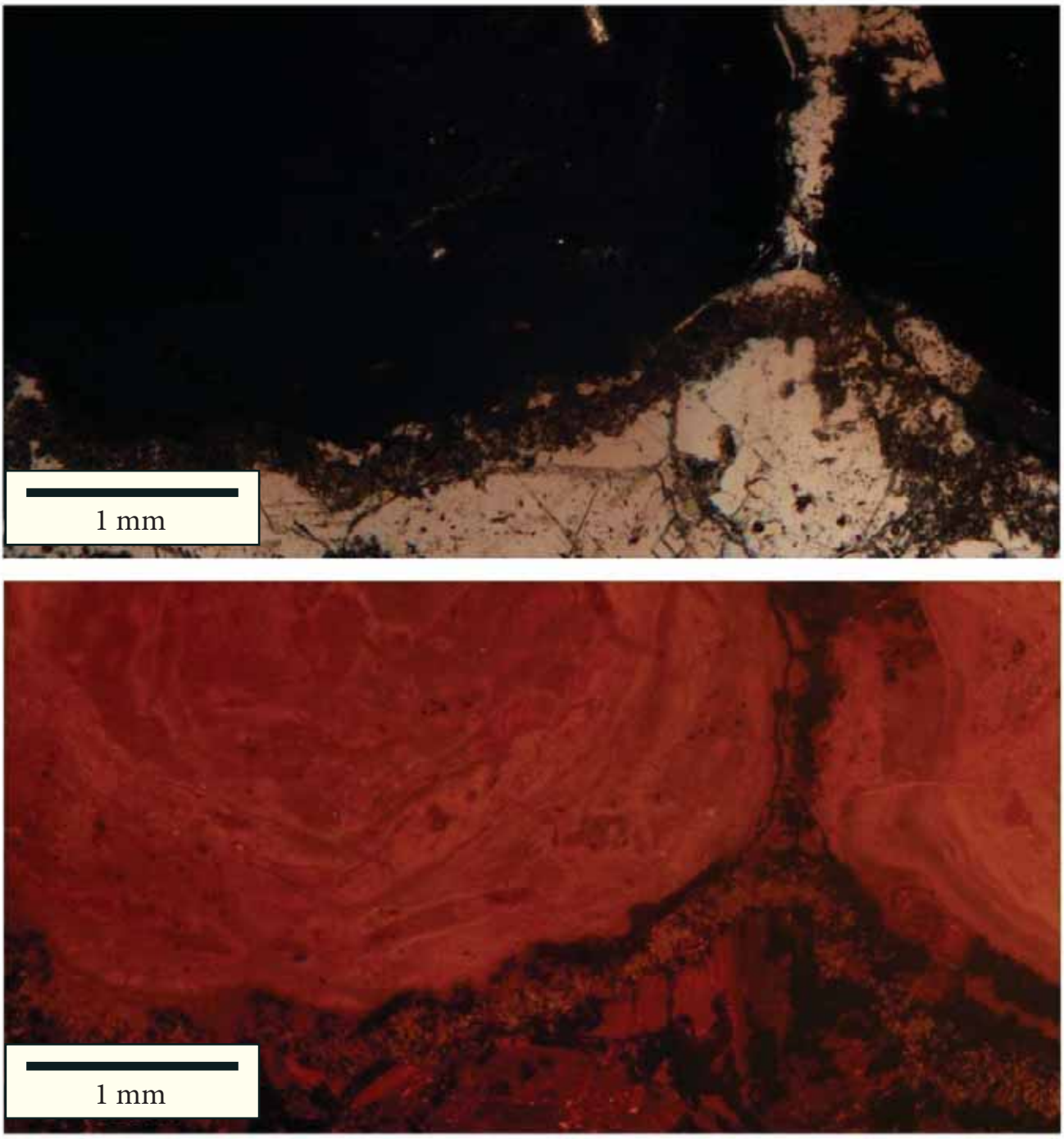

Serie 1. Interpisoid dissolution fabric.

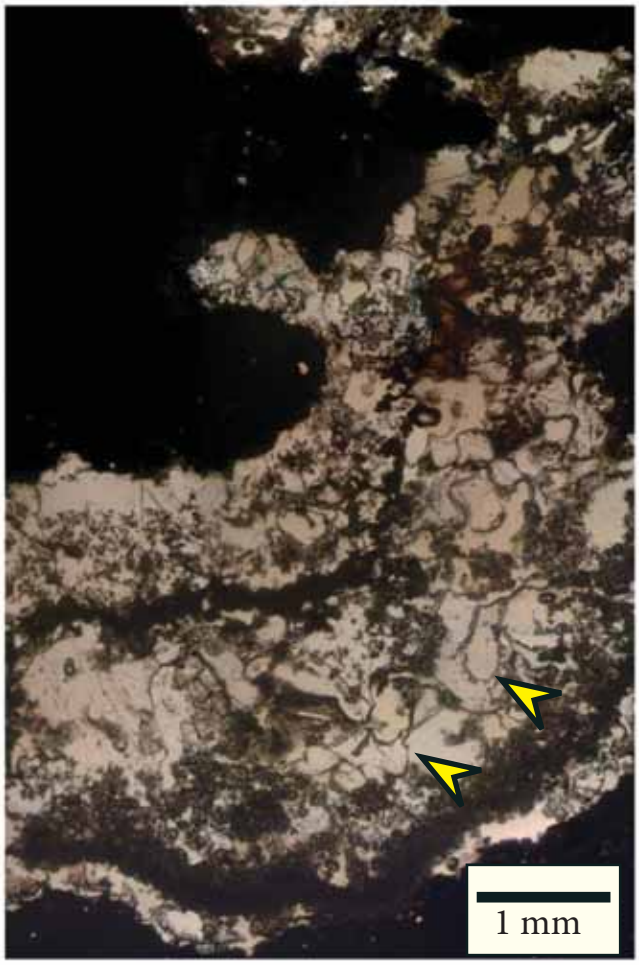

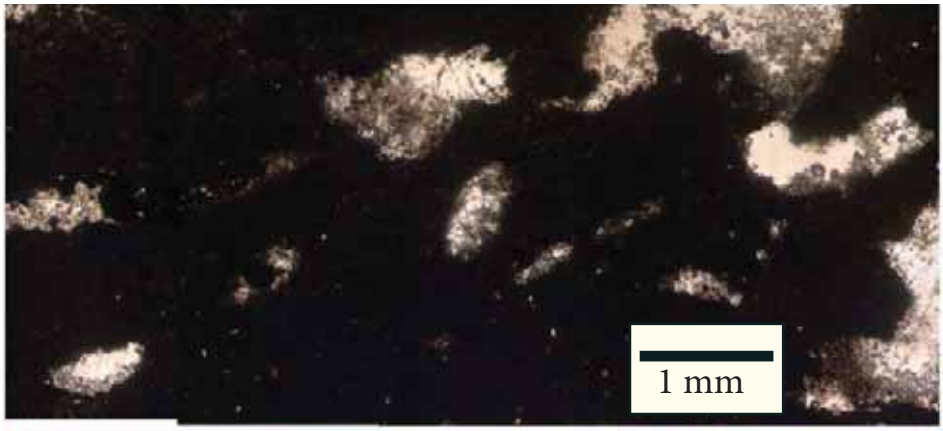

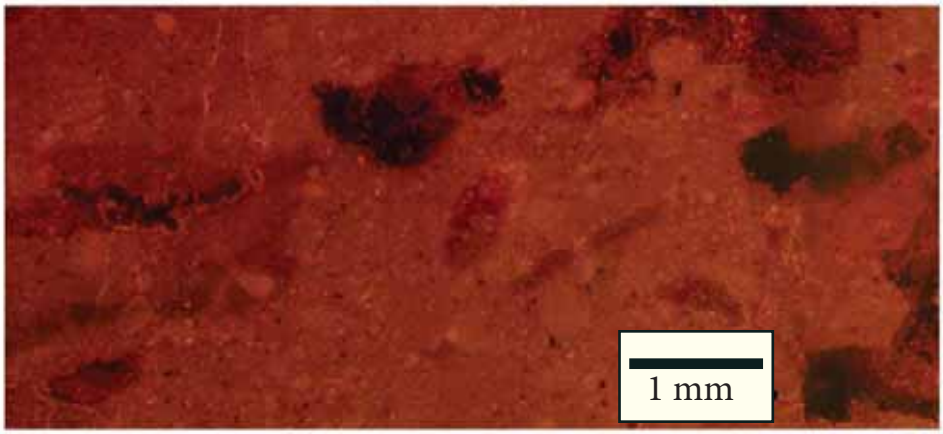

Serie 1 (Above).Note curve calcite crystals (arrows) in this dedolomite cemented cavity.
Serie 2 (Left).
Fenestrae cemented porosity.

Sample 56. Thin section 56B.

Inside the paleocave zone. Below a mosaic breccia deposit. Fault N: middle part of the paleokarst sequence fill.

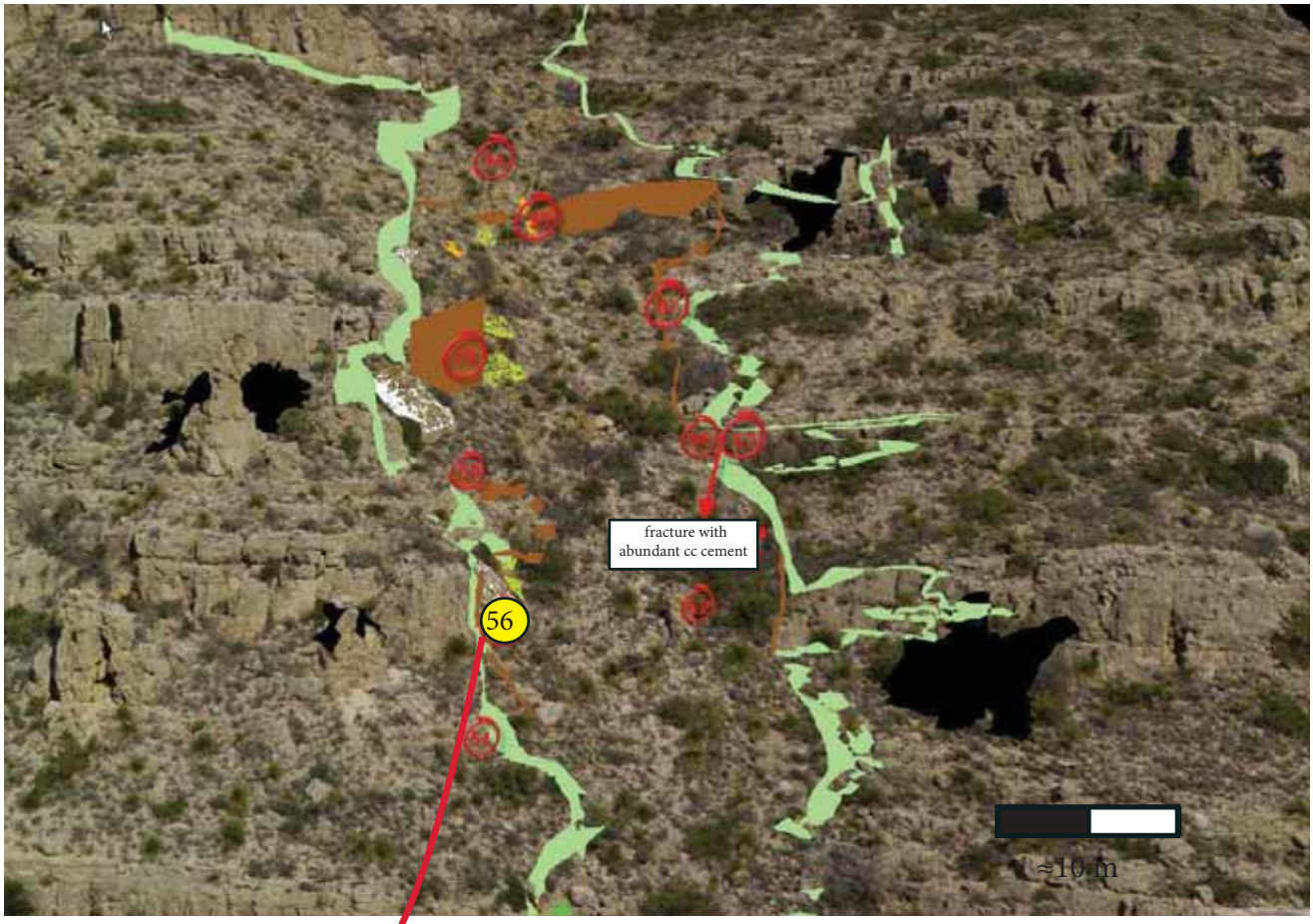

Location of the sample in the field. Note the slight rotation of the clasts in the mosaic breccia deposit.

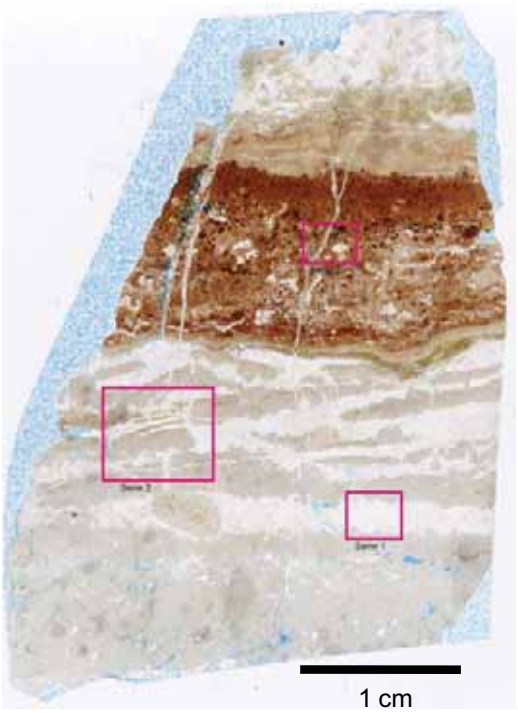

Just above: Photograph of the hand sample. At the right: Scanner of the thin section with the position of CL photomosaics.

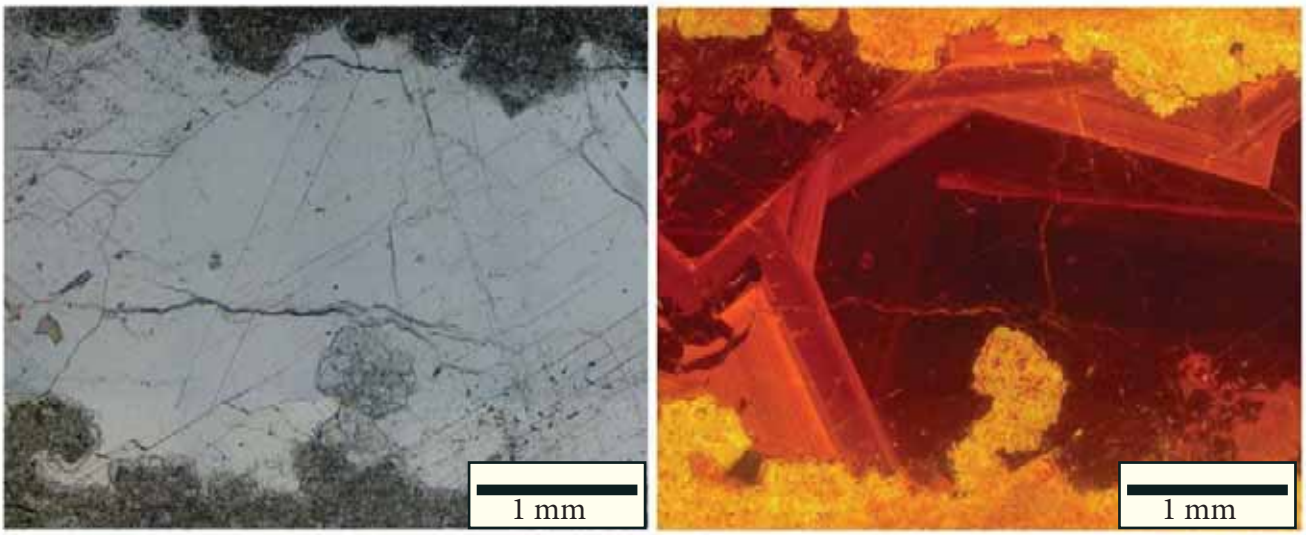

Serie 1. Dedolomite cementation.

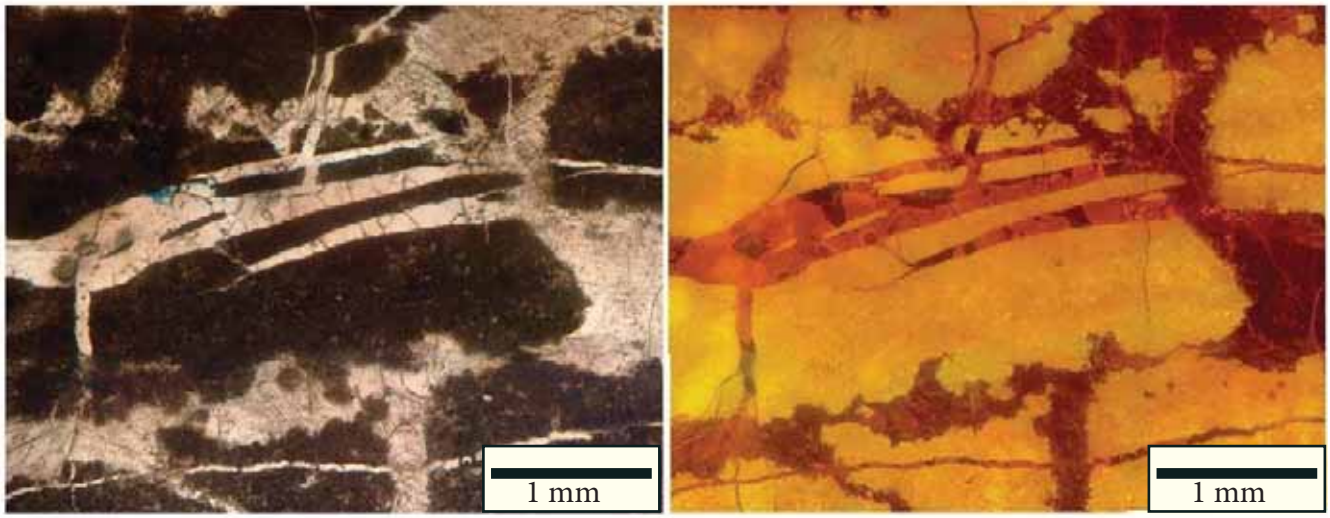

Serie 2. Fracture cements in brecciated zones.

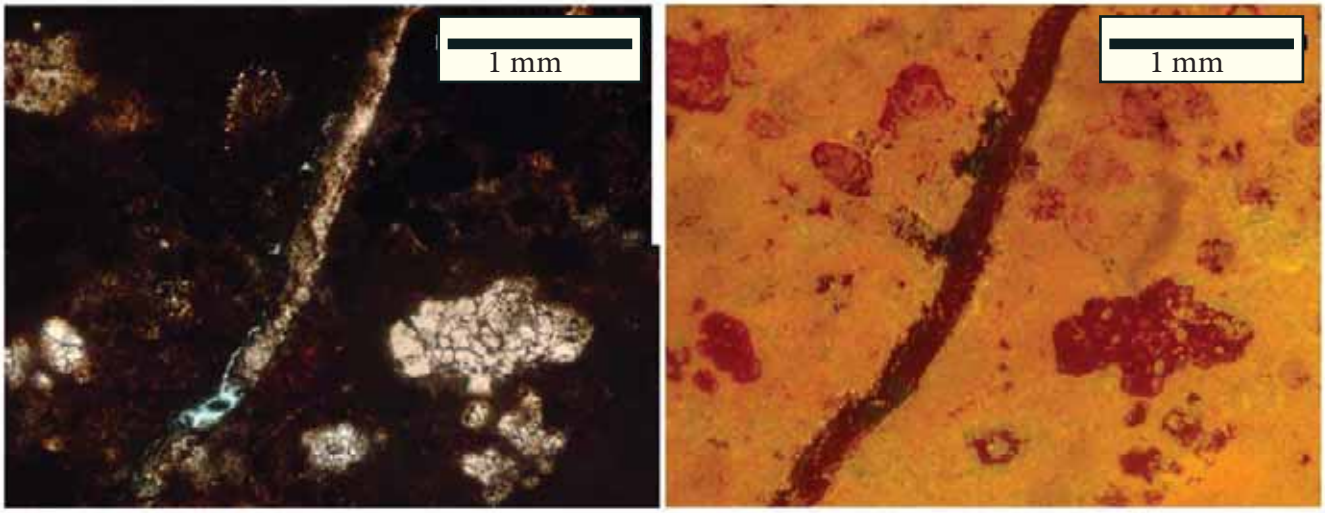

Serie 3. Fracture and nodular cavities fille with dark red calcite.

Sample 62.

Inside the paleocave zone. Microbrecciated deposit. Fault N: middle part of the paleokarst sequence fill.

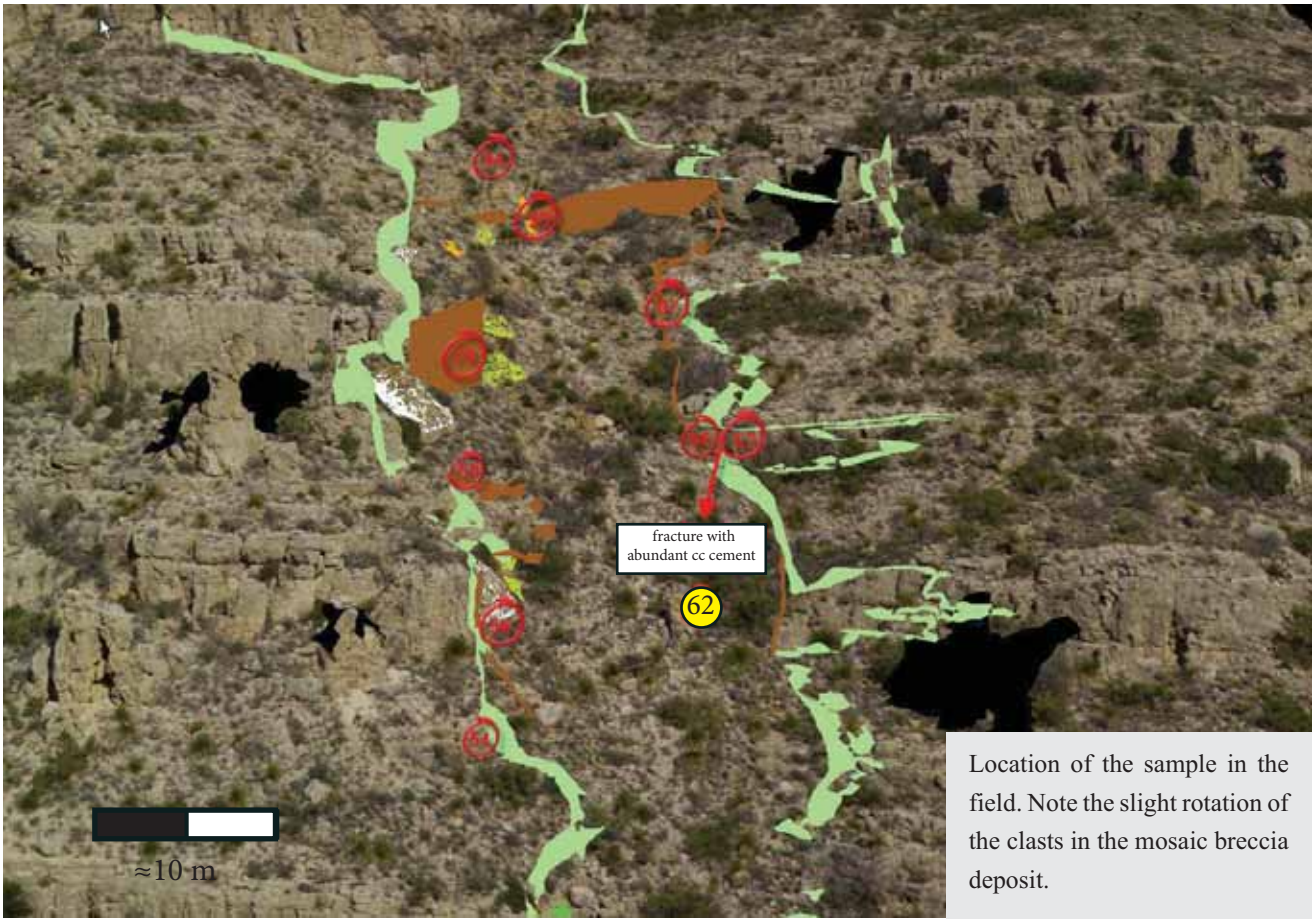

Location of the sample in the field. Note the slight rotation of the clasts in the mosaic breccia deposit.

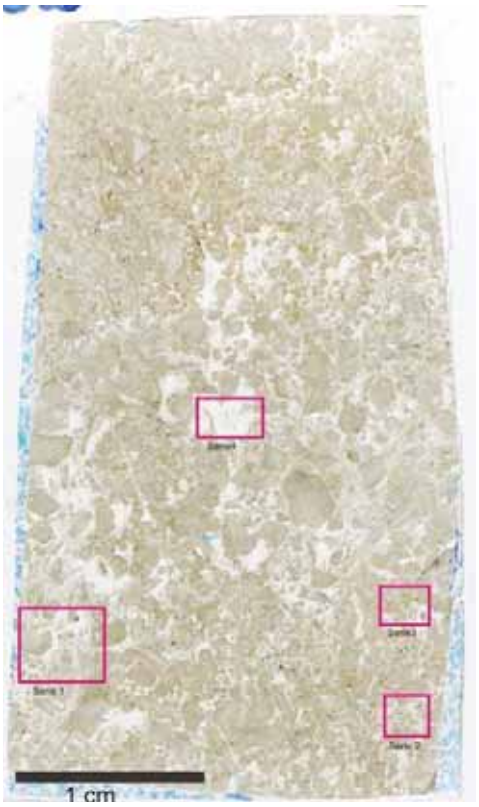

Just above: Photograph of the hand sample. At the right: Scanner of the thin section with the position of CL photomosaics.

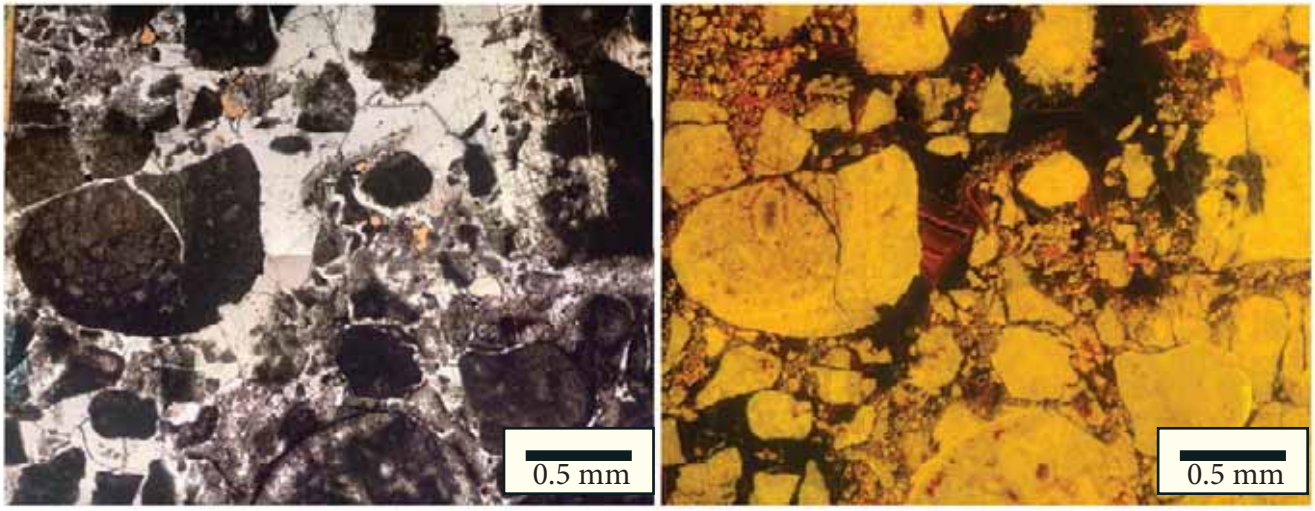

Serie 1. Brecciated fabric. Note the corrosion on the boundaries of the dolomite clasts.

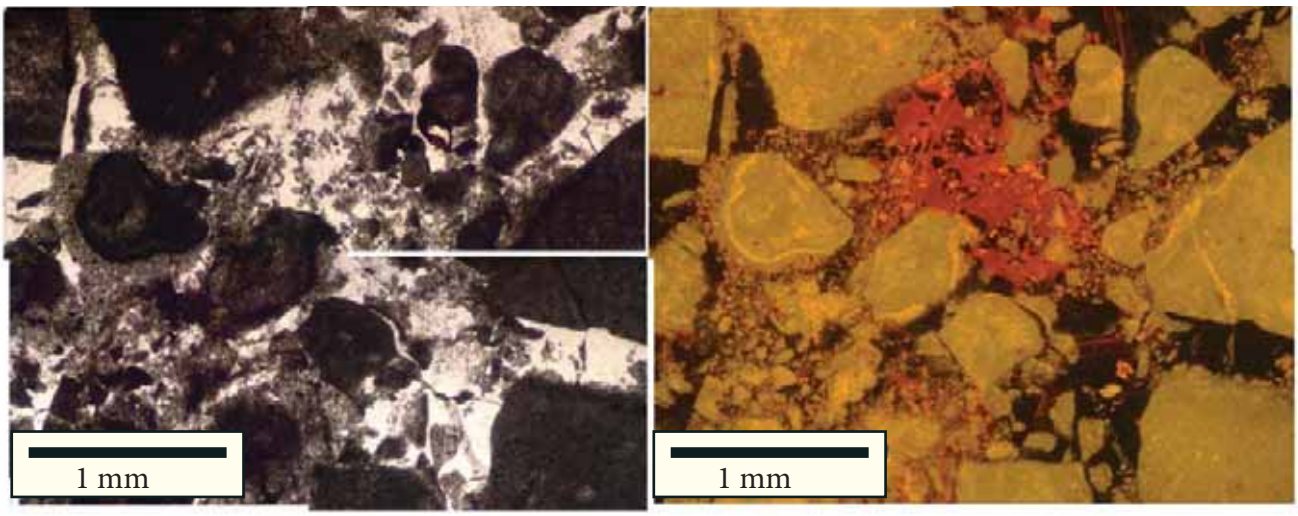

Serie 2. Brecciated fabric. Same pattern as Serie 1.

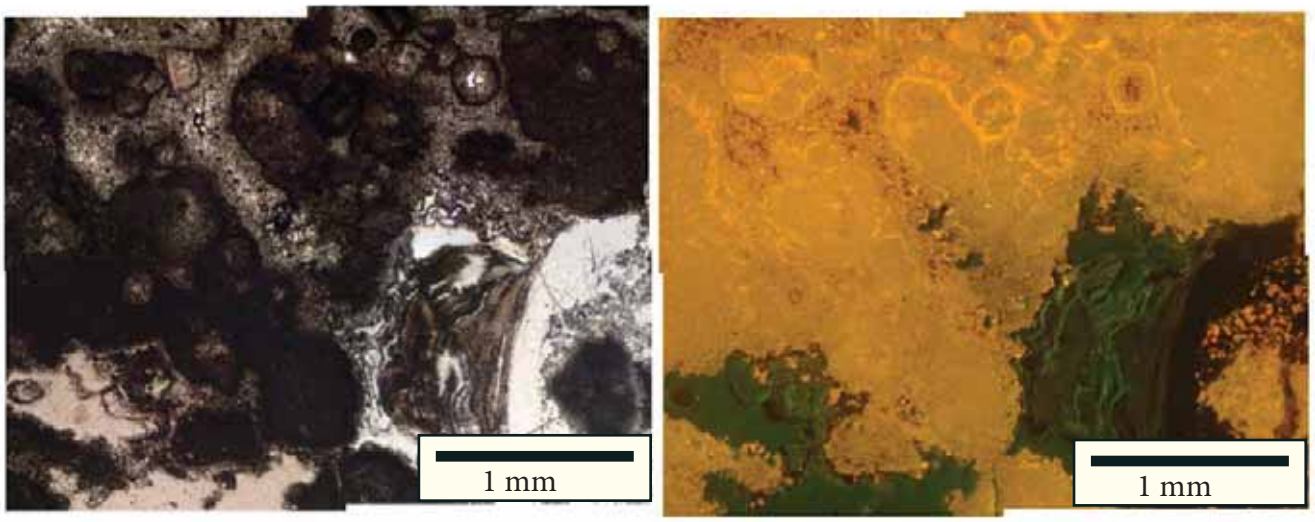

Serie 3. Open porosity.

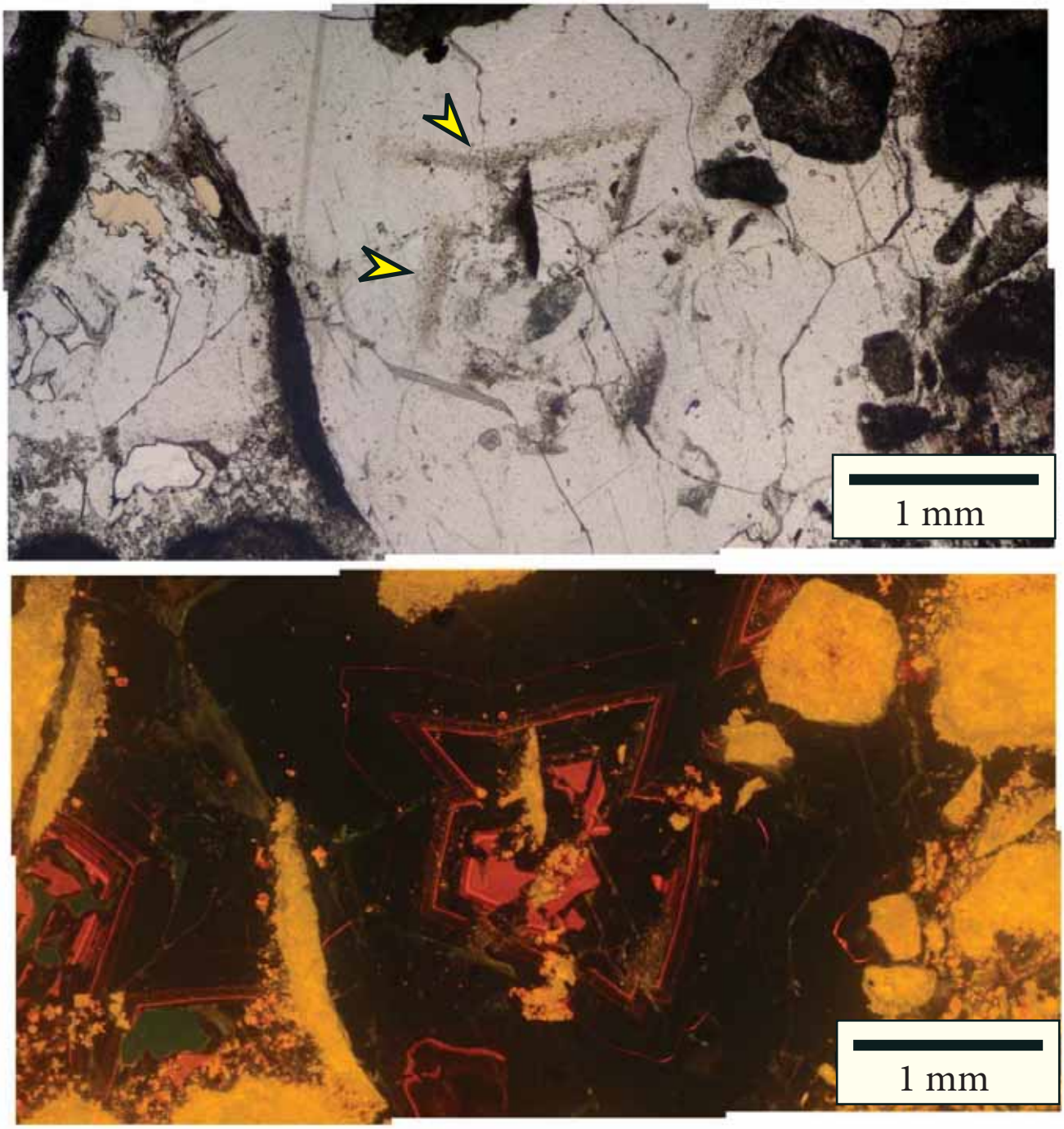

Serie 4. Concentric zonation in a calcite mosaic. Observation under transmitted light reveals relict turbid zones defining the outlines of these zonations (arrows).

Sample 66.

Stratabound infills limiting the paleocave area. Fault N: middle part of the paleokarst sequence fill.

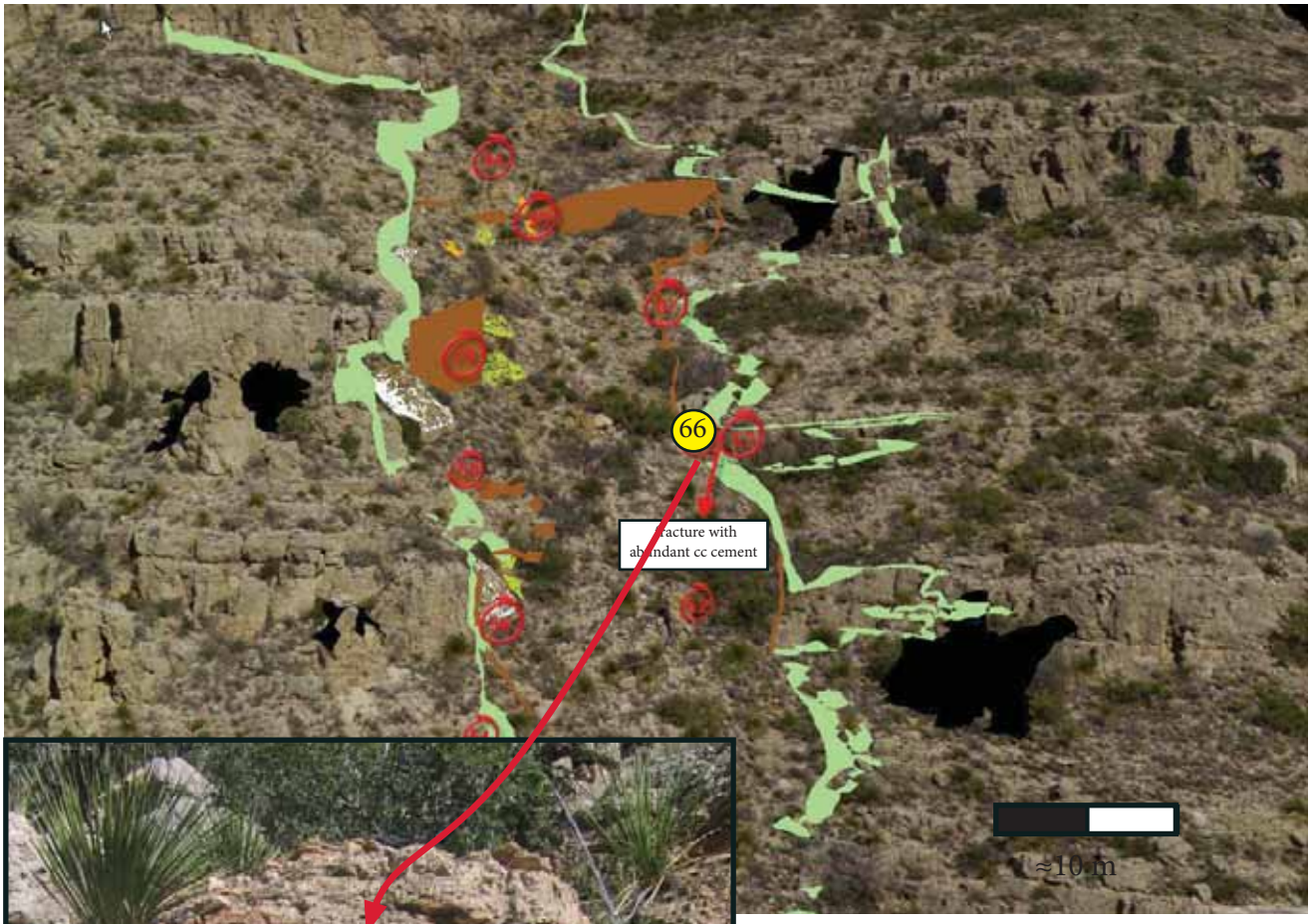

Location of the sample in the field.

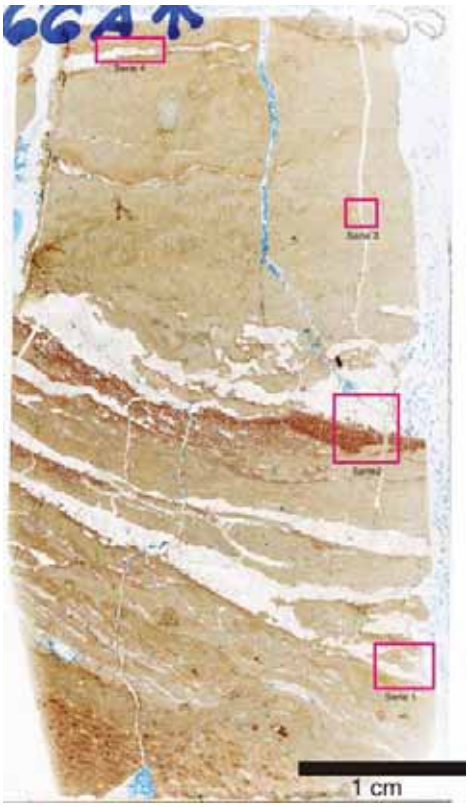

Left: Images of the hand sample.
Just above: Scanner of the thin section with the position of CL photomosaics.

Serie 1. Replacement of laminated evaporites.

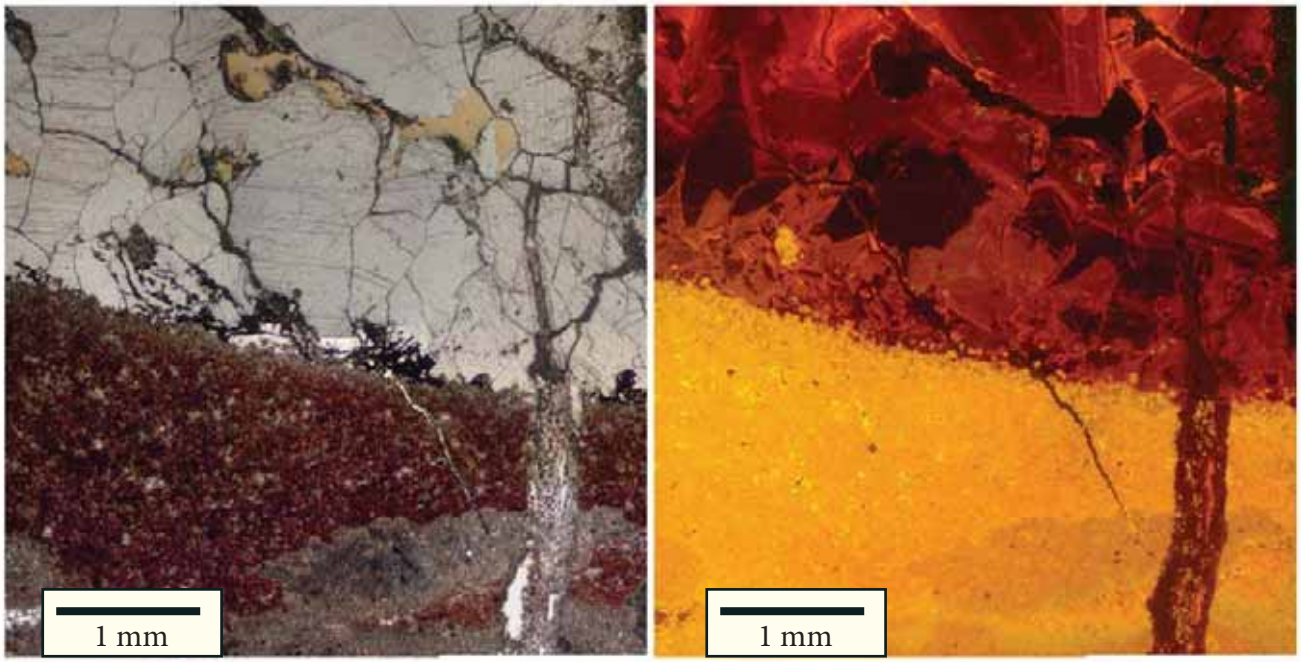

Serie 2. Fracture porosity filled with dedolomite cement. Note that the fracture on the rigt contains fine mud fragments with the same luminescenece of the matrix. It may indicate an early origin for this fracture generation.

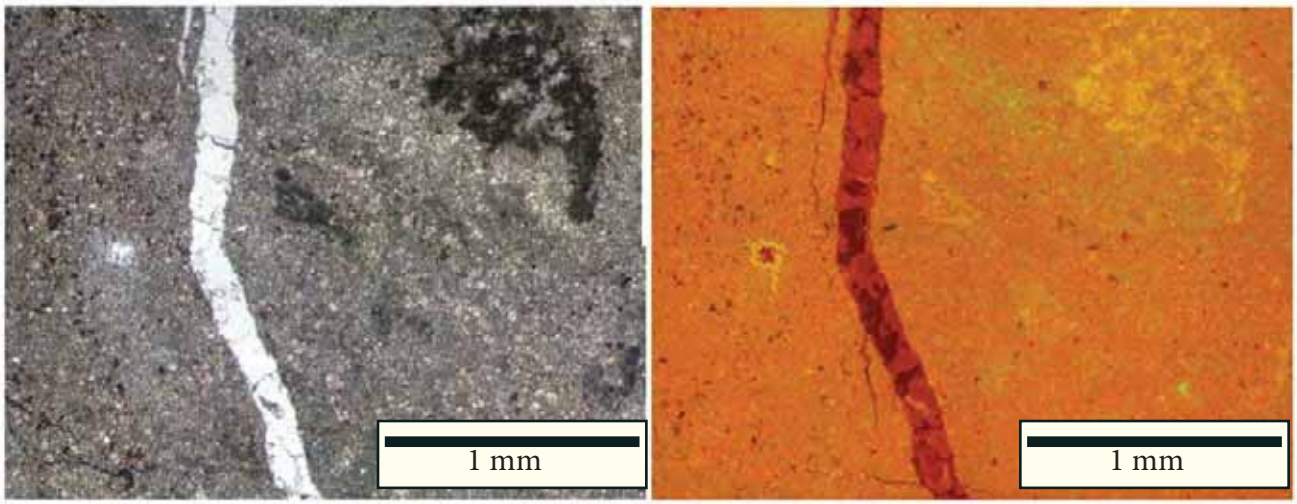

Serie 3. Fracture cement.

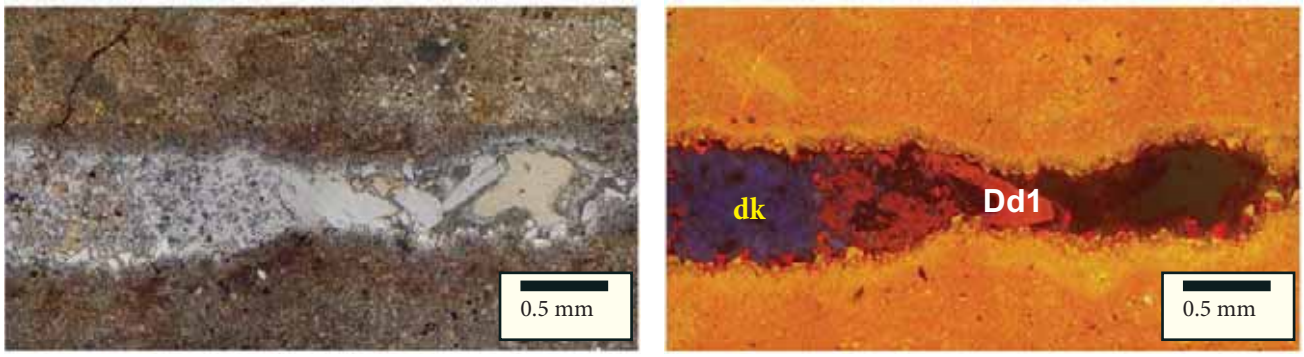

Serie 4. Dedolomite corrosion of Dd1 in a fracture partially sealed with dickite (dk).

Sample 69.

Stratabound infills limiting the paleocave area. Fault N: middle part of the paleokarst sequence fill.

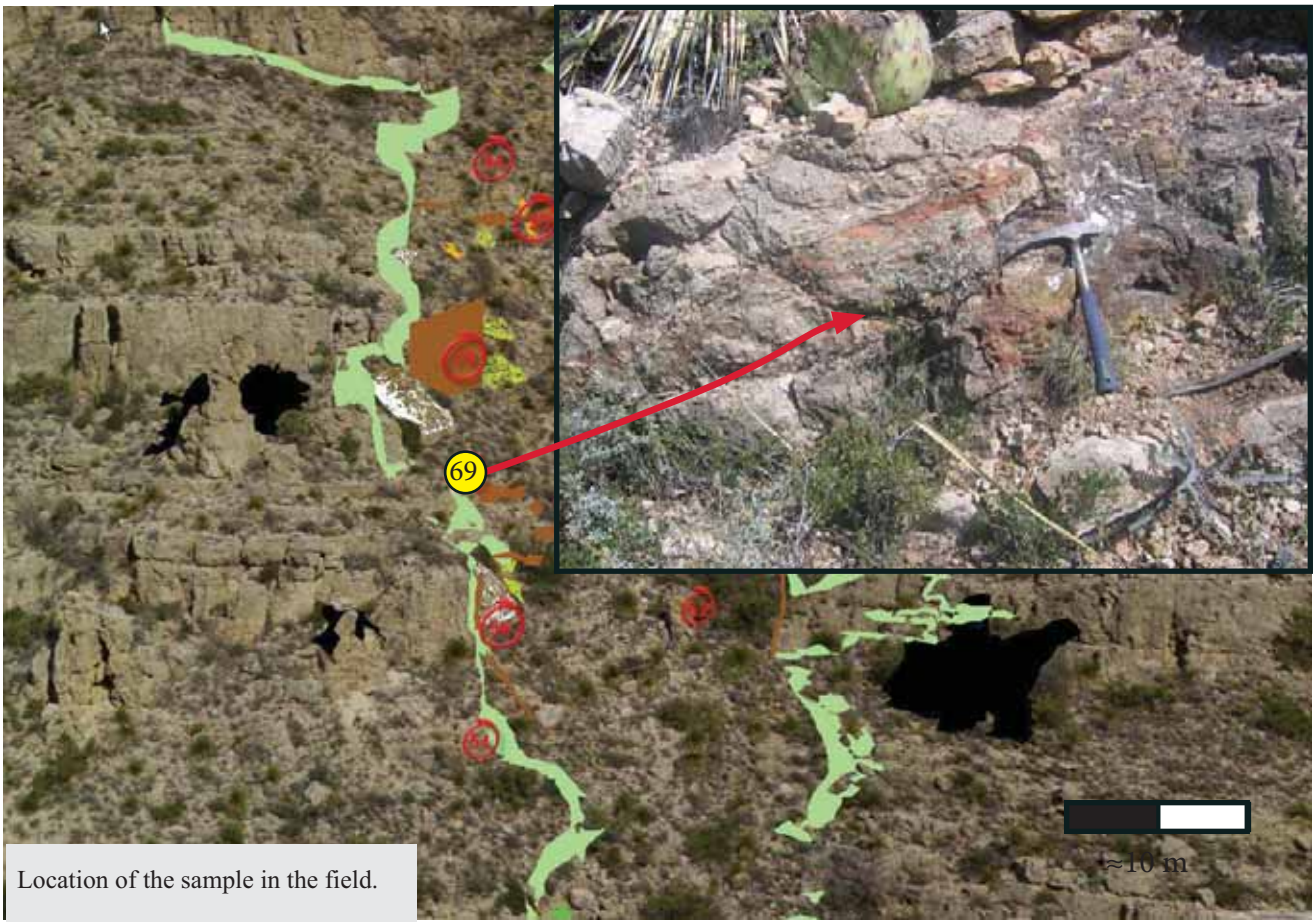

Location of the sample in the field.

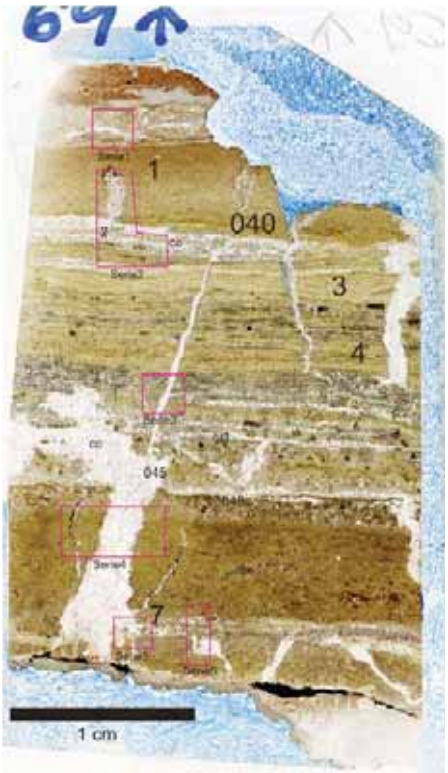

Just above: Photograph of the hand sample. At the right: Scanner of the thin section with the position of CL photomosaics.

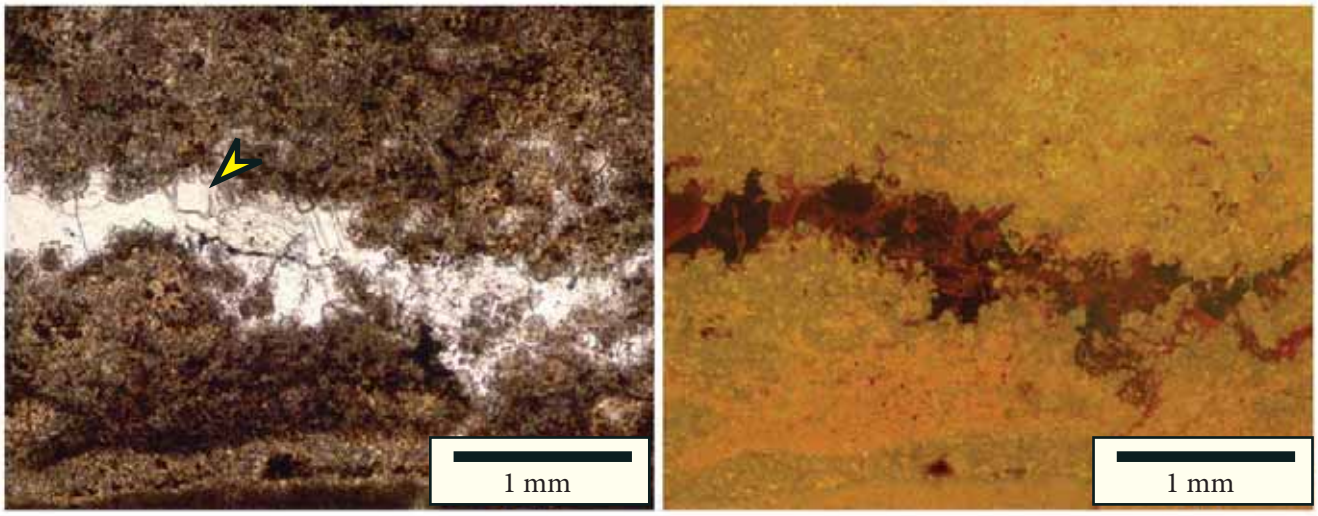

Serie 1. Dedolomite cement. Note rhombs of precursor dolomite (arrow).

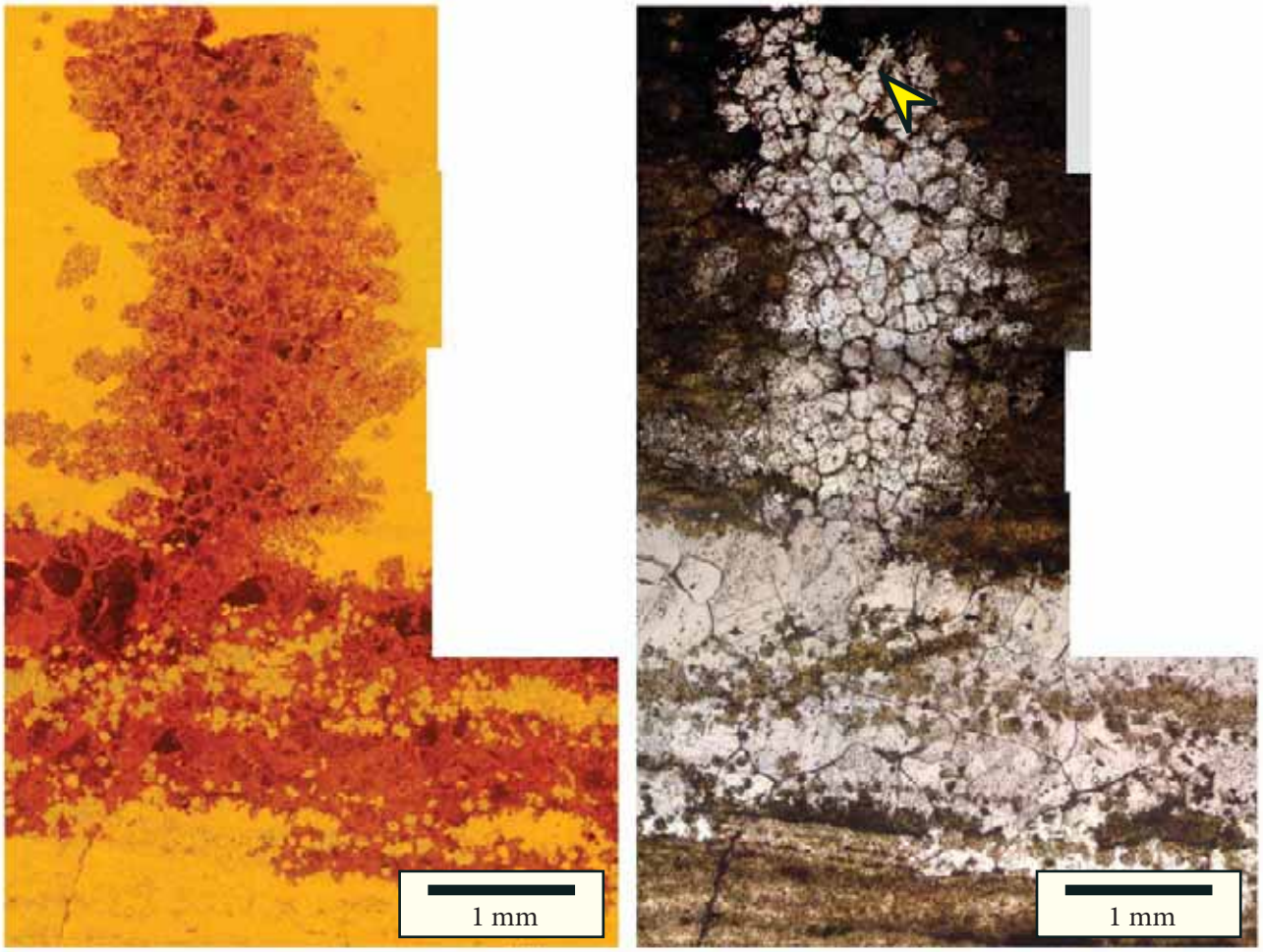

Serie 2. Dedolomite cement.

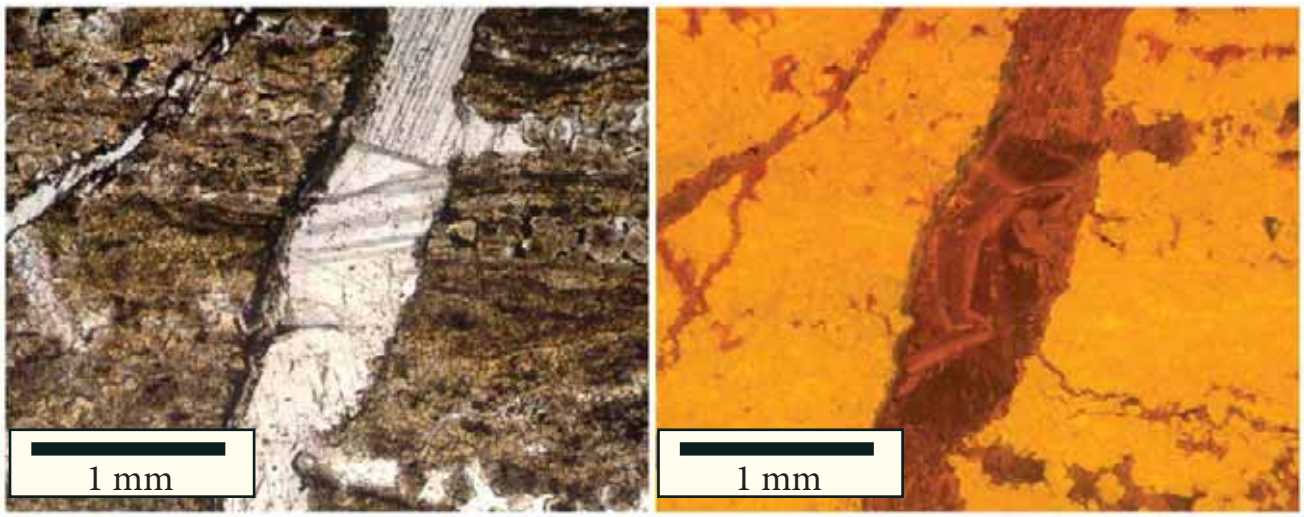

Serie 3. Fracture zoned cement.

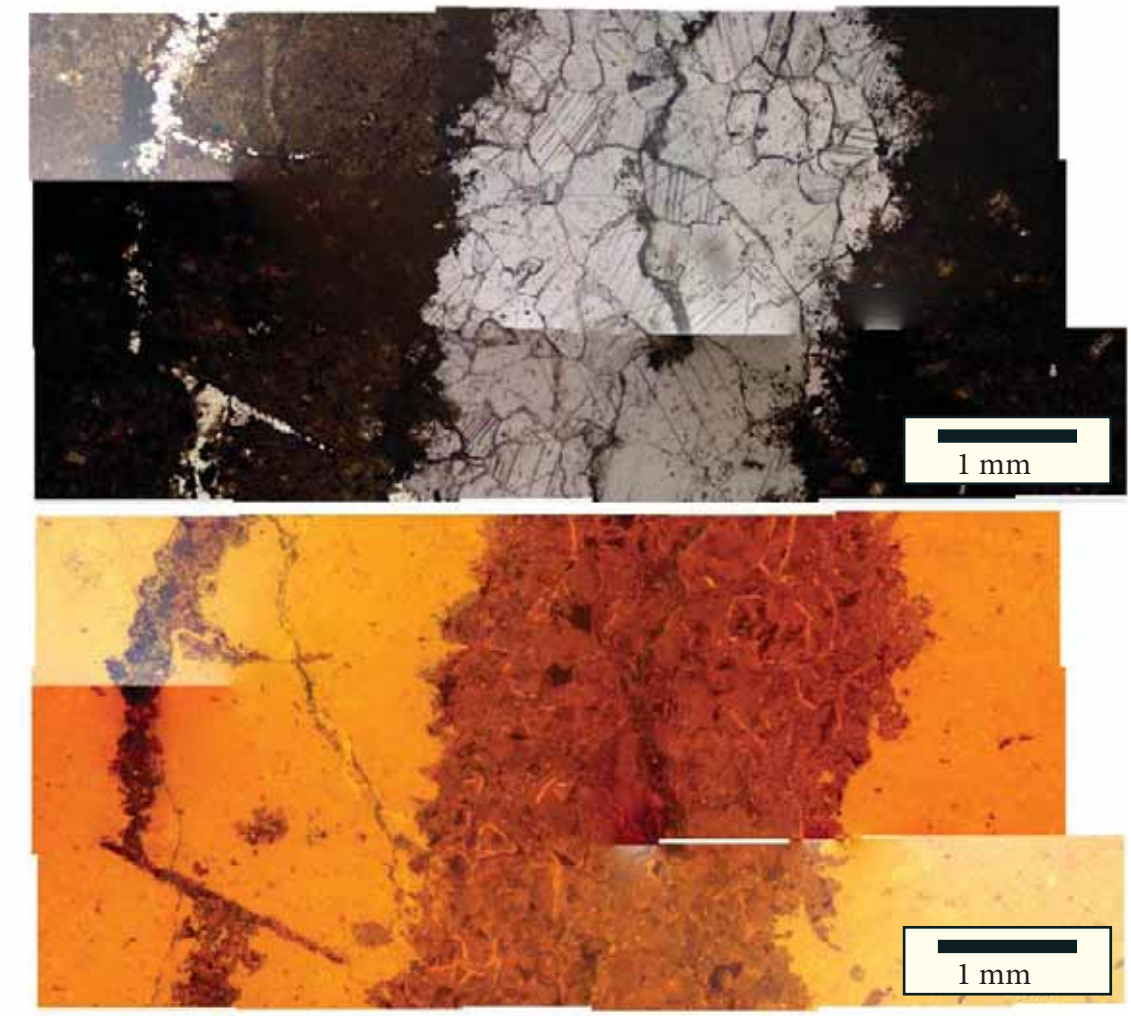

Serie 4. Fracture cement.

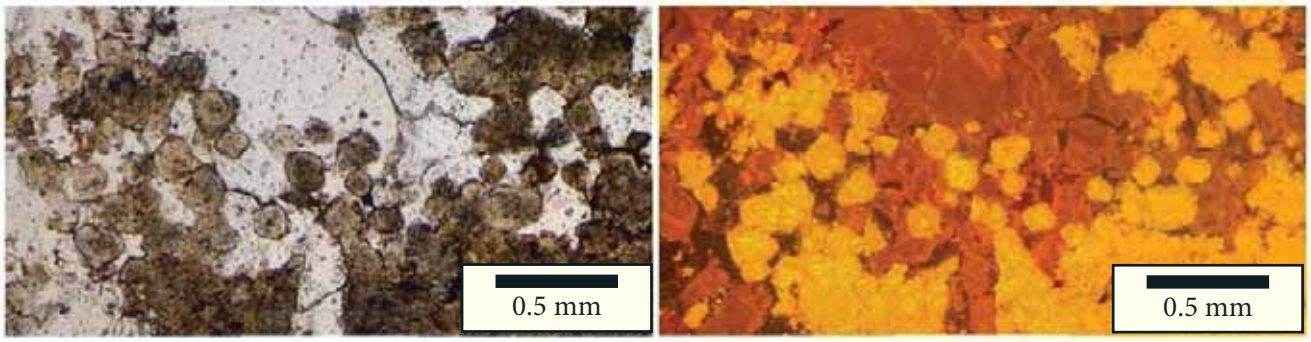

Serie 5. Replacive dolomite rombohedra.

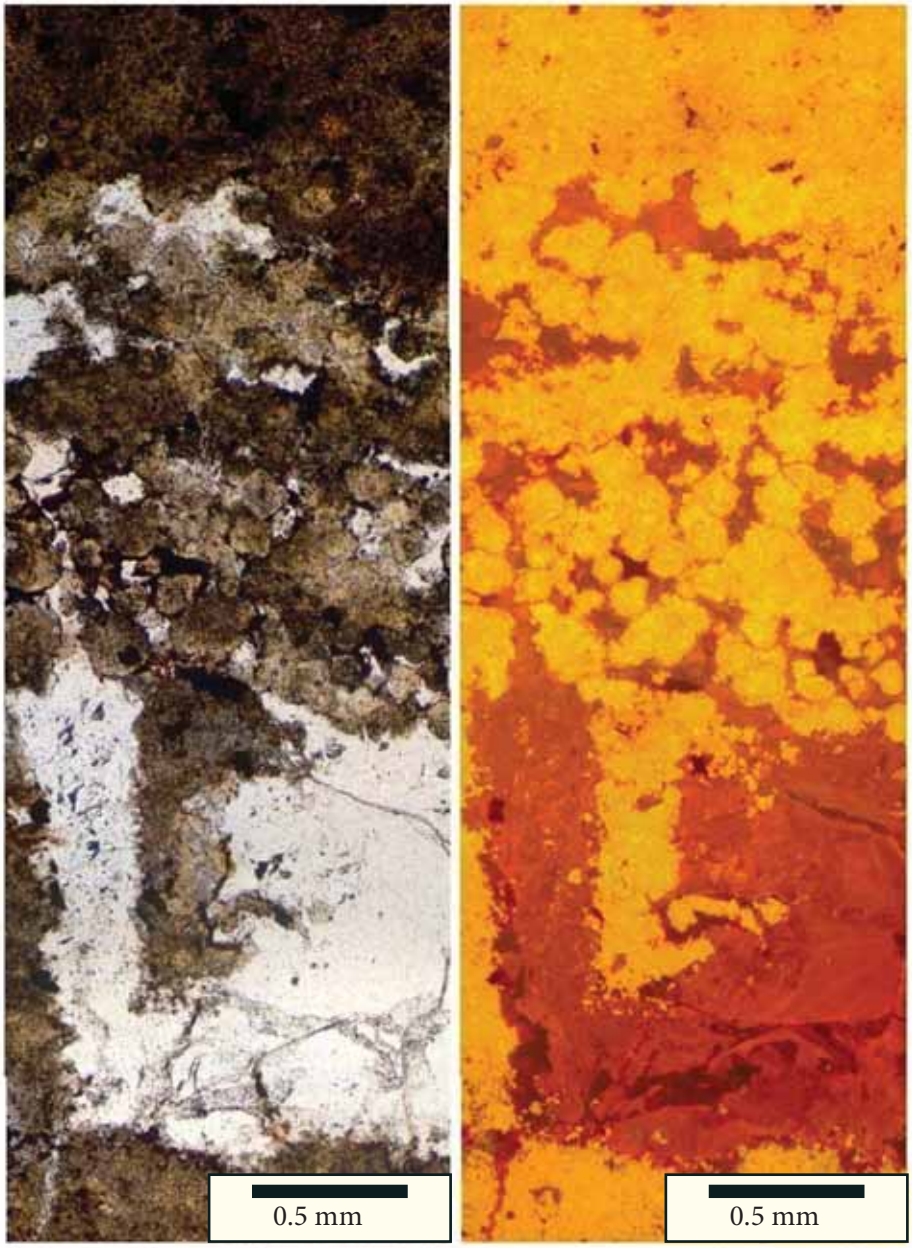

Serie 6. Fenestrae cavities cemented.

Sample 79. Thick section.

Chaotic breccia in the paleocave zone. Fault N: middle part of the paleokarst sequence fill.

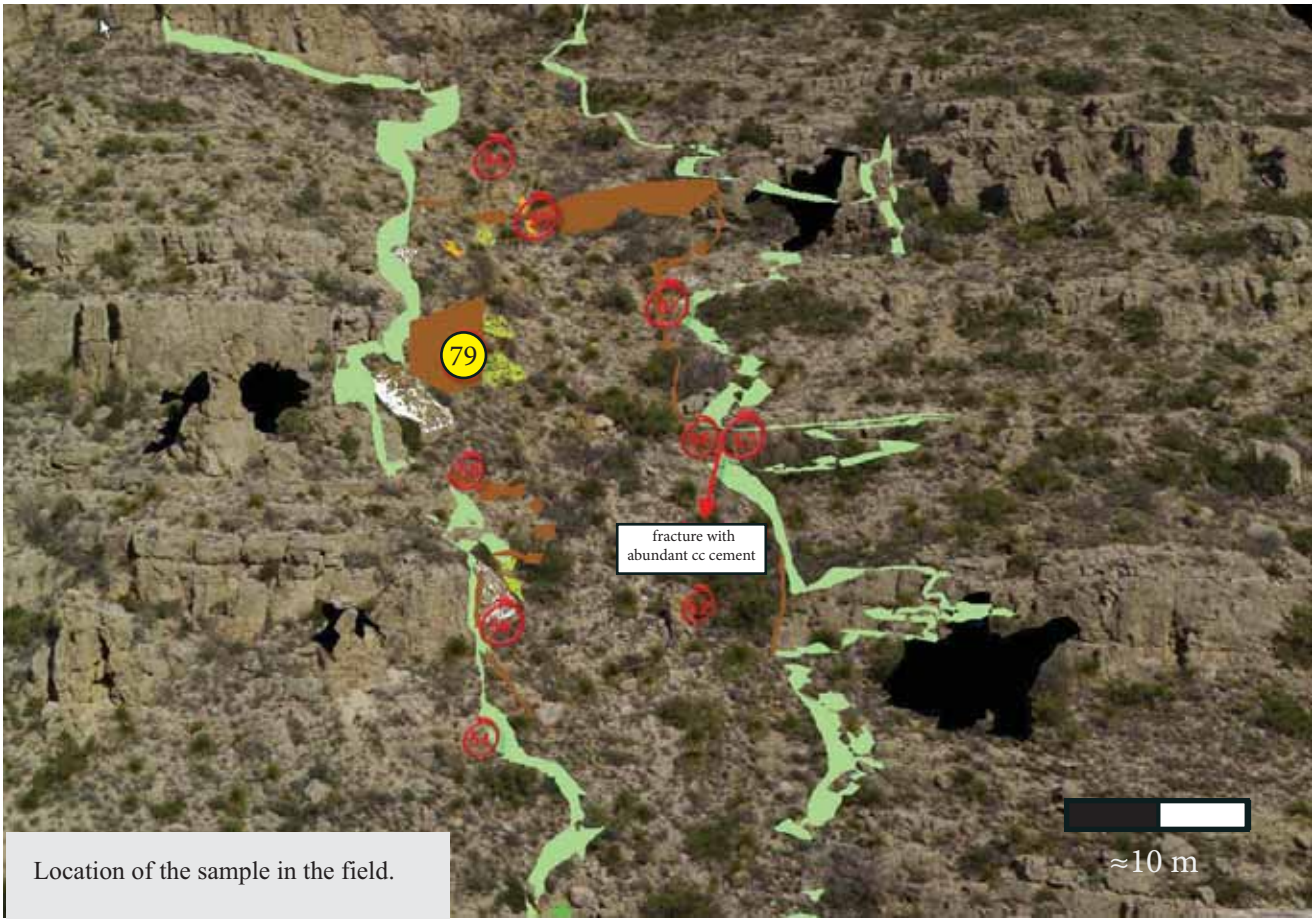

Location of the sample in the field.

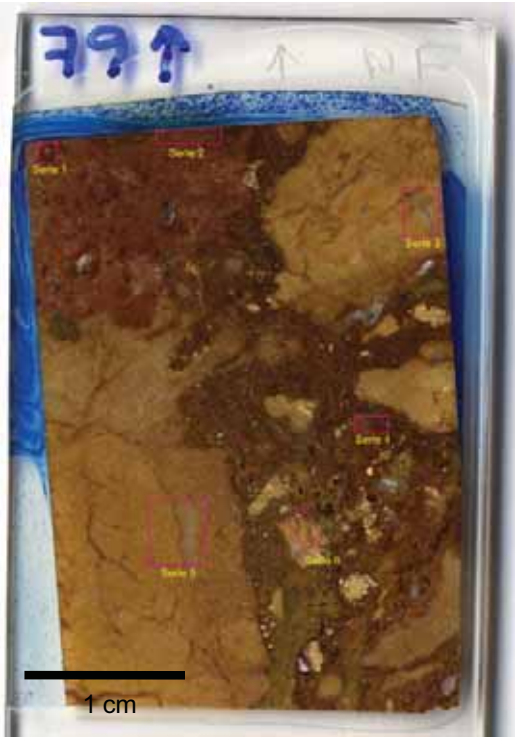

Right: Scanner of the thick section with the position of CL photomosaics.

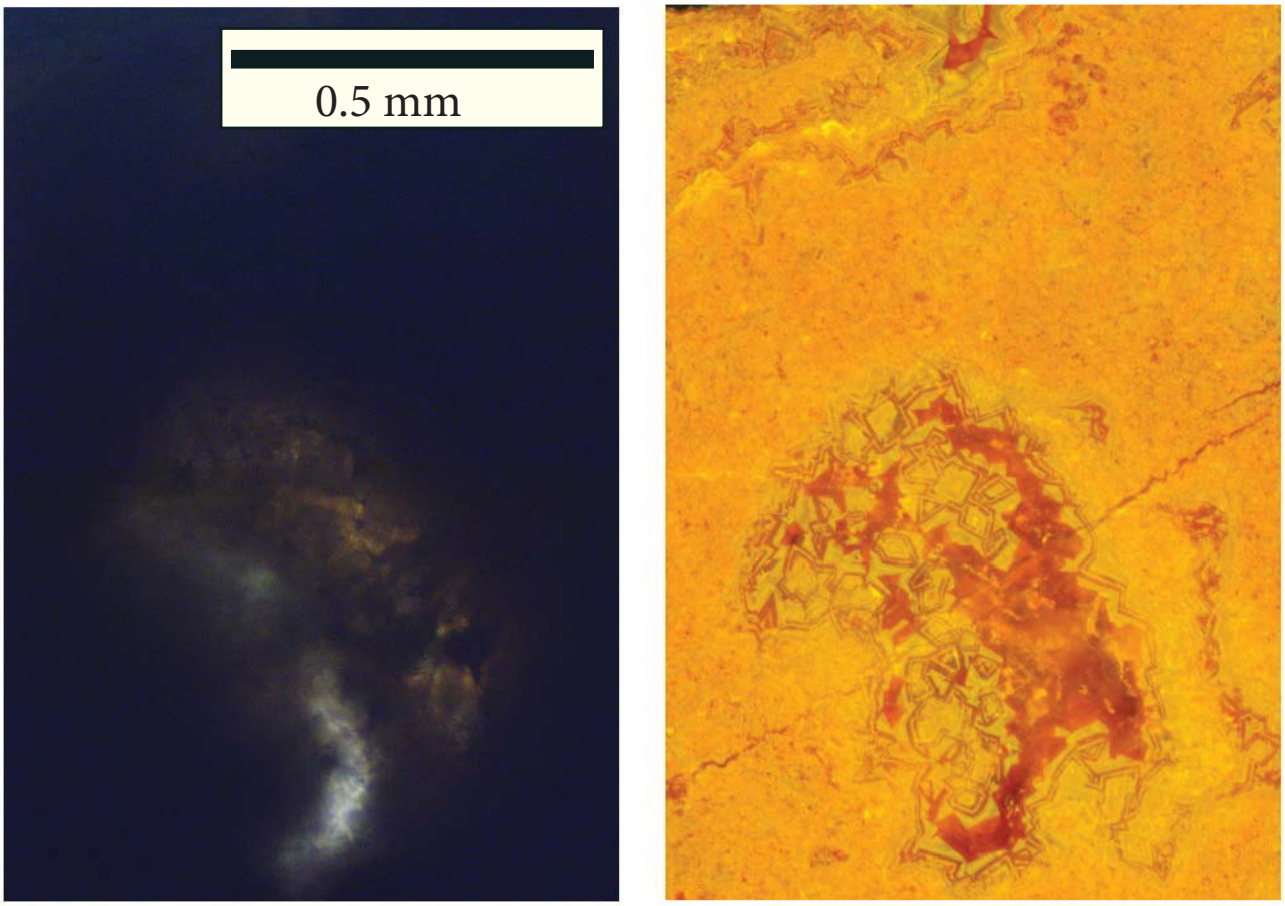

Serie 1. Preservation of vug-filling dolomite cement.

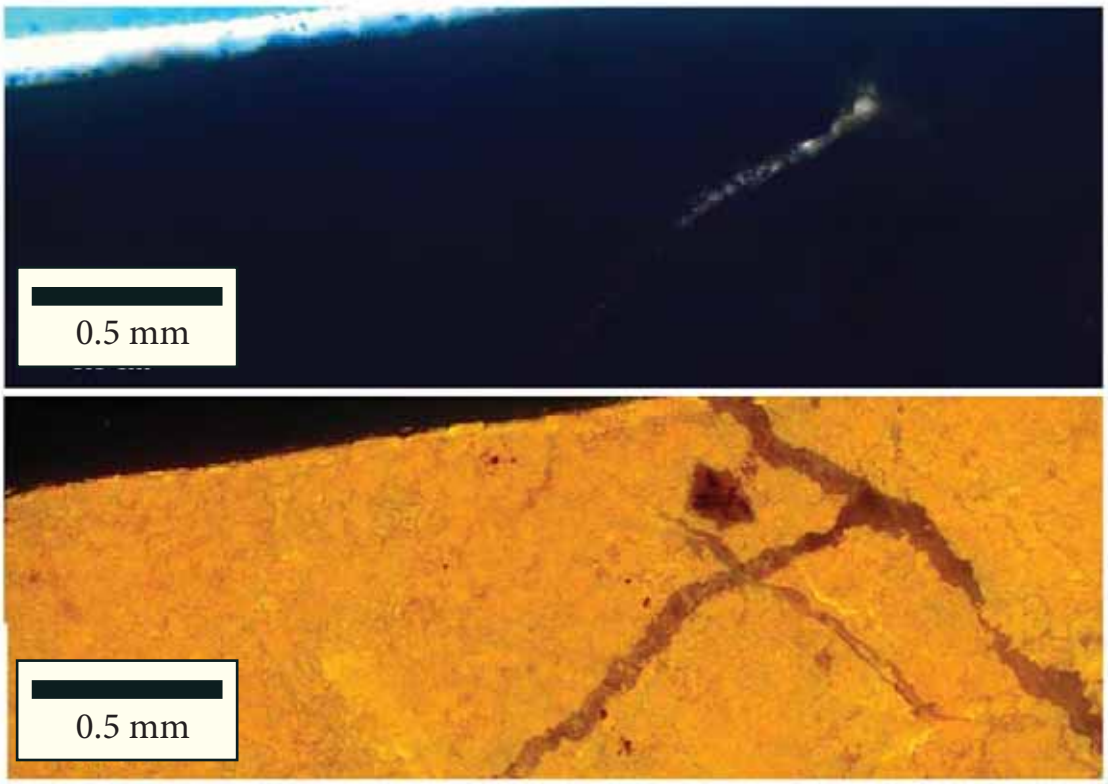

Serie 2. Microfractures cemented with calcite.

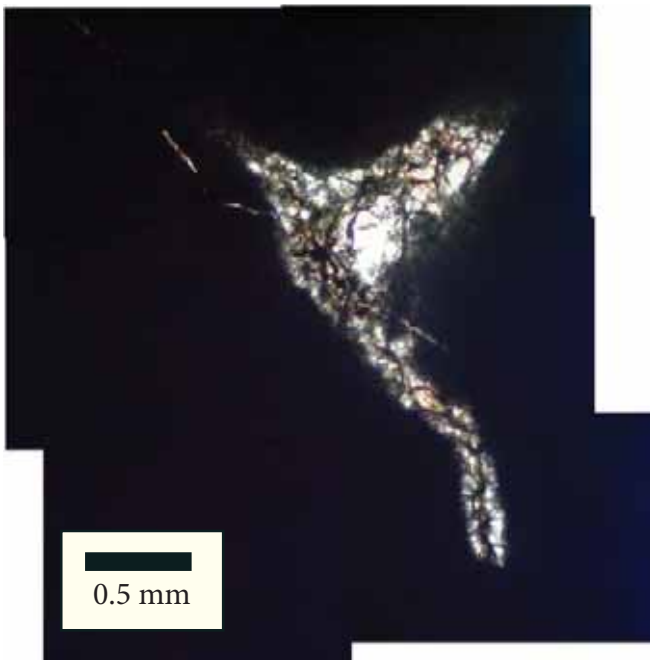

Serie 3. Vug-filling dolomite cement preserved within a reworked clast.

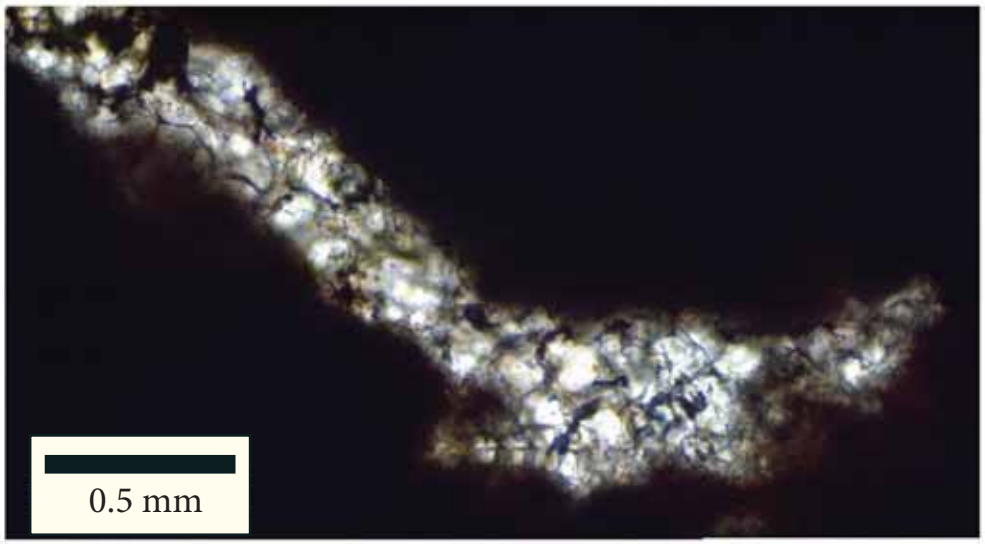

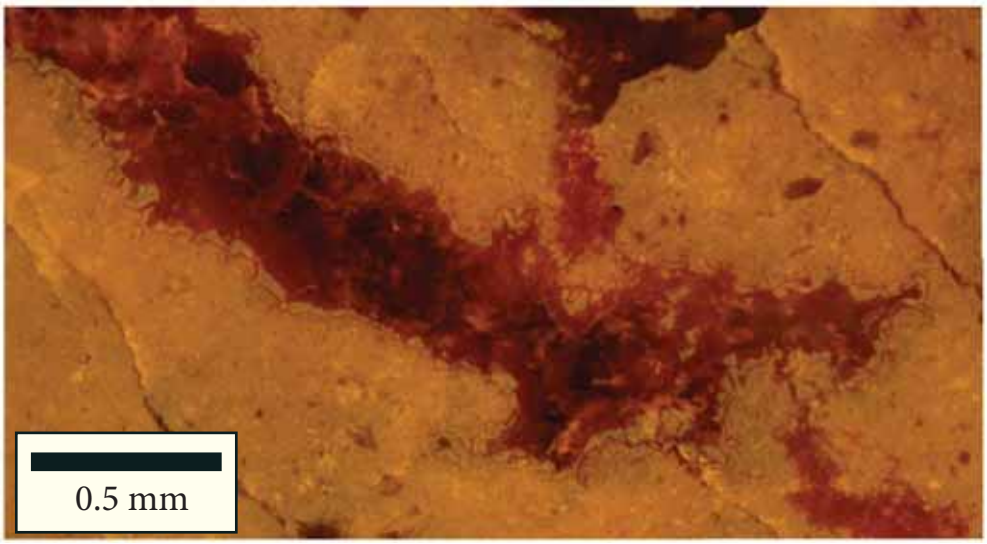

Serie 4. Cemented cavity in the cave sediment fill.
The degree of dedolomitization cannot be deciphered here only by petrographic observations.

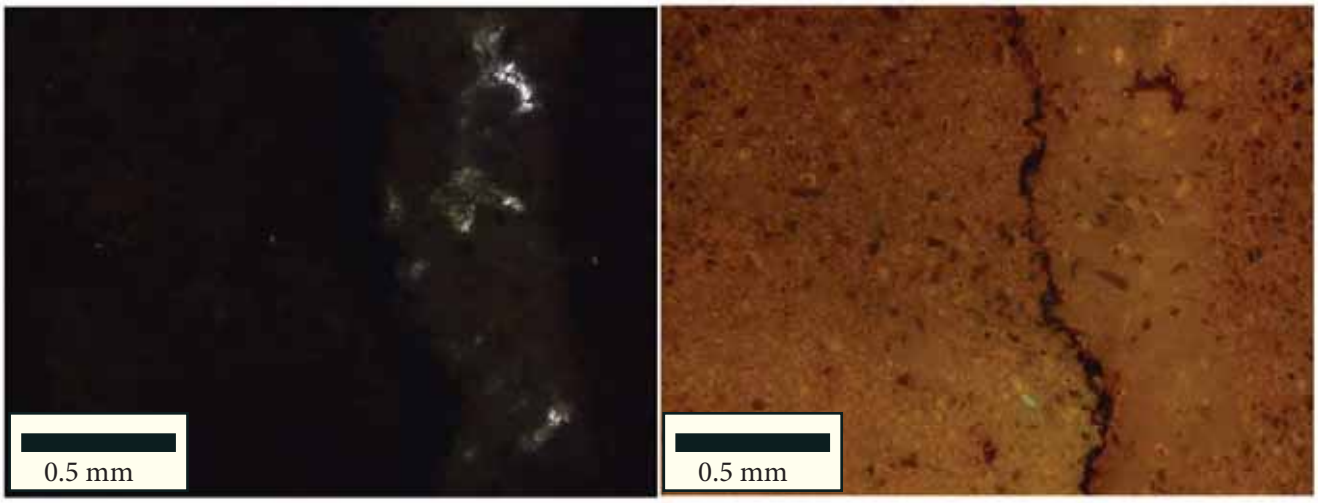

Serie 5. Calcite cement in microfracture..

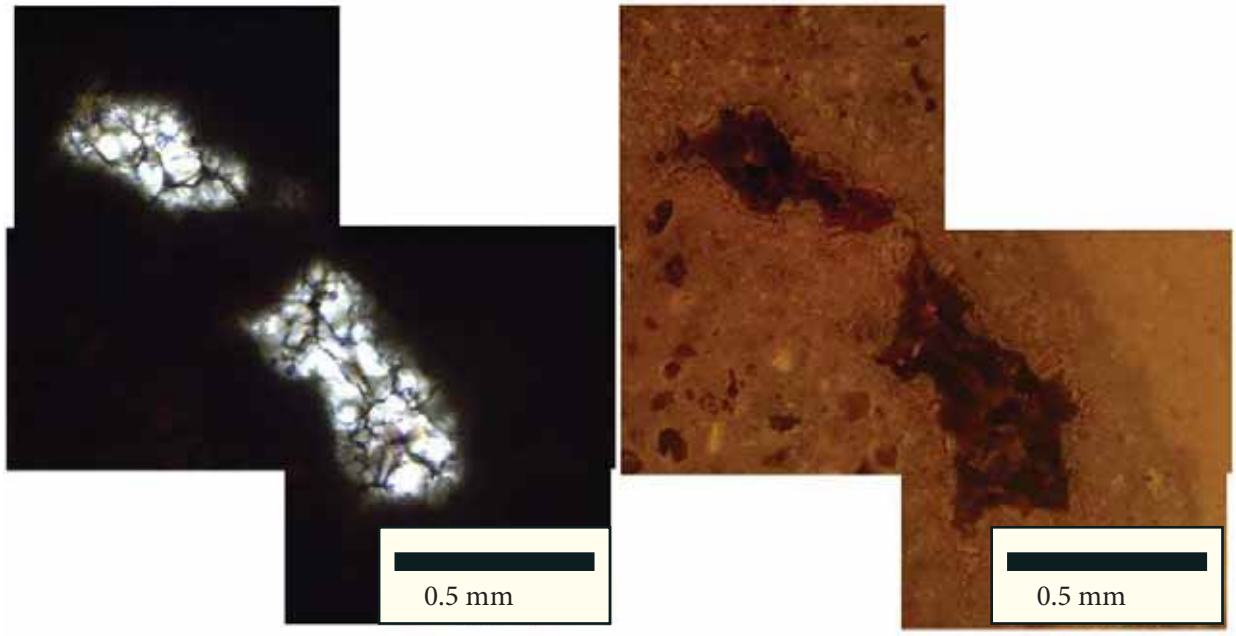

Serie 6. Vug-filling dolomite cement in a reworked clast.

Sample 93. Thick section.

Sand dike contact. Top entrance of the paleocave. Fault N: upper part of the paleokarst sequence fill.

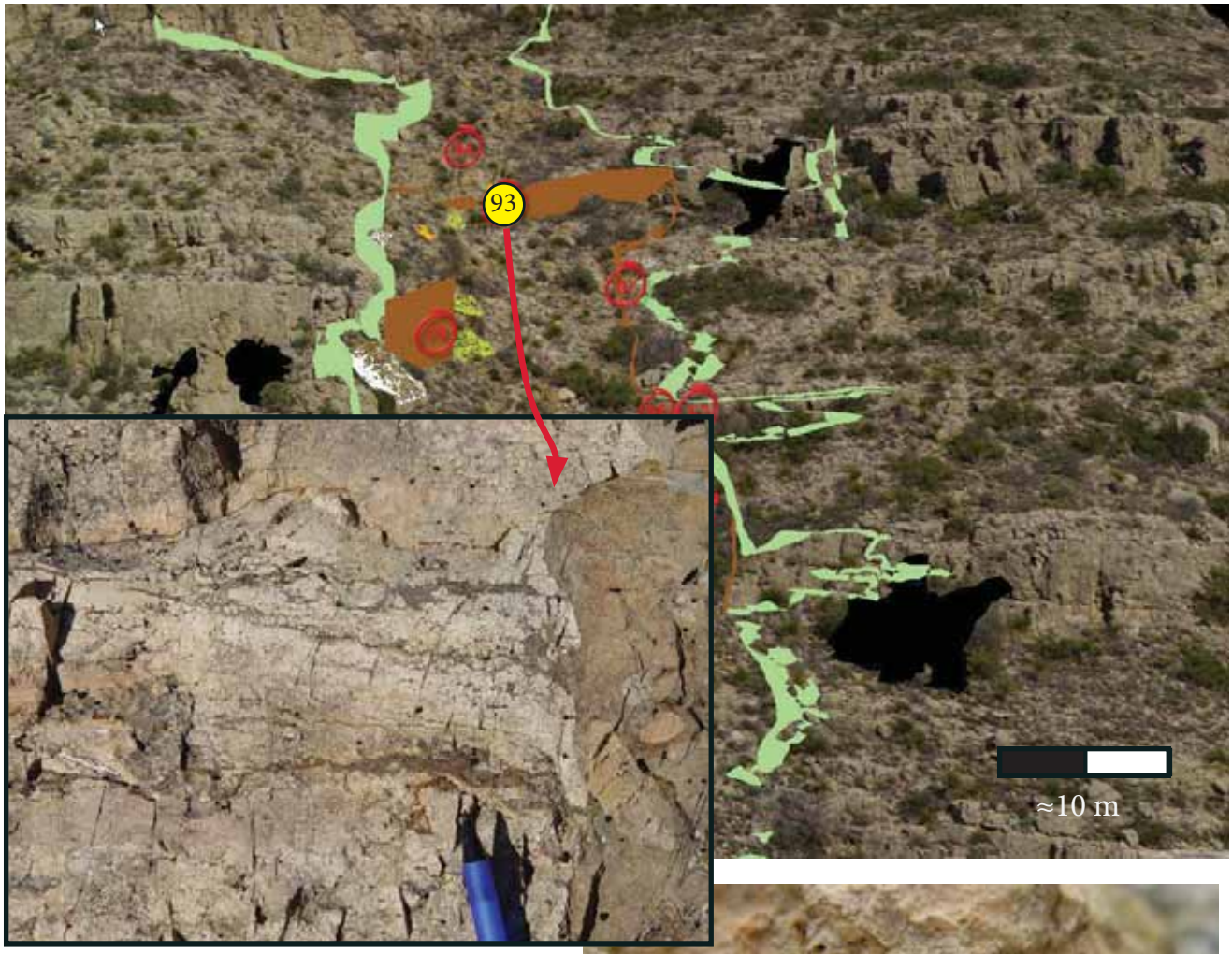

Above: Location of the sample in the field.

Left: Photograph ofthe hand sample.
Above: detail of the hand sample.

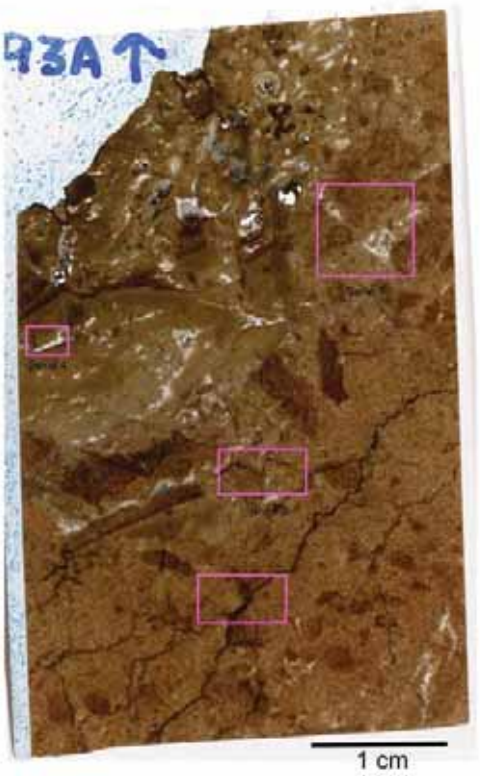

Left: Scanner of the thick section with the position of CL photomosaics.

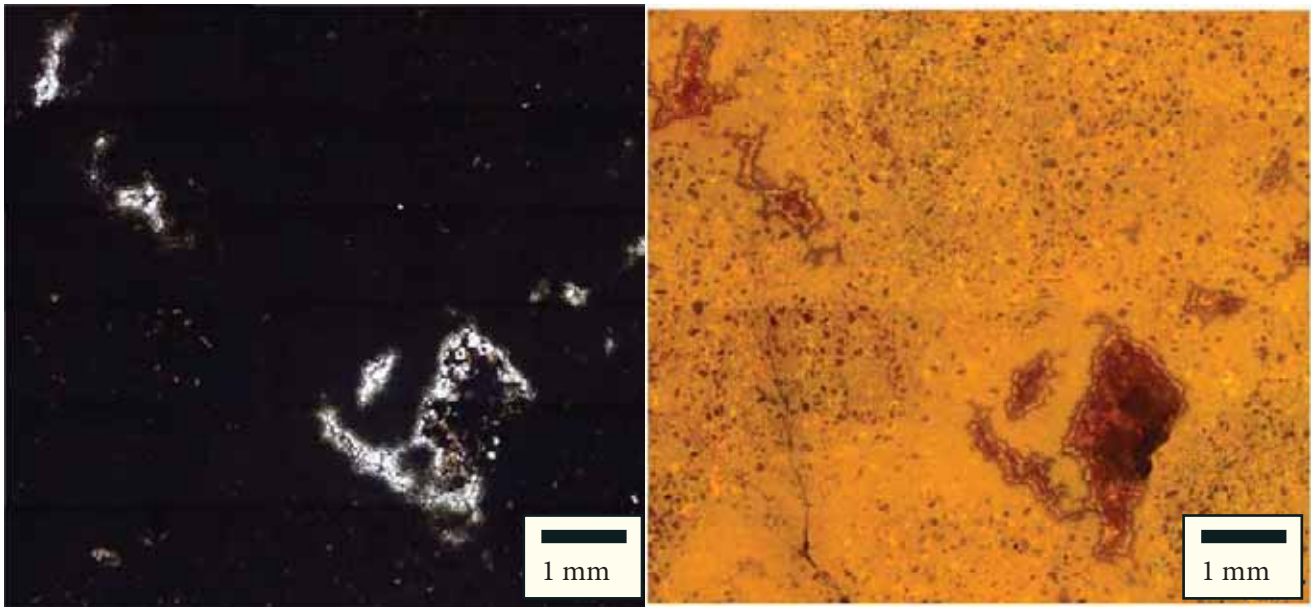

Serie 1. Vug-filling dolomite cement preserved in the upper zones of the paleokarst system.

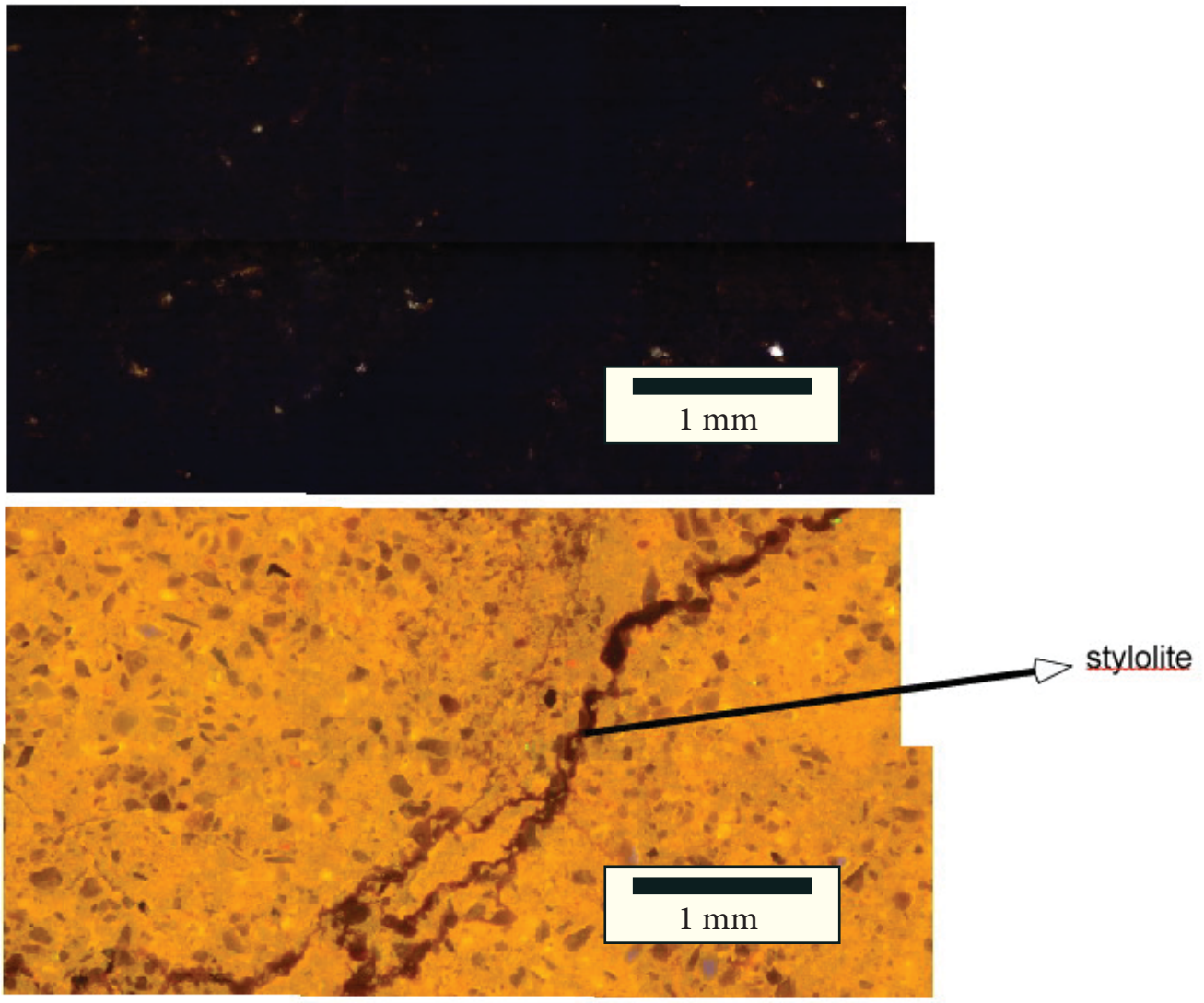

Serie 2. Stylolite cemented with dolomite in a matrix of replacive dolomite with significant detrital content.

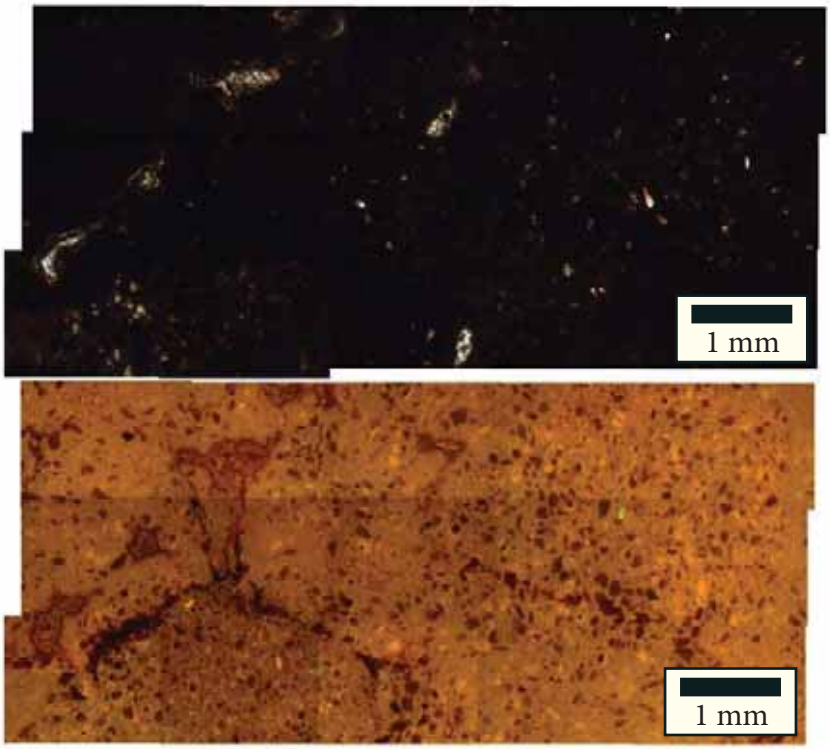

Serie 3. Microcavities with vug-filling dolomite cements are best preserved in the areas of detrital content.

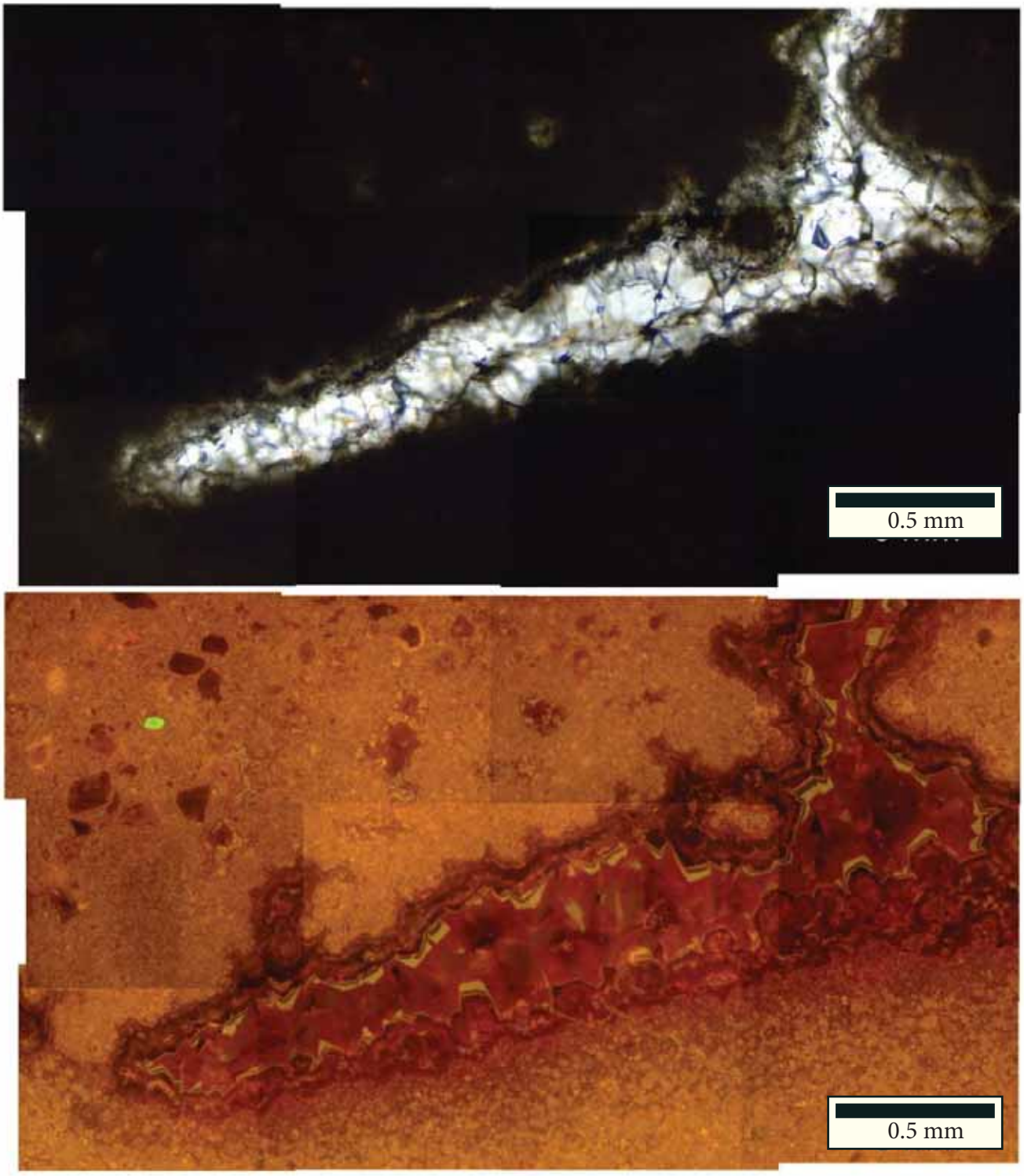

Serie 4. Vug-filling dolomite cement preserved in the upper zones of the paleokarst system.

Sample 101.

Red infill. Fault N: upper part of the paleokarst system.

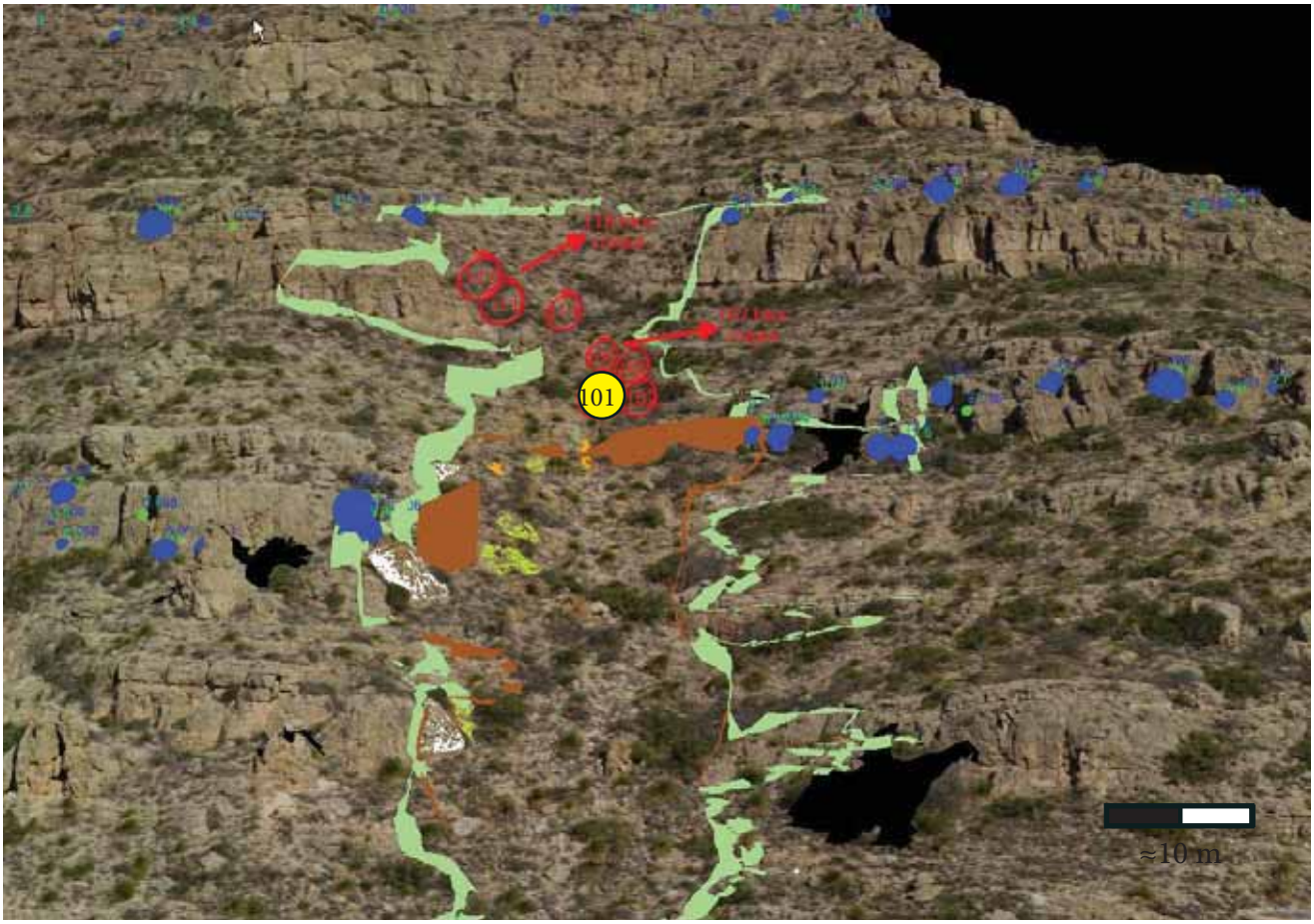

Just above: Photograph of the hand sample. At the right: Scanner of the thin section with the position of CL photomosaics.

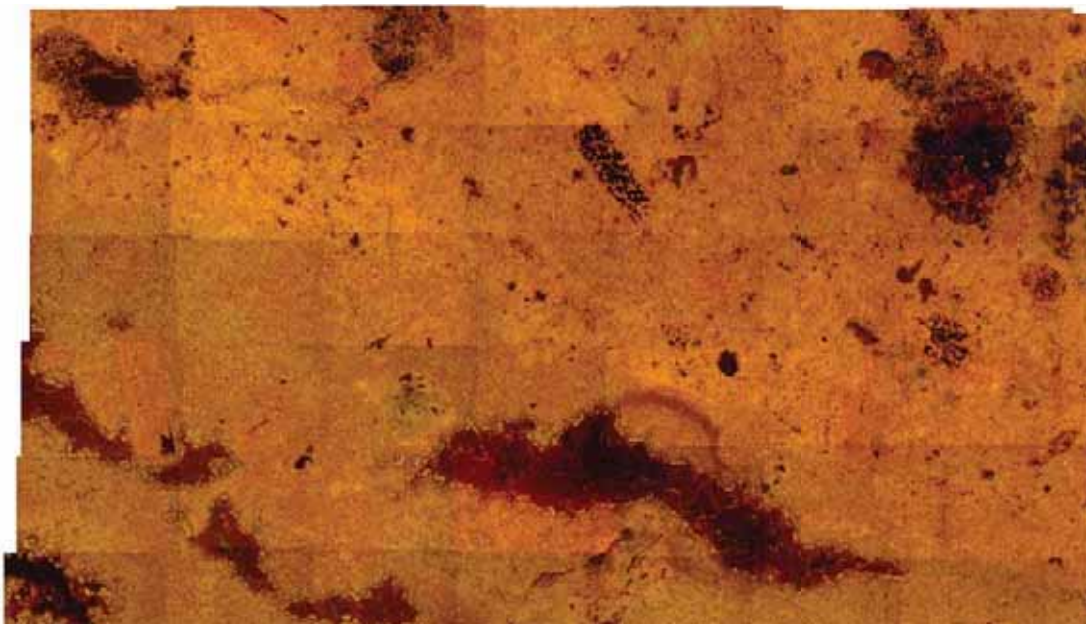

Serie 1. Note the preferential hematite accumulation in the cemented cavities.

Sample 103.

Close to chaotic deposits in fracture areas. Fault N: upper part of the paleokarst system.

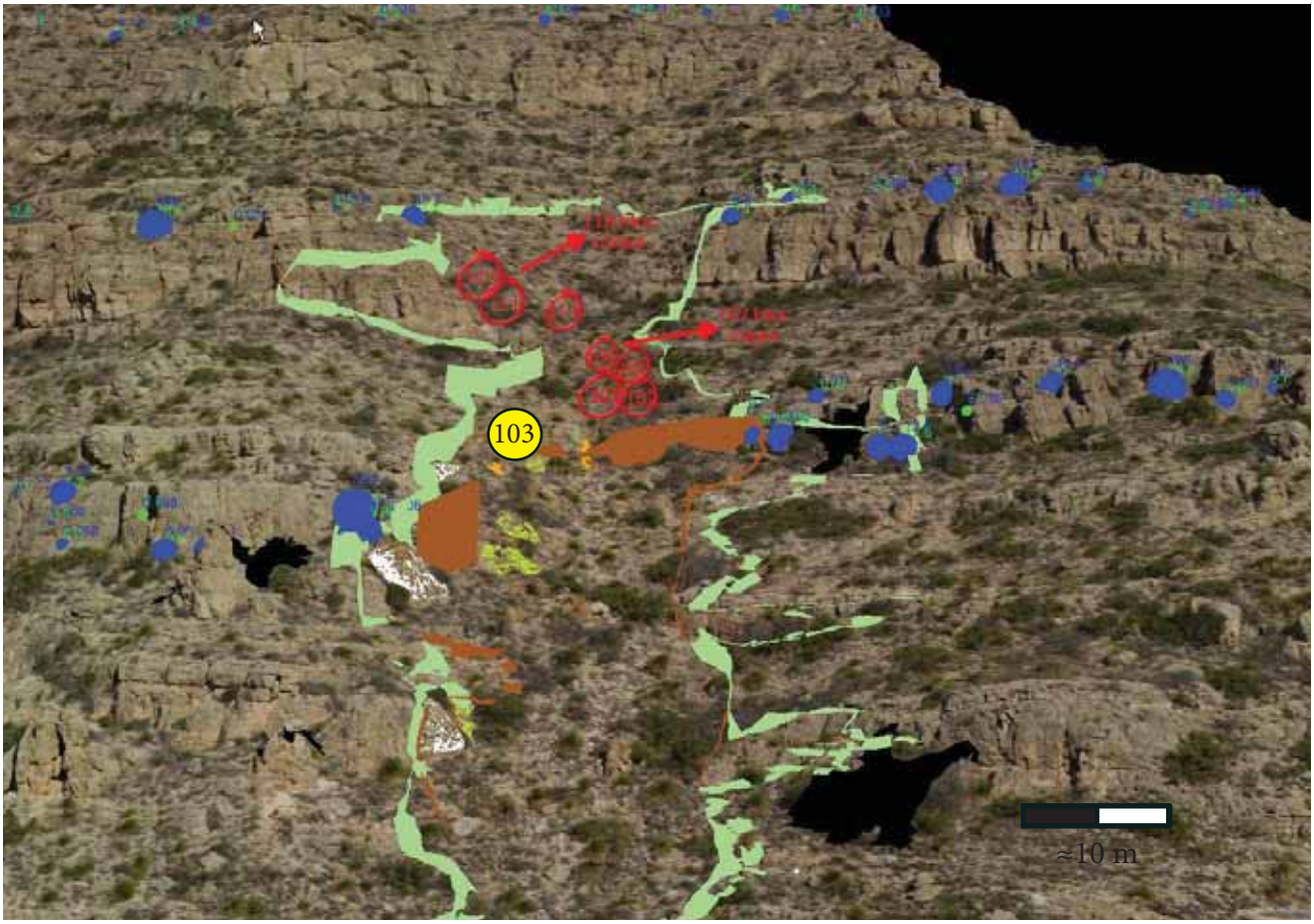

Just above: Photograph of the hand sample. At the right: Scanner of the thin section with the position of CL photomosaics.

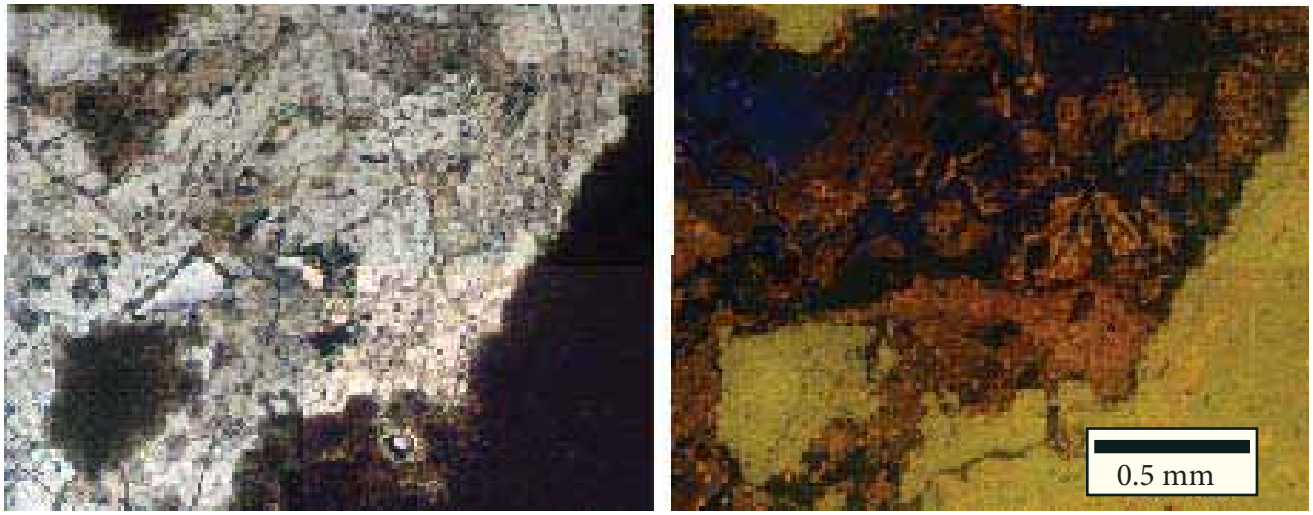

Serie 1. Dedolomite and dickite cements.

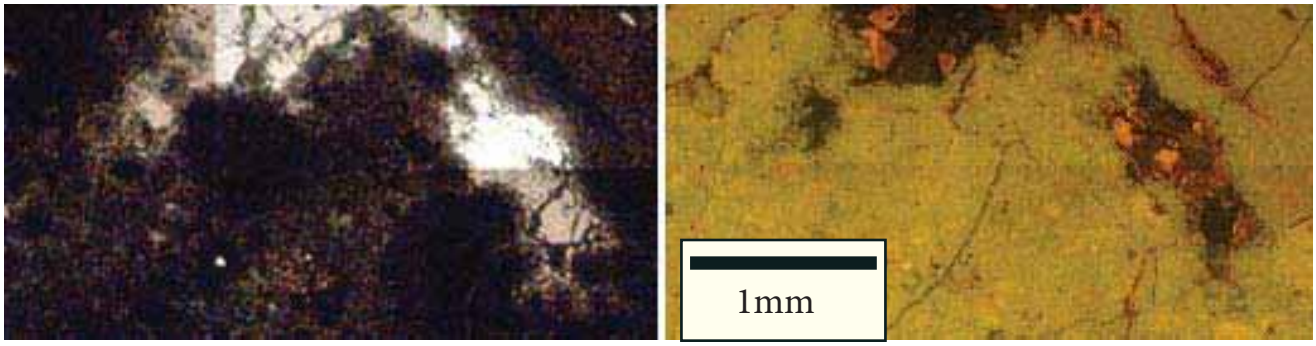

Serie 2. Dedolomite breccia cements.

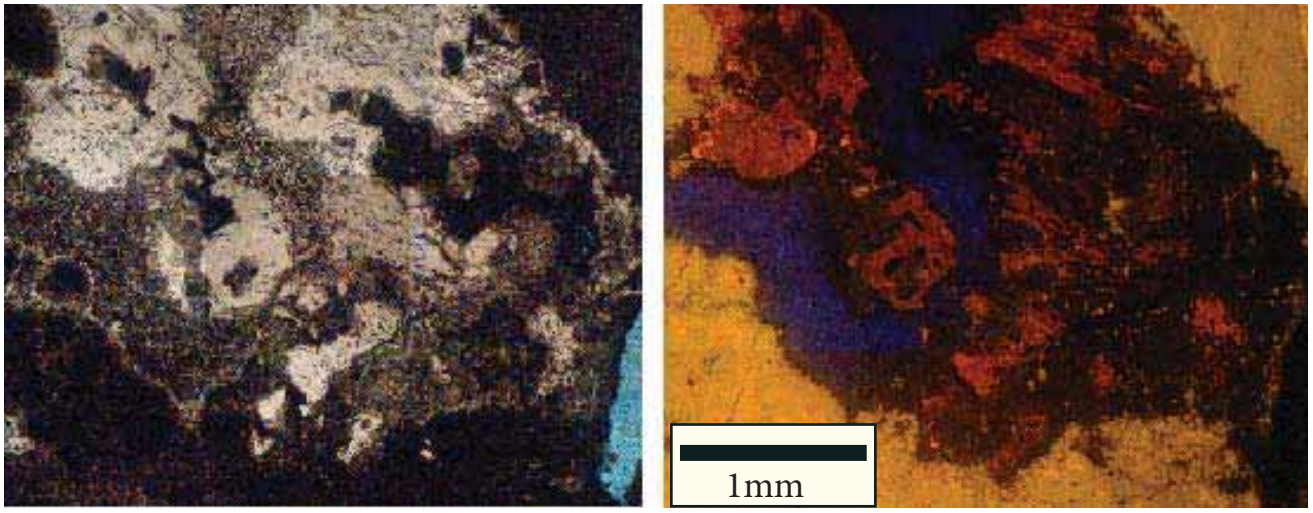

Serie 3. Abundant dickite and dedolomite cements in fracture areas.

Sample 104.

Sand dike. Fault N: upper part of the paleokarst system.

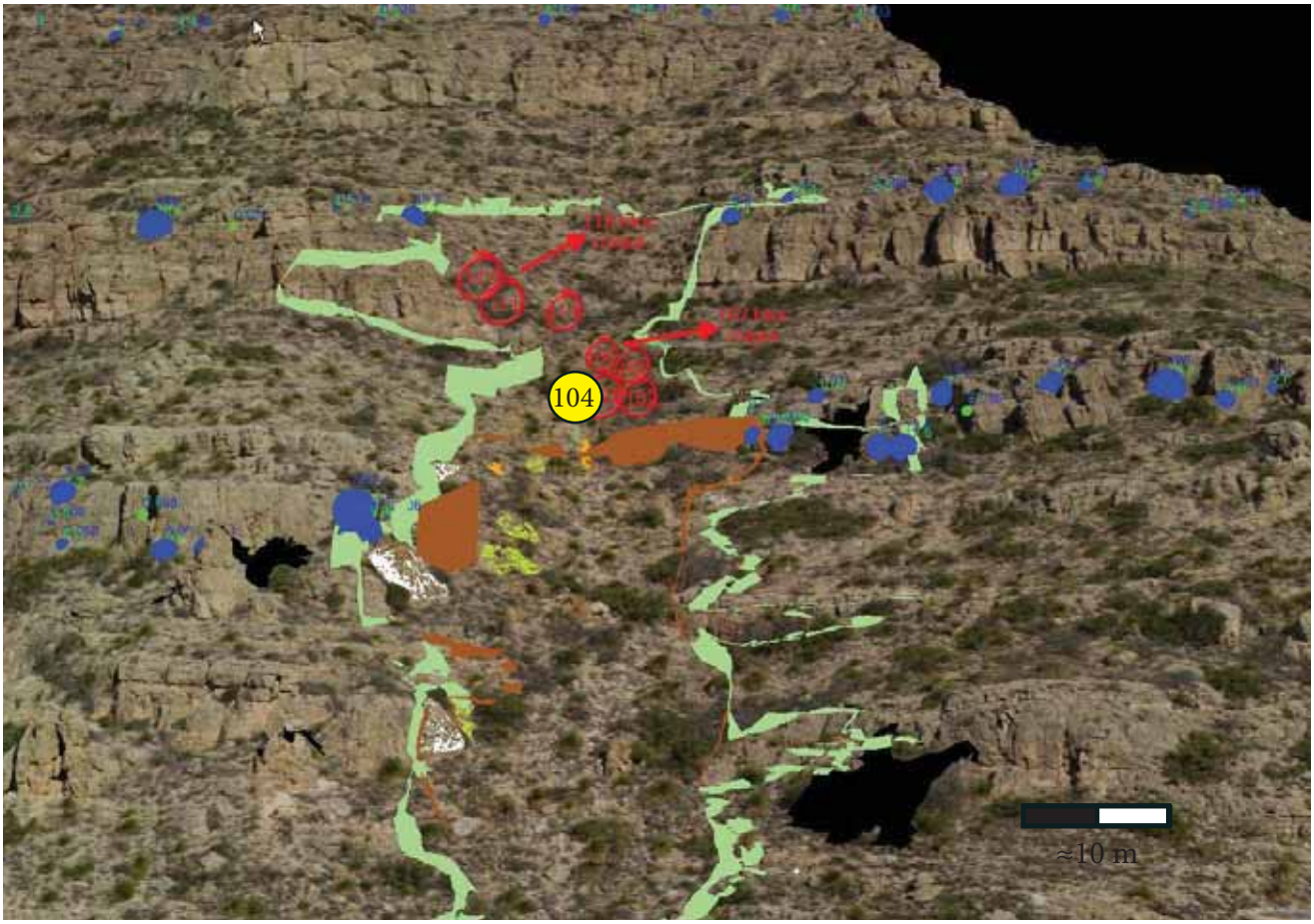

Just above: Photograph of the hand sample. At the right: Scanner of the thin section with the position of CL photomosaics.

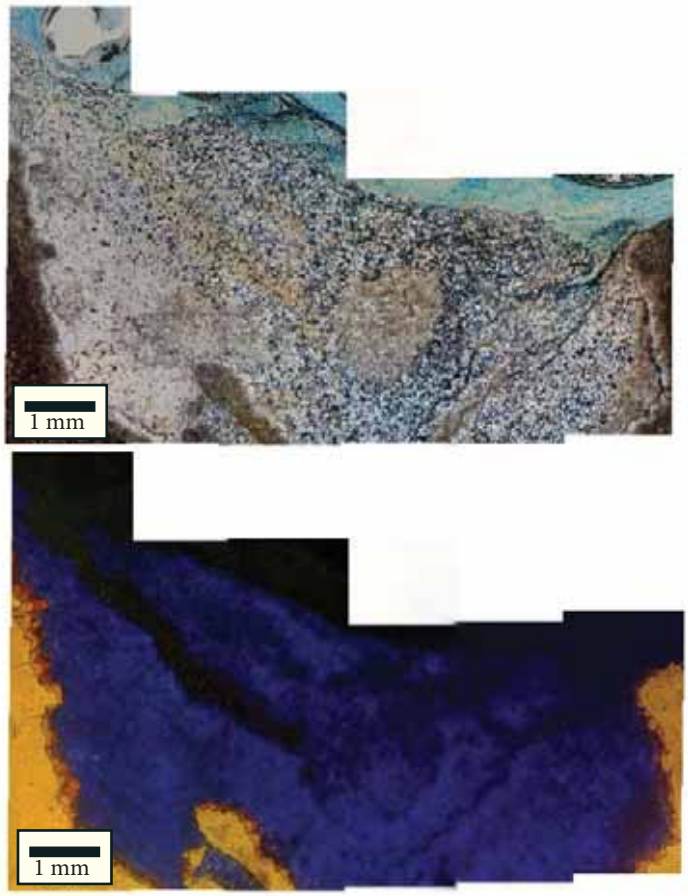

Serie 1. Massive dickite cementation.

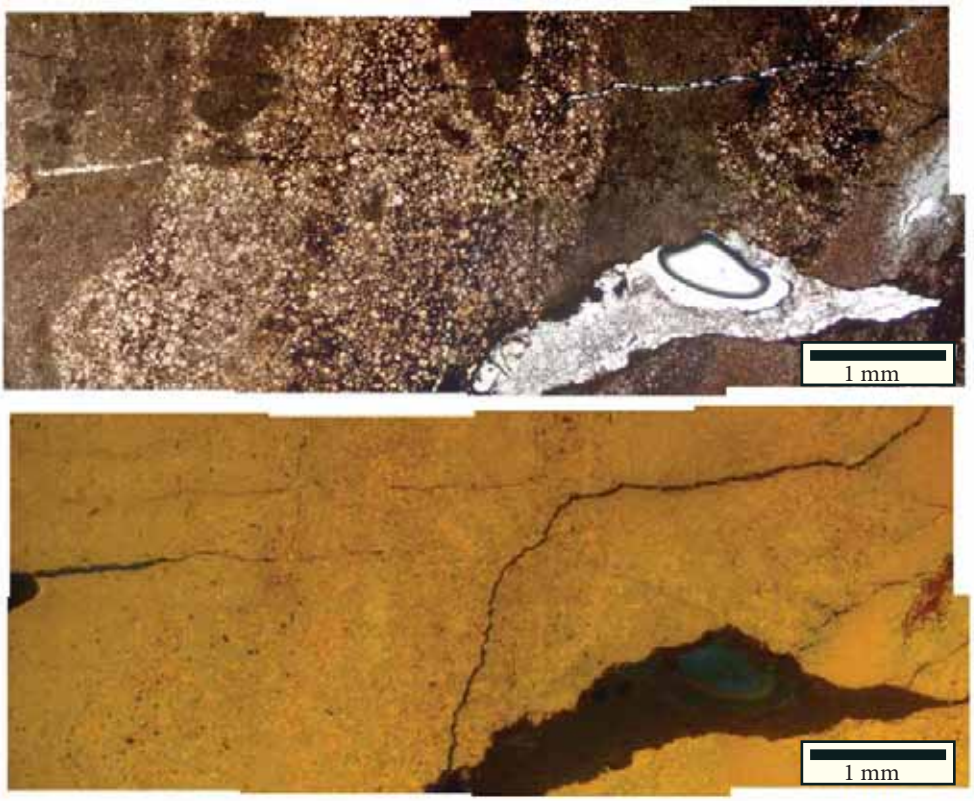

Serie 2. Homogeneous detrital replacive dolomite with calcite cemented cavities.

Appendix Two

Table I **ICP data**

Table II **Stable Isotope data**

Table III **Poroperm data**

Poroperm samples	Table I : ICP data										
Upper level	ICP sample	Description	nº lab sample	ppm Ca	ppm Sr	ppm Mn	ppm Na	ppm Mg	%Mg (weight)	ppm Zn	ppm Fe
67	67_1	pisoid	30	203942	52	50	555	123247	12	21	1065
	67_2	interpisoid cement	31	326774	139	12	895	26038	3	10	81
	67_3	pisoid core	32	201958	43	42	738	121863	12	19	555
63	63_1	bulk	9	220459	48	79	317	113926	11	13	977
	63_2	pisoid	10	213253	37	64	337	114945	11	13	496
50	50_1	bulk	47	215221	42	37	646	130674	13	9	572
53	53_1	cement	37	279077	48	3	206	6356	1	9	39
	53_2	bulk	38	200924	36	45	289	94159	9	99	673
57	57_1	bulk	28	185699	43	35	603	114754	11	12	894
60	60_1	pisoid core	6	177712	39	26	352	106303	11	10	442
	60_2	cement	5	211111	28	44	133	127088	13	10	811
	60_3	bulk	8	207199	73	68	410	122659	12	15	1253
Middle level		Description	nº lab sample	ppm Ca	ppm Sr	ppm Mn	ppm Na	ppm Mg	%Mg (weight)	ppm Zn	ppm Fe
45	45_1	pisoid	33	209202	28	126	161	128454	13	7	529
	45_2	bulk	34	205836	30	134	220	128120	13	12	735
42	42_1	bulk	35	217938	17	49	250	131615	13	10	195
40	40_1	bulk	39	205993	25	108	264	126239	13	8	551
39	39_1	green sediment	19	204452	67	510	349	123388	12	24	1223
	39_2	cement	20	236643	80	18	254	36086	4	38	260
	39_3	bulk	21	199795	59	403	340	106425	11	22	979
77	77_1	matrix	23	207644	77	274	298	127148	13	14	1341

Middle level	ICP sample	Description	nº lab sample	ppm Ca	ppm Sr	ppm Mn	ppm Na	ppm Mg	%Mg (weight)	ppm Zn	ppm Fe
77	77_2	red cement	24	214882	45	531	94	128501	13	11	3113
75	75_1	bulk	36	197475	74	263	355	108383	11	18	739
72	72_1	bulk	13	209176	72	241	254	125054	13	17	937
	72_2	interpisoid cement	14	270995	83	215	641	50866	5	13	235
78	78_1	pisoid	2	220166	62	199	561	134091	13	11	1245
	78_2	interpisoid cement	3	172225	30	325	46	102852	10	11	4192
	78_3	bulk	4	199547	56	193	394	118665	12	16	1472
80	80_1	brown cement	43	44259	55	24	131	24516	2	25	272
	80_2	cement	44	154352	53	146	77	54017	5	14	1393
	80_3	bulk	45	203494	63	215	549	120933	12	10	1032
81	81_1	pink sediment	25	191783	64	150	540	110742	11	23	1476
	81_2	yellow sediment	26	216307	72	168	825	125963	13	17	1211
84	84_1	bulk	18	209477	64	207	260	111951	11	12	816
97	97_1	bulk	11	234260	92	74	258	104039	10	13	655
Lower level		Description	nº lab sample	ppm Ca	ppm Sr	ppm Mn	ppm Na	ppm Mg	%Mg (weight)	ppm Zn	ppm Fe
37	37_1	bulk	46	221041	41	55	715	101776	10	10	486
38	38_2	bulk	49	207464	26	87	502	126974	13	9	846
32	32_1	bulk	29	214565	16	51	288	132273	13	12	291
30	30_1	clast	17	203618	18	36	235	124420	12	8	268

Lower level	ICP sample	Description	nº lab sample	ppm Ca	ppm Sr	ppm Mn	ppm Na	ppm Mg	%Mg (weight)	ppm Zn	ppm Fe
30	30_2	bulk	16	218613	22	70	271	133327	13	10	731
26	26_1	bulk	40	212824	28	71	218	123858	12	10	399
18	18_1	bulk	12	220703	55	180	1243	133153	13	16	1031
16	16_1	bulk	48	200036	38	45	519	50640	5	13	602
15	15_1	bulk	7	187670	47	104	897	106250	11	12	564
10	10_1	bulk	27	174009	35	37	481	105452	11	8	224
8	8_1	bulk	1	226350	37	40	596	112141	11	9	173
7	7_1	bulk	15	211009	24	55	210	127741	13	10	405
5	5_1	bulk	22	209140	21	25	371	125412	13	10	244
6	6_1	pisoid	41	169902	15	25	877	114024	11	40	321
	6_2	bulk	42	207793	15	21	240	129024	13	7	209
Karst samples	ICP sample	Description	nº lab sample	ppm Ca	ppm Sr	ppm Mn	ppm Na	ppm Mg	%Mg (weight)	ppm Zn	ppm Fe
45	45A_1	bulk	84	199798	44	252	299	123391	12	9	1972
46	46A_1	red sediment	78	204439	37	181	410	127567	13	15	2570
	46A_2	cement	79	321135	79	102	168	45614	5	8	965
	46A_3	yellow sediment	80	161455	34	158	468	108928	11	28	1648
52	52_1	bulk	56	231979	49	123	231	95876	10	10	711
	52_2	cement	57	276683	58	112	125	1246	0	7	8
59	59_1	pisoid	60	209946	36	128	216	126700	13	11	1168
	59_2	interpisoid cement	77	311213	71	144	91	6272	1	16	34
65	65A_1	red detrital sediment	81	209954	44	272	462	130400	13	9	2360

Karst samples	ICP sample	Description	nº lab sample	ppm Ca	ppm Sr	ppm Mn	ppm Na	ppm Mg	%Mg (weight)	ppm Zn	ppm Fe
65	65A_2	green sediment	82	210009	53	304	374	127947	13	14	1729
	65A_3	cement	83	375716	85	66	91	2570	0	7	85
66	66C_1	cement	58	376575	85	86	58	1728	0	9	23
	66C_2	yellow/green sediment	59	217459	76	380	560	117322	12	40	1909
69	69_1	black sediment	68	211502	40	343	348	130411	13	13	2992
	69_2	green sediment	69	278164	65	223	468	82434	8	15	1529
	69_3	cement	70	381227	74	108	498	1325	0	10	27
84	84A_1	cement	75	374761	62	49	139	2115	0	6	20
	84A_2	bulk	76	212000	52	432	513	114441	11	13	1737
91	91B_1	brown sediment	73	187660	91	423	564	111502	11	58	3253
	91B_2	pisoid	74	205131	80	336	288	124257	12	14	1661
	91B_3	cement	62	288954	77	41	346	38321	4	24	196
105	105_1	brown sediment	71	209253	80	325	344	108302	11	34	6387
	105_2	pink pisoid	72	216458	73	228	313	128537	13	45	2887
113	113_1	red sediment	50	204821	66	194	647	127156	13	15	1430
	113_2	yellow sediment	52	219852	63	257	263	121304	12	11	1898
	113_3	beige carbonate mud	51	227160	48	123	243	116370	12	10	815

Karst samples	ICP sample	Description	nº lab sample	ppm Ca	ppm Sr	ppm Mn	ppm Na	ppm Mg	%Mg (weight)	ppm Zn	ppm Fe
115	115_1	bulk	86	208433	47	180	412	130256	13	18	1692
117	117_1	yellow sediment	53	206416	58	176	263	126054	13	12	1862
	117_2	pink sediment	54	206726	60	176	272	125900	13	20	1428
	117_3	cement	55	190424	41	178	285	118430	12	8	774
121	121B_1	bulk	61	268733	141	160	286	48619	5	11	1282
122	122_1	bulk	63	208494	32	124	340	124635	12	11	1177
126	126_1	bulk	64	194495	47	236	362	120276	12	12	1399
129	129_1	sand	65	122464	47	181	257	73622	7	18	1540
	129_2	bulk	66	209822	70	284	376	126005	13	46	1512
	129_3	cement	67	364361	62	194	273	2258	0	8	13
131	131_1	bulk	85	28876	9	117	88	14476	1	7	1734

Table I. ICP data from the studied samples of Rattlesnake Canyon.

Table II : Stable Isotope data					
Field Sample	Category	Powder sample	Mineralogy	δ13C (‰PDB)	δ18O (‰PDB)
10 poroperm	adjacent host rock	10_1	cc+dol	4,14	0,03
		10_2	cc+dol	4,89	0,59
15 poroperm		15_1	dol	6,21	1,86
16 poroperm		16_1	dol	5,86	1,81
26 poroperm		26_2	dol	4,89	0,39
32 poroperm		32_1	dol	6,24	1,70
45 poroperm		45_1	dol	6,51	1,23
		45_3	dol	6,29	0,53
46 poroperm		46_1	dol	6,24	2,03
		46_3	dol	6,30	2,10
5 poroperm		5_1	dol	6,07	1,01
		5_2	dol	5,11	0,22
50 poroperm		50_1	dol	7,73	1,28
52 poroperm		52_2	dol	6,06	1,21
		52_3	dol	5,44	0,05
53 poroperm		53_1	dol	6,56	2,22
		53_2	dol	5,98	1,47
57 poroperm		57_1	dol	5,33	-0,20
59 poroperm		59_2	dol	4,81	-0,32
		59_3	dol	6,29	2,00
6 poroperm		6_1	dol	5,74	0,83
		6_2	dol	6,07	1,22
		6_3	dol	6,17	0,67
		6_4	dol	6,13	0,63
		6_5	dol	5,96	0,32
60 poroperm		60_1	dol	7,01	1,66
		60_2	dol	5,53	0,01
63 poroperm		63_1	dol	6,89	2,37
7 poroperm		7_1	dol	5,67	0,35
		7_2	dol	5,98	1,42
80 poroperm		80_1	dol	4,89	-0,58
81 poroperm		81_1	dol	6,76	2,27
		81_2	dol	5,47	0,61
84 poroperm		84_1	dol	4,94	0,63
97 poroperm		97_1	dol	5,72	0,56
		97_2	dol	6,26	0,95

Field Sample	Category	Powder sample	Mineralogy	δ13C (‰PDB)	δ18O (‰PDB)
105 karst	karst	105_1	dol	6,01	0,98
		105_2	dol	6,49	-0,72
		105_3	dol	5,84	1,03
113 karst		113_1	dol	6,70	1,36
		113_3	dol	4,71	0,24
		113_4	dol	6,57	1,21
115 karst		115_1	dol	6,86	0,86
47 karst		47A_4	dol	5,99	1,12
91 karst		91B_3	dol	5,65	1,44
		91B_4	dol	5,67	1,19
115 karst		115_2 mixture dark red+ yellow matrix	dol	0,69	-5,02
		115_4 mixture dark red + yellow matrix	dol	2,91	-1,38
117 karst		117_3	dol	5,15	-0,37
		117_4	dol	4,95	-0,96
121 karst		121B_1	dol	6,23	1,74
		121B_3	dol	6,24	1,96
122 karst		122_2	dol	6,47	1,63
126 karst		126_2	dol	6,64	0,98
129 karst		129_2	dol	6,71	2,04
		129_3	dol	5,66	0,55
18 poroperm		18_1	dol	6,13	1,24
37 karst		37-1	dol	6,19	1,86
38 karst		38_1	dol	6,17	1,50
40 karst		40_1	dol	6,16	0,77
		40_2	dol	6,51	1,20
		40_3	dol	6,03	0,21
		40_4	dol	6,54	0,99
45 karst		45A_2	dol	5,88	0,44
		45A_3	dol	5,73	0,02
46 karst		46A_1	dol	6,34	1,13
		46A_3	dol	6,00	0,77
		46A_4	dol	6,40	1,76
47 karst		47A_1	dol	5,57	0,88
65 karst		65A_2	dol	6,95	1,29
		65A_3	dol	6,78	1,42
66 karst		66C_3	dol	5,82	-0,18
78 karst		78-1	dol	6,19	0,88
69 karst		69_1 stromatolite	dol	-0,30	-3,13
78 karst		78_2	dol	6,60	1,52

Field Sample	Category	Powder sample	Mineralogy	δ13C (‰PDB)	δ18O (‰PDB)
78 karst	karst	78_3	dol	5,55	0,47
84 karst		84A_2	dol	6,23	1,58
		84A_5	dol	5,43	-0,15
Field Sample	Category	Powder sample	Mineralogy	δ13C (‰PDB)	δ18O (‰PDB)
117 karst	dol cements	117_1	dol	6,37	0,13
		117_2	dol	6,30	-2,38
91 karst		91B_1	dol	6,26	-1,00
		91B_2	dol	6,48	-1,11
84 karst		84A_1	dol	6,23	-0,21
		84A_3	dol	4,58	-0,59
60 poroperm		60_3	dol	7,21	1,54
47 karst		47A_2	dol	5,74	-0,65
50 poroperm		50_2	dol	-3,45	-6,75
122 karst		122_1	dol	6,96	1,78
46 poroperm		46_2	dol	6,23	-1,96
45 poroperm		45_2	dol	6,22	-3,14
84 poroperm		84_3 (may include dark red cc)	dol	3,25	-2,22
Field Sample	Category	Powder sample	Mineralogy	δ13C (‰PDB)	δ18O (‰PDB)
37 poroperm	cc cements	37_2	cc	-2,36	-4,22
113 karst		113_2	cc evaporite pseudomorph	-3,20	-5,91
121 karst		121B_2	cc	-1,36	-5,57
		121B_4	cc	-1,56	-7,69
126 karst		126_1	cc	-5,42	-7,85
129 karst		129_1	cc	-5,36	-6,50
84 karst		84A_4	cc	-13,19	-8,67
65 karst		65A_4	cc	-15,64	-9,80
16 poroperm		16_2	cc	-0,42	-4,22
57 karst		57_2	cc	-7,51	-6,63
Field Sample	Category	Powder sample	Mineralogy	δ13C (‰PDB)	δ18O (‰PDB)
63 poroperm	dd cements	63_2	cc	-9,87	-7,09
15 poroperm		15_3	cc+dol	-6,05	-7,34
69 karst		69_2	cc zone 1	-1,51	-7,84
66 karst		66C_1	cc	-2,74	-10,14
		66C_2.1	cc Zone 2+3	-6,16	-9,00
		66C_2.2	cc Zone 1	-3,23	-6,95
59 karst		59_1	cc Zone 2+3	-8,53	-8,11
46 karst		46A_2	cc zone 1	-2,11	-7,40

Field Sample	Category	Powder sample	Mineralogy	δ13C (‰PDB)	δ18O (‰PDB)
47	dd cements	47A_3	cc Zone 2+3	-4,92	-8,02
52		52_1	cc Zone 2+3	-14,03	-9,58
45		45A_1	cc zone 2+3	-13,03	-9,67
37		37_3	cc Zone 2+3	-2,52	-10,97
65		65A_1	cc	4,69	-8,07
Field Sample	Category	Powder sample	Mineralogy	δ13C (‰PDB)	δ18O (‰PDB)
57	thermal spar	57-1	poikilotopic cc with HC	1,76	-11,32
		57-2	poikilotopic cc with HC	1,11	-14,18
58		58-1	poikilotopic cc with HC	1,37	-11,49
		58-2	poikilotopic cc with HC	1,30	-11,59

Zone 1, 2 and 3 refer respectively to luminescent Zones Dd1, Dd2 and Dd3 (Chapter 6)
HC: hydrocarbons
cc: calcite dd: dedolomite dol: dolomite

Table II. Stable Isotope data from the studied samples of Rattlesnake Canyon. See figures 6.1 and 7.1 for the location of the karst samples and the poroperm samples.

Table III : Poroperm data					
Poroperm sample	Perm: Kg (mD)	Perm KL (mD)	Porosity(%)	Gr.Density(g/cm^3)	Level
1	0,015	0,008	6,115382265	2,84	Lower level
2	0,023	0,013	5,86653743	2,83	
3	0,208	0,129	6,149239039	2,83	
4	<0.010	0,005	5,987194967	2,75	
5	0,012	0,006	5,522679954	2,82	
6	5,14	4,21	3,562354996	2,85	
7	13907	13649	22,54168396	2,81	
8	0,127	0,076	2,011362205	2,82	
9	0,651	0,431	6,024858013	2,86	
10	203	185	16,9532347	2,83	
11	0,01	0,005	1,64226673	2,81	
12	48,9	42,5	12,49664148	2,83	
13	0,063	0,036	9,576140597	2,89	
14	14,9	12,5	9,042078112	2,82	
15	15,5	12,9	12,50556719	2,8	
16	7,42	6,18	10,50818936	2,79	
17	0,014	0,007	6,08883491	2,84	
18	24,1	20,5	21,79326768	2,82	
19	1,81	1,28	16,74520544	2,81	
20	1,53	1,07	10,6338663	2,84	
21	0,012	0,006	2,099945279	2,83	
22	0,012	0,006	2,26013793	2,83	
23	415	387	10,51367653	2,83	
24	384	357	19,90289645	2,83	
25	NMP	NMP	NMP	2,82	
26	2,57	1,98	4,848414228	2,84	
27	6,13	5,09	9,783543299	2,83	
28	0,015	0,008	7,607705655	2,83	
29	0,098	0,058	5,984255075	2,75	
30	4,16	3,35	4,245264315	2,82	
31	0,015	0,008	3,823846422	2,85	
32	0,011	0,006	2,028396502	2,81	
33	781	738	12,65839672	2,82	
34	0,18	0,111	2,377580965	2,86	
35	NMP	NMP	2,495463748	2,83	
36	11	9,19	13,25689857	2,81	
37	167	151	8,287047206	2,83	
38	0,245	0,153	5,010327259	2,89	
39	12,5	10,5	10,94800706	2,82	
40	0,015	0,008	8,431549813	2,8	
41	1276	1217	11,41721364	2,79	
42	51	44,5	6,972727286	2,84	
43	1,94	1,37	8,463170773	2,82	
44	0,027	0,015	10,17092756	2,81	
45	0,012	0,006	2,511626451	2,84	
46	0,011	0,006	2,393671239	2,83	
47	0,388	0,249	8,870860467	2,83	

Poroperm sample	Perm: Kg (mD)	Perm KL (mD)	Porosity(%)	Gr.Density(g/cm³)	Level
48	6,48	5,35	12,85878873	2,83	Upper-level
49	0,014	0,007	4,717709299	2,83	
50	5,05	4,13	2,084435564	2,82	
51	0,015	0,008	4,35289846	2,825460468	
52	NMP	NMP	9,837336772	2,81375232	
53	0,038	0,021	7,568573329	2,821902973	
54	0,358	0,229	4,436390626	2,84842126	
55	5,68	4,68	7,583139827	2,829613172	
56	0,966	0,656	8,321935935	2,838834099	
57	0,134	0,081	4,176398444	2,837422955	
58	0,514	0,336	6,085953881	2,82922343	
59	9,07	7,53	9,563073359	2,833786338	
60	0,058	0,033	4,339524826	2,84308037	
61	8	6,6	9,097978075	2,838319127	
62	0,173	0,106	2,200084714	2,81692863	
63	0,077	0,045	3,931543686	2,80817575	
64	6,64	5,41	9,117309208	2,83615685	
65	55	48	14,27595437	2,827205724	
66	1,8	1,27	11,02239815	2,83916725	
67	2,4	1,84	9,260127008	2,907568312	
68	0,105	0,062	4,660640701	2,840165095	
69	0,023	0,012	3,367081219	2,819333386	
70	0,063	0,036	5,078600802	2,825905921	Middle level
71	0,278	0,175	6,621245602	2,830528074	
72	0,275	0,173	8,045457872	2,847735073	
73	0,042	0,024	4,133122158	2,808624689	
74	0,076	0,044	9,469570326	2,837736376	
75	0,152	0,092	7,93017851	2,84706167	
76	3,94	3,15	8,799732208	2,842999917	
77	<0.010	<0.005	2,518827548	2,837072236	
78	1,66	1,16	4,453113097	2,832860889	
79	1,5	1,04	4,746420995	2,832539533	
80	0,018	0,01	2,797890212	2,842006936	
81	1047	995	18,40033856	2,837121831	
82	0,053	0,03	8,804653271	2,837644363	
83	0,035	0,019	4,533040463	2,844117977	
84	52,8	45,9	11,17170367	2,839417601	
90	10,2	8,5	8,088745496	2,838033345	
91	1,59	1,11	10,39961407	2,839867524	
92	0,015	0,008	2,493227843	2,821887934	
93	489	458	7,341117351	2,851513292	
94	141	127	10,94448493	2,849150676	
95	10,8	9,01	6,827331544	2,845447322	
96	0,045	0,026	3,928728089	2,838917563	
97	0,395	0,254	2,41104251	2,818718347	

Table III. Porosity, permeability and grain density values for the samples studied in Rattlesnake Canyon (see figure 7.1 for sample locations). NMP: Non measured parameter.